Linear structure of nonlinear dynamic systems via Koopman decomposition

by

Wei Zhang

B.S., Nanjing University of Aeronautics and Astronautics, China, 2010

M.S., Nanjing University of Aeronautics and Astronautics, China, 2013

M.S., New Mexico State University, U.S.A., 2016

AN ABSTRACT OF A DISSERTATION

submitted in partial fulfillment of the
requirements for the degree

DOCTOR OF PHILOSOPHY

Department of Mechanical and Nuclear Engineering
Carl R. Ice College of Engineering

KANSAS STATE UNIVERSITY
Manhattan, Kansas

2019

Abstract

Linear structure and invariant subspaces of nonlinear dynamics are revealed, extending the superposition principle and invariant subspaces from linear dynamics. They are achieved by considering dynamics in its dual space and the local spectral Koopman theory. The Koopman eigenfunctions constitute invariant subspaces under the given dynamic system, providing convenient bases for the linear structure. On the other hand, the locality and infinite dimensionality are identified as two unique properties of nonlinear dynamics, where the former refers to the spectral problem is locally defined, and the latter refers to Koopman spectrums are recursively proliferated by nonlinear interaction.

Koopman spectral theory is studied. For a linear time-invariant (LTI) system, its linear spectrum is a subset of Koopman spectrums. High order Koopman spectrum can be obtained for nonlinear observables using the proliferation rule. For a linear time-variant system (LTV), Koopman decomposition is obtained by the eigenvalue problem of its fundamental matrix. Besides the general LTV, the periodic LTV system is studied using the Floquet theory. The Floquet spectrums are found to be Koopman spectrums. For a nonlinear system, a local Koopman spectrum problem is defined for a parameterized semigroup Koopman operator, and the simple local spectra are found to be conditionally continuous from the operator perturbation theory. The proliferation is found to recursively applicable to nonlinear dynamics. Moreover, the hierarchy structure of the Koopman decomposition of nonlinear systems is discovered, by decomposing dynamics into base and perturbation on top of it.

The numerical algorithm, dynamic mode decomposition (DMD), is examined for its applicability to capture the spectra and modes for a variety of dynamic systems. A more robust and efficient framework based on generalized eigenvalue problem (GEV) is proposed, which is then solved by a least-square solution (LS) or a total least square solution (TLS).

Therefore, two algorithms, DMD-LS and DMD-TLS algorithm, are developed. DMD-LS algorithm is mathematically equivalent to the standard DMD algorithm first proposed by Schmid (2010) but more robust. DMD-TLS is more accurate for noise data. A residue-based criterion is developed to choose dynamically important or true DMD modes from trivial or spurious modes that often appear in DMD computations.

Linear structure via Koopman decomposition is first applied to a linear dynamic system and an asymptotic nonlinear system, for example. Then flow past fixed cylinder of a Hopf bifurcation process is numerically studied via DMD technique. The equivalence of Koopman decomposition to the GSA is verified at the primary instability stage. The Fourier modes, the least stable Floquet modes, and their high-order derived Koopman modes are found to be the superposition of countable infinite Koopman modes when the flow reaches periodic by considering continuity of Koopman spectrum and the invariance of Koopman modes to the nonlinear transition process. The nonlinear modulation effects, namely, the modulation of the mean flow and the resonance phenomena is explained similarly. The coherent structures are also found to be related to the decomposition.

A DMD based model order reduction method is implemented based on Galerkin projection. The model reduction approach is applied to both the transitional and the periodic stages of flow passing a fixed cylinder. Accurate dynamics and frequencies are rebuilt.

Linear structure of nonlinear dynamic systems via Koopman decomposition

by

Wei Zhang

B.S., Nanjing University of Aeronautics and Astronautics, China, 2010

M.S., Nanjing University of Aeronautics and Astronautics, China, 2013

M.S., New Mexico State University, U.S.A., 2016

A DISSERTATION

submitted in partial fulfillment of the
requirements for the degree

DOCTOR OF PHILOSOPHY

Department of Mechanical and Nuclear Engineering
Carl R. Ice College of Engineering

KANSAS STATE UNIVERSITY
Manhattan, Kansas

2019

Approved by:

Major Professor
Mingjun Wei

Copyright

Abstract

Linear structure and invariant subspaces of nonlinear dynamics are revealed, extending the superposition principle and invariant subspaces from linear dynamics. They are achieved by considering dynamics in its dual space and the local spectral Koopman theory. The Koopman eigenfunctions constitute invariant subspaces under the given dynamic system, providing convenient bases for the linear structure. On the other hand, the locality and infinite dimensionality are identified as two unique properties of nonlinear dynamics, where the former refers to the spectral problem is locally defined, and the latter refers to Koopman spectrums are recursively proliferated by nonlinear interaction.

Koopman spectral theory is studied. For a linear time-invariant (LTI) system, its linear spectrum is a subset of Koopman spectrums. High order Koopman spectrum can be obtained for nonlinear observables using the proliferation rule. For a linear time-variant system (LTV), Koopman decomposition is obtained by the eigenvalue problem of its fundamental matrix. Besides the general LTV, the periodic LTV system is studied using the Floquet theory. The Floquet spectrums are found to be Koopman spectrums. For a nonlinear system, a local Koopman spectrum problem is defined for a parameterized semigroup Koopman operator, and the simple local spectra are found to be conditionally continuous from the operator perturbation theory. The proliferation is found to recursively applicable to nonlinear dynamics. Moreover, the hierarchy structure of the Koopman decomposition of nonlinear systems is discovered, by decomposing dynamics into base and perturbation on top of it.

The numerical algorithm, dynamic mode decomposition (DMD), is examined for its applicability to capture the spectra and modes for a variety of dynamic systems. A more robust and efficient framework based on generalized eigenvalue problem (GEV) is proposed, which is then solved by a least-square solution (LS) or a total least square solution (TLS).

Therefore, two algorithms, DMD-LS and DMD-TLS algorithm, are developed. DMD-LS algorithm is mathematically equivalent to the standard DMD algorithm first proposed by Schmid (2010) but more robust. DMD-TLS is more accurate for noise data. A residue-based criterion is developed to choose dynamically important or true DMD modes from trivial or spurious modes that often appear in DMD computations.

Linear structure via Koopman decomposition is first applied to a linear dynamic system and an asymptotic nonlinear system, for example. Then flow past fixed cylinder of a Hopf bifurcation process is numerically studied via DMD technique. The equivalence of Koopman decomposition to the GSA is verified at the primary instability stage. The Fourier modes, the least stable Floquet modes, and their high-order derived Koopman modes are found to be the superposition of countable infinite Koopman modes when the flow reaches periodic by considering continuity of Koopman spectrum and the invariance of Koopman modes to the nonlinear transition process. The nonlinear modulation effects, namely, the modulation of the mean flow and the resonance phenomena is explained similarly. The coherent structures are also found to be related to the decomposition.

A DMD based model order reduction method is implemented based on Galerkin projection. The model reduction approach is applied to both the transitional and the periodic stages of flow passing a fixed cylinder. Accurate dynamics and frequencies are rebuilt.

Contents

List of Figures

List of Tables

Acknowledgments

First and foremost I would like to express my gratitude to my advisor, Prof. Mingjun Wei, for his continuous support through my Ph.D. studies. He revealed me the fascination of science, mentored me in both academic and personal development. His insight into research helps me distill the vague idea and put in a precise and accurate scientific work. His enthusiasm is contagious and motivational, making every discussion an enjoyable moment for me. His guidance and support are far beyond scientific research but also in my life and future career. It has been an honor for me to be his Ph.D student and I could not have imagined having a better advisor.

I also want to express my appreciation to Prof. Shing I. Chang, Prof. Hitesh Bindra, Prof. Jeremy Roberts, and Prof. Haibo Dong for their encouragement and thoughtful discussions.

My sincere thanks also go to my former and current colleagues, particularly Dr. Min Xu, Dr. Haotian Gao, Dr. Mehdi Tabandeh, Kun Jia, Elnaz Rezaianzadeh, Bolun Xu, Prof. Bashar R. Qawasmeh.

I gratefully acknowledge the financial support from the Air Force Office of Scientific Research (AFOSR), Army High Performance Computing Research Center (AHPCRC) and Micro Autonomous System and Technology (MAST) CTA.

Lastly, I would like to thank my family for all their love and encouragement. It is great to always have them by my side.

Dedication

To my grandparents.

Chapter 1

Introduction

> No man ever steps in the same river twice, for it's not the same river and he's not the same man.
>
> *Heraclitus (Greek), 544-483 BC*

1.1 Introduction of dynamic systems

The Greek philosopher Heraclitus believed that the cosmos was undergoing constant changing, as day became night and hot became cold. To him, the constant changing of reality was one fundamental constancy. All things were always in flux, and the only thing that did not change was changing itself.

Nowadays, what Heraclitus described is known as dynamic systems, which study the changing of objects. Their research topics range from the motion of the smallest scales atoms to the motion of the largest scale celestial objects, or from the growth of living embryo to the mechanical motion of machinery, or from deterministic systems to the highly nonlinear systems which may subject to unpredictable factors such as economics. In short, it studies variables changing with time

$$x = x(t). \tag{1.1}$$

For example, the trajectory of a raindrop falling on a valley, as illustrated in figure 1.1

is a dynamic system.

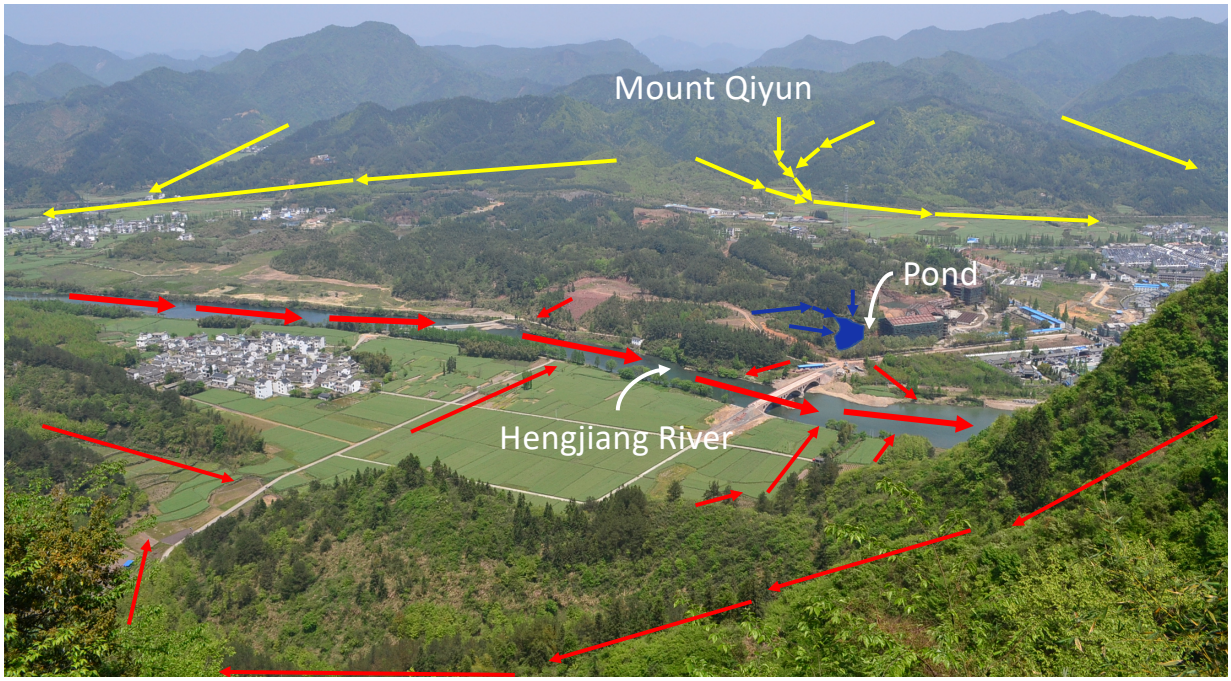

Figure 1.1: *Water drop dynamics on a landform at the valley of Qiyunshan, Anhui, China. Photo courtesy Dr. Tianxiang Xia.*

A water drop subjects to the gravity and the constraint of landform. From one's experience, it is not difficult to conjecture the possible trajectory. For example, a raindrop that falls sufficiently close to the river will flow into it and travel within it, as indicated by the red vectors. Water drops sufficiently close to the water pond may flow into the pond, as illustrated by blue vectors. Alternatively, some raindrops fall on the Qiyun mountain will first travel to the mountain creek and eventually flow into the Hengjiang River, as shown by the yellow arrows.

The above example shows some essential characters of a complex dynamic system. First, a dynamic system is usually quite simple in a local area. It can be joined piece-wisely to give the overall dynamics as the piecewise trajectory shown in figure 1.1. Secondly, the landform represents several key features of a dynamic system. For example, the water pond acts as the attraction basin, and water surrounds it will flow in and stay there. On the contrary, the mountain acts as a repellent from which water flows away. The river represents another phenomenon. It is unstable in one direction, but stable in others.

Though it is easy to find the trajectories for a dynamic system equipped with a convenient geographical view, however, not all dynamic systems are so. Moreover, the crude linearized trajectories may not provide enough accuracy for our needs. A modern dynamic system is usually described by the differential equations following Newton and Leibniz, and dynamics are obtained by solving it

$$\dot{x} = f(x, t). \tag{1.2}$$

Here $\dot{x} = \frac{\partial x}{\partial t}$ is the time change rate of the quantities of interested. $f(x, t)$ is the function of current status and current time.

Unfortunately, without the geographic map, it is hard to obtain the 'bird view' as we did in figure 1.1. Also, the analytical solution is even harder to obtain. Though sometimes the above piecewise study can be carried out, it is usually restricted to the linear stability analysis around specific equilibrium points. A more practical approach is to study the specific trajectory starting from some given initial points. However, in this approach, our understanding of the system is still limited. From time to time, the 'bird view' of the problem, instead of specific trajectories, is needed. To build such a map is the initial motivation for this work.

Though the techniques we developed in this work apply to general dynamic systems, we mainly study the fluid dynamic system, which is introduced in the next section.

1.2 Fluid mechanics and Navier-Stokes equation

> Now I think hydrodynamics is to be the root of all physical science and is at present second to none in the beauty of its mathematics.
>
> *William Thomson (Lord Kelvin), 1824-1907*

Lord Kelvin was right when addressing George G. Stokes in a letter in 1857, remarking the status of fluid mechanics. Especially if one recalls the 200 years' development of mechanics since Newton published the famous '*Philosophia Naturalis Principia Mathematica*' in 1687, the foundation of classical mechanics.

The study of fluid mechanics dates back to the Greek mathematician Archimedes (287-212 BC) provided an exact solution to the fluid-at-rest problem and the expression for the buoyant force on various bodies. The progress is stagnant until the Renaissance genius, Leonardo da Vinci (1452-1519), deduced the conservation of continuity of incompressible flow in one dimension. Moreover, he left detailed descriptions and sketches of the smooth and eddy motions of water up to 121 pages in his notebook (Gad-el Hak, 1998). Even today, his notion, such as coherent structure, eddies, eddying motions are still used in the same way. Besides the interest of water, he also studied aerodynamic. He designed parachutes, jets, helicopters, and wind vanes.

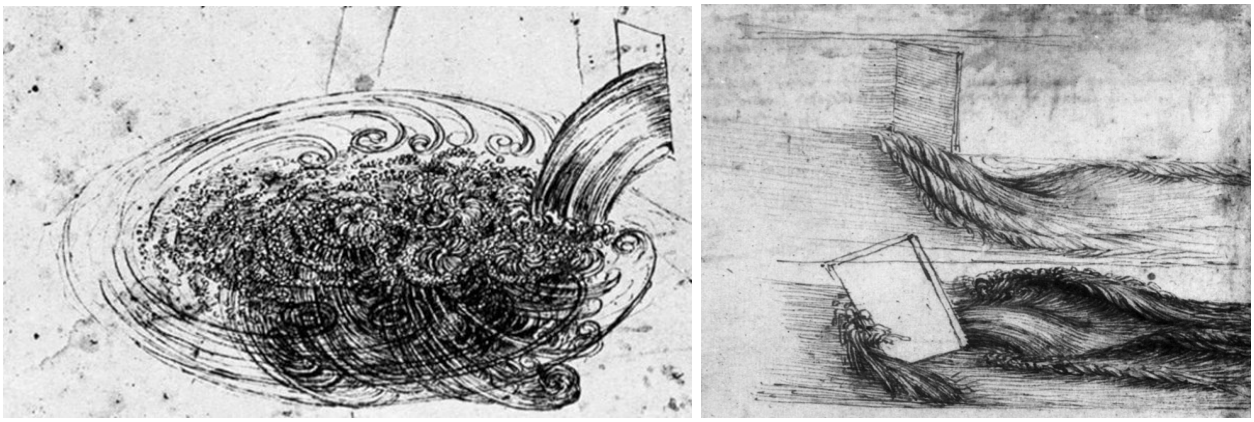

(a) *Water jet from square hole to pond* **(b)** *Water separated by bluff body*

Figure 1.2: *Water motion sketched by Leonardo da Vinci*

Fluid mechanics comes to its summit when the fluid dynamics equations are developed. The principle of fluid mechanics is summarized in the Navier-Stokes equation. Notable names shine during the development of these equations. Navier (1823), Cauchy (1828), Poisson (1829), Saint Venant (1843), and Stokes (1845) provided an excellent model for both laminar and turbulent flows. The set of equations were written

$$\frac{\partial \rho}{\partial t} + \frac{\partial}{\partial x_k}\left(\rho u_k\right) = 0, \tag{1.3}$$

$$\rho\left(\frac{\partial u_i}{\partial t} + u_k \frac{\partial u_i}{\partial x_k}\right) = \frac{\partial \tau_{ki}}{\partial x_k} + \rho g_i, \tag{1.4}$$

$$\rho\left(\frac{\partial e}{\partial t} + u_k \frac{\partial e}{\partial x_k}\right) = -\frac{\partial q_k}{\partial x_i} + \tau_{ki}\frac{\partial u_i}{\partial x_k}. \tag{1.5}$$

where ρ is the fluid density, u_k is the velocity in x, y, z-direction respectively. τ_{ki} is the second order stress tensor. g_i is the body force per unit mass in three dimensional, and e is the internal energy per unit mass. q_k is the heat flux due to conduction and radiation.

However, the flow equation is not closed. The number of unknowns (17) is greater than that of equations (5). To close the Navier-Stokes equations, some efforts need to be undertook. If fluid is Newtonian, isotropic, ideal gas(for gas), and assume Fourier law for heat flux and symmetry of stress tensor, the Navier-Stokes equations are reduced to the following simplified form.

$$\nabla \cdot \boldsymbol{u} = 0, \tag{1.6}$$

$$\frac{\partial \boldsymbol{u}}{\partial t} + (\boldsymbol{u} \cdot \nabla)\boldsymbol{u} = -\nabla p + \frac{1}{Re}\nabla^2 \boldsymbol{u}. \tag{1.7}$$

These are non-dimensional equations, where $x = \frac{x^*}{L}$, $y = \frac{y^*}{L}$, $z = \frac{z^*}{L}$, $t = \frac{t^*}{L/U}$, $u = \frac{u^*}{U}$, $v = \frac{v^*}{U}$, $w = \frac{w^*}{U}$, $p = \frac{p^*}{\frac{1}{2}\rho U^2}$. $(\cdot)^*$ are dimensional variables and $(\cdot)$ is the corresponding non-dimensional ones. L is the characteristic length and U is the reference velocity.

$$Re = \frac{\rho U L}{\mu} \tag{1.8}$$

is called Reynolds number in honer of Osborne Reynolds for his classic experiments in 1883, which revealed the flow instability phenomena.

The above equations are nonlinear. Only a few simple cases can be solved analytically. In practice, people usually observe the experimental result or search the numerical solution with the aid of computers.

1.3 A linear dynamic system example

1.3.1 The superposition principle

It is well known a linear system has superposition principle, that is, net response of a linear system to multiple excitation is the linear sum of each caused by the excitation individually. For instance, water ripples in figure 1.3 on a pond look like one superimposes on another, as wave on water surface is described by linear wave equation (Dean and Dalrymple, 1991).

Figure 1.3: *Water ripples. Photo courtesy of Jim Simandl, Golden Gardens Park, Seattle.*

More specifically, putting above relation in equation, for a linear system

$$\dot{x} = f(x), \tag{1.9}$$

where $f(ax_1 + bx_2) = af(x_1) + bf(x_2)$ for any $x_1, x_2, a, b \in \mathbb{R}$. If x_1, x_2 both satisfy the equation, then $ax_1 + bx_2$ is also its solution, since

$$\frac{d}{dt}(ax_1 + bx_2) = a\dot{x}_1 + b\dot{x}_2 = af(x_1) + bf(x_2) = f(ax_1 + bx_2). \tag{1.10}$$

The principle of superposition provides great advantage to solving and understanding linear dynamics.

1.3.2 The invariant subspace

Linear dynamics can be decomposed into invariant subspaces, which can be illustrated by a linear time-invariant (LTI) system

$$\dot{\boldsymbol{x}} = A\boldsymbol{x}, \quad \boldsymbol{x}(0) = \boldsymbol{x}_0. \tag{1.11}$$

$\boldsymbol{x} \in \mathcal{R}^n$ and $A \in \mathcal{R}^{n\times n}$. If A is diagonalizable, and $A = V\Lambda V^{-1}$, the solution of to equation (1.11) is given

$$\boldsymbol{x}(t) = Ve^{\Lambda t}V^{-1}\boldsymbol{x}_0 = c_1 e^{\lambda_1 t}\boldsymbol{v}_1 + \cdots + c_n e^{\lambda_n t}\boldsymbol{v}_n, \tag{1.12}$$

λ_i is the eigenvalue, and $\boldsymbol{v}_i$ is the eigenvector. $\boldsymbol{c} = V^{-1}\boldsymbol{x}_0$ is the initial condition. Therefore, the solution is decomposed into a set of independent and invariant subspaces spanned by the eigenvectors

$$\mathcal{S}_i = \text{Span}\{\boldsymbol{v}_i\}, \tag{1.13}$$

since $A\boldsymbol{v}_i = \lambda_i \boldsymbol{v}_i \in \mathcal{S}_i$. Additionally, each invariant subspaces has exponential dynamics. The invariant subspaces give extra convenience for dynamics analysis.

1.4 Model decomposition and spectral Koopman decomposition

In the study of the nonlinear dynamic systems, one hardly obtains the dynamics by analytically solving the dynamic equation. Instead, experimental or numerical observation of the dynamics is usually adopted. However, the large volume of data collected can be formidable for such task. The observation is usually more fruitful if the dynamics are decomposed into some finite-dimensional modes since a small number of them is enough to capture the most of the dynamics. The bases or modes for modal analysis are an important topic in dynamic system study. One type of selection is the predetermined modes such as the Fourier series, the

Chebyshev series, the Bessel series, or other trigonometry or polynomial series determined by the Sturm-Liouville theory (Marchenko, 1977). Another type is the dynamics induced modes, often termed empirical modes, usually extracted from snapshots of the dynamic system. They are more efficient than the predetermined modes since fewer modes are needed to produce the equivalent reconstruction. For instance, proper orthogonal decomposition (POD) can efficiently capture the dynamics of turbulent flow (Holmes et al., 1996a). However, POD was criticized for not capturing some essential dynamics. Thus a modification called balanced POD or BPOD based on balanced truncation is proposed (Ilak and Rowley, 2008). Dynamic mode decomposition (DMD) (Schmid, 2010) based on the eigendecomposition of a linear approximation system constitutes another option. Other options are available but not listed here.

Among them, DMD, the one based on linear invariant space of the dynamic system, is of particular interest as the dynamics follow the simple exponential law. This technique works for a linear time-invariant (LTI) system. However, its extension to a linear time-variant (LTV) system and a nonlinear dynamic system is not straightforward. There is no rigorous definition of spectrum for a nonlinear system, not to mention that nonlinearity has the notorious reputation of making the nonlinear dynamic systems more complicated. For example, nonlinearity creates more complicated modes by the interaction of flow structures. Also, it modulates the base flow or other flow structures or changes the otherwise simple linear exponential growth (Landau and Lifshitz, 1959). Moreover, from the theory for nonlinear dynamic systems, they admit more complicated equilibrium points such as stable or unstable nodes, spirals, limit cycle solutions, or even multiple of them, or other complicated solutions such as strange attractor, chaos (Strogatz, 2018).

1.4.1 Koopman operator and spectral decomposition

The study of Koopman operator (Koopman, 1931) on nonlinear dynamic systems can date to the 1920s and 1930s when mathematical physicians are interested in the mathematical formulation for the second law of thermodynamics. They need to describe and identify

"microscopically any system approaches an equilibrium state." (Reed and Simon, 1972)

From the macroscopic point of view, the thermal statement of approaching equilibrium is obvious. However, from a microscopic point of view, a system approaches equilibrium is surprising since microscopically, there is no steady state. Therefore, a microscopic justification of thermodynamics must be able to explain the macroscopic second thermodynamic law.

The explanation comes when realizing thermodynamical systems undergo fluctuations. The equilibrium of the thermodynamic system is not an absolute statement about the system at a fixed time, but rather is the statement made over periods long for some characteristic times. Therefore, the equilibrium of thermodynamics should deal with average measurements of observables during time T_c.

The average of some observable defined on the dynamic system over the periodic T_c reaches some equilibrium is given by

$$\lim_{N\to\infty} \frac{1}{N} \sum_{i=1}^{N} f(T^i x) = f^*, \tag{1.14}$$

assuming in T_c period, the system evolves N steps. The induced operator U by the map T

$$Uf(x) = f(Tx), \tag{1.15}$$

is called *Koopman operator*. Thus the second thermodynamic law is related to the fixed point of Koopman operator.

A fixed point is closely related to the spectra of U. There is a theorem which says the map T is ergodic if and only if 1 is a simple eigenvalue of U, and the corresponding eigenfunction $f^*(x)$ is a constant function. A similar but stronger statement for the 'mixing' is also proved (Reed and Simon, 1972, (see, chap. VII.4)).

The previous works focus on the particular spectrum ($\lambda = 1$) of the dynamic systems. Mezić (2005), on the other hand, studied the spectral decomposition of the induced unitary Koopman operator acting on some measure-preserving systems. His study sheds light on

the nonlinear dynamic systems in that the spectral decomposition of the linear yet infinite-dimensional Koopman operator (Mezić, 2005; Rowley et al., 2009) providing bases for dynamics decomposition. This linear operator captures full dynamic information of the nonlinear systems and is applied to various applications. Mezić (2005) studied the Koopman spectrum of a nonlinear dynamic system working around an attractor by harmonic averaging or discrete Fourier transform. Rowley et al. (2009) numerically studied the spectrum of jet flow. The Koopman spectrum can be obtained by studying its adjoint, the Frobenius-Perron operators (Frobenius et al., 1912; Perron, 1907), of which, Bagheri (2013) computed the Koopman spectrum of Kármán vortex.

The mathematical physicians studied the spectrum of Koopman operator in the global sense, while dynamics oriented researchers studied the spectrum in a local sense (focusing on some particular stages). In this work, a local spectrum definition is given and used to analyzing nonlinear dynamics.

1.5 Highlight of the work

The main contribution of this research is in the following four aspects.

1. A local Koopman spectrum problem is proposed for nonlinear dynamic systems.
   (a) The point spectrums are due to nonlinearity.
   (b) The point spectrums are extended to global domain by employing operator perturbation theory
   (c) The hierarchy structure of Koopman decomposition is discovered for nonlinear dynamics.
2. Linear structure of nonlinear dynamics is proposed.
   (a) The linear structure is due to the completeness of dual space of the dynamics.
   (b) Universal properties of dynamics are linear structure and invariant subspaces.

(c) Nonlinear dynamics have unique properties as locality and infinite-dimensionality.

(d) Other decomposition techniques are found to be related to linear structure.

3. A new framework based generalized eigenvalue problem for DMD algorithm is proposed.

   (a) Generalized eigenvalue problem provides a robust algorithm for DMD algorithm.

   (b) The generalized eigenvalue problem is solved in a projection approach.

   (c) DMD-LS and DMD-TLS algorithms based on least-square and total least-square problem are developed.

   (d) A residue-based mode selection criterion is developed.

4. A nonlinear transition process is studied by the Koopman decomposition. The following are explained by Koopman decomposition.

   (a) Fourier expansion.

   (b) Floquet theory.

   (c) Resonance effect.

   (d) Coherent structure

1.6 Contents of this work

The following summarizes the content of this work.

The Koopman operator and its local spectrums are introduced in chapter 2. We first study the Koopman spectrum of an LTI system. Generalization is made to the local spectrum (in time) for an LTV system. The local spectrum is further extended to the nonlinear autonomous dynamic systems. The hierarchy of Koopman decomposition for nonlinear dynamics is introduced. A proliferation rule is derived for the nonlinear observable, which applies recursively to the nonlinear systems. Discussion of continuity of these point Koopman spectrum is undertaken.

Koopman modes are discussed in chapter 3. They are state-independent if the local spectrum is continuous. Koopman modes of linear systems are first analyzed. A multiple-scale analysis and the asymptotic expansion are performed on a nonlinear system. Koopman decomposition provides a full solution of global stability analysis and carries rich information about the dynamic systems.

DMD, a data-driven technique, is examined its applicability to capture the spectrum and modes of various dynamic systems in chapter 4. A new and general framework based on generalized eigenvalue problem (GEV) for DMD algorithm is proposed. The GEV is then transformed into a solvable form by projection, resulting in the projected-GEV. Two related algorithms, DMD-LS and DMD-TLS algorithm, are proposed. A residue-based process to identify the Koopman modes is introduced.

The linear structure of nonlinear dynamics is explained in chapter 5. Particularly, we discussed the significance of Koopman decomposition for dynamic analysis. Moreover, other bases for the linear structure are discussed.

The numerical algorithm for simulating fluid dynamics is introduced and benchmarked in chapter 6.

The newly developed projected-DMD algorithm is benchmarked at chapter 7. The dynamics of Kármán vortex after a fixed cylinder is studied and compared with the literature. The DMD-TLS is shown to be more accurate for noisy data.

Dynamic systems with constant spectra are studied in chapter 8. A mass-spring linear system is first studied using a modified DMD-TLS algorithm. The second example studies an asymptotic nonlinear system. Though simple, it illustrates that Koopman decomposition is ideal for modal analysis or instability analysis of nonlinear systems.

The nonlinear transition of a Hopf bifurcation problem is studied in chapter 9. The transition from the fixed unstable equilibrium to the stable limit cycle is studied using the linear structure via Koopman decomposition. The study provides an insight into the transition of the nonlinear systems.

The locality of Koopman decomposition requires an efficient algorithm to provide the global dynamics, reduced-order modeling based on Koopman modes by Galerkin projection

is then presented in chapter 10.

Chapter 2

Koopman operator and Koopman spectrum

> After endless mountains and rivers that leave doubt whether there is a path out, suddenly one encounters the shade of a willow, bright flowers and a lovely village.
>
> *Lu You (China), 1125 - 1210*

The Chinese Southern Song Dynasty poet Lu You described his pleasant journey to a country village 800 years ago after a frustrating struggle for a route. Those trials are rewarding, as there might be a delightful experience awaiting us.

2.1 Introduction to Koopman operator and Koopman spectrum

Considering the following dynamic system evolving on a manifold $\mathcal{M}$ such that ,

$$\boldsymbol{x}_{k+1} = f(\boldsymbol{x}_k), \tag{2.1}$$

$\boldsymbol{x}_k \in \mathcal{M}$. f is the map from $\mathcal{M}$ to itself evoluting the dynamics one step forward, and k is an integer index. (Though a somewhat different definition for the continuous differential

system will be given later, we will focus on the discretized form as if the continuous one can be reasonably discretized.)

An *observable* g is a function defined on the manifold $\mathcal{M}$, $g : \mathcal{M} \to \mathbb{R}$. The use of observable to study dynamics introduces more flexibility for many applications. Moreover, for some systems, the trajectories $\boldsymbol{x}$ may not always be available or of interest. For example, Lasota and Mackey (2013) studied the probability density function (PDF) instead of the sensitive chaotic trajectory to understand the dynamics of the nonlinear deterministic system.

The *Koopman operator* U (Koopman, 1931) is a linear operator defined on the observable, such that it evolves the observable one-step forward.

$$Ug(\boldsymbol{x}_i) = g(\boldsymbol{x}_{i+1}) = g(f(\boldsymbol{x}_i)). \tag{2.2}$$

Koopman operator is linear, since

$$U(\alpha g_1 + \beta g_2)(\boldsymbol{x}_i) = \alpha g_1(\boldsymbol{x}_{i+1}) + \beta g_2(\boldsymbol{x}_{i+1}) = \alpha U g_1(\boldsymbol{x}_i) + \beta U g_2(\boldsymbol{x}_i). \tag{2.3}$$

The linearity of Koopman operator facilitates the spectrum analysis. In fact, the Koopman operator admits a unique decomposition into the singular and regular part (Mezić, 2005; Reed and Simon, 1972).

$$U = U_s + U_r \tag{2.4}$$

U_s, U_r are the singular and regular operator defined on the same domain as U. U_s has pure discrete spectrums while U_r has continuous spectrums. For simplicity this work consider the singular part such that $U = U_s$. Following Mezić (2005), the spectrums of Koopman operator

$$U\phi_i(\boldsymbol{x}) = \rho_i \phi_i(\boldsymbol{x}), \quad i = 1, 2, \cdots, \tag{2.5}$$

where $\phi_i(\boldsymbol{x}) : \mathcal{M} \to \mathbb{R}$ is the Koopman eigenfunction, and $\rho_i \in \mathbb{C}$ is the Koopman spectrum.

However, continuous spectrums are not uncommon in many systems. For a bounded domain or discrete system, its spectrum is usually expected to be discrete. While for the

unbounded system, such as Bénard convection between infinite horizontal planes and plane Poiseuille flow, the spectrums of the linearized perturbation equation are found to be continuous (see Drazin et al., 1982, topic 49), which provide the continuous Koopman spectrums.

The infinite dimensional eigenfunctions $\phi_i(\boldsymbol{x})$ then provide a set of bases for functional analysis. A function, or more specifically the observable on $\mathcal{M}$, can be expanded by

$$g(\boldsymbol{x}) = \sum_i a_i \phi_i(\boldsymbol{x}) + r(\boldsymbol{x}). \tag{2.6}$$

If $\phi(\boldsymbol{x})$s are complete bases for mapping $\mathcal{M} \to \mathbb{R}$, then the residue $r(\boldsymbol{x})$ is zero. The evolution of this observable, residing on the dynamics system, is obtained by applying the Koopman operator

$$\begin{aligned} g(\boldsymbol{x}_{n+1}) = Ug(\boldsymbol{x}_n) = U\left(\sum_i a_i \phi_i(\boldsymbol{x}_n) + r(\boldsymbol{x}_n)\right) = \sum_i U a_i \phi_i(\boldsymbol{x}_n) + Ur(\boldsymbol{x}_n) \\ = \sum_i a_i \rho_i \phi_i(\boldsymbol{x}_n) + r(\boldsymbol{x}_{n+1}) \end{aligned} \tag{2.7}$$

The above equation switched the Koopman operator and summation operator by the linear property of Koopman operator. Moveover,

$$g(\boldsymbol{x}_n) = U^n g(\boldsymbol{x}_0) = \sum_i a_i \rho_i^n \phi_i(\boldsymbol{x}_0) + r(\boldsymbol{x}_n) = \sum_i a_i \rho_i^n \tag{2.8}$$

by absorbing the constant $\phi_i(\boldsymbol{x}_0)$ to a_i and assuming $\phi_i(\boldsymbol{x})$s are complete. On the bases of Koopman eigenfunction, the dynamics evolve like a linear system. The difficulty with Koopman decomposition is the theory is non-constructive, nothing about these Koopman spectrums and eigenfunctions are told.

2.2 Koopman spectrum of LTI systems

A continuous linear time-invariant dynamic system is given by

$$\dot{\boldsymbol{x}} = A\boldsymbol{x}. \tag{2.9}$$

Its discretized form evolving at a constant time interval τ is given by (Boyce et al., 1992)

$$\boldsymbol{x}_{n+1} = e^{\tau A}\boldsymbol{x}_n = A'\boldsymbol{x}_n. \tag{2.10}$$

The matrix exponential $e^{\tau A}$ is defined by

$$e^{\tau A} = I + \tau A + \frac{\tau^2 A^2}{2!} + \cdots + \frac{\tau^n A^n}{n!} + \cdots. \tag{2.11}$$

It is easy to see A and $e^{\tau A}$ share the same eigenvectors, and the spectrums (λ of A and ρ of $e^{\tau A}$) are related by

$$\rho = e^{\tau\lambda}. \tag{2.12}$$

For a continuous LTI system (2.9), Koopman operator is then defined on the discretized equation (2.10).

2.2.1 Spectrum for the linear observable

A linear observable studied by (Rowley et al., 2009)

$$\phi(\boldsymbol{x}) = (\boldsymbol{x}, \boldsymbol{w}), \tag{2.13}$$

is found to be the Koopman eigenfunction

$$U\phi(\boldsymbol{x}) = (A'\boldsymbol{x}, \boldsymbol{w}) = (\boldsymbol{x}, A'^*\boldsymbol{w}) = (\boldsymbol{x}, \bar{\rho}\boldsymbol{w}) = \rho(\boldsymbol{x}, \boldsymbol{w}) = \rho\phi(\boldsymbol{x}). \tag{2.14}$$

The corresponding Koopman spectrum ρ is the spectrum of linear matrix A'. Here $\boldsymbol{w}$ is the left eigenvector of A' ($A'^{*}\boldsymbol{w} = \bar{\rho}\boldsymbol{w}$), and $(\cdot,\cdot)$ is the inner-product.

To the continuous form, the Koopman spectrum computed from (2.12) ($\lambda = \frac{\ln(\rho)}{\tau}$) equals to the spectrum of A. For distinguishing purpose, we will call the spectrum of the discrete form (ρ) the *Koopman multiplier* and the spectrum of the continuous form (λ) the *Koopman exponent*.

The above completes the Koopman spectrums of a linear system for linear observables.

2.2.2 Spectrum of the nonlinear observable

If quadratic observable such as $\boldsymbol{x}^T M\boldsymbol{x}$ is given, we may define a quadratic observable to obtain the corresponding spectrums and eigenfunctions

$$\phi(\boldsymbol{x}) = (\boldsymbol{x}, \boldsymbol{w}_i)(\boldsymbol{x}, \boldsymbol{w}_j). \tag{2.15}$$

The above function is the Koopman eigenfunction since

$$U\phi(\boldsymbol{x}) = \phi(A'\boldsymbol{x}) = (A'\boldsymbol{x}, \boldsymbol{w}_i)(A'\boldsymbol{x}, \boldsymbol{w}_j) = \rho_i\rho_j(\boldsymbol{x}, w_i)(\boldsymbol{x}, w_j) = \rho_i\rho_j\phi(\boldsymbol{x}). \tag{2.16}$$

Thus if ρ_i, ρ_j is spectrum of A', $\rho_i\rho_j$ is the Koopman multiplier corresponding the quadratic observable. Or $\lambda_i + \lambda_j$ is the Koopman exponent for the continuous dynamic system. Similar conclusion was also drawn by a couple of authors, for example, Budišić et al. (2012) under the term 'algebraic structure of eigenfunction under products'. The derived spectrum reflects the dynamics of the quadratic observable.

Another type of nonlinear observable is $\frac{1}{\boldsymbol{x}}$. Then a rational of $(\boldsymbol{x}_n, \boldsymbol{w})$ can be defined

$$\phi(\boldsymbol{x}) = \frac{1}{(\boldsymbol{x}, \boldsymbol{w})}. \tag{2.17}$$

The defined observable is the Koopman eigenfunction since

$$U\phi(\boldsymbol{x}) = \phi(A'\boldsymbol{x}) = \frac{1}{(A'\boldsymbol{x}, \boldsymbol{w})} = \frac{1}{\rho}\phi(\boldsymbol{x}). \tag{2.18}$$

As a result, if $\boldsymbol{x}_n$ is not orthogonal to $\boldsymbol{w}$ and ρ is the spectrum of A', $\frac{1}{\rho}$ is the Koopman multiplier of the discrete dynamic system. Alternatively, $-\lambda$ is the Koopman exponent.

We call (2.16) and (2.18) the *proliferation rule* of Koopman spectrum since new spectrum is produced by nonlinearity. Other nonlinear observables can be first decomposed by the Taylor expansion, or rational series if needed. Koopman eigenfunctions and Koopman spectrums are then obtained by the proliferation rule accordingly.

2.3 Koopman spectrum of LTV systems

2.3.1 The local spectrum of an LTV system

For the linear time-variant system

$$\dot{\boldsymbol{x}} = A(t)\boldsymbol{x}, \quad \boldsymbol{x}(t_0) = \boldsymbol{x}_0, \tag{2.19}$$

$\boldsymbol{x} \in \mathbb{R}^N$ and $A(t) \in \mathbb{R}^{N\times N}$. It is evident that the spectrums are no longer constant and do not reflect the global (in the sense of time) property of the system. Instead, it should be defined in a local sense. However, the spectrum problem is not defined on the matrix $A(t)$, since it ignores the influence of time-varying $A(t)$ on dynamics.

Instead, the spectrum of *fundamental matrix* of the linear dynamic system is adopted. We call $\Psi(t) \in \mathbb{R}^{N\times N}$ the *fundamental matrix* of system (2.19) if each column of $\Psi(t)$ satisfies (2.19) and $\Psi(t)$ is not singular (Boyce et al., 1992). The fundamental matrix provides useful dynamics and stability information, and dynamics of LTV systems only relate to the fundamental matrix but not the transient spectrums of $A(t)$ (Wu, 1974). Moreover, the fundamental matrix provides global (in the sense of time) stability indicator of the system but not $A(t)$. Wu (1974); Zubov (1962) further gave examples where even with the constant

negative/positive eigenvalue of $A(t)$, the system was unstable/stable.

As $\Psi(t)$ is non-singular, a particular fundamental matrix $\Phi(t)$ is defined

$$\Phi(t, t_0) = \Psi(t)\Psi(t_0)^{-1}. \tag{2.20}$$

It is found $\Phi(t_0, t_0) = I$, and the solution to LTV system (2.19) is given by

$$\boldsymbol{x}(t) = \Phi(t, t_0)\boldsymbol{x}_0, \tag{2.21}$$

since $\boldsymbol{x}(t)$ satisfies the LTV system (2.19) and the initial condition $\boldsymbol{x}(t_0) = \boldsymbol{x}_0$.

The discretized form of LTV (2.19) is written

$$\boldsymbol{x}_{n+1} = \Phi(t_{n+1}, t_n)\boldsymbol{x}_n, \tag{2.22}$$

where $\Phi(t_{n+1}, t_n)$ is the matrix (2.20).

Koopman operator can be similarly defined on the dynamic system (2.22) to evolve the dynamics of observable $g(\boldsymbol{x})$. The eigenvalue $\rho(t_n)$ of matrix $\Phi(t_{n+1}, t_n)$, and the function

$$\phi(\boldsymbol{x}, t_n) = (\boldsymbol{x}, \boldsymbol{w}_n), \tag{2.23}$$

are the Koopman eigenvalue and eigenfunction, since

$$\begin{aligned} U\phi(\boldsymbol{x}, t_n) &= \phi(\Phi(t_{n+1}, t_n)\boldsymbol{x}, t_n) = (\Phi(t_{n+1}, t_n)\boldsymbol{x}, \boldsymbol{w}(t_n)) = (\boldsymbol{x}, \Phi(t_{n+1}, t_n)^*\boldsymbol{w}(t_n)) \\ &= (\boldsymbol{x}, \bar{\rho}(t_n)\boldsymbol{w}(t_n)) = \rho(t_n)\phi(\boldsymbol{x}, t_n). \end{aligned} \tag{2.24}$$

$\boldsymbol{w}_n$ is the right eigenvector of $\Phi(t_{n+1}, t_n)$. The time-dependent Koopman spectrum $\rho(t_n)$ provides the growth or decay rate for the corresponding eigenmode during period t_n to t_{n+1}.

After obtaining the transient spectrum and eigenspace, the one-step evolution of dynam-

ics is achieved by Koopman decomposition

$$g(\boldsymbol{x}_{n+1}) = Ug(\boldsymbol{x}_n) = U\left(\sum_{i=1}^{\infty} a_i(t_n)\phi_i(\boldsymbol{x}_n, t_n)\right) = \sum_{i=1}^{\infty} a_i(t_n)\rho_i(t_n)\phi_i(\boldsymbol{x}_n, t_n), \tag{2.25}$$

where the observable g is decomposed by the Koopman eigenfunction at time t_n

$$g(\boldsymbol{x}) = \sum_{i=1}^{\infty} a_i(t_n)\phi_i(\boldsymbol{x}, t_n). \tag{2.26}$$

The Koopman exponent for the underlined continuous system is then defined by

$$\lambda(t_n) = \frac{\ln \rho(t_{n+1}, t_n)}{t_{n+1} - t_n}, \tag{2.27}$$

$t_{n+1} - t_n \to 0$ will provide the instant spectrum. Two following special cases exist.

$\tau = t - t_0$ goes to ∞

A special case is $\tau \to \infty$, and if the limit exist,

$$\lambda(t_0) = \lim_{\tau \to \infty} \frac{\ln \rho(t_0 + \tau, t_0)}{\tau}. \tag{2.28}$$

$\lambda(t_0)$ decides the exponential stability (ES) of the dynamic system. $\mathrm{Re}(\lambda(t_0)) \leq 0$ is stable, otherwise unstable. The ES can derive the well known asymptotic stable (AS). If $\lambda(t_0)$ is further independent on t_0, the uniform asymptotic stable (UAS) is obtained (Antsaklis and Michel, 2007; Zhou, 2016), which is an uniform global stability indicator.

Another important case is when $A(t)$ is periodic.

2.3.2 Periodic LTV systems

For periodic $A(t)$

$$\dot{\boldsymbol{x}} = A(t)\boldsymbol{x}, \quad A(t+T) = A(t) \text{ and } \boldsymbol{x}(t_0) = \boldsymbol{x}_0 \tag{2.29}$$

T is the smallest positive value for above relation. The dynamic system is the Floquet system and described by the following theory (Coddington and Levinson, 1955):

Theorem 1. *If Θ is a fundamental matrix for (2.19 and 2.29), then so is Ψ, where*

$$\Psi(t) = \Theta(t+T), \quad (-\infty < t < \infty).$$

Corresponding to every such Θ, there exist a periodic nonsingular matrix P with period T, and a constant matrix R (e^{TR} is called the monodromy matrix) such that

$$\Theta(t) = P(t)e^{tR}. \tag{2.30}$$

In the periodic LTV case, let $\tau = t_n - t_{n-1} = T$ and notice $e^{0R} = I$. The fundamental matrix $\Phi(t, t_0)$ is

$$\Phi(t, t_0) = \Theta(t)\Theta(t_0)^{-1} = P(t)e^{tR}P(t_0)^{-1}. \tag{2.31}$$

The discrete form of the periodic LTV can be derived by

$$\begin{aligned}
\boldsymbol{x}_{n+1} &= \Phi(t_{n+1}, t_0)\boldsymbol{x}_0 \\
&= P\left(t_0 + (n+1)T\right) e^{(t_0+(n+1)T)R}P(t_0)^{-1}\boldsymbol{x}_0 \\
&= P(t_0)e^{TR}e^{(t_0+nT)R}P(t_0)^{-1}\boldsymbol{x}_0 \\
&= P(t_0)e^{TR}P(t_0)^{-1}\left(P(t_0+nT)e^{(t_0+nT)R}P(t_0)^{-1}\boldsymbol{x}_0\right) \\
&= \Phi(t_{n+1}, t_n)\boldsymbol{x}_n.
\end{aligned} \tag{2.32}$$

Here $\Phi(t_{n+1}, t_n)$ is

$$\Phi(t_{n+1}, t_n) = P(t_0)e^{TR}P(t_0)^{-1}. \tag{2.33}$$

The above derivation used the properties that $P(t)$ is T-periodic, nonsingular(as the result of fundamental matrix $\Theta(t)$), and the properties of matrix exponential which are not hard to found from matrix textbook.

Therefore the Floquet multiplier ρ (the eigenvalue of e^{TR}), is also the Koopman multiplier,

which can be easily derived if substituting (2.33) to (2.24). Floquet exponent

$$\lambda = \frac{\ln \rho}{T} \tag{2.34}$$

is then the Koopman exponent. Thus the Koopman spectrums of Periodic LTV system are constant if the discrete time interval τ is taken the period T.

Koopman decomposition for the T-periodic discretized system

Different from the general LTV systems, the periodic LTV system which evolves at period T has constant evolving matrix like the LTI systems. Therefore, the Koopman eigenfunction is

$$\phi_i(\boldsymbol{x}) = (\boldsymbol{x}, \boldsymbol{w}_i) \tag{2.35}$$

where $\boldsymbol{w}_i$ is the right eigenvector of $\Phi(t_n, t_{n-1})$ and $t_n - t_{n-1} = T$, since

$$U\phi_i(\boldsymbol{x}) = (\Phi(t_n, t_{n-1})\boldsymbol{x}, \boldsymbol{w}_i) = (\boldsymbol{x}, \Phi(t_n, t_{n-1})^* \boldsymbol{w}_i) = (\boldsymbol{x}, \bar{\rho}_i \boldsymbol{w}_i) = \rho\phi_i(\boldsymbol{x}). \tag{2.36}$$

Similary, the observable $g(\boldsymbol{x})$ can be decomposed by Koopman decomposition by the infinite expansion

$$g(\boldsymbol{x}) = \sum_{i=1}^{\infty} a_i \phi_i(\boldsymbol{x}). \tag{2.37}$$

Thus the dynamics of the observable can be obtained by evolving the Koopman operator

$$g(\boldsymbol{x}_n) = U^n g(\boldsymbol{x}_0) = \sum_{i=1}^{\infty} a_i \rho_i^n \phi_i(\boldsymbol{x}_0). \tag{2.38}$$

This is similar LTI system. However, this decomposition only works for fixed discretization time interval T, other discretization time does not have this convenient property.

The solution of continuous periodic LTV system

The above discrete spectrum is obtained by considering the dynamics of at every other T instance (one period). In the continuous form (2.29), richer information on the dynamics will be obtained.

From Floquet solution (2.31), we have

$$\boldsymbol{x}(t) = \Phi(t, t_0)\boldsymbol{x}_0 = P(t)e^{(t-t_0)R}P(t_0)^{-1}\boldsymbol{x}_0. \tag{2.39}$$

Consider the simple case when R is diagonalizable ($V^{-1}RV = \Lambda$).

$$\boldsymbol{x}(t) = \underbrace{P(t)V}_{Q(t)}\underbrace{e^{(t-t_0)\Lambda}}_{\text{Diag}}\underbrace{V^{-1}P(t_0)^{-1}\boldsymbol{x}_0}_{\boldsymbol{c}_0} = \sum_{i=1}^{n} c_i e^{\mu_i(t-t_0)}\boldsymbol{q}_i(t). \tag{2.40}$$

$P(t)$ is periodic, so are $Q(t)$ and $\boldsymbol{q}(t)$ (the column vector of $Q(t)$). c_i is component of $\boldsymbol{c}_0$. Therefore, the Floquet solution contains the exponential growth part $e^{\mu t}$ and periodic part $\boldsymbol{q}(t)$. We then expand $\boldsymbol{q}_i(t)$ by Fourier series

$$\boldsymbol{x}(t) = \sum_{i=1}^{n} c_i e^{\mu_i(t-t_0)} \sum_{l=-\infty}^{\infty} \boldsymbol{q}_{il} e^{jl\omega t} = \sum_{i=1}^{n}\sum_{l=-\infty}^{\infty} c_i e^{(\mu_i + jl\omega)t}\boldsymbol{q}_{il}. \tag{2.41}$$

Here $j = \sqrt{-1}$ and $\omega = \frac{2\pi}{T}$. The $e^{\mu_i t_0}$ is absorbed into c_i in the final result.

Equation (2.40) expands the Floquet solution by Floquet modes $\boldsymbol{q}_i(t)$ with time coefficient $e^{\mu_i t}$, while equation (2.41) expands the Floquet solution further by Fourier expansion, with $\boldsymbol{q}_{il}$ as the modes and $e^{(\mu_i + jlw)t}$ time coefficient. It is interesting to know if they are the Koopman modes and eigenvalues.

The Koopman spectrums and eigenfunction for continuous periodic LTV system

Use the same notation as previous section, and let

$$Q^{-1}(t) = \begin{bmatrix} \boldsymbol{w}_1^H(t) \\ \vdots \\ \boldsymbol{w}_n^H(t) \end{bmatrix}. \tag{2.42}$$

Define the observable

$$\phi_i(\boldsymbol{x}, t) = (\boldsymbol{x}, \boldsymbol{w}_i(t)) = \boldsymbol{w}_i^H(t)\boldsymbol{x}. \tag{2.43}$$

Then

$$\begin{aligned} U^\tau \phi_i(\boldsymbol{x}, t) &= \phi_i(\boldsymbol{x}(t+\tau), t+\tau) = \boldsymbol{w}_i^H(t+\tau)\boldsymbol{x}(t+\tau) \\ &= \boldsymbol{w}_i^H(t+\tau)P(t+\tau)Ve^{((t+\tau)-t)R}V^{-1}P^{-1}(t)\boldsymbol{x}(t) \\ &= \boldsymbol{w}_i^H(t+\tau)Q(t+\tau)e^{\tau R}\left(Q^{-1}(t)\boldsymbol{x}(t)\right) \\ &= \boldsymbol{e}_i^H e^{\tau R}\boldsymbol{\phi}(\boldsymbol{x}, t) \\ &= e^{\mu_i \tau}\phi_i(\boldsymbol{x}, t) \end{aligned} \tag{2.44}$$

proves $\phi_i(\boldsymbol{x}, t)$ is the Koopman eigenfunction corresponding Koopman exponent μ_i. On the other hand, from Appendix B, the Koopman eigenfunctions defined by

$$\boldsymbol{\phi}(\boldsymbol{x}) = V^{-1}P^{-1}(t)\boldsymbol{x} \tag{2.45}$$

is actually two consecutive coordinates transformations from $\boldsymbol{x}$ to the invariant subspaces.

$$\begin{array}{ccccc} \boldsymbol{x} & \xrightarrow{P^{-1}(t)\boldsymbol{x}} & \boldsymbol{y} & \xrightarrow{V^{-1}\boldsymbol{y}} & \boldsymbol{z} \\ \text{periodic bases} & & \text{fixed bases} & & \text{Invariant bases} \\ \dot{\boldsymbol{x}} = A(t)\boldsymbol{x} & & \dot{\boldsymbol{y}} = R\boldsymbol{y} & & \dot{\boldsymbol{z}} = \Lambda\boldsymbol{z} \end{array}$$

Figure 2.1: *Coordinate transformation of periodic LTV.*

We can further define the observable

$$\phi_{il}(\boldsymbol{x}, t) = e^{jl\omega t}\phi_i(\boldsymbol{x}, t). \tag{2.46}$$

Then

$$\begin{aligned}
U\phi_{il}(\boldsymbol{x}, t) &= \phi_{il}\left(\boldsymbol{x}(t+\tau), t+\tau\right) = e^{jl\omega(t+\tau)}\phi_i\left(\boldsymbol{x}(t+\tau), t+\tau\right) \\
&= e^{jl\omega(t+\tau)}\boldsymbol{w}_i^H(t+\tau)\boldsymbol{x}(t+\tau) \\
&= e^{jl\omega(t+\tau)}\boldsymbol{w}_i^H(t+\tau)P(t+\tau)Ve^{((t+\tau)-t)\Lambda}V^{-1}P^{-1}(t)\boldsymbol{x}(t) \\
&= e^{jl\omega(t+\tau)}\boldsymbol{w}_i^H(t+\tau)Q(t+\tau)e^{\tau\Lambda}Q^{-1}(t)\boldsymbol{x}(t) \\
&= e^{jl\omega(t+\tau)}\boldsymbol{e}_i^H e^{\tau\Lambda}\boldsymbol{\phi}(\boldsymbol{x}, t) \\
&= e^{jl\omega(t+\tau)}e^{\mu_i\tau}\phi_i(\boldsymbol{x}, t) \\
&= e^{(\mu_i+jl\omega)\tau}e^{jl\omega t}\phi_i(\boldsymbol{x}, t) \\
&= e^{(\mu_i+jl\omega)\tau}\phi_{il}(\boldsymbol{x}, t)
\end{aligned} \tag{2.47}$$

proves $\phi_{il}(\boldsymbol{x}, t)$ and $\mu_i + jl\omega$ are the Koopman eigenfunction and exponent.

2.3.3 The continuity of local Koopman spectrum for LTV

The local Koopman spectrums defined In chapter 2.3.1 were used to advance the dynamics from time t_n to t_{n+1}. Such local analysis can be joined together to give the overall dynamics for $\{t_0, t_1, \cdots, t_n, \cdots\}$. Before doing that, we need to consider the continuity properties of the Koopman spectrum, which may be stated as the following question.

"Does the $\phi_i(\boldsymbol{x}, t_n)$ and $\phi_i(\boldsymbol{x}, t_{n+1})$ the same eigenfunction?"

Otherwise, at every time step, we have a set of totally different Koopman modes, which makes tracing the dynamics very hard. They can change in a continuous manner at most.

The matrix perturbation theory (Wilkinson, 1965) provides the solution towards above question. If $\Phi(t, t_0)$ is the fundamental matrix of the LTV system (2.19), and if $\Phi(t, t_0)$ is

continuous with respect to t, the continuity allows

$$\Phi(t + \delta t, t_0) = \Phi(t, t_0) + \delta t H. \tag{2.48}$$

The perturbation matrix H is some finite norm matrix. From matrix perturbation theory, the eigenvalues and eigenvectors of $\Phi(t + \delta t, t_0)$ are arbitrarily close to the $\Phi(t, t_0)$, which is to say the eigenvalues of $\Phi(t, t_0)$ is continuous, at least for the simple ones.

The continuity of a spectrum plays a vital role in studying the dynamics. The continuous spectrum shows that the dynamics persist along with specific Koopman modes, and the continuous evolvement of the spectrum further tells the evolution of dynamics during the transition. Moreover, the discontinuity is of its own interested, which may mean old dynamics disappear, and new ones emerge. However, a complete theorem regarding the discontinuity of the spectrum of matrix $\Phi(t, t_0)$ is lacking.

2.4 Koopman spectrum for nonlinear system

2.4.1 Global and local Koopman spectrum

For an autonomous nonlinear dynamic system with initial condition

$$\dot{\boldsymbol{x}} = \boldsymbol{f}(\boldsymbol{x}), \quad \boldsymbol{x}(0) = \boldsymbol{x}_0, \tag{2.49}$$

the Koopman spectrum defined in equation (2.5) gives the global dynamic characteristics. This global spectrum (independent of $\boldsymbol{x}$) are more familiar with mathematical physicians, who relate the ergodic system and spectrum of Koopman operator by the theory which says the system is ergodic if and only if all fixed points of U are constant functions (Lasota and Mackey, 2013, (see, chap. 4.2)). That is, $\lambda = 1$ is the spectrum for the discretized system, and the corresponding eigenfunction is an everywhere constant function.

We noticed two difficulties when applying above global Koopman spectrum for dynamics analysis. First, the above global Koopman spectrums and eigenfunctions are hard to find, if

they exist. Another difficulty is that some important spectrums characterizing the dynamics are not included in the global Koopman spectrum. For example, in a Hopf bifurcation problem, the spectrums around the unstable equilibrium are not. Otherwise, we could find a particular initial condition, where only components associated with the growing spectrums nontrivial. From this particular initial condition, the system exponentially grows without bound, which is contradictory to the physical system we have.

However, the spectral decomposition of the Koopman operator is still of interest to dynamics study. The local spectrums of Koopman operator are usually computed, though several authors may or may not point it out (Bagheri, 2013; Mezić, 2005; Schmid, 2010).

Semigroup Koopman operator

As spectrums vary from point to point, for an approximate discretized system, they must depend on the time step of the discretization. To include this effect, it would be wise to consider such a time-parameterized Koopman operator.

In this case, a semigroup operator is defined on the system (2.49) such that the solution to the autonomous nonlinear system is given by

$$\boldsymbol{x}(t) = T^t \boldsymbol{x}_0 \tag{2.50}$$

for $\forall t \in [0, \infty)$. T^t is the semigroup operator which satisfy the following two requirement

- the initial condition: $T^0 = I$,
- time-translation invariance: $T^{t+s} = T^t T^s$

The first requirement is easy to check. For the second, it is straight forward

$$T^{t+s}\boldsymbol{x}_0 = \boldsymbol{x}(t+s). \tag{2.51}$$

Notice the system is autonomous

$$T^t T^s \boldsymbol{x}_0 = T^t(T^s \boldsymbol{x}_0) = T^t(\boldsymbol{x}(s)) = \boldsymbol{x}(t+s). \tag{2.52}$$

From the uniqueness of solution of system (2.49), the second requirement is satisfied.

The induced semigroup Koopman operator is defined such that

$$U^t g(\boldsymbol{x}) = g(T^t \boldsymbol{x}). \tag{2.53}$$

It can be checked U^t is linear and satisfies the two semigroup operator requirements. Here we drop the suffix 0 of equation (2.49) to indicate it can take arbitrary initial condition.

$t \in [0, \infty)$ is the parameter for the evolution interval. In the following application, we will assume t is a fixed value of τ; that is, we will discretize the system (2.49). For simplicity, we drop the parameter τ and write the semigroup Koopman operator in the usual way U.

Local Koopman spectrum

To make the local spectrum idea clear, its definition is given as follows: $\forall \boldsymbol{x} \in \mathcal{M}$

$$U\phi(\boldsymbol{x}) = \rho\phi(\boldsymbol{x}), \quad \boldsymbol{x} \in D(\boldsymbol{x}) \tag{2.54}$$

Here $D(\boldsymbol{x})$ is an open domain covering $\boldsymbol{x}$. λ is the local spectrums and $\phi(\boldsymbol{x})$ is the corresponding eigenfunction. It can be seen the local spectrum is backward compatible with the global spectrum. In that case, $D(\boldsymbol{x})$ is the domain of Koopman operator $\mathcal{M}$.

2.4.2 Hierarchy of local Koopman spectrum

Koopman spectrums for arbitrary nonlinear systems pose a significant challenge. Currently, only a few particular dynamic systems are studied analytically.

A clear vision towards Koopman eigenspaces is its hierarchy structure. That is, the dynamics can be decomposed into the base and small magnitude perturbation, and then the

spectrum is divided into the base and perturbation naturally. This insight originates from the linearity of the Koopman operator.

The spectrum of base

For simple base flow, its Koopman spectrum can be obtained analytically. For instance, the nonlinear system at a fixed equilibrium state, such as the stable/unstable nodes/spirals or the saddle points. The base flow is the fixed equilibrium state. The dynamics of this base flow are merely given by a fixed spectrum of $\rho = 1$ or $\lambda = 0$ (discretize or continuous system).

Another example is the periodic solution embedded in the limit cycle solution of a nonlinear dynamic system. The Fourier expansion provides the spectrums of the periodic base flow, that is, Fourier spectrums.

One more complicated example is quasiperiodic motion. The base is then decomposed into the superposition of several periodic solutions, and the Koopman spectrum is the union of these Fourier spectrums.

For a more general dynamic system, where above simple base flow is not available, a practical choice of base flow is the *real trajectory* $\boldsymbol{u}(t)$. We may resort to numerical techniques like DMD to reveal the spectrum of the base.

If failed to provide a real trajectory, fake spectrums may be introduced. Such an example pointed out by Rowley et al. (2009) is that mean subtraction introduces the fake Fourier spectrum when the mean flow is not the solution of the dynamic system. However, if the system is ergodic and the sampling is long enough, the mean is the fixed point of a unitary operator U, whose spectrums indeed includes the Fourier spectrums (Mezić, 2005). Thus removing the mean flow will not change the spectrum. Besides data are time-resolved, Fourier spectrums are obtained, no contradiction thereafter.

A somewhat interesting example is to subtract the snapshots from itself. If real trajectory $X = \{\boldsymbol{x}_1, \cdots, \boldsymbol{x}_{N+1}\}$ of a dynamic system is given, we can construct the perturbation $X' = \{\boldsymbol{x}'_1, \cdots, \boldsymbol{x}'_N\}$, and perform DMD algorithm on X'

$$\boldsymbol{x}'_i = \boldsymbol{x}_{i+1} - \boldsymbol{x}_i. \tag{2.55}$$

Though this procedure does not provide new information (compared to data X), it provides a method to subtract the base dynamics from the data and focus on the spectrum of perturbation.

The spectrum of perturbation

We now shift the focus to the spectrum of the small magnitude perturbation. Since the dynamics is decomposed into base and perturbation,

$$u = U + u' \tag{2.56}$$

where U is the base flow satisfying $\dot{U} = f(U)$. u' is the small magnitude perturbation deviate from the base flow and $||u'|| \ll ||U||$. Then the dynamics of the perturbation is described by the nonlinear perturbation equation

$$u' = Au' + \mathcal{N}(u') \tag{2.57}$$

for a steady equilibrium solution U, $A = \frac{\partial f}{\partial u}|_U$, or

$$u' = A(U(t))u' + \mathcal{N}(u'), \tag{2.58}$$

for unsteady equilibrium solution $U(t)$, $A(U(t)) = \frac{\partial f}{\partial u}|_{U(t)}$. $\mathcal{N}(u')$ is the terms for the nonlinear interaction of u'. It is not hard to see the spectrums of the underlined linear systems ($\dot{u}' = Au'$ or $\dot{u}' = A(t)u'$ considered in § 2.2 or 2.3) provide a subset of local spectrums of the Koopman operator since $u' \to 0$, $\mathcal{N}(u') \to 0$.

From the nonlinear perturbation equation (2.57) or (2.58), u' is a nonlinear function of itself, so it is the nonlinear observable. If the nonlinear term $\mathcal{N}(u')$ can be expanded by Taylor series, such that

$$\mathcal{N}(u') = \mathcal{N}_2 u'^2 + \mathcal{N}_3 u'^3 + \cdots . \tag{2.59}$$

We should be able to use the proliferation rule to obtain derived spectrums for the nonlinear

observable. Here $\mathcal{N}_i u'^i$ is the symbolic notation, which should be understood as tensor product of order i tensor u^i and order $i+1$ tensor $\mathcal{N}_i$. For each component $\mathcal{N}_i u'^i$, the proliferation rule applies accordingly. Moreover, the proliferation rule should be applied in a recursive manner, since the nonlinear relation is implicit. In contrast, the linear dynamics system with a nonlinear observable only admits one proliferation, as shown in section 2.2.

2.4.3 Proliferation of spectrum

Since each spectrum represents the dynamics of each particular mode, therefore, it is useful to consider the proliferation of them.

Self interaction

For example if λ is the Koopman exponent for the underlined linear system of

$$\dot{\boldsymbol{x}} = A\boldsymbol{x} + \mathcal{N}_2 \boldsymbol{x}^2, \tag{2.60}$$

by the recursive proliferation rule, the following are also Koopman spectrum.

$$\lambda, \lambda+\lambda, (\lambda+\lambda)+\lambda, ((\lambda+\lambda)+\lambda)+\lambda, \cdots$$

The spectrua are shown in figure 2.2a and they fall on an affine line.

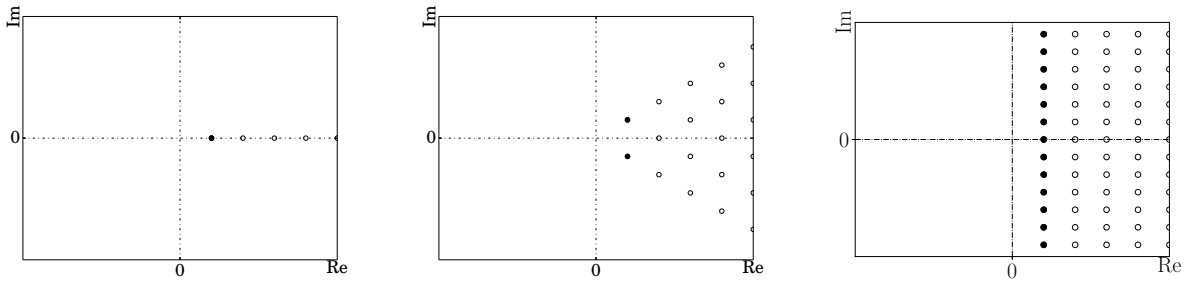

(a) $\lambda > 0$ **(b)** $Im(\lambda) \neq 0$ **(c)** *limit cycle system*

Figure 2.2: *Self interaction of Koopman spectrum. The filled circle shows the original linear spectrum, high order are shown by hollow circle.*

If complex conjugate λ, $\bar{\lambda}$ are the spectrums of the underlined linear system of (2.60), by the recursive proliferation rule, the Koopman spectrums proliferated by them build a chain of triad shown in figure 2.2b.

Another example is the following time-dependent system

$$\dot{\boldsymbol{x}} = A(t)\boldsymbol{x} + \mathcal{N}_2\boldsymbol{x}^2,$$

$A(t)$ is periodic. From Floquet theory the linear part provide the base spectrum $\lambda \pm jmw$, where $j = \sqrt{-1}$ and m is the integer. After considering the nonlinear proliferation, the lattice distribution of Koopman spectrums are obtained

$$n\lambda \pm jmw,$$

and shown in figure 2.2c. n is a positive integer. Bagheri (2013) drew the same conclusion by analytically computing the Koopman spectrum for the Kármán vortex.

All the self-interacted spectrum has the same positive or negative real part as their parental spectrums λ and $\bar{\lambda}$. Therefore, $\mathcal{N}_2\boldsymbol{x}^2$ term does not change the stability of the dynamic system in the asymptotic case, neither other $\mathcal{N}_i\boldsymbol{x}'^i$ nonlinearity. In this sense, the spectrums of the linearized perturbation equation determine the stability of nonlinear perturbation.

Cross interaction

Except the self-interaction between one mode and its complex conjugate, it is possible different modes interact with each other. If λ_1, λ_2 are two different linear spectrums, and if they both have positive or negative real part, then the derived spectrum should have the same positiveness or negativeness. But if they are of different sign, it may be possible to excite some unstable derived modes as illustrated by figure 2.3. In either case, $\mathrm{Re}(\lambda_1 + \lambda_2) > 0$ or $\mathrm{Re}(\lambda_1 + \lambda_2) < 0$, there will be unstable derived children spectrums.

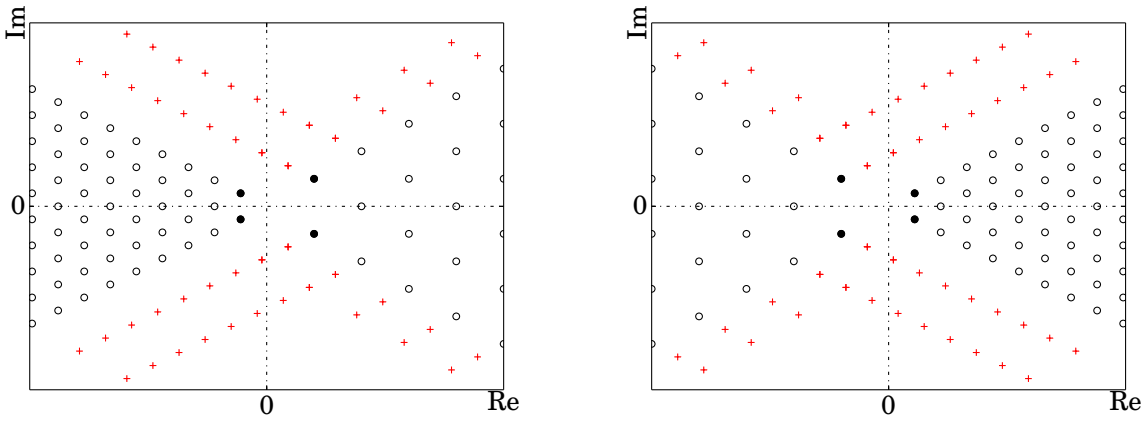

(a) $Re(\lambda_1 + \lambda_2) > 0$ **(b)** $Re(\lambda_1 + \lambda_2) < 0$

Figure 2.3: *Cross interaction of Koopman modes. The filled circle shows the original spectrum, high order derived spectrums are shown by the hollow circle. Part of the cross interaction spectrum are shown by the red cross.*

Rational nonlinear terms

For the rational nonlinearity $\frac{1}{\boldsymbol{x}}$, the system has the derived Koopman spectrum shown in figure 2.4, which indicate it is always unstable at the neighborhood of $\boldsymbol{x}$.

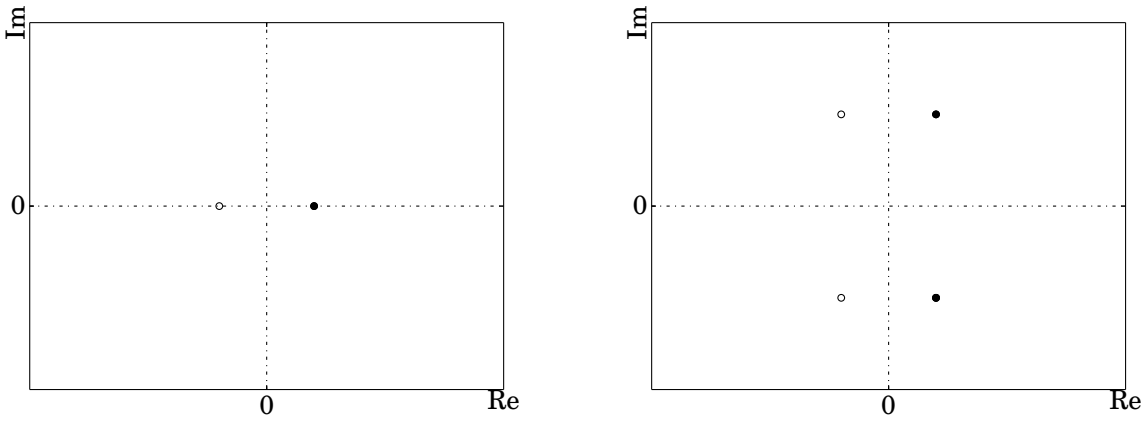

(a) $\lambda > 0$ **(b)** $Re(\lambda) > 0$ *and* $Im(\lambda) \neq 0$

Figure 2.4: *Self interaction for* $\frac{1}{\boldsymbol{x}}$.

Fluid dynamics system

For fluids dynamics, the nonlinearity usually comes from the convection, written as $u_i \frac{\partial u_j}{\partial x_i}$, which gives the $\mathcal{N}_2 u^2$ expansion. Therefore, the nonlinear interaction will create children spectrum as shown in figure 2.2 and figure 2.3. The derived modes (studied in the next chapter), particularly the unstable ones, may develop into the complex flow pattern and make the nonlinear dynamic system much more complicated. The nonlinear interaction generating new modes was discovered and documented by many authors, for instance, resonant wave interaction by Drazin et al. (1982, (see §51)) and three-wave interaction by Schmid and Henningson (2012, (see §5.4)) and others but not listed here. Now it is apparent they are all described by the proliferation rule of Koopman spectrums.

2.5 The linear properties of nonlinear system

We expressed the desire to analyze the nonlinear dynamics using the linear properties (superposition and invariant subspaces if they exist in the nonlinear dynamic system) in chapter 1.3. Now the idea is more clear, to use the Koopman decomposition.

Let $T(\mathcal{M}, \mathcal{R})$ to be the collection of function $\mathcal{M} \to \mathcal{R}$. Then the observable $g(\boldsymbol{x})$ and the eigenfunctions $\phi_i(\boldsymbol{x})$ are the element of $T(\mathcal{M}, \mathcal{R})$. The eigenfunctions clearly form some invariant subspaces of the dynamic system T^t, since the induced linear Koopman operator U has

$$U\phi_i(\boldsymbol{x}) = \phi_i(T^t(\boldsymbol{x})) = \lambda_i \phi_i(\boldsymbol{x}). \tag{2.61}$$

However, unlike the linear system $\dot{\boldsymbol{x}} = A\boldsymbol{x}$ where each eigenvector is totally decoupled from others, the Koopman eigenfunctions for the nonlinear system are still entangled. Since if ϕ_i and ϕ_j are the Koopman eigenfunction, $\phi_i \phi_j$ is also Koopman eigenfunction, which means some eigenfunction depends on others.

To better express the idea, we define the *atom Koopman spectrum* to be the one not derived from other Koopman spectrums, such as those solid spectrums shown in figure 2.2a, 2.2b or 2.3. The rest of them are called the derived spectrums from the atom ones. Note some

of the solid circles in figure 2.2c are the atom Koopman spectrums, and rest are not, which will be in explained chapter 9.2.1. Correspondingly we can define the *atom Koopman eigenfunction*.

Then the *invariant subspace* is the union of some atom Koopman eigenfunctions and all their derived eigenfunctions. For example, a single atom Koopman eigenfunction and its derived eigenfunctions form an invariant subspace. The corresponding spectrums form an affine dot line, as shown in figure 2.2a. If two complex conjugated atom eigenfunctions are encountered, they and the interaction of them also form an invariant subspace, and the corresponding spectrums are shown in figure 2.2b. If multiple complex conjugated pairs of atom eigenfunctions are used, they and the interaction of them also form the invariant subspace, where their spectrums are shown in figure 2.3.

Then observable $g(\boldsymbol{x})$ in $T(\mathcal{M}, \mathcal{R})$ is uniquely decomposed into the invariant subspace

$$g(\boldsymbol{x}) = \sum a_i \phi_i(\boldsymbol{x}) + r(\boldsymbol{x}), \quad a \in \mathcal{D}(x) \tag{2.62}$$

For vector valued observable the decomposition is carried out element-wisely.

After above Koopman decomposition, the 'one-step' step dynamics is given by the linear superposition of components from the invariant subspace.

$$g(T^t \boldsymbol{x}) = U g(\boldsymbol{x}) = \sum a_i \lambda_i \phi_i(\boldsymbol{x}) + r(T^t \boldsymbol{x}). \tag{2.63}$$

With vector observable $\boldsymbol{g}(\boldsymbol{x}) = \boldsymbol{x}$, we have the dynamics of the nonlinear system.

We shall not be frustrated by the complexity of the dynamics (2.63) expressed by the daunting space spanned by all the atom Koopman eigenfunctions. Most often, only a few of the above atom Koopman eigenfunctions are important. Therefore we usually ignore many of them and related invariant subspaces. It greatly simplifies the solution space and introduces the topic of reduced-order modeling. Besides, the dynamics of the remaining bases are described by their spectrums, making the analysis of dynamics tractable.

We must emphasize the 'one-step' in equation 2.63 since the spectrums are local. Af-

ter mapping T^t, the system no longer works at point $\boldsymbol{x}$, therefore the perturbation theory developed in the next section is useful to expand the dynamics to the whole domain $\mathcal{M}$.

2.6 The continuity of local Koopman spectrum

2.6.1 The global spectrums theory for the linear space

Continuity of the local Koopman spectrum plays an essential role in analyzing the transition of dynamics. We need this information to consider the transition process of nonlinear dynamics. Unfortunately, this is ongoing research. Part of its difficulty comes from nonlinearity or unbounded differential operator (Reed and Simon, 1972) or the more complex Hilbert space, also contribute to its complexity.

We now focus on the linear measured space equipped with the inner product operation to facilitate the previous definition of Koopman eigenfunction. The *Hilbert space* is a *complete inner product* space. A *bounded operator* from a normed linear space $\langle V_1, ||\cdot||_1\rangle$ to a normed linear space $\langle V_2, ||\cdot||_2\rangle$ is a map T, which satisfies

1. $T(\alpha v + \beta w) = \alpha T(v) + \beta T(w), \quad (\forall v, w \in V_1 \text{ and } \forall \alpha, \beta \in \mathbb{R} \text{ or } \mathbb{C})$,
2. Exists some $C \geq 0$, $||T(v)||_2 \leq C||v||_1, \quad \forall v \in V_1$.

The spectrum for bounded operator is well studied. The spectrum is known not empty on the more general Banach space (Reed and Simon, 1972, (see, chap. VI.3)). The spectrums for the unbounded operator is more complex (Reed and Simon, 1972, (see, chap. VIII)).

Unfortunately, the Koopman operator defined on Navier-Stokes equation may not always bounded. Figure 2.5 shows two possible examples. The first is a shockwave problem in the hyperbolic problem. The differential operator $\frac{\partial}{\partial x}$ in the Navier-Stokes equation incur ∞ at the discontinuity, which may result in the failure of the second condition of bounded operator. The second example is a moving solid in the incompressible flow. As it moves, the differentiation at the position initially occupied by solid but filled with fluids later (or vise versa) incurs infinite differential, resulting the failure of second condition.

(a) *shock wave* **(b)** *moving body*

Figure 2.5: *Discontinuity and unbounded operator. (a) Shock wave. (b) Moving body.*

2.6.2 The local spectrums theory and continuity property

The global spectrums theory addressed in various references provides a subset of the local spectrums discussed in this paper. We do not have the rigorous proof of the existence of other local spectrums. Instead, we point such local spectrums do exist in a lot dynamic systems (Bagheri, 2013; Mezić, 2005; Rowley et al., 2009; Schmid, 2010). Besides, the continuity extends local spectrums to the global domain.

The perturbation theory of linear operator provides the valuable tool to study the continuity of the local spectrums. Let us consider a simple case where g and T^τ are analytic and their 'derivative' are uniform continuous. We then consider the local spectrums at the two infinitesimally close state $\boldsymbol{x}$ and $\boldsymbol{x}+\boldsymbol{h}$, where $\boldsymbol{h}\to\boldsymbol{0}$. The Koopman operator at state $\boldsymbol{x}+\boldsymbol{h}$ can be viewed as the perturbed Koopman operator at $\boldsymbol{x}$ such that

$$\begin{aligned} Ug(\boldsymbol{x}+\boldsymbol{h}) &= g(T^\tau(\boldsymbol{x}+\boldsymbol{h})) = g(T^\tau\boldsymbol{x}+T'^\tau\boldsymbol{h}+O(\boldsymbol{h}^2)) \\ &= g(T^\tau\boldsymbol{x})+g'(T'^\tau\boldsymbol{h})+O(\boldsymbol{h}^2) \\ &\approx (U^\tau+V^\tau)g(\boldsymbol{x}). \end{aligned} \tag{2.64}$$

Here T'^τ is the differential of T^τ at $\boldsymbol{x}$ and g' is the differential of g at $T^\tau\boldsymbol{x}$. And V^τ is the perturbation operator defined by

$$V^\tau g(\boldsymbol{h}) = g'(T'^\tau(\boldsymbol{h})). \tag{2.65}$$

In the condition that g and T^τ is continuous differentiable and uniform bounded,

$$||V^\tau g(\boldsymbol{h})|| = ||g'(T'^\tau(\boldsymbol{h}))|| \leq C||\boldsymbol{h}||. \tag{2.66}$$

From perturbation theory (Reed and Simon, 1978, (see, chap. XII)), the simple local spectrum is not only continuous but also analytic.

2.6.3 Continuity and global decomposition

In the following discussion, we assume the flow and the observable are uniformly continuous differentiable. Thus the simple Koopman spectrum is continuous. Then we can glue equation (2.54) piece-by-piece, then the global eigen-relations of the Koopman operator acting on the whole domain hold

$$U\phi_i(\boldsymbol{x}) = \rho_i(\boldsymbol{x})\phi_i(\boldsymbol{x}), \quad \boldsymbol{x} \in \mathcal{M}. \tag{2.67}$$

$\rho_i(\boldsymbol{x})$ is the continuous state-dependentent spectrum, and $\phi_i(\boldsymbol{x})$ is the eigenfunction. The observable $g(\boldsymbol{x})$ is then decomposed by the Koopman eigenfunctions

$$g(\boldsymbol{x}) = \sum_{i=0}^{\infty} a_i\phi_i(\boldsymbol{x}), \quad \boldsymbol{x} \in \mathcal{M}. \tag{2.68}$$

Notice the decomposition coefficients a_is are constants. Therefore, the dynamics of the observable is obtained by

$$g(\boldsymbol{x}_n) = U^n g(\boldsymbol{x}_0) = U^n \sum_{i=0}^{\infty} a_i\phi_i(\boldsymbol{x}_0) = \sum_{i=0}^{\infty} a_i\phi_i(\boldsymbol{x}_0) \prod_{k=0}^{n-1} \rho_{ik}, \tag{2.69}$$

where $\rho_{ik} = \rho_i(\boldsymbol{x}_k)$ are the local spectrums. We thus expand the overall dynamics using the local Koopman spectrums and eigenfunctions.

2.6.4 Discontinuity and local decomposition or state-dependent modes

Besides the continuous spectrums case mentioned above, we are also interested in the more general conditions where the domain $\mathcal{M}$ is the Hilbert space $\mathcal{H}$, which allows discontinuity such as shockwave in the hyperbolic Navier-Stokes systems, or moving body problem.

Two issues arise. The first one is the existence of such a spectrum, and the second one is the continuity of it.

The spectrum for unbounded operator may provide some insight for the first problem, alternatively we can consider the spectrum for the more flexible compact operator. We refer reader to the discussion of compact operator to Reed and Simon (1972, see, chap. VI.5). However, if such discontinuous local spectrum exist, we won't have the convenient relation (2.67) for whole domain. But the local spectrum may be still valuable for studying the transient dynamics in a local manner

$$g(\boldsymbol{x}) = \sum_{i=0}^{\infty} a_i(\boldsymbol{x})\phi_i(\boldsymbol{x}), \quad \boldsymbol{x} \in D(\boldsymbol{x}). \tag{2.70}$$

Unfortunately, this gives state-dependent Koopman decomposition and only hold locally around $\boldsymbol{x}$.

Chapter 3

Koopman modes

3.1 Koopman modes and its invariant property

In many application, the observable is usually a vector valued function defined on the dynamic system, such that

$$\boldsymbol{g}(\boldsymbol{x}) = \begin{bmatrix} g_1(\boldsymbol{x}) \\ \vdots \\ g_n(\boldsymbol{x}) \end{bmatrix}. \tag{3.1}$$

Koopman decomposition for this observable is obtained by expanding each component of $\boldsymbol{g}$ by the Koopman eigenfunction $\phi_i(\boldsymbol{x})$ by equation (2.6)

$$\boldsymbol{g}(\boldsymbol{x}) \approx \sum \boldsymbol{v}_i \phi_i(\boldsymbol{x}) \tag{3.2}$$

Here $\boldsymbol{v}_i$ is the *Koopman mode*.

For constant Koopman spectrum system, such as LTI system, or the asymptotic system around fixed equilibrium point or periodic or quasi-periodic system, the evolution of the observable is given similar as (2.8)

$$\boldsymbol{g}(\boldsymbol{x}_n) \approx \sum \boldsymbol{v}_i \rho_i^n \tag{3.3}$$

Similar result is obtained for the periodic LTV in chapter 2.3.2 or nonlinear system considered in chapter 2.6.3

$$\boldsymbol{g}(\boldsymbol{x}_n) = \sum_{i=0}^{\infty} \boldsymbol{a}_i \phi_i(\boldsymbol{x}_n) = \sum_{i=0}^{\infty} \boldsymbol{a}_i' \prod_{k=0}^{n} \rho_{ik}. \tag{3.4}$$

A remarkable feature of Koopman modes is that they are *state independent* for autonomous nonlinear system.

Koopman modes reveal the structure of the given observable, thus differs by observables. They can provide rich information about the given dynamic system, especially when the full-state observable $\boldsymbol{x}$ is investigated. In the following discussion, we consider Koopman modes for the full-state observable $\boldsymbol{x}$.

The following examples demonstrate the eigenvectors for the linear system.

3.1.1 Example 1. Koopman modes of LTI system

Consider the dynamic system

$$\boldsymbol{x}_{n+1} = A\boldsymbol{x}_n, \quad A \in \mathbb{R}^{n\times n}. \tag{3.5}$$

Let A diagonalizable and $A = V\Lambda V^{-1}$. Let λ_i, $\boldsymbol{r}_i$, $\boldsymbol{l}_i$ are the eigenvalue, right and left eigenvector. The observable $\boldsymbol{x}$ is decomposed by

$$\boldsymbol{x} = VV^{-1}\boldsymbol{x} = \left(\sum_{i=1}^{n} \boldsymbol{r}_i \boldsymbol{l}_i^H\right)\boldsymbol{x} = \sum_{i=1}^{n} \boldsymbol{r}_i \boldsymbol{l}_i^H \boldsymbol{x} = \sum_{i=1}^{n} \boldsymbol{r}_i \phi_i(\boldsymbol{x}), \tag{3.6}$$

where $\phi(\boldsymbol{x}_i)$ is the Koopman eigenfunction defined in chapter 2.2.1. Therefore the right eigenvectors of A are the *Koopman modes* for the full-state observable $\boldsymbol{x}$.

The dynamics of observable $\boldsymbol{x}$ is evaluated by the Koopman operator

$$\boldsymbol{x}_k = U^k \boldsymbol{x}_0 = \sum_{i=1}^{n} \boldsymbol{r}_i \rho_i^k \phi_i(\boldsymbol{x}_0), \tag{3.7}$$

which gives the solution of (3.5) since

$$\boldsymbol{x}_k = \sum_{i=1}^{n} \boldsymbol{r}_i \rho_i^k \phi_i(\boldsymbol{x}_0) = V \Lambda^k V^{-1} \boldsymbol{x}_0 = A^k \boldsymbol{x}_0. \tag{3.8}$$

3.1.2 Example 2. Koopman modes of LTV system

Similarly for LTV system

$$\boldsymbol{x}_{k+1} = A_k \boldsymbol{x}_k, \quad A_k \in \mathbb{R}^{n \times n}. \tag{3.9}$$

Assuming matrix A_ks are diagonalizable and $\boldsymbol{r}^k$, $\boldsymbol{l}^k$ are the right and left eigenvectors. The full-state observable $\boldsymbol{x}$ can be decomposed by

$$\boldsymbol{x} = V_k V_k^{-1} \boldsymbol{x} = \left(\sum_{i=1}^{n} \boldsymbol{r}_i^k \boldsymbol{l}_i^{kH} \right) \boldsymbol{x} = \sum_{i=1}^{n} \boldsymbol{r}_i^k \boldsymbol{l}_i^{kH} \boldsymbol{x} = \sum_{i=1}^{n} \boldsymbol{r}_i^k \phi_i(\boldsymbol{x}, t = k). \tag{3.10}$$

$\phi_i(\boldsymbol{x}, t = k)$ is the eigenfunction (2.35) for the LTV system, therefore the time-variant $\boldsymbol{r}_i^k$s are the *Koopman modes* for observable $\boldsymbol{x}$.

3.1.3 Example 3. Koopman modes of periodic LTV system

The Koopman modes for a periodic LTV system were mentioned in chapter 2.3.2. We summarize the results and provide the proof.

For the T-periodic discretized system. The Koopman modes are given by the column of matrix $Q(t_0)$

$$Q(t_0) = P(t_0) V. \tag{3.11}$$

For the continuous periodic LTV system, Koopman modes corresponding eigenfunction $\phi_i(\boldsymbol{x}, t)$ (2.43) is obtained by

$$\boldsymbol{x} = Q(t) Q^{-1}(t) \boldsymbol{x} = \sum_{i=1}^{n} \boldsymbol{q}_i(t) \phi_i(\boldsymbol{x}, t). \tag{3.12}$$

Therefore, the columns of $Q(t)$, also known as the Floquet modes, are the Koopman modes.

For eigenfunction $\phi_{il}(\boldsymbol{x},t)$ (2.46) the corresponding Koopman mode is obtained by expanding the solution (2.40)

$$\begin{aligned}
U^{\tau}\boldsymbol{x}(t) &= \boldsymbol{x}(t+\tau) \\
&= P(t+\tau)Ve^{((t+\tau)-t)\Lambda}V^{-1}P^{-1}(t)\boldsymbol{x}(t) \\
&= Q(t+\tau)e^{\tau\Lambda}Q^{-1}(t)\boldsymbol{x}(t) \\
&= \left(\sum_{k=\infty}^{\infty} Q_k e^{jk\omega(t+\tau)}\right) e^{\tau\Lambda}\boldsymbol{\phi}(\boldsymbol{x},t) \\
&= \sum_{i=1}^{n}\sum_{k=-\infty}^{\infty} \boldsymbol{q}_{ki}e^{jk\omega(t+\tau)}e^{\tau\mu_i}\phi_i(\boldsymbol{x},t) \\
&= \sum_{i=1}^{n}\sum_{k=-\infty}^{\infty} \boldsymbol{q}_{ki}e^{(\mu_i+jk\omega)\tau}\left(e^{jk\omega t}\phi_i(\boldsymbol{x},t)\right) \\
&= \sum_{i=1}^{n}\sum_{k=-\infty}^{\infty} \boldsymbol{q}_{ki}e^{(\mu_i+jk\omega)\tau}\phi_{ik}(\boldsymbol{x},t).
\end{aligned} \tag{3.13}$$

$\boldsymbol{q}_{ki}$, the i-th column of k-th Fourier component of $Q(t)$ provides the Koopman modes.

3.2 Koopman modes of nonlinear asymptotic system

Multi-scale assumption and asymptotic expansion

For a nonlinear system, it is not straightforward what the Koopman modes are. We follow the hierarchy discussion introduced in section 5.3.2 and decompose the dynamics to base and perturbation and obtain the Koopman modes contained in each part.

In the following section, a fluid system is considered. Koopman modes generated from nonlinear self-interaction will be derived. A perturbation technique, known as multiple-scale analysis, will be used. This technique is based on the observation that the dynamics of such small perturbation usually characterized by disparate time scale motion. One is a fast scale oscillating motion. One is a much slower time scale motion describing the slow changing of its magnitude. The multiple-scale analysis is accomplished by introducing a fast-scale t

and a slow-scale τ ($\tau = \epsilon t$) as two independent variables. In the solution process of the perturbation problem, the additional freedom, introduced by a new independent variable τ, is used to remove the unwanted secular terms. The latter put constraints on the approximate solution, which are called solvability conditions (Kevorkian and Cole, 2012).

After introducing the multiple-scale, we proceed to expand the dynamics by the following asymptotic expansion

$$\boldsymbol{q}(t) = \boldsymbol{q}_0 + \epsilon \boldsymbol{q}_1(t,\tau) + \epsilon^2 \boldsymbol{q}_2(t,\tau) + \epsilon^3 \boldsymbol{q}_3(t,\tau) + \cdots . \tag{3.14}$$

$\boldsymbol{q}_0$ is the base flow, here is assumed to be the fixed equilibrium point of the dynamics system. $\boldsymbol{q}_i(t,\tau)$ is small perturbation with intensity of ϵ^i. Substituting above asymptotic expansion into original dynamic equation, and taking into account that the slow time scale τ, the following differential relation is obtained

$$\frac{\partial}{\partial t} = \frac{\partial}{\partial t} + \epsilon \frac{\partial}{\partial \tau}. \tag{3.15}$$

Expanding the dynamic equation and collecting terms according the different order of ϵ, a set of equations are obtained, which then asymptotically solve the dynamics system.

A caveat here is the successful application of multiple-scale analysis relies on the implicit assumption that the time scale is disparate. Thus this technique may fail for more general cases. However, some of the conclusions draw here which conform to Koopman decomposition are still valid to describe the dynamics.

Fluid dynamic system

To give a concrete example, the above asymptotic expansion is carried out on the incompressible viscous fluid system

$$\begin{aligned} \frac{\partial \boldsymbol{u}}{\partial t} + \nabla \boldsymbol{u} \cdot \boldsymbol{u} &= -\nabla p + \frac{1}{Re} \nabla^2 \boldsymbol{u}, \\ \nabla \cdot \boldsymbol{u} &= 0. \end{aligned} \tag{3.16}$$

$\boldsymbol{u}$ is the velocity of fluids and p is the pressure. Re is the dimensionless Reynolds number. Let

$$\boldsymbol{q} = \begin{bmatrix} \boldsymbol{u} \\ p \end{bmatrix}. \tag{3.17}$$

The global stability analysis

A proper example for multiple-scale analysis in fluids is the Hopf bifurcation occurred in many flows, where the original steady flow develops periodic oscillation after an increasing or decreasing of some critical parameter. For instance, Stuart (1960) found Reynolds number controls the bifurcation of flow when he studied two-dimensional Poiseuille flow. He found the linear growth rate at $Re > Re_c$ ($Re - Re_c \ll 1$, Re_c is the critical Reynolds number) is of order ϵ^2 (ϵ^2 is a small parameter characterizing weak nonlinear effects)

$$\epsilon^2 = \frac{1}{Re_c} - \frac{1}{Re}, \tag{3.18}$$

whereas the time scale on which nonlinear interactions affect the evolution of the fundamental mode is of order (linear growth rate)$^{-1}$. The second time scale is introduced

$$\tau \equiv \epsilon^2 t. \tag{3.19}$$

τ is the slow time scale, and affects the time derivative by

$$\frac{\partial}{\partial t} = \frac{\partial}{\partial t} + \epsilon^2 \frac{\partial}{\partial \tau} \tag{3.20}$$

Substituting the asymptotic expansion into the incompressible Navier-Stokes equation, a series of equations at various orders of ϵ are obtained.

(i). At order ϵ^0, a steady Navier-Stokes equations at Re are obtained

$$\begin{aligned} \nabla \boldsymbol{u}_0 \cdot \boldsymbol{u}_0 &= -\nabla p_0 - \frac{1}{Re}\nabla^2 \boldsymbol{u}_0, \\ \nabla \cdot \boldsymbol{u}_0 &= 0. \end{aligned} \tag{3.21}$$

These equations take the original boundary condition, and have a fixed equilibrium solution, which is then chosen as the base flow for asymptotic expansion $\boldsymbol{q}_0 = [\boldsymbol{u}_0^T, p_0]^T$. Here the Koopman spectrum is $\lambda = 0$, and $\boldsymbol{q}_0$ is the corresponding base Koopman mode.

(ii). At order ϵ^1, an homogeneous linear systems are obtained

$$\begin{bmatrix} \frac{\partial}{\partial t} + \nabla() \cdot \boldsymbol{u}_0 + \nabla \boldsymbol{u}_0 \cdot () - \frac{1}{Re}\nabla^2 & \nabla \\ \nabla^T & 0 \end{bmatrix} \boldsymbol{q}_1 = \boldsymbol{0} \tag{3.22}$$

with a homogeneous boundary condition. This is an eigenvalue problem. Its solution, is dominated by the most unstable modes $\boldsymbol{q}_1$

$$\boldsymbol{q}_1 = \begin{bmatrix} \boldsymbol{u}_1 \\ p_1 \end{bmatrix} = A(\tau) e^{iwt} \boldsymbol{v}_1 + c.c. \tag{3.23}$$

$\boldsymbol{v}_1$ is the most unstable mode, and $A(\tau)$ is its magnitude varying on the slow time scale τ, at initial stage $A(\tau)$ grows at $e^{\epsilon^2 t}$ or e^{τ}. Therefore, we know $A(\tau)e^{iwt}$ provide the Koopman eigenfunction and $\boldsymbol{v}_1$ is the Koopman mode.

(iii). At order ϵ^2, inhomogeneous linear equations will be obtained with homogeneous boundary condition.

$$\begin{bmatrix} \frac{\partial}{\partial t} + \nabla() \cdot \boldsymbol{u}_0 + \nabla \boldsymbol{u}_0 \cdot () - \frac{1}{Re}\nabla^2 & \nabla \\ \nabla^T & 0 \end{bmatrix} \boldsymbol{q}_2 = \begin{bmatrix} |A|^2 \boldsymbol{F}_2^{|A|^2} + A^2 e^{2iwt} \boldsymbol{F}_2^{A^2} + \bar{A}^2 e^{-2iwt} \boldsymbol{F}_2^{\bar{A}^2} \\ 0 \end{bmatrix} \tag{3.24}$$

Left hand side contains the same linear differential operator similar to that at order ϵ^1, and the right side contains the forcing terms aroused by nonlinear interaction of $\boldsymbol{q}_1$. $|A|^2$, A^2, $\bar{A}^2$

representing the increasing forcing magnitude. The $\boldsymbol{F}$ terms are

$$\begin{aligned}\boldsymbol{F}_2^{|A|^2} &= -\nabla \boldsymbol{u}_1^A \cdot \boldsymbol{u}_1^{\bar{A}} - \nabla \boldsymbol{u}_1^{\bar{A}} \cdot \boldsymbol{u}_1^A \\ \boldsymbol{F}_2^{A^2} &= -\nabla \boldsymbol{u}_1^A \cdot \nabla \boldsymbol{u}_1^A \\ \boldsymbol{F}_2^{\bar{A}^2} &= -\nabla \boldsymbol{u}_1^{\bar{A}} \cdot \boldsymbol{u}_1^{\bar{A}}\end{aligned}$$

where $\boldsymbol{u}_1^A$ and $\boldsymbol{u}_1^{\bar{A}}$ are the solution of equation (3.22) on ϵ^1 expansion. It is expected for the forced LTI system, the solution would have the following component

$$\boldsymbol{q}_2 = A(\tau)^{|A|^2}\boldsymbol{v}^{|A|^2} + A(\tau)^{A^2}e^{i2wt}\boldsymbol{v}^{A^2} + A(\tau)^{\bar{A}^2}e^{-i2wt}\boldsymbol{v}^{\bar{A}^2}.$$

$\boldsymbol{v}^{(\cdot)}$ is the symbolic spatial mode. $A(\tau)^{(\cdot)}$ is the symbolic representation for slow varying magnitude. e^{inwt} is its pulsation. The modes $\boldsymbol{v}^{(\cdot)}$ are Koopman modes, the slow varying magnitude $A(\tau)$ and pulsation e^{inwt} together provide the Koopman eigenfunction.

(iv). Higher-order ϵ^i expansions can be further carried out to derive the linear equations, which generate the high order Koopman modes. In those equations, we will have the same left-hand side linear differential operator with almost periodic but increasing forcing terms on the right-hand side. The particular solution of these forced linear dynamic system then provides higher-order Koopman modes and Koopman eigenfunctions.

Some comments are followed:

1) Degenerated cases occur on the ϵ^3 or other ϵ^{2i+1} order expansions, where secular terms, which contains e^{iwt} or e^{-iwt} pulsation occurs in the right-hand side as the forcing term. A compatibility condition is required to remove them, which derives the well-known Stuart-Landau equation (Stuart, 1960). On ϵ^3 expansion, it is

$$\frac{\partial A}{\partial \tau} = \sigma A - l|A|^2 A. \tag{3.25}$$

It provides a good approximation of the magnitude of the critical normal mode $\boldsymbol{v}_1$.

2) The above asymptotic expansion is similar to the one used by various authors (Meliga

and Chomaz, 2011; Sipp and Lebedev, 2007) to study the Hopf bifurcation of wake after blunt bodies at the critical Reynolds number but with some difference. We expand the Navier-Stokes equation at Re, while the above authors expand at Re_c ($\frac{1}{Re_c} - \frac{1}{Re} \ll 1$) to study the bifurcation. The difference was characterized by a base flow modification of u_2^1 (in Sipp's notation). Moreover, as the slight difference in base flow, the eigenvalue problem is slightly different. However, as the Re is so close to Re_c, it will be shown later, the Koopman modes numerically computed by the current authors are very similar to the modes computed by Sipp and Lebedev (2007) and Meliga and Chomaz (2011).

3) Moreover, information transfer is *directional*; that is, the information transfer from the low order Koopman modes to higher-order Koopman modes. From expansion at ϵ^2 or higher, equation (3.24), for example, the coupling of low order Koopman modes occur in the right-hand side, and the higher-order modes are generated on the left hand. This direction is also described by the proliferation rule, that is, $\lambda_i, \lambda_j \to \lambda_i + \lambda_j$ and only summation operation allowed.

The directional transformation of information may provide a framework to describe the energy cascading. On the one hand, information transfers from low-frequency modes to high-frequency ones such as $\lambda_i \to n\lambda_i$, typical energy cascading route. On the other hand, the information can transfer back from high frequency to low frequency such as $\lambda_i, \bar{\lambda}_i \to 2\text{Real}(\lambda)$, resulting the so-called the backscattering phenomena (Pope, 2001).

4) The Koopman modes originate from the forced terms. As we know, the linear differential operator has its natural frequency, under which the magnitude would be amplified. That is, some frequencies and modes are much easier amplified than others. It will be illustrated in more detail later.

5) If the underlined base flow is time-variant and let $\boldsymbol{q}_0(t)$ the time-variant base flow, $\boldsymbol{q}_0$ is substituted by $\boldsymbol{q}_0(t)$ in the asymptotic expansion (3.14). Then at all orders of ϵ^i, a linear time-variant coefficient system is obtained, and the analysis can proceed accordingly. For example, if $\boldsymbol{q}_0(t)$ is periodic, at order ϵ^0, an unsteady Navier-Stokes equation is obtained and solved by $\boldsymbol{q}_0(t)$. At ϵ^1 order, homogeneous periodic coefficient linear equations with homogeneous boundary conditions are obtained. Therefore a Floquet system is to be solved.

On higher-order (ϵ^2 or higher), periodic linear differential systems with varying magnitude periodic forcing terms need to be solved. The exact solution of these equations is too complex to consider here. The reader is referred to monographs such as Bittanti and Colaneri (2009); Kuchment (2012); Shmaliy (2007) for more detail. More general $\boldsymbol{u}(t)$ may also be considered similarly, but not addressed here.

3.3 Modal decomposition using Koopman modes

In the modal analysis, one is interested in finding the most efficient modes that capture the dynamics of the system, for example, the POD and DMD method.

For a linear system, the eigenvectors may provide a set of complete bases to describe the dynamics. A common understanding of completeness is that it contains a set of independent eigenvectors, and the rank is full.

However, for nonlinear system, the basis are the Koopman eigenfunction, not the Koopman modes, see equation (2.5), (2.26) and (2.67). The completeness Koopman spaces require the Koopman eigenfunctions are complete in the mapping space: $\mathcal{M} \to \mathbb{R}$. $\mathcal{M}$ is the manifold of the dynamics system. Therefore the completeness of Koopman modes does not help to describe the dynamics system. In chapter 2.5, we talked the reduced-order can be carried efficiently by directly throw away some unimportant atom Koopman function and related invariant subspaces. In a real application, usually, a small subset of the Koopman eigenfunctions provides an adequate basis. Moreover, Koopman modes may not even form linear independent bases at all.

The difference between LTI and the nonlinear system is bridgeable since the Koopman operator also unifies the linear system.

The asymptotic expansion shows an example where a subset Koopman modes (containing the base flow, the critical unstable normal modes $\boldsymbol{v}_1$ and $\bar{\boldsymbol{v}}_1$, and the high order derived modes) dominate the suitably perturbed flow. Therefore it might be plausible to conjecture if other normal modes were initially perturbed, or they are unstable, then Koopman modes constitute by these normal modes, and their derived Koopman modes are needed to describe

the transient stage.

Since the role of Koopman modes for modal analysis, it is desired to obtain them by some method. For example, the DMD algorithm detailed in the next chapter or the generalized Laplace analysis (GLA) method (Budišić et al., 2012), which requires the knowledge of Koopman eigenfunction. None of these techniques require explicit knowledge of dynamic equations. Instead, they apply to snapshots.

Chapter 4

Dynamic mode decomposition

> The artisan, who wishes to do his work well, must first sharpen his tools.
>
> *Confucius (China), 551 - 479 BC*

The wise Chinese mentor Confucius told his students to prepare good tools for their work. In this chapter, we introduce an efficient and robust DMD algorithm to perform Koopman analysis.

4.1 DMD algorithm review

Dynamic mode decomposition (DMD) (Schmid, 2010) is a data-driven technique to extract dynamic relevant information from time-resolved snapshots provided either by experiments or numerical simulations. Its data-driven nature makes it convenient to extract information such as dominant frequencies and spatial structures from fluid flows (Rowley et al., 2009; Schmid, 2011) without pre-knowledge of the complex physics behind it. DMD provides a way to extract coherent structures from fluid flows (Frederich and Luchtenburg, 2011; Schmid et al., 2009; Seena and Sung, 2011; Zhang et al., 2014), and provide base functions for the construction of reduced-order models (ROM) (Bistrian and Navon, 2015; Tissot et al., 2014; Zhang and Wei, 2017). Therefore, it has been gaining popularity, along with the well-known proper orthogonal decomposition (POD) (Holmes et al., 1996b; Wei and Rowley,

2009a), among data analysis and model reduction techniques. DMD is also known as a numerical approximation of the spectral of Koopman operator (Mezić, 2005; Rowley et al., 2009), a linear and infinite-dimensional operator, that can be defined in non-linear dynamic systems. The data-driven nature of DMD leads to its application of fields other than fluid flows. Erichson et al. (2015); Grosek and Kutz (2014) apply DMD to real-time video to subtract background for surveillance and recognition purpose. DMD is found to be effective and efficient in analyzing spatial-temporal data to study the infectious disease dynamics and plan intervention (Proctor and Eckhoff, 2015). Brunton et al. (2016) adapted DMD to analyze the coupled spatial-temporal neuron recording data to study the sleep spindle networks of human.

Despite the mentioned success, DMD still faces its difficulties in computation. For instance, generating the approximation matrix is time-consuming, and the operation to invert a matrix suffers from the singularity when data is rank deficient or nearly rank deficient. To avoid the singularity issue, a manual truncation of singular value is usually adopted by setting an artificial threshold (Schmid, 2010). However, the influence of truncation is not fully understood. Besides, it becomes more contradicting to one's expectation that the singularity comes from more data sampling with the intention for better accuracy. There are also concerns regarding the dynamic interpretation of some DMD modes. Efforts, such as optimized DMD (Chen et al., 2012) or sparsity promoting DMD (Jovanović et al., 2014), have been taken to reduce or remove spurious DMD modes.

Currently there are several numerical procedures available to identify dynamic relevant information, for example, the standard DMD algorithm by Schmid (2010), the companion matrix approach adopted by Rowley et al. (2009), a least square fitting approach (Tu et al., 2014) or a total-least-square fitting approach (Hemati et al., 2017), the Koopman operator and its associated numerical methods (Williams et al., 2015). All the above approaches involve computing an approximate matrix of the mapping explicitly, and the computation is achieved by having a singular value decomposition (SVD) of input data followed by matrix inversion. Even though SVD, as a typical operation used by many numerical algorithms (Golub and Kahan, 1965), is a backward stable procedure, the step of matrix inversion proposes nu-

merical challenges when the matrix is singular or nearly singular.

In the current work, to deal with the challenge in solving the mapping matrix, we avoided the mapping matrix entirely. Instead, a generalized eigenvalue (GEV) problem is formulated and solved without obtaining the mapping matrix (or its approximation) directly. The solution of GEV allows extracting dynamic information in the same way as being provided by the standard DMD method. This paper though entirely treating the DMD algorithm, the GEV-projection approach can be equivalently applicable to other dynamics information extraction techniques (Hemati et al., 2017; Tu et al., 2014; Williams et al., 2015). This approach avoids singularity issues, and projection onto different spaces generates different DMD algorithms, for example, the DMD-LS or DMD-TLS algorithm.

4.2 DMD in the formulation of GEV

4.2.1 The standard DMD algorithm

The standard DMD algorithm (Schmid, 2010) was introduced to extract dynamic relevant information form time-resolved snapshots, and is summarized below for comparison.

Let $\{\boldsymbol{x}_1, \boldsymbol{x}_2, \cdots, \boldsymbol{x}_M, \boldsymbol{x}_{M+1}\}$ be a collection of dynamic variables from a dynamic system, where $\boldsymbol{x}_i = \boldsymbol{x}(t_0 + i\Delta t) \in \mathbb{R}^N$. t_0 is the initial time, $i \in \mathbb{N}$ is integer and Δt is the sampling time interval. An projection of the linear mapping onto data space is given

$$A\boldsymbol{x_i} = \boldsymbol{x}_{i+1}. \tag{4.1}$$

Let $X = [\boldsymbol{x}_1\, \boldsymbol{x}_2\, \cdots\, \boldsymbol{x}_M]$, $Y = [\boldsymbol{x}_2\, \boldsymbol{x}_3\, \cdots\, \boldsymbol{x}_{M+1}]$, so $X, Y \in \mathbb{R}^{N\times M}$. In matrix form, the above relations is written

$$AX = Y. \tag{4.2}$$

On the other hand, a least-square approximation between data X, Y can be given

$$Y = XC + \boldsymbol{r}\boldsymbol{e}_M^T \tag{4.3}$$

and C is the companion matrix and has the form

$$C = \begin{bmatrix} 0 & & & a_1 \\ 1 & 0 & & a_2 \\ & \ddots & \ddots & \vdots \\ & & 1 & a_n \end{bmatrix}. \tag{4.4}$$

$\boldsymbol{e}_M \in \mathbb{R}^M$ and $\boldsymbol{e}_M = [0, 0, \cdots, 1]^T$. $\boldsymbol{r}$ is the residue of the following least-square problem.

$$\boldsymbol{x}_1 a_1 + \boldsymbol{x}_2 a_2 + \cdots + \boldsymbol{x}_N a_N = \boldsymbol{x}_{N+1} \tag{4.5}$$

and a_1, a_2, $\cdots$, a_N are the least square solution of above equation. By solving the eigenvalue problem of companion matrix C

$$C\boldsymbol{v} = \lambda \boldsymbol{v}, \tag{4.6}$$

DMD eigenvalues and eigenvectors are given by λ and $X\boldsymbol{v}$.

$$A(X\boldsymbol{v}) = Y\boldsymbol{v} \approx XC\boldsymbol{v} = \lambda X\boldsymbol{v}. \tag{4.7}$$

The least square problem is normally in good condition. However, the companion matrix C is usually ill-conditioned for eigenvalue problem (Trefethen, 1991), resulting in a large deviation from the correct eigenvalues even under small perturbation. A more stable algorithm is to decompose data X by SVD (Schmid, 2010)

$$X = U\Sigma V^T, \tag{4.8}$$

and project A onto space spanned by X by

$$\tilde{A} \triangleq U^T A U = U^T Y V \Sigma^{-1}, \tag{4.9}$$

which is used to compute the Ritz value and vector of A.

$$\tilde{A}\boldsymbol{v} = \lambda \boldsymbol{v} \tag{4.10}$$

DMD eigenvalue and eigenvector are approximated by the eigenpair $(\lambda, U\boldsymbol{v})$. When X is singular, the direct inverse of matrix Σ is replaced by the pseudo-inverse (Moore-Penrose inverse). The inverse operation (including the pseudo-inverse) is numerical stable when any non-zero singular value of X is much larger than 0. Ironically, the Ritz value and Ritz vector become a good approximation of the true ones if the following residue goes to zero (Sorensen, 1992),

$$AU = U\tilde{A} + \boldsymbol{r}e_r^T, \tag{4.11}$$

where

$$\boldsymbol{r}e_r^T = \left(\boldsymbol{I} - UU^T\right) YV\Sigma^{-1}, \tag{4.12}$$

which further requires the snapshots in $\{\boldsymbol{x}_1, \boldsymbol{x}_2, \cdots, \boldsymbol{x}_M, \boldsymbol{x}_{M+1}\}$ to be nearly linearly dependent. However, it contradicts to the requirement the nonsingular value of X to be isolate from 0. Though accurate SVD algorithms for small singular values may alleviate above paradox, they are usually expensive. Schmid (2010) suggested truncating the singular values by some artificial threshold. However, the influence of such truncation is unclear, and the appropriate threshold is empirical. Some alternative DMD algorithms are available but they more or less suffer the same issue stated here.

4.2.2 The GEV formulation for DMD

The algorithm proposed here to avoiding the above issue is to use the generalized eigenvalue problem to capture dynamic relevant information.

Assume the same collection of data and matrix notation as in the previous section and the same linear relation given by (4.1). We further assume X to be a good sampling of the dynamic system, such that any interested system state $\boldsymbol{v}$ can be represented by a linear

combination of X. Then the following generalized eigenvalue problem

$$Y\boldsymbol{v} = \lambda X\boldsymbol{v} \tag{4.13}$$

captures the dynamic information such as frequency and growth rate by λ, and dynamic modes by $X\boldsymbol{v}$. That is

$$A(X\boldsymbol{v}) = Y\boldsymbol{v} = \lambda(X\boldsymbol{v}). \tag{4.14}$$

It is readily verifiable that the eigenpairs of GEV (4.13) satisfy the standard eigenvalue problem (SEV) of (4.14). To make it a sufficient condition, we assumed X to be a good sampling of the dynamic system. Then the interested eigenvector can be expressed by the linear combination of X. Let us say (λ, $X\boldsymbol{v}$) is the eigenpair of A. Substituted into the standard eigenvalue problem of A and make use of linear relation (4.1), we derived the GEV (4.13), thus proved the reversed statement is conditionally true.

The assumption of 'good' sampling can be further relaxed. If only the eigenvector representable by the data space is interested, the GEV formulation still computes correct eigenvectors. The relaxation may be useful in the case when X is a partial sampling of the dynamic system, but only some dominant flow structures and frequencies are desired.

The GEV formulation (4.13) captures the same dynamic relevant information as the standard DMD algorithm. It is a 'matrix-free' method, and the generalized eigenvalue problem circumvents the singularity issue by its definition.

However, the GEV problem is more complicated than the SEV problem. To better understand the structure of eigenpairs of GEV and prepare for the numerical solution, the following section introduces the relevant theories.

4.3 Solution to GEV problem

GEV is different from the SEV problem in several aspects. This section introduces some related definitions and theories. In compliance with the most mathematic monographs, we

use A, B for Y, and X, respectively.

4.3.1 Introduction of GEV

The eigenvalue of matrix pair (A, B) is also known as the eigenvalue of matrix pencil $A - \lambda B$ (a family of matrices parameterized by λ) in many matrix theory monographs. The generalized eigenvalue problem is to find the λ such that the pencil $A - \lambda B$ is rank deficient and corresponding kernel if required.

$$(A - \lambda B)\boldsymbol{v} = \mathbf{0}, \tag{4.15}$$

Not like the SEV, where a full set of finite eigenvalues is guaranteed if counting the algebraic multiplicity, GEV does not guarantee the existence of eigenvalues or eigenvectors at all. An illustrative example is given by

$$A = \begin{bmatrix} 1 & \\ & \alpha \end{bmatrix}, \quad B = \begin{bmatrix} 1 & \\ & \beta \end{bmatrix}. \tag{4.16}$$

If $\alpha \neq \beta$, there is no eigenvalue for pencil $A - \lambda B$. The concept of an invariant subspace is central to the SEV problem. The invariant subspace gives the solution of the eigenvalue problem. A generalization of invariant subspace to the GEV is the deflating subspace. Let (A, B) be a matrix pair, and let $(\mathcal{S},\mathcal{U})$ be a pair of subspaces of $\mathbb{C}^n$ and of the same dimension k. Then $(\mathcal{S},\mathcal{U})$ is called a deflating pair for (A, B) if $A\mathcal{S} \subseteq \mathcal{U}$ and $B\mathcal{S} \subseteq \mathcal{U}$. A necessary condition for (4.13) is the existence of non-empty deflating subspace.

Another difference is that GEV generalizes eigenvalue to include infinity numbers. For example, if B is singular, see equation (4.15), $\boldsymbol{c}$ is in the kernel of B and $A\boldsymbol{c}$ is nontrivial. We call $(\infty, \boldsymbol{c})$ the eigenpair of the (4.13). In fact, eigenvalue λ is generalized as the ratio of two variables α, β in numerical computation (Kågström and Poromaa, 1996), such that the GEV is written

$$\beta A\boldsymbol{v} = \alpha B\boldsymbol{v}. \tag{4.17}$$

And the finite eigenvalues are given by the ratio

$$\lambda = \alpha/\beta, \quad \beta \neq 0. \tag{4.18}$$

Otherwise, if $\beta = 0$, B must be rank deficient(column). In this case,

- if $\boldsymbol{v}$ is in the kernel of only matrix B, $\lambda = \alpha/\beta = \infty$,
- if $\boldsymbol{v}$ is in the kernel of both A and B, $\lambda = \alpha/\beta$ admits all values in $\mathbb{C}$. Under this situation, the eigenvalues are the full complex plane, no meaningful eigenvalues can be calculated. This is the ill-posed problem and should be avoided.

At this stage, let us introduce the essential definition revealing the structure of eigenpairs, the *regular pencil* or *singular pencil* and the relevant theory (Gantmakher, 1998).

Definition 1. *A pencil of matrices $A - \lambda B$ is called regular if*

- *A and B are square matrices of the same order n.*
- *The determinant $|A - \lambda B|$ does not vanish identically.*

In all other cases ($m \neq n$, or $m = n$ but $|A - \lambda B| \equiv 0$), the pencil is called singular.

4.3.2 Regular matrix pencil

By the definition of regular pencil, a pencil is regular only if it is square. So either $|A| \neq 0$ or $|B| \neq 0$ makes a regular pencil. But it is possible that $|A| = |B| = 0$ makes a regular pencil. For example,

$$A = \begin{bmatrix} 1 & 0 \\ 0 & 0 \end{bmatrix}, \quad B = \begin{bmatrix} 0 & 0 \\ 0 & 1 \end{bmatrix},$$

$|A - \lambda B| = \lambda$ vanishes only at $\lambda = 0$. It can be verified that 0 and ∞ are the two eigenvalues. $[0, 1]^T$, $[1, 0]^T$ are the corresponding eigenvectors. In fact, regular pencil requires the square matrices A and B to share empty kernel.

For regular pencil, there exist a full set of eigenvalues if counting the infinite eigenvalues and algebraic multiplicities (Wilkinson, 1979). The eigenvalue is revealed by the following generalized Schur theorem.

Theorem 2 (generalized Schur theorem)**.** *Let $A, B \in \mathbb{C}^{n\times n}$. Then there exist unitary $Q, Z \in \mathbb{C}^{n\times n}$ and upper triangular $T, S \in \mathbb{C}^{n\times}$ such that $A = QTZ^*$ and $B = QSZ^*$. Z^* is the Hermitian of Z. In other words,*

$$A - \lambda B = Q(T - \lambda S)Z^*$$

Then eigenvalue is calculated by $\lambda_i = t_{ii}/s_{ii}, i = 1, \cdots, n$, if $s_{ii} \neq 0$. t_{ii}, s_{ii} are the diagonal elements of T and S. λ_i is infinite if $s_{ii} = 0$. Schur theorem is non-constructive, it can not be used directly to solve eigenvalues and eigenvectors. Some popular eigensolvers are using QZ algorithm (Moler and Stewart, 1973) or Arnoldi iterative method (Sorensen, 1997).

4.3.3 Singular matrix pencil

Compare to a regular pencil, the eigenstructure of a singular pencil is more complicated. The illustrative example (4.16) shows the situation when eigenvalue does not exist. The singular pencil case deserves more attention since for DMD problem, the data X and Y usually rectangular, forms the singular pencil.

In SEV, the structure of eigenpair is revealed by reducing the matrix to the Jordan canonical form (JCF). The Kronecker canonical form (KCF) is its generalization to GEV (Van Dooren, 1981).

Theorem 3 (Kronecker canonical form)**.** *Any matrix pencil $\lambda B - A$ can be reduced to*

$$S(\lambda B - A)T = diag\{L_{l_1}, \cdots, L_{l_s}, L_{r_1}^T, \cdots, L_{r_t}^T, \lambda N - I, \lambda I - J\} \tag{4.19}$$

i) S, T are constant invertible row and column transformations, ii) L_k is the $(k+1) \times k$

bidiagonal pencil, iii) N is nilpotent, and both N and J are in Jordan canonical form.

$$L_k = \begin{bmatrix} \lambda & & \\ -1 & \ddots & \\ & \ddots & \lambda \\ & & -1 \end{bmatrix}.$$

The Jordan block $\lambda I - J$ reveals the finite eigenvalue of the system, while nilpotent block $\lambda N - I$ computes the infinite eigenvalues. The corresponding eigenvectors are obtained by solving the eigenvectors of the corresponding block and then do a coordinate transformation. A detailed description of Kronecker canonical form using the elementary divisors is given by Gantmakher (1998, (see, ch. XII)). An intuitive explanation regarding the solution of the linear differential equation is given by Wilkinson (1978).

Direct calculating KCF poses the same numerical difficulties as the Jordan form. A numerically stable algorithm that unitarily transforms two matrices to low triangular blocks called the pencil algorithm is given by Van Dooren (1979). The eigenvalues and eigenvectors can be computed by the corresponding blocks in the resultant decomposition.

4.3.4 Solution regarding perturbation of data

Though the eigenpair of a rectangular matrix pencil can be solved by the so-called pencil algorithm, equation (4.16) shows a critical issue that eigenpair is very sensitive to the matrix element. Any perturbation on α or β, the eigenpair may disappear. Such a GEV solution is useless for flow analysis unless we can find some solutions which are robust to perturbation.

To mitigate the influence of noise or machine precision, several techniques is proposed. One of them is to define the eigenvalue in a minimal perturbation approach (Boutry et al.,

2005), to find the eigenpair of a slightly modified pair (A_0, B_0) such that

$$\begin{aligned} &\min_{\{A_0,B_0,\{\lambda_k,\boldsymbol{v}_k\}_{k=1}^n\}} ||A_0 - A||_F^2 + ||B_0 - B||_F^2 \\ &\text{subject to } \{(A_0 - \lambda_k B_0)\boldsymbol{v}_k = \mathbf{0} \text{ and } ||\boldsymbol{v}_k||_2 = 1\}_{k=1}^n \end{aligned} \tag{4.20}$$

As mentioned by Chu and Golub (2006), this is still an opening research and has no explicit solution.

Another possibility is to solve the pseudospectra (Trefethen and Embree, 2005). The pseudospectra is introduced as an alternative for the spectral of nonnormal matrix. The ϵ-pseudospectra of A is defined as

$$\Lambda_\epsilon(A) = \{z \in \mathbb{C} : \quad ||(zI - A)^{-1}|| \geq \epsilon^{-1}\}. \tag{4.21}$$

The ϵ-pseudospectra is a closed region in the complex plane. Generalization of pseudospectra to matrix pencil is done by Embree and Trefethen (2001); Wright and Trefethen (2002). A package based Krylov subspace iterative method to compute pseudospectra is given by Wright and Trefethen (2001).

The minimal perturbation approach or pseudo spectrum provides two frameworks to calculate eigenvalues that are robust to noise. However, they both have difficulties. First, the computation is expensive. Secondly, the minimal perturbation approach does not have an explicit solution, while pseudospectra does not provide meaningful eigenvectors. These factors limit the data-driven approach to flow analysis.

4.4 DMD by approximate solution of GEV

In this section, the GEV is solved robustly and efficiently by projecting it into some subspace. This approach will capture the true eigenpairs if they exist and give good approximation otherwise.

4.4.1 Projection

A direct solution of GEV (4.13) in the large space $\mathbb{R}^N$ is difficult, if possible, it is easier to restrain the solution in some reduced subspace. To do that, let's introduce the idea of projection.

$$\mathcal{P} : \boldsymbol{x} \to \boldsymbol{y}, \quad \boldsymbol{x} \in \mathbb{R}^N, \boldsymbol{y} \in \mathcal{D} \subset \mathbb{R}^N, \text{rank}(\mathcal{D}) = M.$$

$\mathcal{D}$ is the subspace to project to. Its dimension is usually much smaller, $M \ll N$. The projector can be written in the matrix form P. The projection matrix has the following properties.

$$P^2 = P\,, \tag{4.22}$$

$$rank(P) = M\,. \tag{4.23}$$

If

$$P = P^T \tag{4.24}$$

P is called the orthogonal projector. The orthogonal projection gives the unique vector in $\mathcal{D}$ that is closest to $\boldsymbol{v}$ (Meyer, 2000, (see, chap. 5.13)). That is

$$\min_{\boldsymbol{p}\in\mathcal{D}} ||\boldsymbol{v} - \boldsymbol{p}||_2 = ||\boldsymbol{v} - P_{\mathcal{D}}\boldsymbol{v}||_2. \tag{4.25}$$

Here $P_{\mathcal{D}}$ represent the orthogonal projection to space $\mathcal{D}$.

An orthogonal projection is illustrated by figure 4.1. Space $\mathcal{D}$ has two orthonormal basis $\boldsymbol{q}_1$ and $\boldsymbol{q}_2$, a vector $\boldsymbol{v}$ projected into space $\mathcal{D}$ is denoted by $\mathcal{P}_{\mathcal{D}}\boldsymbol{v}$. The residue $\boldsymbol{v} - \mathcal{P}_{\mathcal{D}}\boldsymbol{v}$ is of minimum 2-norm.

The orthogonal projection gives the unique solution of a least square problem, for example, equation (4.5) is solved by

$$X\boldsymbol{a} = P_X\boldsymbol{x}_{M+1}. \tag{4.26}$$

$a = [a_1 \cdots a_M]^T$. $P_X\boldsymbol{x}_{M+1}$ denotes orthogonal projection of $\boldsymbol{x}_{M+1}$ onto space spanned by

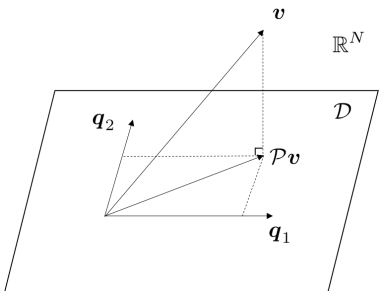

Figure 4.1: *Orthogonal projector onto subspace $\mathcal{D}$. $\boldsymbol{q}_1$, $\boldsymbol{q}_2$ are the orthonormal basis. $\mathcal{P}\boldsymbol{v}$ is the projection of $\boldsymbol{v}$ onto space $\mathcal{D} \subset \mathbb{R}^N$*

column vector of X.

If $Q = [\boldsymbol{q}_1, \boldsymbol{q}_2, \cdots, \boldsymbol{q}_M] \in \mathbb{R}^{N \times M}$ is a set of orthonormal basis of $\mathcal{D}$.

$$P_{\mathcal{D}} = QQ^T \tag{4.27}$$

defines an orthogonal projector.

4.4.2 Solving the GEV by projecting to lower-order subspace

Projecting the GEV into subspace $\mathcal{D}$, we obtain

$$P_{\mathcal{D}} Y \boldsymbol{v} = \lambda P_{\mathcal{D}} X \boldsymbol{v}, \tag{4.28}$$

$X, Y \in \mathbb{R}^{N \times M}$, $P_{\mathcal{D}} \in \mathbb{R}^{N \times N}$.

If Q is a set of orthonormal basis of $\mathcal{D}$, $P_{\mathcal{D}}$ is given by equation (4.27). Taking equal of the abscissa the above projected GEV is reduced to

$$Y' \boldsymbol{v} = \lambda X' \boldsymbol{v}, \tag{4.29}$$

X' and Y' are the abscissa on basis Q

$$X' = Q^T X,$$
$$Y' = Q^T Y.$$

The eigenpairs of GEV (4.13) is a subset of the of projected one (4.29), thus will be captured by (4.29). The projection transforms the GEV from size $N \times M$ to $M \times M$, reducing the size when $N > M$. The small square matrix pencil is simple both in theoretical and numerical aspect. The simplest projection comes by let P to be X or Y. (If X is linear independent but not orthonormal, P is defined by $P_X = X\left(X^T X\right)^{-1} X^T$. The projected system is then $X' = X^T X$, $Y' = X^T Y$.) Since X is assumed a good sampling for the state variables, let $P = X$, the projection $X^T X$, $X^T Y$ only takes $2Nm^2$ multiplication operation counts.

As for the robustness, we notice if $|X| \neq 0$, $|P^T X| \neq 0$. By the continuity property of determinant, we know there exist δ and a matrix $||E|| < \delta$, $E \in \mathbb{R}^{N \times M}$, such that $|P^T(X + E)| \neq 0$. Then the eigenpairs exist and continuously change with the perturbation. Thus our approach is robust to small perturbation for nonsingular X.

To show the accuracy, the projected GEV is reformulated to be

$$P_{\mathcal{D}}(Y\boldsymbol{v} - \lambda X\boldsymbol{v}) = 0. \tag{4.30}$$

The residual vectors are orthogonal to the subspace $\mathcal{D}$. Therefore increasing the dimension of $\mathcal{D}$ will increase the projection accuracy.

4.4.3 Residue criterion for filtering spurious mode

Two issues perplex the application of above DMD algorithm. One issue associating the projection is that it admits spurious eigenvalues and eigenvectors since the eigenpair of projected GEV (4.29) is not limited to the ones of original GEV (4.13). To filter out those

spurious modes the residue is calculated.

$$||\boldsymbol{r}|| = \frac{||Y\boldsymbol{v} - \lambda X\boldsymbol{v}||}{||Y\boldsymbol{v}||} \tag{4.31}$$

Another issue is the clustering of eigenpairs; that is, several similar eigenvalues and eigenvectors exist in the solution. To be specific, we notice when data covers multiple periods, say p periods, the eigenvalues usually clustered around some values in the complex plane with each cluster contains p eigenvalues. Multiplicities happen especially when sampling interval aligns with a period of the dynamic system. That is, there exists an integer q, such that the sampling interval Δt and period of the system T has relation $q\Delta t \approx T$. The phenomenon was also observed in Chen et al. (2012), where the authors tried to optimize redundant ones out.

When such multiplicitiness occurs, a convenient criterion to assess the quality of those eigenpairs is the residue (Watkins, 2007, (see, chap. 2.7)). The tiniest residue among the clustered eigenpairs indicates it subjects to least perturbation compared to others, thus the corresponding eigenpair can be taken as a good approximation to the true eigenpair. This can be illustrated with a SEV problem, if

$$\boldsymbol{r} = A\boldsymbol{v} - \lambda\boldsymbol{v} \tag{4.32}$$

is the residue. Let $||\boldsymbol{v}|| = 1$, then the following equation holds

$$(A + \boldsymbol{r}\boldsymbol{v}^T)\boldsymbol{v} = \lambda\boldsymbol{v}. \tag{4.33}$$

$E \triangleq \boldsymbol{r}\boldsymbol{v}^T$ is the perturbation towards matrix A to obtain eigenpair $(\lambda, \boldsymbol{v})$. $||\boldsymbol{r}|| = ||E||$ measures the perturbation magnitude. Thus a small residue magnitude means the eigenpair is subject to less perturbation. Therefore the residue defined for the projected GEV

$$||\boldsymbol{r}'|| = \frac{||Y'\boldsymbol{v} - \lambda X'\boldsymbol{v}||}{||Y'\boldsymbol{v}||}, \tag{4.34}$$

measures the quality of each eigenpair. Since tiny $\boldsymbol{r'}$ usually indicate tiny $\boldsymbol{r}$, besides $\boldsymbol{r'}$ removes the possible multiplicities, $\boldsymbol{r'}$ is used as the criterion to pick the good eigenpairs.

Additionally, a low condition number indicates error is not sensitive to perturbation. The product of condition number κ and perturbation magnitude $||\boldsymbol{r'}||$ gives an error estimation

$$\epsilon_i = \kappa_i ||\boldsymbol{r}'_i||. \tag{4.35}$$

ϵ can be used instead when condition number is available. By this criterion, we can pick modes perturbed by least noise and not sensitive to perturbation.

4.4.4 DMD-LS: the least square solution

In the previous section, the projection was assumed to carry out onto subspace span(X). From section 4.4.1, the orthogonal projection is equivalent to seek the least-square solution of a linear relation (4.5) using given snapshots. Here, we consider the efficiency and stability of this projection and give a practical algorithm for DMD.

Since X^TY and X^TX suffer overflow or underflow issues, a stable algorithm is given by decomposition of X by QR or SVD first and uses the resultant Q or U for the projection. Theoretically, two matrixes give the same orthogonal projection, thus producing the same eigenvalues and eigenvectors for the GEV. However, they differ in efficiencies. The typical operation counts for QR is of $2NM^2 - \frac{2}{3}M^3$ (Anderson et al., 1999), slightly heavier than the direct projection by X, but cheaper than SVD. The coefficients of projected GEV (4.29) are

$$X' = Q^TX = R, \tag{4.36}$$

$$Y' = Q^TY \tag{4.37}$$

$X = QR$ is the QR decomposition. We call this DMD-LS algorithm.

The DMD-LS algorithm is equivalent to the standard DMD algorithm. To see that, let

the projection $P = UU^T$ and U is from the SVD of X. $X = U\Sigma V^T$. The projected GEV is

$$U^T Y \boldsymbol{v} = \lambda \Sigma V^T \boldsymbol{v}. \tag{4.38}$$

A coordinate transformation $\boldsymbol{e} = \Sigma V^T \boldsymbol{v}$ makes the GEV to SEV

$$U^T Y V \Sigma^{-1} \boldsymbol{e} = \lambda \boldsymbol{e}, \tag{4.39}$$

where $U^T Y V \Sigma^{-1}$ is the projection matrix calculated by DMD algorithm, see equation (4.9). Since U and Q are the basis of the same subspace and the projection is unique. It can be derived DMD-LS algorithm is equivalent to standard DMD.

DMD-LS algorithm has several advantages over the standard DMD algorithm (4.9). First, this algorithm computes a QR decomposition instead of SVD decomposition. It is much efficient when the data is large. Secondly, it is robust even when the input snapshots are singular or nearly singular. The QZ algorithm can elegantly handle such near-singular matrix (Moler and Stewart, 1973). Alternatively, the iterative method based on Arnoldi procedure (Sorensen, 1997) has a null space purification built in to resolve such an issue.

As a data analysis technique, the capability of parallelization is also important for analyzing large or distributed data. The projected GEV method can be easily parallelized since the parallel QR decomposition (Buttari et al., 2008; Demmel et al., 2012) and parallel GEV solver (Maschhoff and Sorensen, 1996; Stewart, 1987) are the only components needed.

4.4.5 DMD-TLS: the total least-square solution

Total least-square for unbiased estimation

The DMD-LS algorithm implicitly assumes that error occurs only in the last snapshot, $\boldsymbol{x}_{M+1}$. However, every snapshot may contain noise as they were collected by the same experimental instruments or numerical algorithms. Therefore an algorithm that removes the noise simultaneously from every snapshot is desired.

This is accomplished by considering the following problem. Let $S = [\boldsymbol{x}_1 \cdots \boldsymbol{x}_M \, \boldsymbol{x}_{M+1}]$ is the data subject to noise.

$$S = \hat{S} + \Delta S, \tag{4.40}$$

where $\hat{S}$ is the noise-free data and ΔS is the noise. We then resolve equation 4.5 with the restriction that every snapshots are subject to noise $\boldsymbol{x}_i = \hat{\boldsymbol{x}}_i + \Delta \boldsymbol{x}_i$. Rewriting equation 4.5 in augmented form

$$[\boldsymbol{x}_1 \cdots \boldsymbol{x}_M \, \boldsymbol{x}_{M+1}] \begin{bmatrix} a_1 \\ \vdots \\ a_M \\ -1 \end{bmatrix} = \mathbf{0} + \boldsymbol{r}. \tag{4.41}$$

Here $[\boldsymbol{a}_1 \cdots \boldsymbol{a}_M \; -1]^T$ is the solution of unperturbed system

$$a_1 \hat{\boldsymbol{x}}_1 + \cdots + a_M \hat{\boldsymbol{x}}_M - \hat{\boldsymbol{x}}_{M+1} = 0. \tag{4.42}$$

And

$$\boldsymbol{r} = a_1 \Delta \boldsymbol{x}_1 + \cdots + a_M \Delta \boldsymbol{x}_M - \Delta \boldsymbol{x}_{M+1}$$

is the noise.

The pursued solution should be nontrivial, and the residue should be minimized. These requirements is usually written into the following optimization problem

$$\min_{\substack{\hat{S} \in \mathbb{R}^{N \times (M+1)} \\ \hat{\boldsymbol{x}}_{M+1} \in \mathrm{span}(\hat{\boldsymbol{S}})}} ||\Delta S||_2. \tag{4.43}$$

The optimization problem is solved by the total least-square solution (Van Huffel and Vandewalle, 1991). To obtain the solution, ΔS is taken as

$$\Delta S = \sigma_{M+1} \boldsymbol{u}_{M+1} \boldsymbol{v}_{M+1}^T,$$

where σ_{M+1}, u_{M+1}, v_{M+1} are from SVD of S

$$S = U\Sigma V^T = [\boldsymbol{u}_1 \cdots \boldsymbol{u}_{M+1}] \begin{bmatrix} \sigma_1 & & \\ & \ddots & \\ & & \sigma_{M+1} \end{bmatrix} [\boldsymbol{v}_1 \cdots \boldsymbol{v}_{M+1}]^T . \tag{4.44}$$

$||\Delta S||_2 = \sigma_{M+1}$ is of the minimum value to make $\hat{S}$ rank deficient. And

$$[a_1, \cdots, a_M, -1]^T = \frac{-1}{v_{M+1,M+1}} \boldsymbol{v}_{M+1}, \tag{4.45}$$

is the TLS solution. $v_{M+1,M+1} \neq 0$, otherwise, the non-generic TLS solution is applied (Van Huffel and Vandewalle, 1991).

DMD-TLS algorithm solves the generalized eigenvalue problem by projecting it to the modified data space spanned by the first M singular vectors.

$$\hat{\mathcal{S}} = \text{span}(\boldsymbol{u}_1, \cdots, \boldsymbol{u}_M) \tag{4.46}$$

Notice the noise ΔS are in the direction of $\boldsymbol{u}_{M+1}$, which is orthogonal to space $\hat{\mathcal{S}}$. This suggests the total least-square makes the residue of every snapshot to be orthogonal to the modified data space, thus minimizes the total error of all snapshots. After projecting GEV (4.29) to the modified data space, X' and Y' are

$$X' = \begin{bmatrix} \sigma_1 & & \\ & \ddots & \\ & & \sigma_M \end{bmatrix} \begin{bmatrix} v_{11} & \cdots & v_{1M} \\ \vdots & \ddots & \vdots \\ v_{M1} & \cdots & v_{MM} \end{bmatrix}^T , \tag{4.47}$$

$$Y' = \begin{bmatrix} \sigma_1 & & \\ & \ddots & \\ & & \sigma_M \end{bmatrix} \begin{bmatrix} v_{21} & \cdots & v_{2M} \\ \vdots & \ddots & \vdots \\ v_{M+1,1} & \cdots & v_{M+1,M} \end{bmatrix}^T , \tag{4.48}$$

v_{ij} is given by SVD (4.44).

TLS provides an unbiased estimation of a system with noised data. Van Huffel and Vandewalle (1991) pointed out TLS was effective when the noise was independent, of zero mean and of equal variance.

$$E(\boldsymbol{r}_i) = 0, \quad E(\boldsymbol{r}_i \boldsymbol{r}_j) = \sigma \delta_{ij},$$

$\boldsymbol{r}$ is the noise added to the data. Otherwise, it may not provide better solution than LS method.

The total-least-square solution was used with DMD to identify dynamic information by several authors (Dawson et al., 2016; Hemati et al., 2017). DMD-TLS differs with them in the sense that DMD-TLS applies to state variables thus reveal the dynamics in state space $Ax_i = x_{i+1}$, while the mentioned algorithm applied to the system transfer matrix $y_i = Ax_i$, where (x_i, y_i) is the input and output pair of the dynamic system, thus reveals the dynamics therein. Besides, the augmented snapshots constructed by DMD-TLS is half the size of the mentioned algorithm, which is beneficial for big data analysis. The DMD-TLS algorithm is somewhat similar to the dynamic information extraction technique developed by Liu and Shepard Jr (2005). However, DMD-TLS algorithm is different from above methods by avoiding calculating explicitly the solution of $[a_1, \cdots, a_M, -1]^T$, thus circumvents the numerical issue that TLS may be sensitive to perturbation (Golub and Van Loan, 1980) and the numerical instability when computing the eigenvalue of a companion matrix.

An illustrative example of TLS

It might be useful to understand the modified data space by the following example. Consider three consecutive vectors shown in figure 4.2

$$\boldsymbol{x}_1 = \begin{bmatrix} 1 \\ 0 \\ 0 \end{bmatrix}, \quad \boldsymbol{x}_2 = \begin{bmatrix} 0 \\ 1 \\ 0 \end{bmatrix}, \quad \boldsymbol{x}_3 = \begin{bmatrix} 0 \\ \cos\theta \\ \sin\theta \end{bmatrix},$$

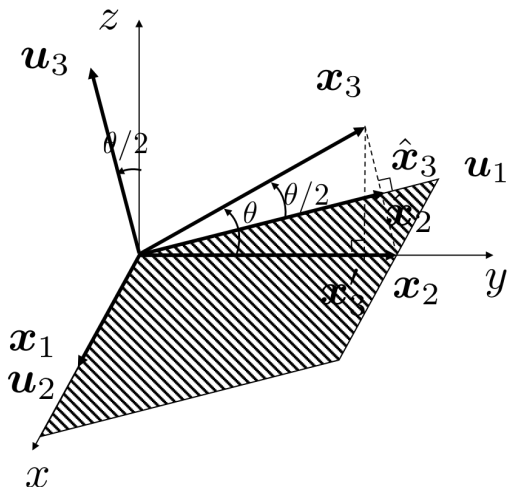

Figure 4.2: *TLS and LS solution of S.*

from a dynamic system, $0 < \theta \ll \pi/2$. In DMD-LS algorithm, all dynamics was projected to the x-y plane, thus solving a dynamic problem using $(\boldsymbol{x}_1, \boldsymbol{x}_2, \boldsymbol{x}_3')$. While DMD-TLS project dynamics into the shaded plane constructed by two main singular vectors of the snapshots. To determined it, decompose snapshots by SVD

$$
\begin{aligned}
S &= [\boldsymbol{x}_1, \boldsymbol{x}_2, \boldsymbol{x}_3] \\
&= \begin{bmatrix} 0 & 1 & 0 \\ \cos\frac{\theta}{2} & 0 & -\sin\frac{\theta}{2} \\ \sin\frac{\theta}{2} & 0 & \cos\frac{\theta}{2} \end{bmatrix} \begin{bmatrix} \sqrt{2}\cos\frac{\theta}{2} & & \\ & 1 & \\ & & \sqrt{2}\sin\frac{\theta}{2} \end{bmatrix} \begin{bmatrix} 0 & 1 & 0 \\ \frac{\sqrt{2}}{2} & 0 & \frac{-\sqrt{2}}{2} \\ \frac{\sqrt{2}}{2} & 0 & \frac{\sqrt{2}}{2} \end{bmatrix}^T
\end{aligned}
$$

The modified space is then

$$
\hat{\mathcal{S}} = \text{span}\left(\begin{bmatrix} 0 \\ \cos\frac{\theta}{2} \\ \sin\frac{\theta}{2} \end{bmatrix}, \begin{bmatrix} 1 \\ 0 \\ 0 \end{bmatrix} \right)
$$

This is shown as the shaded plane. The vectors used to determine the dynamics by DMD-TLS algorithm is $(\boldsymbol{x}_1, \hat{\boldsymbol{x}}_2, \hat{\boldsymbol{x}}_3)$. The residue of each snapshots is along $\boldsymbol{u}_3 = \left[0, -\sin\frac{\theta}{2}, \cos\frac{\theta}{2}\right]^T$ and orthogonal to the modified space $\hat{\mathcal{S}}$.

Noise filtering by SVD

It is often hard to obtain the modes by standard DMD technique for noise snapshots, as the noise intensity may on the same energy level of some modes. Without filtering the noise, modes obtained by DMD algorithm can be useless. To obtain reasonable DMD modes and maximize the signal-to-noise ratio (maximum MSNR), data is often filtered by the SVD (Van Huffel and Vandewalle, 1991, (see, chap. 3.6)). In this approach, only singular vectors with eigenvalue larger than R_v are kept

$$\sigma_1 \geq \sigma_2 \geq \cdots \geq \sigma_r \geq R_v \geq \sigma_{r+1} \geq \cdots \geq \sigma_{M+1}. \tag{4.49}$$

R_v is so-called rank determinant provided either by the user or by the following formula

$$R_v = \sqrt{2 \max\{N, M+1\}} \sigma^{Noise}, \tag{4.50}$$

M is the snapshots number and N is snapshot size. σ^{Noise} is the intensity of noise.

Notice the DMD-TLS decompose data by SVD. It is convenient to compute DMD modes by following formula

$$X\boldsymbol{v} \approx [\boldsymbol{u}_1, \cdots, \boldsymbol{u}_r] \begin{bmatrix} x'_{11} & & x'_{1M} \\ & \ddots & \\ x'_{r1} & & x'_{rM} \end{bmatrix} \begin{bmatrix} v_1 \\ \vdots \\ v_M \end{bmatrix} \tag{4.51}$$

where x'_{ij} is from equation (4.47). $r \in \mathbb{N}$ and is determined by (4.49). $\boldsymbol{v}$ is the eigenvector.

4.5 DMD algorithm and Koopman decomposition

DMD algorithm can effectively approximate the spectra and modes of systems with constant spectra. However, it may fail to capture the spectrum of the LTV system or nonlinear system, except for the following particular case.

1. The transient spectrum: If the observation period is much smaller than the characteristic time T of the dynamics system, DMD algorithm may be useful to compute the transient spectrums and modes.

2. The infinity spectrum: If the observation duration is large enough such that $\tau \to \infty$ in equation (2.28) is approximately satisfied, $\lambda(\infty, t_0)$ defined in equation (2.28) will be approximated. If the system is further UES (or UAS), the spectra are time-independent and can be computed correctly by the DMD algorithm.

3. The periodic system: As stated earlier, a Floquet system has constant Koopman spectrums. DMD algorithm will correctly reveal the Koopman modes and spectrum.

In practical application, the transient spectrum may still cumbersome to compute. We may save trouble by noticing Koopman mode is invariant for some cases. Therefore we first compute the Koopman modes at the asymptotic case, then using the techniques such as the least square solution to obtain the decomposition. However, this approach may produce unsatisfactory results since Koopman modes are non-orthogonal. What is more, this approach requires that the modes to be 'atomic', that is, they are not the superposition of several modes as will be talked in chapter 9.2.

DMD only reveals dynamics implied by the data, which requires the snapshots to contain both base and the perturbation to reveal their spectra. For example, if only periodic snapshots are given, the spectrum for the perturbation cannot be obtained.

Chapter 5

Linear structure of nonlinear dynamics

If I have seen further it is by standing on the shoulders of giants.

Issac Newton (English), 1642-1726

5.1 Introduction

Dynamic systems are widely studied in fields such as mathematics, physics, engineering, chemistry, biology, economics, etc. For instance, the dynamics of particles subject to external forces is usually described by differential equations following Newton's law

$$\dot{x} = f(x). \tag{5.1}$$

If $f(x)$ is a linear function of x (where $f(\alpha x + \beta y) = \alpha f(x) + \beta f(y)$, $\alpha, \beta \in \mathbb{R}$, $x \in \mathbb{R}^n$), the dynamic system is linear, otherwise nonlinear.

The categorization of linear and nonlinear dynamics is of practical importance. Linear systems are theoretically well-studied and straightforward. However, most systems are inherently nonlinear. On the other hand, nonlinear systems are usually approximated by

linear ones through linearization, such as the linear stability analysis. Unfortunately, this only works for short term prediction. Lorenz (1963) published a numerically work on solving a nonlinear modal system and revealed the remarkable fact that nonlinear dynamics could have chaotic solution for specific parameters and initial conditions. Many more works showed that nonlinear dynamics could be chaotic, unpredictable, or counter-intuitive contrasting with linear systems (Feigenbaum, 1983; May, 1987; Ruelle and Takens, 1971; Russell, 1844; Strogatz, 2018; Winfree, 1967).

Despite the dramatic difference between linear and nonlinear dynamic systems, efforts exist to reduce the nonlinear dynamics to some form of linear ones. For instance, by defining Koopman operator (Koopman, 1931), or its adjoint Frobenius-Perron operator (Frobenius et al., 1912; Perron, 1907) on nonlinear dynamic systems, researchers instead studied dynamics of functionals defined on the systems and evolved by the linear operators (Lasota and Mackey, 2013; Reed and Simon, 1972). Recently, spectral Koopman decomposition was introduced to study dynamics of ergodic systems and fluid systems (Bagheri, 2013; Mezić, 2005; Rowley et al., 2009). Our work continues these efforts. A direct motivation is to understand various decomposition techniques, such as Fourier decomposition, proper-orthogonal decomposition (POD) (Holmes et al., 1996a), and dynamic mode decomposition (DMD) algorithms (Schmid, 2010) on nonlinear dynamics which lacks superposition principle. It is found that completeness of dual space of dynamic state introduces what we called linear structure of dynamics, resulting in the various decomposition techniques mentioned above. Further, by considering the local Koopman spectrum problem, invariant subspaces of nonlinear dynamics are introduced, an analog to the linear dynamics. Following the linear structure via Koopman decomposition, two unique properties of nonlinear dynamics are identified, the locality and infinite-dimensionality of Koopman spectrums. By this understanding, the gap between dynamics and various mathematical oriented decomposition techniques is bridged.

5.2 The universal and unique properties of nonlinear dynamic systems

Chapter 1.3 summarized two important properties of linear dynamic systems. They have superposition principle and invariant subspaces. In the following chapter, these universal properties are extended to nonlinear dynamics. Besides, two unique properties of nonlinear dynamics are revisited.

5.2.1 Linear structure

Unfortunately, the superposition principle does not hold for nonlinear dynamics. One would ask how to understand those decomposition techniques, such as Fourier decomposition, POD, DMD without superposition principle. If nonlinear dynamics are not decomposable, one has to take them as a magic black box and has difficulty understanding them. Fortunately, the linear-sum capability of nonlinear dynamics comes from what we called the linear structure of dynamics. To explain that, let us introduce some definitions from operator theory (Reed and Simon, 1972).

- A complete normed linear space is called a *Banach space*.
- A *bounded linear transformation* (or *bounded operator*) from a normed linear space $< V_1, ||\,||_1 >$ to a normed linear space $< V_2, ||\,||_2 >$ is a function, T, from V_1 to V_2 which satisfies the following two conditions
  (1) $T(\alpha v + \beta w) = \alpha T(v) + \beta T(w)$,
  (2) For some $c \geq 0$, $||Tv||_2 \leq c||v||_1$.
  The smallest such c is called the norm of T

$$||T|| = \sup_{||v||_1=1} ||Tv||_2 \tag{5.2}$$

- The set of bounded linear transformations from one Banach space $\mathbb{X}$ to another $\mathbb{Y}$ is itself a Banach space, noted by $\mathcal{L}(\mathbb{X}, \mathbb{Y})$. In the case where $\mathbb{Y}$ is the complex numbers,

this space $\mathcal{L}(\mathbb{X}, \mathbb{C})$ is denoted by $\mathbb{X}^*$ and called the *dual space* of $\mathbb{X}$.

Therefore, the dual space $\mathbb{X}^*$ contains all the Lipschitz continuous functionals of $\mathbb{X}$.

Since the completeness of Banach space, any element $g(x)$ in the dual space can find a Cauchy sequence such that

$$g(x) = \lim \sum_{i=0}^{\infty} f_i(x). \tag{5.3}$$

Then dynamics $g(x)(t)$ is transferred to dynamics of the bases $f_i(x)(t)$ and then sum all these sub-dynamics together. That is, the linear summation in the decomposition techniques stems from the linearity and completeness of dual space $\mathbb{X}^*$. Since it is different from the superposition principle of linear systems, we call it *linear structure* of dynamics for differentiation.

Apply the linear structure to state variable x

$$x = \lim \sum_{i=0}^{\infty} c_i f_i'(x). \tag{5.4}$$

$f_i'(x)$ is some functional of $\mathbb{X}^*$, and c_i is corresponding coefficient. If x is a vector, the above expansion is carried elementwisely, then c_i are vectors and called *modes*. In short, the linear structure makes use of functional analysis, and decomposes the dynamic variables by a series of functionals, and studies sub-dynamics of the functionals.

5.2.2 Invariant subspaces

Various choices of Cauchy sequence may be available and result in different decomposition techniques. However, the choice may significantly affect dynamics analysis. Motivated by the LTI system and the recent development of linear time-variant (LTV) systems (Wu, 1974; Zhou, 2016), it is desired to use similar linearly independent and invariant bases if available for nonlinear dynamics.

Unfortunately, extending the invariant subspace to the nonlinear dynamic system is not straightforward. No spectral theory is defined on nonlinear dynamic systems to the authors' knowledge. An attractive idea is to look into the dynamics in its dual space since the

dynamics system defines a linear yet infinite-dimensional map on a linear space (Lasota and Mackey, 2013; Reed and Simon, 1972), known as Koopman operator. Recently, the spectral decomposition is introduced to dynamics study by Mezić and Rowley, as the linear operator defined on linear space naturally raises the spectral problem.

However, the spectrum theory of linear operator is a non-trivial extension to the finite-dimensional matrix spectral problem, partly because of the infinite-dimensionality of the operator. It is known only bounded operator is guaranteed bounded spectrum. Other than that, unbounded operators may or may not have spectrum (Reed and Simon, 1972). As a result, previous researchers focused on some particular dynamic system. For example, the ergodic system results in a unitary operator, one type of well-propertied bounded operator Mezić (2005).

In part I we proposed to relax the definition to the local spectrum as there were signs they depended on the state of the system for nonlinear dynamics. Consider the dynamics of an observable $g(x)$ under the dynamics T^τ, where T^τ represents the dynamic mapping $T^\tau : \mathbb{X} \to \mathbb{X}$ for a given time interval τ. And the Koopman operator U evolutes the dynamics of $g(x)$ by

$$Ug(x) = g(T^t x) \tag{5.5}$$

The Koopman operator is linear (Reed and Simon, 1972; Rowley et al., 2009). Therefore, the local Koopman spectrum is defined by

$$\phi(T^\tau x) = U\phi(x) = \lambda(x)\phi(x), x \in D_{x_0}. \tag{5.6}$$

The local eigenvalue problem is only required to hold in a neighborhood around the state x_0.

Further, utilizing the perturbation theory of operator (Kato, 2013; Reed and Simon, 1978), the local spectral $\lambda(x)$ and eigenfunction $\phi(x)$ can analytically extend to the whole space under the condition that the Koopman and perturbation operator is bounded. The requirements can be satisfied by many practical dynamic systems. With this extension, both

the eigenvalue $\lambda(x)$ and the eigenfunction $\phi(x)$ will be continuous and analytical in $\mathbb{X}^*$. The resulting eigenfunctions $\phi(x)$s constitute bases for the linear structure.

The newly defined local Koopman is backward-compatible to the global Koopman spectral that appeared in previous literature. Under this situation, the domain D is the whole space $\mathbb{X}$, for example, the LTI system.

5.2.3 Unique properties of nonlinear dynamics

The locality Koopman spectrum

For an LTI system, the Koopman spectrum problem is globally defined, and the Koopman spectrums are constant. They are independent of the state. However, for nonlinear systems, it was found that the spectrums were no longer constant and are state-dependent. Therefore, the local Koopman spectrum problem is defined. Notice that general LTV systems usually represent linearized nonlinear systems, the time-variant spectrum are consistent with the state-dependent Koopman spectrum.

Nonlinear interaction and infinite-dimensionality of nonlinear dynamics

Another fundamental difference between linear and nonlinear dynamics is the dimensionality. For linear systems, dynamics are decoupled into invariant subspaces and no interaction among them. However, for nonlinear dynamics, interaction exists among its sub-dynamics. These recursive interaction promotes the system to infinite-dimensional. Under Koopman decomposition, this effect is conveniently summarized by the recursive proliferation rule. For instance, some critical Koopman spectrum generated by self-interaction are shown in figure 2.2. By the interaction, each Koopman eigenfunction can generate an infinite-dimensional Koopman eigenfunctions grouping all the nonlinear interaction. This infinite-dimensionality results in many important phenomena in nonlinear dynamics as will be illustrated later.

5.3 Examples of linear structures via Koopman decomposition

5.3.1 A linear dynamic system

Let's take the LTI systems (1.11) for an example. Assuming A is diagonalizable

$$A = V\Lambda W \tag{5.7}$$

where V and W contains the right and left eigenvectors of A, the diagonal elements of Λ are the spectrum, so $AV = V\Lambda$ and $WA = \Lambda W$. From part I, it is known for LTI systems, the eigenfunction is given by the inner-product of the left eigenvectors and state variable.

$$x = VWx = V\begin{bmatrix} f_1(x) \\ f_2(x) \\ \vdots \\ f_n(x) \end{bmatrix} = \begin{bmatrix} v_{11}f_1 + \cdots v_{1n}f_n \\ v_{21}f_1 + \cdots v_{2n}f_n \\ \vdots \\ v_{n1}f_1 + \cdots v_{nn}f_n \end{bmatrix} \tag{5.8}$$

where $W = [w_1 \cdots w_n]^T$, and $f_i(x) = w_i^T x$. We therefore obtain the Koopman decomposition. The dynamics of $x(t)$ is transferred to the components $f_i(x(t))$. Though literally complex, $f_i(x(t))$ is of the simple form $c_i e^{\lambda_i t}$ for LTI systems. It is then easier to trace the dynamics through these eigenfunctions $f_i(x)$. For instance, the dynamics of x_1, the first component of vector x, is given by

$$x_1 = v_{11}f_1 + \cdots v_{1n}f_n. \tag{5.9}$$

Each subcomponent has the dynamics $f_i(x(t))$, and the total dynamics is given by the linear sum (5.9). Moreover, the dynamics of $f_i(x)(t)$ are linearly independent and invariant, therefore each sub-dynamics is totally decoupled from others.

Sometimes nonlinear observables may be presented, for instance, the total kinetic energy

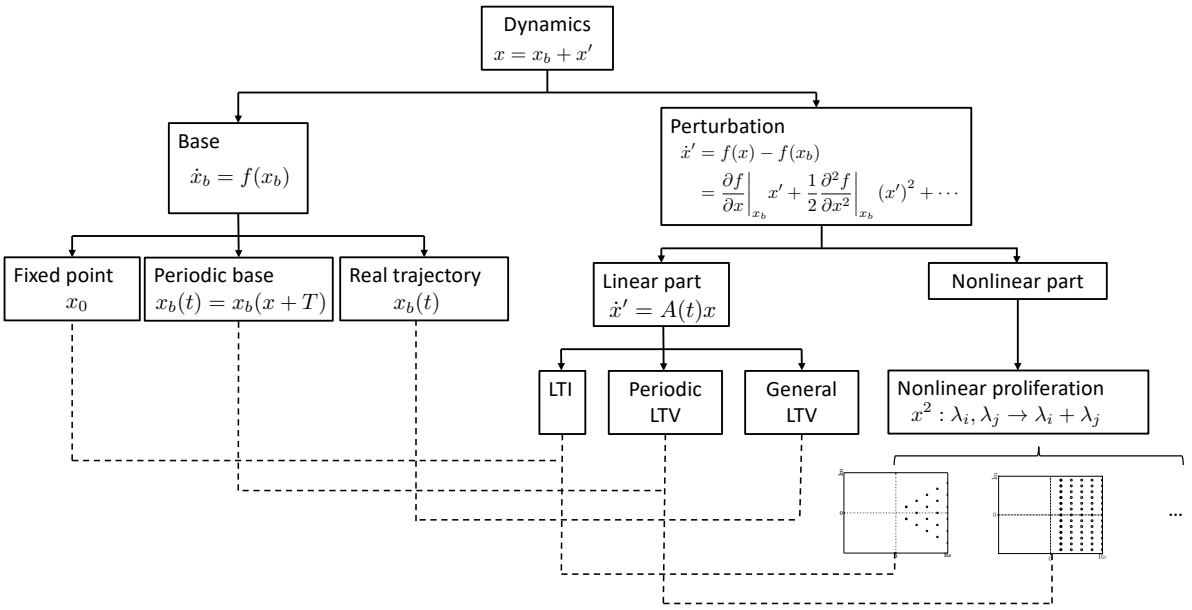

Figure 5.1: *The hierarchy of Koopman decomposition.*

is expressed as

$$e = \frac{1}{2}\sum_i \dot{x}_i^2 = \sum_k \sum_l b_{lk} f_l f_k \tag{5.10}$$

where b_{lk} is the element of $B = \frac{1}{2}\Lambda^T V^T V \Lambda$. $f_l f_k$ is the Koopman eigenfunction given by the multiplication of $f_l(x)$ and $f_k(x)$, as described by the proliferation rule in part I. The dynamics of the total kinetic energy is obtained simply replacing $f_l(x)f_k(x)$ by $f_l(x(t))f_k(x(t))$.

5.3.2 Hierarchy of nonlinear dynamics

Unfortunately, general formulation of Koopman spectrum or Koopman eigenfunctions are not available for nonlinear dynamic system. However, hierarchy structure discussed in part I made it easier to understand and compute Koopman decomposition. The hierarchy is illustrated by figure 5.1.

The hierarchy structure decomposes dynamics into base dynamics and perturbation. The base dynamics are required to be a real trajectory of the system such that it will not introduce fake spectrums into the system. Typically, they are simple dynamics such as a fixed point, or a periodic solution whose spectrum are already studied, or the real trajectory whose

spectrum is numerically studied by the DMD algorithm. The perturbation is described by the nonlinear perturbation equation, whose linear part was studied by the spectrum of LTI system or periodic/non-periodic LTV system in part I. Further, the nonlinear perturbation terms are obtained by recursively applying proliferation rule. Then all the spectrum and the decomposition is obtained.

5.4 Linear structure and other decomposition techniques

As discussed in chapter 3.2, linear structure via Koopman decomposition was found to provide a foundation for global stability analysis. In fact, the linear structure provides not only bases for stability analysis, but also many other decomposition techniques as well.

5.4.1 Understanding the DMD and POD techniques

DMD and POD are both data-driven techniques for dynamics analysis, and often compared to each other. DMD is the data-driven tool for Koopman decomposition, or more accurately, a time-averaged approximation to the local Koopman spectrum since the sampled data last some time. For instance, data collected at the approximate linear stage provides an excellent approximation to the primary stability or secondary stability spectrum, see Part I.

Linear structure provide foundation for POD as well, but relies on a different set of bases, the eigenfunctions of the second order correlation function of the dynamics

$$R_x(t,t') = \int_{\Xi} x(\xi,t)x(\xi,t')d\xi \tag{5.11}$$

where t, t' is the time lapse of observation, ξ is the spatial coordinate for the dynamic system. The correlation has the following properties: *symmetry* as $R_x(t,t') = R_x(t',t)$, *continuous* as long as $x(\xi,t)$ is continuous, and *positive semi-definite*, since for any nonzero function $\psi(t)$

$$\int_a^b \psi^2(t)dt > 0, \tag{5.12}$$

satisfies the following relation

$$\begin{aligned}\int_a^b \int_a^b R_x(t,t')\psi(t)\psi(t') &= \int_a^b \int_a^b \int_\Xi x(\xi,t)x(\xi,t')\psi(t)\psi(t')d\xi dt dt' \\ &= \int_\Xi \left(\int_a^b u(\xi,t)\psi(t)dt\right)^2 d\xi \geq 0.\end{aligned} \tag{5.13}$$

The continuous, symmetry, positive semi-definite kernel $R_x(t,t')$ satisfies the Mercer's theorem (Mercer, 1909), also known more generally as Fredholm eigenvalue problem (Edmunds and Evans, 2018), therefore can be expanded by series

$$R_x(t,t') = \sum_{i=1}^{\infty} \lambda_i e_i(t) e_i(t') \tag{5.14}$$

where the functions $e_i(t)$ are the eigenfunctions of the following eigenvalue problem.

$$\int_a^b R_x(t,t')e_{xi}(t')dt' = \lambda_{xi}e_{xi}(t). \tag{5.15}$$

The eigenfunction $e_{xi}(t)$ may then act as the bases for duration from a to b. We may then take limit $b-a \to 0$ to define the functional at x

$$\phi_i(x) = \lim_{b\to a} e_{ix}(t) \tag{5.16}$$

and use the functionals $\phi_i(x)$ for linear structure, which results in the POD decomposition. As $R_x(t,t')$ is symmetrical, the eigenvalues are all real numbers and therefore naturally ordered by corresponding eigenvalues. which then givens the POD decomposition. It is noticed by taking limit of above Fredholm problem, a local spectrum is defined.

It is well known that the POD gives the most efficient decomposition as it captures the most energy with the same amount of modes. It is seen in the Mercer's theorem, the eigenfunctions corresponding to the largest eigenvalue and the eigenfunctions are orthogonal to each other. However, POD decomposition has disadvantages. First, these eigenfunctions are not the eigenfunctions of the dynamics system, therefore not invariant under the dynamics

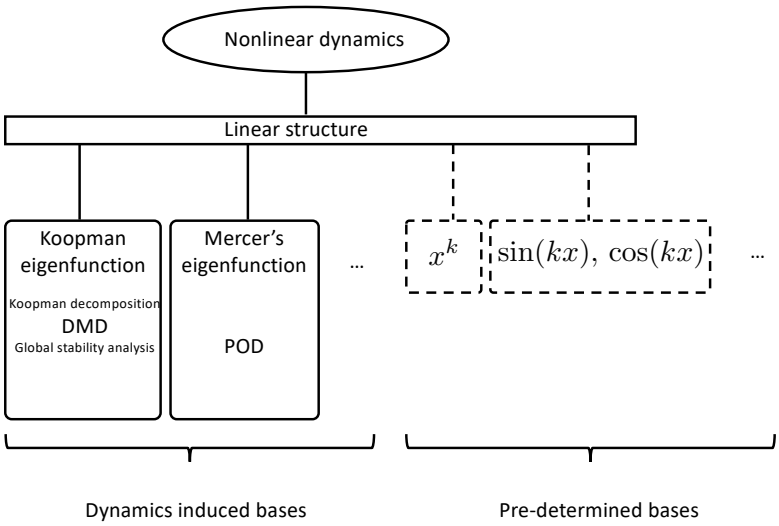

Figure 5.2: *The linear structure and bases*

mapping. Secondly, POD eigenfunctions do not support the proliferation rule, and the sub-dynamics are coupled. Further, Koopman spectrum problem only requires the Banach space with a norm defined, while the POD requires the Hilbert space with inner-product defined such that its application may be further limited. Therefore, Koopman decomposition may be more suitable for dynamic analysis.

Both the Koopman eigenfunctions and eigenfunctions of Mercer's theorem are dynamics induced bases. Besides them, there exists fixed bases as well, see figure 5.2, such as polynomials $1, x, x^2, \cdots$ or the trigonometric series, where the former was extensively used to derive the proliferation rule. Though these bases are readily available, they may subject the same disadvantages as Mercer's eigenfunctions.

Chapter 6

Fluid dynamic system, numerical algorithm and benchmark

After introducing Koopman spectrum theory and DMD algorithm, let us consider a physical problem, the fluids past a fixed cylinder. The flow phenomena, instability mechanism, and numerical simulation algorithm are discussed in this chapter.

6.1 Flow past fixed cylinder, the physical problem

The flow passing a fixed cylinder is chosen as a classical benchmark problem for its simple configuration and geometry and rich dynamics. The non-dimensional Reynolds number $Re = \frac{\rho U D}{\mu}$ influences the instability of wake. U is the incoming flow velocity, D is the diameter of the cylinder, and μ is the viscosity of the fluids. For low Reynolds number, such that $Re < Re_{c1} \approx 6$ (Jackson, 1987), viscosity effect dominates. The flow is laminar, steady and does not separate from the cylinder. Above Re_{c1}, the flow separates from the cylinder surface and rejoins in the wake, creating a recirculating zone with two counter-rotating vortices. At this time, the flow is still symmetry, steady and laminar. Experimental show at around $Re_{c2} \approx 50$ (Roshko and for Aeronautics, 1954; Tritton, 1959), the wake will break symmetry. The original two steady vortices will shed alternatively off the cylinder,

creating the well-known Kármán vortex street. Further increasing the Reynolds number, it is observed at some point, after $Re_{c3} \approx 190$ (Williamson, 1988), there is a sharp drop in the lift, drag, and shedding frequency, indicating a transition occurs. At this Reynolds number, the original two-dimensional Kármán vortex begins to wobble in the spanwise direction, and eventually develops the three-dimensional wake. The above phenomena are summarized in figure 6.1.

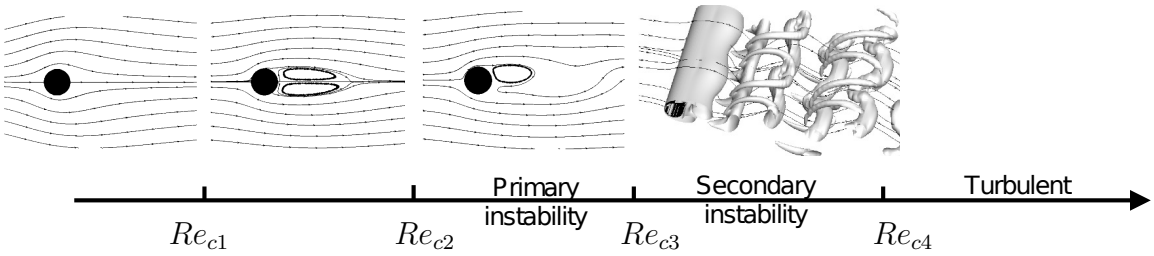

Figure 6.1: *Cylinder wake for different Reynolds number.*

Above instability phenomena are all attributed to the linear instability mechanism. To perform linear stability analysis, we decompose the flow into an equilibrium base flow and perturbation on top of it and substitute them into the Navier-Stokes equations. After canceling the base flow and nonlinear perturbation terms, a linear perturbation equation is obtained. In the range of $Re_{c2} < Re < Re_{c3}$, the linearized homogeneous Navier-Stokes equation around the steady base flow will provide a pair of unstable complex conjugate normal modes (Jackson, 1987). They grow exponentially when the perturbation is small and later are saturated by the nonlinear effect. The oscillation of paired unstable modes breaks the symmetry of flow and eventually leads to the alternatively shedding vortices. This wake developing process corresponds to the Hopf bifurcation (Provansal et al., 1987). That is, flow in the primary instability range has two critical elements co-existing: an attracting limit cycle and an unstable equilibrium.

Further increasing the Reynolds number, the primary modes keep growing and distorting the mean flow. When Re exceeds the critical Re_{c3}, a three-dimensional secondary wave is formed and superimposed on the primary wave (Landahl, 1972). Orszag and Kells (1980) expanded the three-dimensional perturbation around the essential two-dimensional periodic base flow and obtained the Floquet system for the perturbation. The exponential growth

of three-dimensional perturbation is thus attributed to the linear stability mechanism and analyzed using the Floquet theory. The universal of secondary instability for the various wall-bounded shear flow was confirmed by Orszag and Patera (1983). Other flow, such as boundary layer, was inspected by Herbert (1988), and blunt bodies wake was studied by Barkley and Henderson (1996).

The secondary instability for the wake past cylinder mentioned in the previous section is around $Re = 180 \sim 190$. The Strouhal number St is usually checked for this transition. Roshko and for Aeronautics (1954) found it increased steadily except after some critical number Re_c, where the coefficients experienced a sudden drop. More dedicated experiments (Miller and Williamson, 1994; Prasad and Williamson, 1997; Williamson, 1988, 1992) confirmed the above observation and found two discontinuities existed instead of one. They found in the range $Re_{c3A} < Re < Re_{c3B}$, a three-dimensional wave with a spanwise wavelength of $L_z \approx 3D$ appeared, they call it the mode A instability. Further increasing Re, a fine-scale pattern with $L_z \approx 1D$ occurred, and the St increased abruptly. It is the so-called mode B instability. The transition is hysteretic and two critical Reynolds number is $Re_{c3A} = 180 \sim 190$ and $Re_{c3B} = 230 \sim 260$. Linear stability analysis based on Floqeut theory reveals that mode A and mode B corresponds to two distinct unstable Floquet modes (Barkley and Henderson, 1996). They also determined that the onset of mode A secondary instability occurred at $Re_{c3A} = 188.5$, and the wavelength was $Lz = 3.96D$. And the mode B secondary instability occurred at $Re_{c3B} = 259$ and $Lz = 0.82D$.

Since the well-known mechanism and relatively simple flow dynamics, We choose this physical problem as our study subject. The research objective is two-fold.

The first one is the desire to study the instability via the data-driven approach. The primary and secondary instability are studied by the DMD algorithm. Two cases, $Re = 50$ and $Re = 200$, are chosen. The study will focus on the initial development of small perturbation and will be presented in chapter 9.1 and chapter 8.2.

The second objective is to study the nonlinear dynamics by the Koopman decomposition. The focus is the full Hopf bifurcation transition process. The result will be presented in chapter 9.2.

6.2 Numerical simulation algorithm for incompressible Navier-Stokes equation

Computational fluid dynamics (CFD) provides rich information on the flow field. Our data is numerically collected by integrating the governing equations. In the following chapter, the numerical algorithm to solve Navier-Stokes equations is introduced.

In chapter 1.2, the incompressible Navier-Stokes equations are introduced.

$$\nabla \cdot \boldsymbol{u} = 0, \tag{6.1}$$

$$\frac{\partial \boldsymbol{u}}{\partial t} + (\boldsymbol{u} \cdot \nabla)\boldsymbol{u} = -\nabla p + \frac{1}{Re}\nabla^2 \boldsymbol{u}. \tag{6.2}$$

where u, v, w are the velocity, p is the pressure and Re is the Reynolds number.

6.2.1 Time discretization scheme

A second order, time-discrete semi-implicit form of Eqn. (6.1, 6.2) is given by

$$\begin{aligned} \nabla \cdot \boldsymbol{u}^{n+1} &= 0 \\ \frac{\boldsymbol{u}^{n+1} - \boldsymbol{u}^{n}}{\nabla t} &= -\left[(\boldsymbol{u} \cdot \nabla)\boldsymbol{u})\right]^{n+\frac{1}{2}} - \nabla p^{n+\frac{1}{2}} + \frac{1}{Re}\nabla^2(\boldsymbol{u}^{n+1} + \boldsymbol{u}^{n}) \end{aligned} \tag{6.3}$$

This is a second order center scheme at time $t + \frac{1}{2}$. However, the implicit nature requires solving a coupled system of $\boldsymbol{u}^{n+1}$, p^{n+1}, which is cumbersome.

Before proceeding any further, let us re-examine the incompressible Navier-Stokes equations. Equation (6.1) enforces the divergence free constraint to the momentum equation (6.2), which can be rewritten as

$$\frac{\partial \boldsymbol{u}}{\partial t} + \nabla p = -(\boldsymbol{u} \cdot \nabla)\boldsymbol{u} + \frac{1}{Re}\nabla^2 \boldsymbol{u}. \tag{6.4}$$

Therefore, role of pressure in the momentum equation is to enforce the divergence free constrain in the velocity field. In fact, equation (6.4) is the hodge decomposition and can be

written

$$\frac{\partial \boldsymbol{u}}{\partial t} = \mathcal{P}\left[-(\boldsymbol{u}\cdot\nabla)\boldsymbol{u} + \frac{1}{Re}\nabla^2\boldsymbol{u}\right]. \tag{6.5}$$

$\mathcal{P}$ represents the divergence-free projector.

Projection methods pioneered by Chorin (1968) for numerically integrating Eqn. (6.1, 6.2) are based on above observation. It approximates the solution of the coupled system by first solving an analog to the discretized Eqn. (6.3) without considering the divergence constraint on the intermediate velocity $\boldsymbol{u}^*$. After that, the intermediate velocity is projected onto a space of divergence-free, yielding $\boldsymbol{u}^{n+1}$. To be specific, this procedure is given in the following steps.

- Step 1: Solve for the intermediate field $\boldsymbol{u}^*$

$$\begin{aligned} &\frac{\boldsymbol{u}^* - \boldsymbol{u}^n}{\Delta t} = [-(\boldsymbol{u}\cdot\nabla)\boldsymbol{u}]^{n+\frac{1}{2}} - \nabla p^{n+\frac{1}{2}} + \frac{1}{Re}\nabla^2(\boldsymbol{u}^* + \boldsymbol{u}^n), \\ &\boldsymbol{u}^*|_{\partial\Omega} = \boldsymbol{u}_b^{n+1}. \end{aligned} \tag{6.6}$$

- Step 2: Perform the divergence free projection

$$\begin{aligned} \boldsymbol{u}^* &= \boldsymbol{u}^{n+1} + \Delta t \nabla \phi^{n+1}, \\ \nabla\cdot\boldsymbol{u}^{n+1} &= 0, \end{aligned} \tag{6.7}$$

  by solving the following Poisson equation

$$\begin{aligned} \nabla^2\phi^{n+1} &= \frac{\nabla\cdot\tilde{\boldsymbol{u}}}{\Delta t}, \\ (\boldsymbol{n}\cdot\nabla\phi)^{n+1}\Big|_{\partial\Omega} &= 0, \end{aligned} \tag{6.8}$$

  where $\tilde{\boldsymbol{u}} = \boldsymbol{u}^* - \boldsymbol{u}^n$, and obtain $\boldsymbol{u}^{n+1} = \boldsymbol{u}^* - \Delta t\nabla\phi^{n+1} = \tilde{\boldsymbol{u}} + \boldsymbol{u}^n - \Delta t\nabla\phi^{n+1}$ to finish the divergence free projection.

- Step 3: Update the pressure

$$p^{n+\frac{1}{2}} = p^{n-\frac{1}{2}} + \phi^{n+1} - \frac{\Delta t}{2Re}\nabla^2\phi^{n+1}. \tag{6.9}$$

Some comments are followed.

1. The convective term is approximated by the second-order-explicit Adams-Bashforth scheme

$$[-(\boldsymbol{u}\cdot\nabla)\boldsymbol{u}]^{n+\frac{1}{2}} = \frac{3}{2}[-(\boldsymbol{u}\cdot\nabla)\boldsymbol{u}]^{n} - \frac{1}{2}[-(\boldsymbol{u}\cdot\nabla)\boldsymbol{u}]^{n-1}. \tag{6.10}$$

2. The semi-implicit Crank-Nicholson method applied on the viscous term in Eqn. (6.6) eliminates the numerical viscous stability restriction, which is particularly severe for low-Reynolds number and stretched grids (Kim and Moin, 1985) considered in this work.

3. $\nabla p^{n+\frac{1}{2}}$ in the momentum equation (6.6) is approximated by $\nabla p^{n-\frac{1}{2}}$ to reach the second-order temporal accuracy. A more accurate approximation would interpolate $\nabla p^{n+\frac{1}{2}}$ by

$$\nabla p^{n+\frac{1}{2}} = 2\nabla p^{n-\frac{1}{2}} - \nabla p^{n+\frac{3}{2}}. \tag{6.11}$$

4. Boundary conditions for intermediate velocity $\boldsymbol{u}^*$ in Eqn. (6.6) are compatible for $\boldsymbol{u}^{n+1}$ and $p^{n+\frac{1}{2}}$ to achieve second order temporal accuracy up to boundary (Brown et al., 2001).

5. The last term on the right-hand side of Eqn. (6.9) is essential for pressure to achieve second-order temporal accuracy (Brown et al., 2001).

6.2.2 Staggered grid and spatial discretization

Staggered grid is adopted to avoid 'checkerboard' decoupling of velocity and pressure (Harlow and Welch, 1965). Velocity variables u, v, w are placed on the surface of the cell. Pressure

p and the variable ϕ are placed at the center of the cell. A two-dimensional arrangement is shown in figure 6.2.

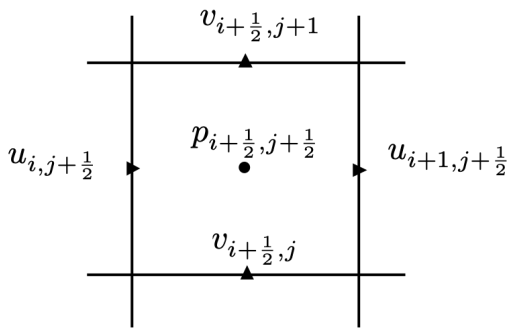

Figure 6.2: *Staggered grid configuration and location of velocities and pressure*

In the staggered grid, the momentum u, v and the variable ϕ are evaluated by different stencils, which are illustrated in figure 6.3. To achieve second order accuracy in space, the derivatives are evaluated by central difference scheme, except for some flux terms on the right hand side, which are interpolated to the required position.

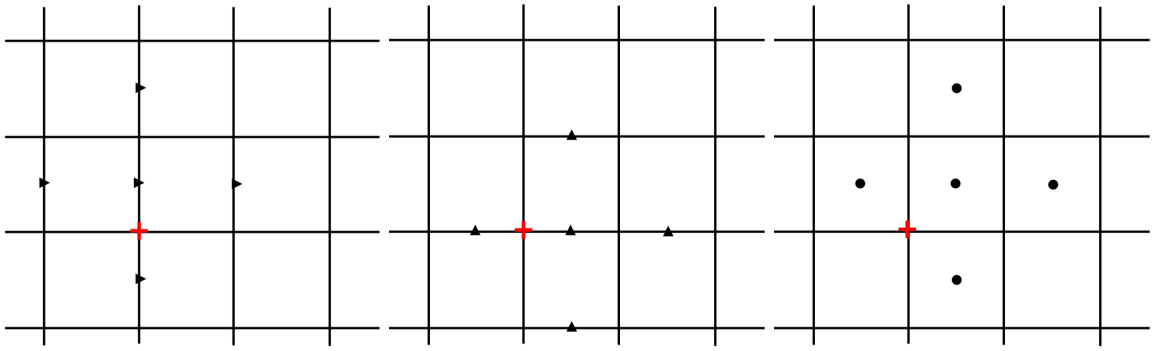

(a) *u stencil* **(b)** *v stencil* **(c)** *p or ϕ stencil*

Figure 6.3: *2D stencils for evaluating momentum/pressure. Red cross label the grid (i, j).*

Momentum equation

$$\tilde{\boldsymbol{u}} - \lambda \nabla^2 \tilde{\boldsymbol{u}} = RHS \tag{6.12}$$

is solved by the approximate factorization (Kim and Moin, 1985). $RHS = -\left[(\boldsymbol{u}\cdot\nabla)\boldsymbol{u}\right]^{n+\frac{1}{2}} - \nabla p^{n+\frac{1}{2}} + \frac{2}{Re}\nabla^2 \boldsymbol{u}^n$ and $\lambda = \frac{\Delta t}{Re}$.

$$\left(I - \lambda \frac{\partial^2}{\partial x^2}\right)\left(I - \lambda \frac{\partial^2}{\partial y^2}\right)\left(I - \lambda \frac{\partial^2}{\partial z^2}\right)\tilde{\boldsymbol{u}} = RHS. \tag{6.13}$$

The discretized poisson equation (6.8) (2D)

$$(l_{i,j-1}\phi_{i,j-1} + l_{i,j}\phi_{i,j} + l_{i,j+1}\phi_{i,j+1}) + (m_{i-1,j}\phi_{i-1,j} + m_{i,j}\phi_{i,j} + m_{i+1,j}\phi_{i+1,j}) = RHS_{i,j} \quad (6.14)$$

is solved by cyclic reduction (Buneman, 1969), which is implemented by FISHPACK (Adams et al., 1980). The third-dimension (z-direction) of Poisson equation is converted to Fourier space

$$\left(\frac{\partial^2}{\partial x^2} + \frac{\partial^2}{\partial y^2} - k^2\right)\hat{\phi} = \widehat{RHS}, \quad (6.15)$$

k is the wave number in spanwise direction. Then the Helmholtz equation is further solved by cyclic reduction mentioned above.

6.2.3 Cartesian Grid and IBM method

The simulation uses the Cartesian gridy. It is the nonconforming grid if solid is presented in the computational domain. In that case, an immersed boundary method (IBM) is implemented. In this study, a sharp interface IBM (Mittal et al., 2008) is used.

Instead of applying BC on the whole solid boundary, the sharp interface method enforce the conformal of boundary condition at a set of Lagrangian points, the boundary interception points (BP), which is illustrated in figure 6.4.

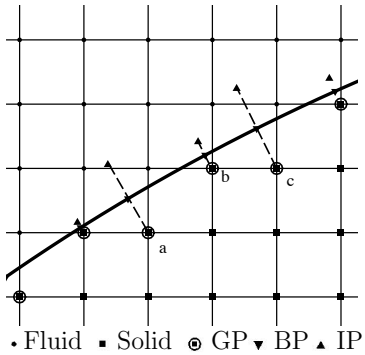

Figure 6.4: *The immersed boundary method. GP: ghost point; BP: boundary point; IP: image point.*

The following steps summarize the procedure.

1. First, we categorize the Cartesian nodes in solid to be solid nodes and the rest to be fluid nodes.

2. The ghost points (GP) are determined to be solid nodes who at least have one neighbor fluid node.

3. For each GP, the closest boundary facet is determined. The boundary point (BP) is obtained by orthogonally projecting the GP to the facet.

4. The image point (IP) is determined by mirroring the GP through the boundary facet.

5. The value for u, v, ϕ on the GP is reconstructed from IP, the later is interpolated by surrounding fluid nodes. To enforce the no-slip velocity condition

$$V_{GP} = 2V_{BP} - V_{IP}. \tag{6.16}$$

   Here V_{BP} is the velocity at point BP. For Neumann BC of ϕ,

$$\phi_{GP} = \frac{\partial \phi}{\partial n}\bigg|_{BP} \Delta l + \phi_{IP}. \tag{6.17}$$

   $\frac{\partial \phi}{\partial n}$ is the derivative in the normal direction at point BP, and Δl is the length from GP to IP. V_{IP} and ϕ_{IP} are values at IP and obtained by bilinearly or (trilinearly for 3D) interpolated from the surrounding fluids nodes by the method provided by Mittal et al. (2008).

More detailed information can be found in the reference (Mittal et al., 2008)

6.3 Simulation configuration

Since the focus is to study the instability or transition of flow past cylinder at $Re = 50$ or 200, and three-dimensional secondary instability starts after the critical Reynolds number $Re_{c3} \approx 187$, therefore, a two-dimensional simulation for $Re = 50 < Re_{c3}$ is sufficient to reveal

the dynamics of primary instability. A three-dimensional simulation is only performed at $Re = 200 \geq Re_{c3}$ for secondary instability.

Two more cases will be computed. A two-dimensional simulation at $Re = 100$ is conducted to benchmark our code as abundant experiments and numerical simulation data are available. Another one is the two-dimensional simulation at $Re = 200$. It has two purposes. One is to estimate the domain size and grid resolution for the three-dimensional simulation at $Re = 200$. Another one is to provide a perfect initial flow field for three-dimensional instability simulation.

Since truncated domain is used for the simulation, the artificial boundary conditions have to be applied. In general, those artificial BCs cannot provide the exact flow at the boundary, inevitably introducing error to the simulation. A large enough domain may solve the problem, but a proper domain size can effectively reduce computational resources. Figure 6.5 shows the configuration for the simulation.

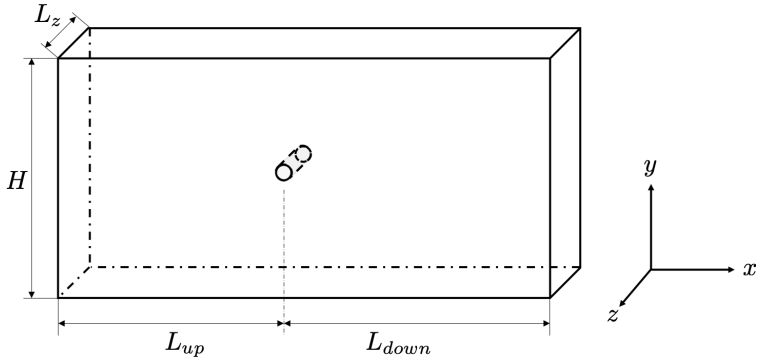

Figure 6.5: *Configuration for numerical simulation of 3D cylinder.*

The upstream L_{up}, downstream L_{down}, and height H are affected by both the Re and BC used. A summary of the reference lengths is provided in table 6.1. As the incoming boundary is set to be uniform, it is required the boundary to be far away from the cylinder. The downstream length is mainly affected by the outflow boundary condition used. The height H of the domain is influenced by the solid in the domain. The solid, up and bottom boundaries together created a narrow 'channel', which can block the flow and increase drag on the cylinder. The spanwise length is related to the most critical three-dimensional secondary wave.

Table 6.1: *The reference domain size from various research.*

Re	L_{up}/D	L_{down}/D	H/D	L_z/D	Note	Reference
100	10				2D	Norberg et al. (1995)
100		20			Neumann	Behr et al. (1991)
100		10			convective	Park et al. (1998)
100			16		free stream BC	Behr et al. (1995)
			24		symmetric BC	
190			44			Barkley and Henderson (1996)
200			80			Posdziech and Grundmann (2007)
188.5				8∼9	$l_z = 4$	Barkley and Henderson (1996)

For two-dimensional simulation, L_z is not required. For three-dimensional simulation, periodic BC is applied along the spanwise direction, and L_z is chosen the wavelength of most critical mode $L_z = 4D$ (Barkley and Henderson, 1996).

For velocity boundary, Dirichlet BC is applied to the inlet, top and bottom boundary, periodic in the z-direction. The inviscid convective BC is applied at the outlet

$$\frac{\partial \boldsymbol{u}}{\partial t} + U\frac{\partial \boldsymbol{u}}{\partial x} = 0. \tag{6.18}$$

Neumann BC is applied at all the boundary for the variable ϕ

$$\left.\frac{\partial \phi}{\partial n}\right|_{\partial\Omega} = 0. \tag{6.19}$$

Stretched grid is used as shown in figure 6.6 for efficiency. Uniform grid is adopted around the solid. The stretch ratio is smaller than 1.05 and continuous changes by the hyper-tangential law to avoid large stretching or sudden change of grid ratio.

6.4 Numerical simulation results

Simulation results compared with references are presented in this section.

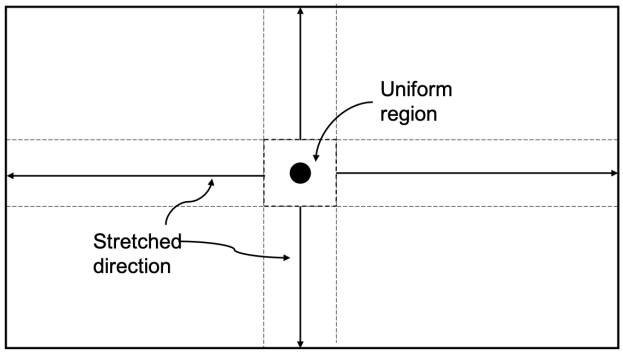

Figure 6.6: *Stretched grid for simulation*

6.4.1 $Re = 100$, 2D

Two-dimensional simulation at $Re = 100$ is performed primarily to understand the developed code, such as the domain, grid, or CFL dependence. Some reference data is compiled in table 6.2. The reference range of C_D is $1.25 \sim 1.36$ and C_L^{RMS} is between $0.2 \sim 0.28$.

Table 6.2: *Reference data at $Re = 100$ for Strouhal number St, C_L^{RMS}, $\bar{C}_D$ from various sources. Experiments are label with *. For numerical study, the discretization method is FD: finite difference; CD: compact difference; B-SP: B-spline spectral method based on Galerkin method. $\bar{(\cdot)}$ for averaged values and $(\cdot)^{RMS}$ for rooted-mean-square values*

St	C_L^{RMS}	$\bar{C}_D$	Grid Resolution	Method	Reference
0.164	-	-	-	Exp	Williamson (1996)*
-	-	1.25	-	Exp	Tritton (1959)*
0.163	0.223	1.3123	-	SP	Posdziech and Grundmann (2007)
0.173	0.25	1.425	0.1667	FD	Zhang et al. (1995)
0.165	0.078	1.253	0.077	FV	Persillon and Braza (1998)
-	0.28	-	-	FE	Li et al. (1991)
0.164	0.24	1.36	0.02	FD	Beaudan and Moin (1994)
0.164	0.2	1.32	0.004	FD	Tang and Aubry (1997)
0.164	0.22	1.31	0.0314	CD/4/6-2	Visbal and Gaitonde (1999)
0.165	0.24	1.35	96×128	FD	Liu et al. (1998)
0.164	0.22	1.314	0.0035	B-SP	Kravchenko et al. (1999)

Unfortunately, some of the results in table 6.3 suggest our code is sensitive to the domain size, which may be because the relative simple BC used. Among the computed values, the Strouhal number St is not sensitive to the domain size or grid resolution, but C_D and C_L does.

Table 6.3: *2D simulation results for $Re = 100$. Strouhal number St, C_L^{RMS}, $\bar{C}_D$ with different domain length and grid resolution. $CFL \sim 0.6$. N_x, N_y is the total grids in x and y direction. Δx and Δy is the grid resolution around the cylinder.*

CASE	L_{up}	L_{down}	H	N_x	N_y	Δx	Δy	St	C_L^{RMS}	$\bar{C}_D$
I	20	40	40	600	400	0.01	0.02	0.167	0.188	1.404
II	20	40	40	600	420	0.01	0.01	0.166	0.181	1.544
III	20	40	60	600	500	0.01	0.01	0.166	0.181	1.539
IV	20	40	40	800	640	0.005	0.005	0.169	0.195	1.672
V	20	40	80	800	700	0.005	0.005	0.167	0.211	1.589
VI	40	40	80	600	440	0.01	0.01	0.167	0.192	1.482
VII	40	80	80	600	440	0.01	0.01	0.167	0.192	1.482
VIII	40	40	80	800	340	0.005	0.02	0.167	0.198	1.353
IX	40	40	80	800	440	0.005	0.01	0.166	0.190	1.419
X	20	40	80	850	800	0.0044	0.005	0.167	0.205	1.634
XI	20	40	80	920	840	0.004	0.004	0.167	0.198	1.571

Increasing the height H, the C_L^{RMS} approaches to reference values, as seen from case II, III, IV, and V. Meanwhile, the drag coefficient $\bar{C}_D$ also drops to the reference range. So a height $H = 80$ is chosen.

Increasing the upstream length L_{up} to 40 improves C_L^{RMS} and $\bar{C}_D$, which can be seen from case II, VI. $L_{down} = 40$ seems to be large enough, as shown by case VI, VII.

The influence of grid resolution is subtle. Increasing grid resolution may favor C_L but be adverse for C_D. For example, case I vs. IV, and VIII vs. IX, these simulations suggest some optimum grid resolution with better accuracy and efficiency.

CFL number has significant influence on the result. As shown in table 6.4, decreasing CFL number (by decreasing integration step Δt), the C_L^{RMS} and $\bar{C}_D$ are improved simultaneously, see figure 6.7. A further investigation shown in figure 6.11 indicates the algorithm is almost first-order accurate in time for C_L and C_D.

6.4.2 $Re = 50$, 2D

To study the instability problem (Re in the range $Re_{c2} < Re < Re_{c3}$), a 2-D simulation at $Re = 50$ was carried out. Some of the reference values for $Re = 50$ are shown in table 6.5. Our study closely matches the experimental data as well as other numerical simulations.

Table 6.4: *Simulation results at $Re = 100$ by 2D simulation with different CFL number. The domain size and grid is the same as case VI in the previous tables.*

CFL	Δt	St	C_L^{RMS}	C_D^{mean}
0.6	0.012	0.167	0.192	1.482
0.5	0.010	0.167	0.197	1.459
0.4	0.008	0.165	0.204	1.437
0.2	0.004	0.167	0.215	1.388
0.1	0.001	0.167	0.220	1.359

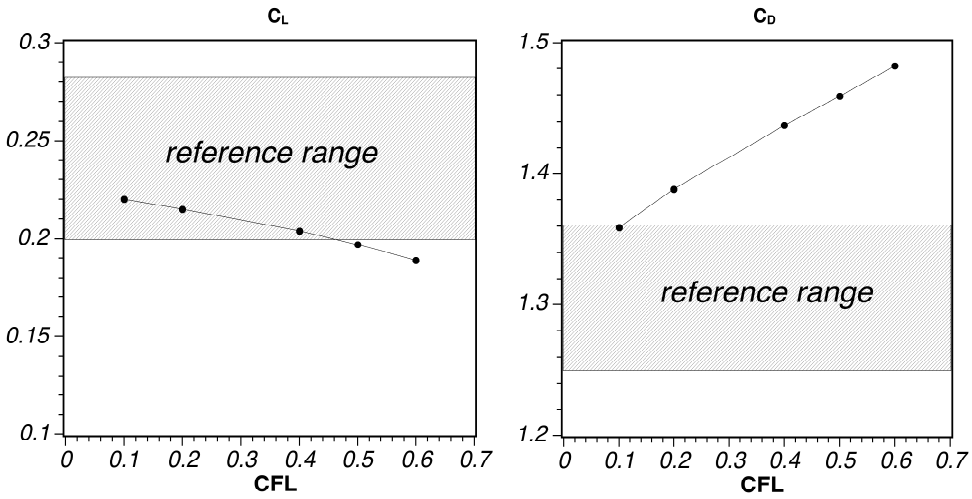

Figure 6.7: *CFL influence on simulated C_L and C_D at $Re = 100$.*

For the low Re case, the domain dependence is not severe as the previous ($Re = 100$) case, thus a smaller domain is adopted. As the CFL dependence revealed in previous section, $CFL = 0.3, 0.2, 0.1$ is tested and result is shown in table 6.6. $CFL = 0.1$ provides good match to the reference St, C_L^{RMS}, C_D which is already listed in table 6.6.

The domain size was $60D \times 40D$ to minimize the effects of domain dependence. A total number of $450 \times 300 = 135,000$ grids was used. The grid was non-uniform, with a minimum interval of 0.0333 around the cylinder. The CFL number was 0.1 and the non-dimensional step time was $\Delta t = 0.00333$. To minimize the influence of non-important normal modes, we first obtained the equilibrium solution by setting a symmetry restriction of the field through the central plane of the cylinder. After the flow reached the equilibrium, we removed the symmetry restriction and added white noise at the incoming flow, which had an intensity

Table 6.5: *Reference for $Re = 50$, Strouhal number, C_L, C_D from various sources. Experiments are label with *.*

C_D^{mean}	C_L^{RMS}	St	Source
$1.45 \sim 1.38$	-	-	Tritton (1959)*
-	-	0.125	Williamson (1996)*
-	-	0.127	Barkley and Henderson (1996)
-	-	0.123	Berger and Wille (1972)
1.43	0.035	0.125	This study

Table 6.6: *Simulation results at $Re = 50$ by 2D simulation with different CFL number.*

CFL	L_{up}	L_{down}	H	Nx	Ny	dx	dy	St	C_L^{RMS}	$\bar{C}_D$
0.3	20	40	40	450	300	0.033	0.033	0.125	0.034	1.470
0.2	20	40	40	450	300	0.033	0.033	0.125	0.035	1.452
0.1	20	40	40	450	300	0.033	0.033	0.125	0.035	1.432

of 10^{-3}. The perturbation was removed after a short time excitation, and the simulation continued until it reached the periodic solution.

Time history for lift and drag coefficient is shown in figure 6.8. After the initial exponential growth, those values are stabilized at a certain level. Figure 6.9 shows the unperturbed and fully developed vortex of the wake.

6.4.3 $Re = 200$, 2D/3D

Table 6.7 lists some reference values for case $Re = 200$. Our three-dimensional simulation results match well with the reference. Here, the two-dimensional simulation is carried out merely for the three-dimensional simulation.

2D simulation

Several simulations with $CFL = 0.1$ are conducted and the result are list in table 6.8. Refining the grid resolution from 0.01 to 0.008 does not improve the result, as seen from case II and IV. Bigger domain slightly improves the result, which can be seen from case I and II in table 6.8, and figure 6.10.

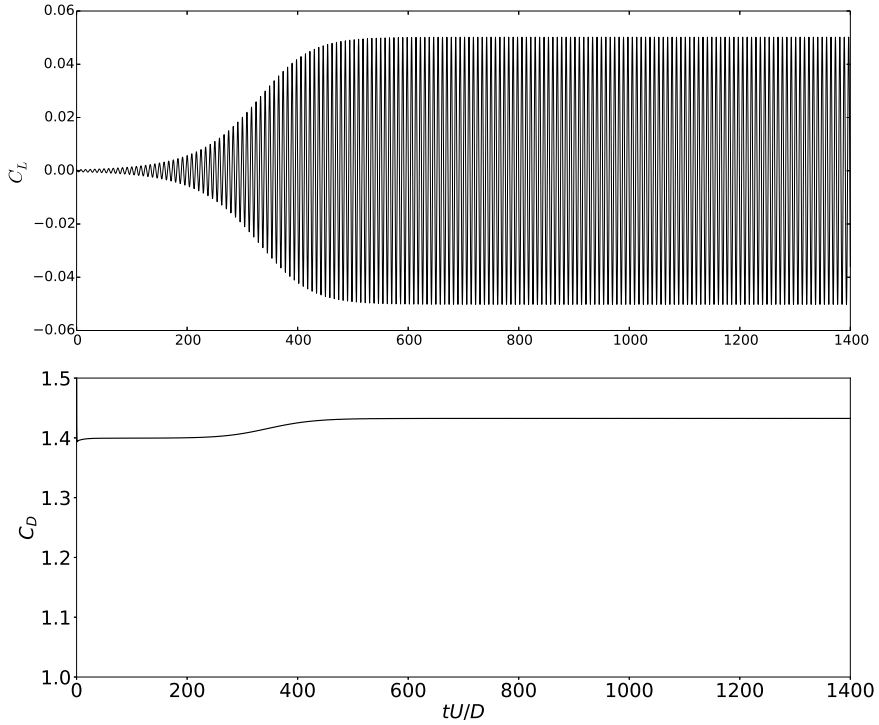

Figure 6.8: *Time history of C_L and C_D at $Re = 50$. $CFL = 0.1$ in table 6.6*

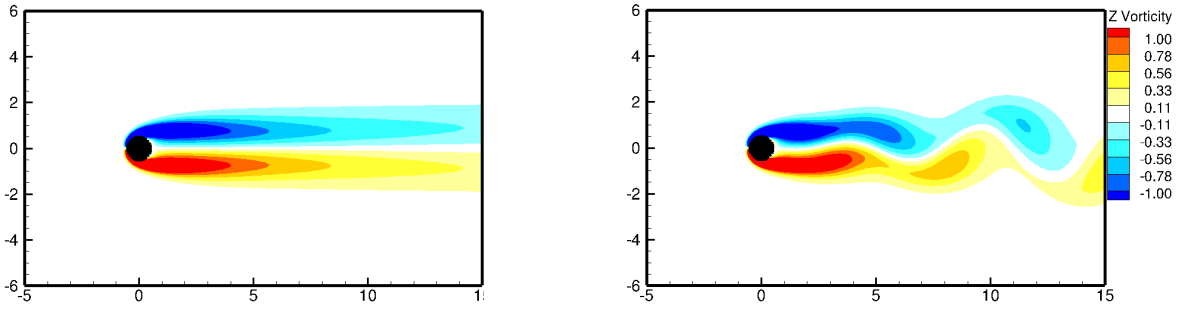

(a) *initial field* **(b)** *fully-developed field*

Figure 6.9: *Vortex of initial and fully developed stage for $Re = 50$. $CFL = 0.1$ in table 6.6*

Table 6.7: *Reference values for* $Re = 200$.

C_D^{mean}	C_L^{RMS}	St	Note	Source
1.26	-	-		Tritton (1959)*
-	-	0.184		Williamson (1992)*
1.28	-	0.187		Henderson (1997)
1.321	0.301	0.198	2D simulation	Persillon and Braza (1998)
1.306	0.254	0.181	3D simulation	Persillon and Braza (1998)
1.24	0.358	0.182		Posdziech and Grundmann (2001)
1.32	0.48	0.19		Zhang and Dalton (1998)
1.3086	0.4676	0.1940		Posdziech and Grundmann (2007)
1.377	0.457	0.198	2D simulation	This study
1.325	0.329	0.181	3D simulation	This study

Table 6.8: *Domain size and grid resolution for 2D simulation of* $Re = 200$. $CFL = 0.1$

CASE	L_{up}	L_{down}	H	Nx	Ny	dx	dy	St	C_L^{RMS}	$\bar{C}_D$
I	20	40	60	600	500	0.01	0.01	0.200	0.462	1.385
II	40	40	60	600	500	0.01	0.01	0.200	0.457	1.376
III	40	40	60	600	500	0.008	0.008	0.203	0.462	1.402
IV	40	40	60	700	500	0.008	0.008	0.198	0.457	1.377

The comparison in figure 6.10 clearly indicates the biggest influence come from CFL. By decreasing the integration step Δt, the lift and drag coefficient are improved significantly. A further study indicates the accuracy for the C_L and C_D is approximately first order, as illustrated in figure 6.11. The fully developed 2D Karman vortex is shown in figure 6.12.

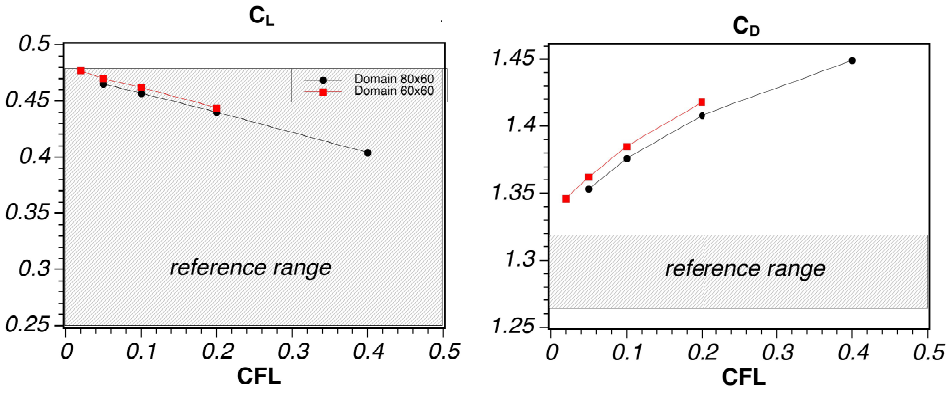

Figure 6.10: *CFL influence on simulated result and reference values for* C_D *and* C_L *at* $Re = 200$ *using two-dimensional simulation.*

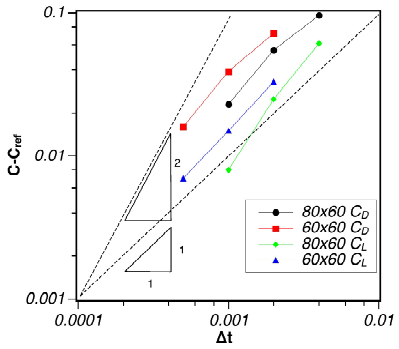

Figure 6.11: *The numerical error in logscale, $Re = 200$, 2D*

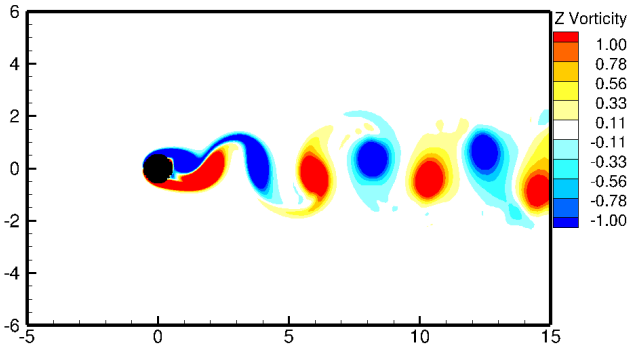

Figure 6.12: *Fully developed Kármán vortex at $Re = 200$, 2D.*

3D simulation

The final configuration for three-dimensional simulation is shown in figure 6.13.

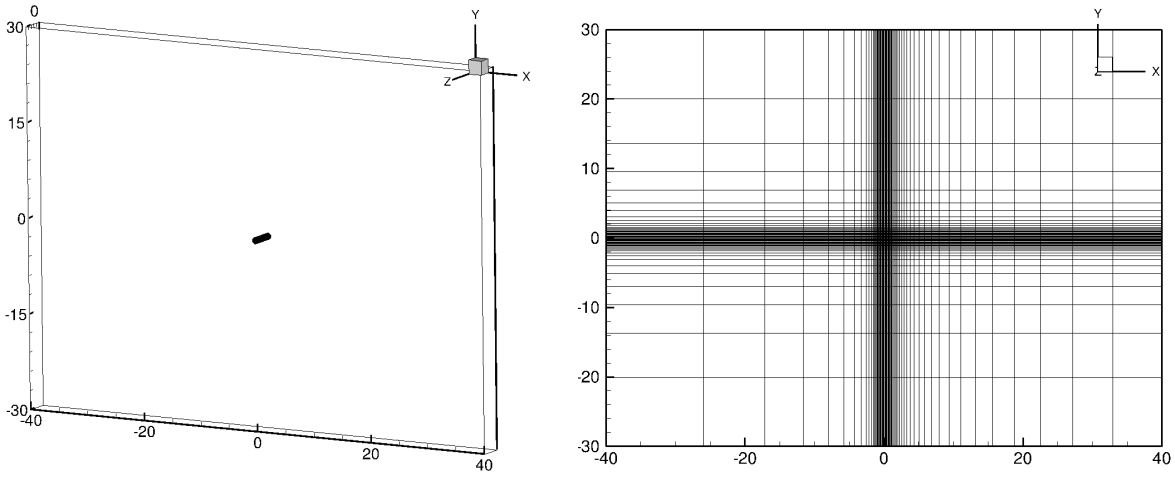

Figure 6.13: *The configuration of domain size and stretched grid (coarsen for illustration) for 3-D flow past a fixed cylinder.*

The three-dimensional simulation at $Re = 200$ was carried out in the following manner to capture the secondary instability. First, a two-dimensional cylinder flow was simulated until it reached periodic (see figure 6.12). Then the two-dimensional flow was interpolated to three-dimensional field, using it as the initial flow for the three-dimensional simulation. A short time three-dimensional simulation was carried out until it settled down to a periodic solution (in case there were errors introduced by the interpolation). We then added a line perturbation immediately above and below the cylinder. The perturbation was sine wave which had the

form $u' = A\cos\left(\frac{2\pi}{L_z}z\right)\delta(x-0.5)\delta(y-0.5)\delta t$ and $u' = -A\cos\left(\frac{2\pi}{L_z}z\right)\delta(x-0.5)\delta(y+0.5)\delta t$. A was the magnitude of perturbation and chosen 10^{-3}. The pulse excitation in x, y, and t would arouse full wavelength response in these directions, but only the unstable modes would grow and develop.

Two-dimensional simulation reaches almost grid independence when $L_x \times L_y = 80D \times 60D$ with a grid size of 600×500. The minimum grid interval around the cylinder is 0.01×0.01. Barkley and Henderson (1996) had shown for an infinitely long cylinder, the unstable Floquet mode had a continuous spectrum. For the sake of simulation, a truncated domain has to be adopted in the spanwise direction. The truncation would induce the continuous spectrum collapsing to some discrete spectrum, therefore suitable for DMD analysis. The domain length in the spanwise direction was determined to be the wavelength of the most unstable Floquet mode. Several researches (Barkley and Henderson, 1996; Williamson, 1988, 1992) had suggested $L_z = 4D$ for $Re = 200$. A uniform grid was used in the spanwise direction, with a total of 160 grids. The grid resolution at the spanwise direction was 0.025. Periodic BC was applied in the spanwise direction, and Fourier transform was adopted in this direction.

Simulation with two different CFL number is carried out and the results are listed in Table 6.9, where apparently $CFL = 0.1$ case provide better match to the reference shown in table 6.7. The corresponding time history of drag is shown in figure 6.14. The initial change of C_D is slow due to the small growth rate of the secondary instability and the small perturbation. However, after $t = 200$, the flow undergoes a rapid change, and C_D drops rapidly to a lower level. The rapid drop of C_L and St from two-dimensional simulation to three-dimensional simulation is in table 6.7.

Table 6.9: *Simulation results at $Re = 200$ by 3D simulation with different CFL number.*

CFL	Δt	L_{up}	L_{down}	H	L_z	Nx	Ny	Nz	dx	dy	dz	St	C_L^{RMS}	$\bar{C}_D$
0.3	0.003	40	40	60	4	440	440	160	0.01	0.01	0.025	0.201	0.409	1.385
0.1	0.001	40	40	60	4	600	500	160	0.01	0.01	0.025	0.181	0.329	1.325

Figure 6.15 shows the fully developed vortex, repeated 1 time in the spanwise direction (z-direction) for better view. Figure shows except the original Kármán vortex, spanwise waves

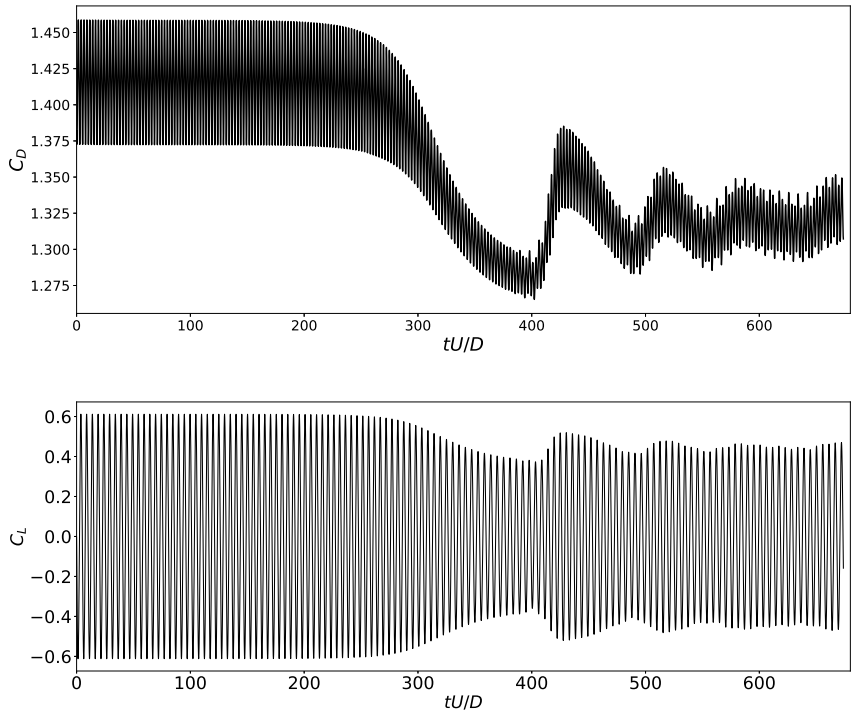

Figure 6.14: *Time history of drag and lift coefficient C_D, C_L for flow past fixed cylinder at $Re = 200$.*

were also developed. The main Kármán vortex cores were bended. Small rib vortex grew from the bend area and stretched downstream connecting the counterrotating vortex pairs. The simulation shows the same vortex structure experimentally observed by Williamson (1992).

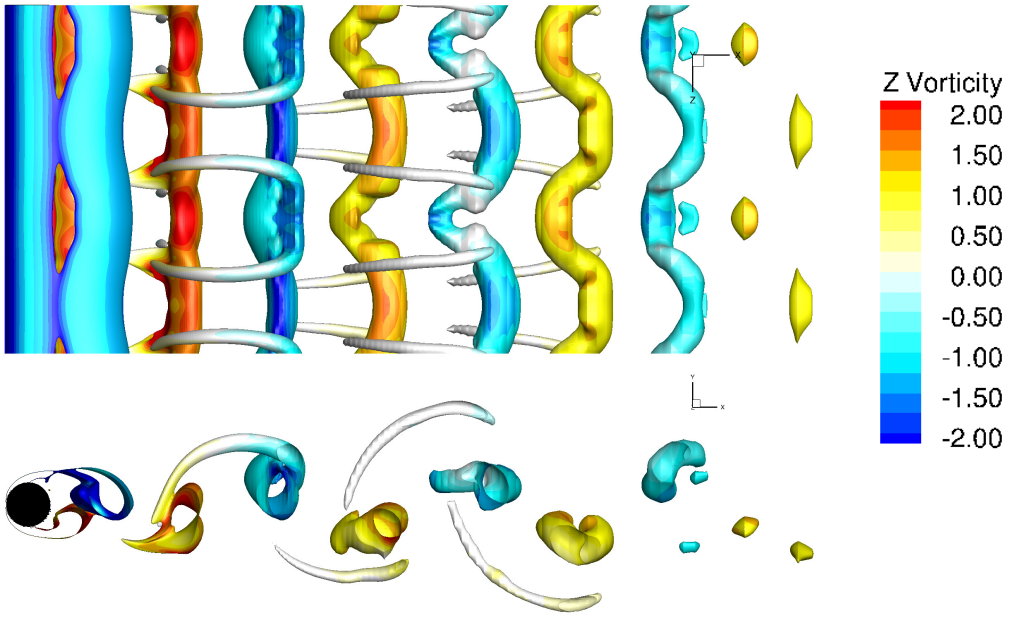

Figure 6.15: *Fully developed vortex after cylinder at $Re = 200$ with 3D simulation. Isosurface of Q-criterion of fully developed secondary instability wave of three-dimensional flow past fixed cylinder at $Re = 200$, repeated 1 time (by periodicity) in spanwise direction to show the repeated structure. The isosurface is contoured with spanwise vorticity. A top view (x-z plane) and a side view (x-y plane) are shown.*

Chapter 7

Benchmark DMD algorithm

This chapter tests the accuracy and efficiency of DMD-LS and DMD-TLS algorithm.

7.1 DMD-LS algorithm for noise-free data

Bagheri (2013) studied the Koopman spectrum of Kármán vortex. By investigating the Perron-Frobenius operator (Lasota and Yorke, 1982), the adjoint operator of Koopman operator, he was able to compute the eigenvalue by forming the trace of this linear operator (Cvitanovic and Eckhardt, 1991). Therefore, we can compare our results with his.

Figure 7.1 presents the DMD eigenvalues. The dimensionless growth rate σ and angular velocity ω are compared, since

$$\sigma + i\omega = log(\lambda)/\Delta t, \tag{7.1}$$

λ is the DMD eigenvalue, and Δt is the time interval between snapshots. Frequency f of DMD modes is related to the angular velocity by

$$\omega = 2\pi f \tag{7.2}$$

DMD modes are picked by the residue criterion presented in section 4.4.3, and the computed spectrum are presented in figure 7.1. Alternatively, if an error is admissible, modes

can be picked by their energy magnitude from our previous report (Zhang and Wei, 2017). At each harmonic frequency, three of the top DMD modes either picked by tiny residue or large energy were presented.

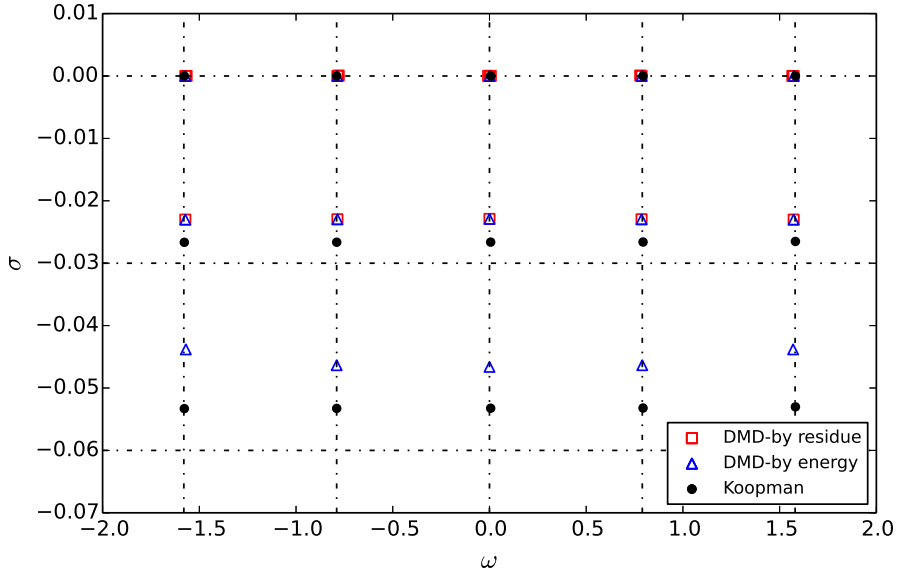

Figure 7.1: *The dimensionless eigenvalue ω-σ of flow past cylinder at $Re = 50$ by DMD-LS algorithm. • (Black) solid circle represents the Koopman spectral by Bagheri (2013); □ (red square) or △ (blue triangle) indicates values computed by DMD-LS algorithm and picked by tiny residue or most energy respectively. Three modes around each harmonic frequency are picked by either criterion.*

In this example, the lattice distribution of DMD eigenvalues discovered by Bagheri (2013) is obtained. Following the notation of Bagheri, the DMD eigenvalues are denoted by

$$\lambda_{j,m} = \sigma_{j,m} + i\omega_{j,m}, \tag{7.3}$$

where $i = \sqrt{-1}$, j-index represents the growth, such that $j = 0$ corresponds to $\sigma \approx 0$, $j = 1$ corresponds $\sigma = -0.023$, $j = 2$ corresponds to $\sigma = -0.046$ and so on. m-index represent the frequency, such that $m = 0$ corresponds to $\omega = 0$, $m = 1$ corresponds $\omega = \pm 0.79$ and so on. Since some of the eigenvalues coincides with others and may be not discernible in the figure, we list them in table 7.1. We call the modes corresponds $j = 0$ harmonic, $j = 1$ the first transient, and $j = 2$ the second transient.

Table 7.1: *Growth rate and frequency (σ, ω) of flow past fixed cylinder at $Re = 50$. The second row of harmonic modes indicates high-frequency modes, where $+1$ indicates the frequency need to add π.*

DMD modes	j-index	$m = 0$	$m = 1$	$m = 2$
harmonic	$j = 0$	(-0.000, 0.000)	(-0.000, 0.786)	(-0.000, 1.573)
	$j = 0$	(-0.000, 0.007)+1	(-0.000, 0.779)+1	(-0.000, 1.566)+1
first transient	$j = 1$	(-0.023, 0.000)	(-0.023, 0.786)	(-0.023, 1.572)
second transient	$j = 2$	(-0.046, 0.000)	(-0.046, 0.790)	(-0.046, 1.570)

The higher the order of j, the eigenvalue is more sensitive to the input data. Adding or removing a few snapshots may result in slight movement of (σ, ω) pairs in the complex plane. However, low order j-index modes are usually not affected. The frequency (the m-index) is not sensitive to perturbation.

The residue and energy generally consider different aspects of the calculated modes. However, as enough snapshots are collected, and space spanned by them become linearly dependent, the dominant eigen-modes are computed more accurately. Therefore, criterion based on residue or energy usually picks the same modes.

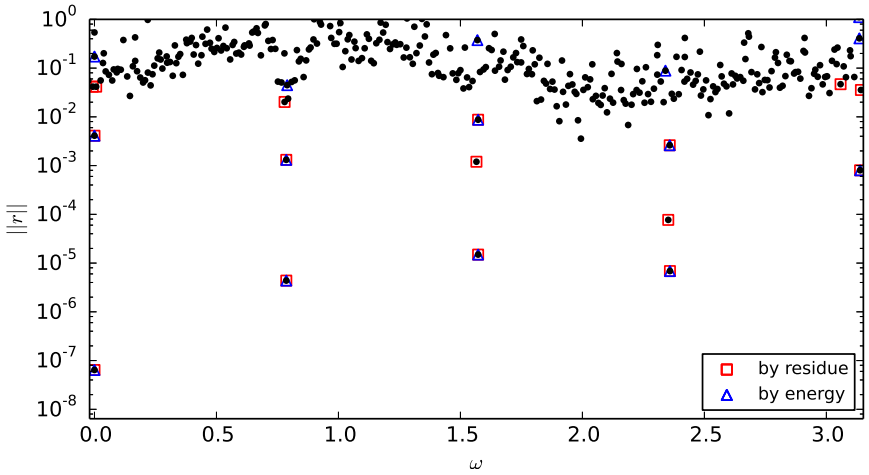

Figure 7.2: *Residue of DMD modes for fixed cylinder at $Re = 50$. □ (Red square) labels those picked by tiny residue and △ (blue triangle) labels those picked by higher energy.*

The residue of DMD eigenpairs is shown in figure 7.2. Smaller value indicates good quality. The good quality eigenpairs only appear near the integer multiple of shedding frequency of the vortex. This phenomenon conforms to the fact that only 1 attracting limit

cycle exists in this flow. The dynamic modes captured are related to the limit cycle. With the residue or energy criterion, the true dynamic modes are kept. In figure 7.2, only three of the top eigenvalues at each harmonic frequency picked either by the residue with (red) square or energy with the (blue) triangle are shown. At each harmonic frequency, the mode most accurately computed also contains the most significant energy. They are the harmonic modes and will be presented in figure 7.4a.

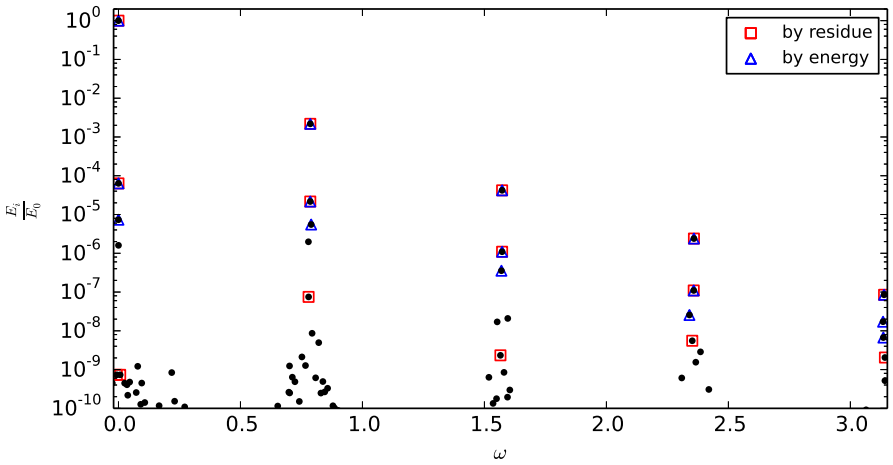

Figure 7.3: *The energy of DMD modes for fixed cylinder at Re = 50. □ (red square) labels those picked by tiny residue and △ (blue triangle) labels those picked by bigger energy.*

The energy of DMD modes is shown in figure 7.3, the energy definition is the same as our previous report (Zhang and Wei, 2017). At each harmonic frequency, three of the top modes picked either by residue or energy criterion are labeled with the same symbols as in figure 7.1.

The harmonic modes are shown in figure 7.4a. The mean mode ($\sigma = 0.000$, $\omega = 0.000$) captures the most energy of the flow. The first harmonic mode ($\sigma = 0.000$, $\omega = 0.786$) captures the dominant vortex shedding movement in the flow. It is similar to the critical normal modes obtained by Jackson (1987). These two modes capture more than 99% energy of the whole flow. They are symmetric with respect to the centerline. The second harmonic mode $\sigma = 0.000$, $\omega = 1.573$ captures an asymmetric mode.

The first set of transient modes are shown in figure 7.4b. The first one is similar to the shift mode discovered by Noack et al. (2003). It captures the transition from the unstable

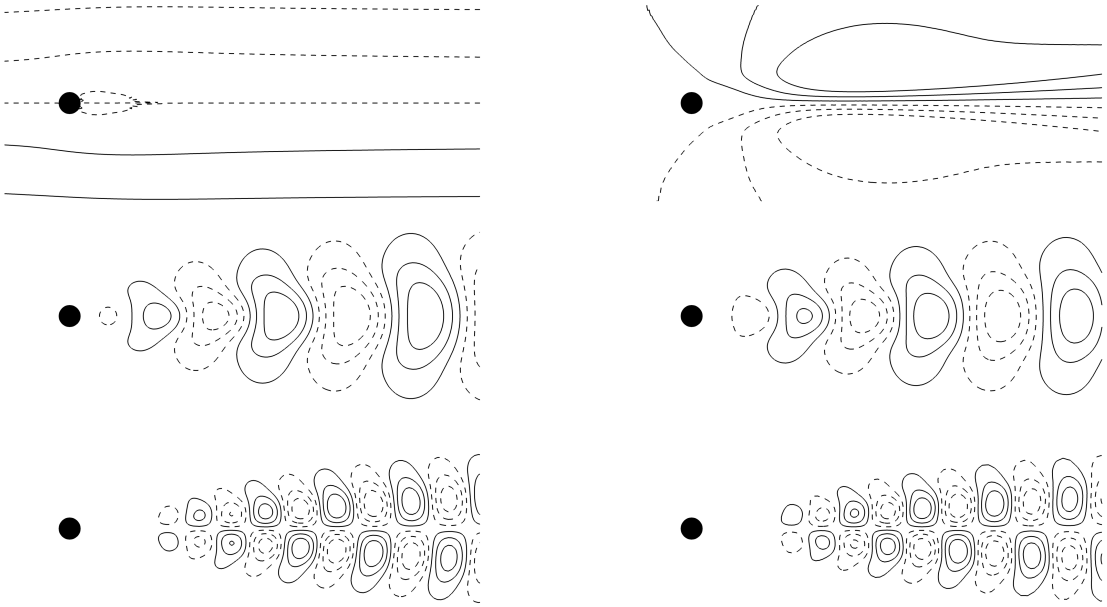

(a) *Harmonic DMD modes.* $\sigma = 0$ **(b)** *1st transient DMD modes.* $\sigma \approx -0.024$

Figure 7.4: *Modes of harmonic and first set of transient DMD modes (figure shows the stream function). Left column is harmonic DMD modes, right column is the 1st set of transient DMD modes. From top to bottom* $\omega = 0, 0.786, 1.573$

equilibrium to the mean flow. This mode is different from the mean mode and other harmonic or transient modes. The rest two modes resemble the corresponding harmonic modes but differ in some detail and energy magnitude.

The second set of transient modes $\sigma \approx -0.048$ are shown in figure 7.5b. The second set of transient modes resembles those of the first set but captures transient motion with a faster-decaying ratio.

7.1.1 DMD algorithm and Fourier transform on periodic data

It is proved DMD algorithm applied to periodic data will result in the Fourier transform (Mezić, 2005; Rowley et al., 2009). However, the equivalence works for infinite dimensional analysis but not a finite dimension. It is well known that a finite Fourier transform

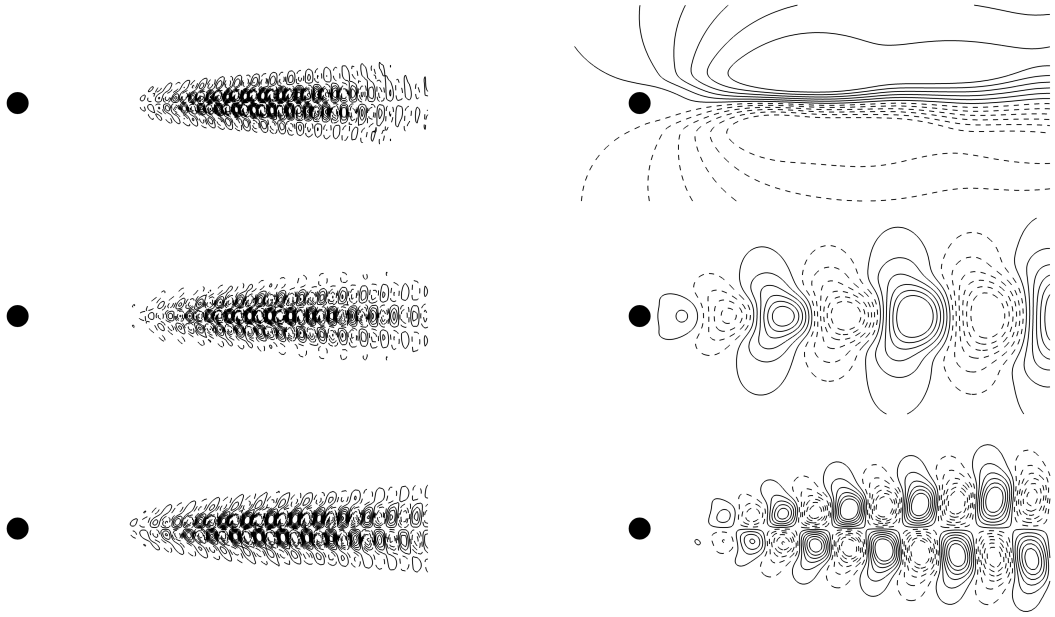

(a) *High-frequency harmonic modes.* $\sigma \approx 0$ **(b)** *Second set of transient modes.* $\sigma \approx -0.047$

Figure 7.5: *DMD modes of high-frequency harmonics and second set of transients (figure shows the stream function). a) Right column shows the high-frequency harmonic modes, from top to bottom* $\omega \approx 3.14, 3.92, 4.71$. *b) Left column shows the second set of transient modes, from top to bottom* $\omega \approx 0, 0.78, 1.57$.

contains alias error, where the high-frequency components are folded to low frequency.

$$\begin{aligned} f(x_k) &= \sum_{i=-\infty}^{\infty} a_i e^{jiwx_k} = \sum_{i=-\infty}^{\infty} a_i e^{ji\frac{2\pi}{T}\frac{kT}{N}} = \sum_{i=-\infty}^{\infty} a_i e^{jik\frac{2\pi}{N}} \\ &= \sum_{i=0}^{N} a'_i e^{jik\frac{2\pi}{N}} \end{aligned} \tag{7.4}$$

where $a'_i = \sum_{l=-\infty}^{\infty} a_{i+lN}$. The finite dimensional Fourier transform will 'fold' the high-frequency components to low-frequency, increasing their magnitude and contaminating the Fourier modes. For example, if sampling interval is Δt, the information in frequency range $[-f_c, f_c]$ is captured by discrete Fourier transform (DFT), here $f_c = \frac{1}{2\Delta t}$ is the critical frequency (Nyquist frequency), correspondingly angular frequency is $\omega = 2\pi f_c \in [-\frac{\pi}{\Delta t}, \frac{\pi}{\Delta t}]$.

However, there is no alias error for DMD, that is, high-frequency modes are separate from low-frequency ones, and they will not be folded together. To see that, consider the

eigenvalue problem described by

$$A\boldsymbol{v} = \lambda\boldsymbol{v}$$

The eigenpair $(\lambda, \boldsymbol{v})$ is distinguishable by both its eigenvalue and eigenvector. Even if frequency λ is equal, the eigenpair can be distinguished by the mode.

The angular frequency of DMD modes is given by

$$\omega = \frac{\mathrm{Im}(\ln\lambda)}{\Delta t} \in \frac{[-\pi - n\pi, \pi + n\pi]}{\Delta t} \tag{7.5}$$

n is some integer to be determined. Unfortunately, it is often taken $n = 0$ for granted, which is not correct. To determine the exact value of n, it often needs to consider the energy of that mode as well as the mode geometry. The correct frequencies for these high-frequency modes are listed in table 7.1, where we have '+1' indicate the frequency need to add $\frac{\pi}{\Delta t}$.

In the previous section, a set of high-frequency harmonic DMD modes was revealed by residue criterion, see figure 7.5a. In the frequency plot (figure 7.1) they were hidden by low frequency modes as we computed the angular velocity by $\omega = \mathrm{Im}(\ln(\lambda)) \in (-\pi, \pi]$. We correct the frequencies in table 7.1 by considering their energy and modes geometry. These high frequency spectrums and modes are confirmed with DMD analysis on data sampled at high-frequency ($\Delta t = 0.5$).

Therefore, DMD is free of alias error for a finite-dimensional analysis. The frequency is determined up to some constant value. It can capture high-frequency modes higher than the critical frequency of $\frac{1}{\Delta t}$. These high-frequency modes are separated modes rather than folded to the low-frequency ones. Some of these high-frequency modes can be picked by residue criterion.

7.2 DMD-LS and DMD-TLS algorithm with noise

The previous section demonstrates identifying system dynamical information using DMD-LS algorithm. In this section, noised data is considered to test the DMD-LS and DMD-TLS

algorithm. It is found the modified space $\hat{\mathcal{S}} = \text{span}(\hat{\boldsymbol{x}}_1, \cdots, \hat{\boldsymbol{x}}_M, \hat{\boldsymbol{x}}_{M+1})$ is generally better than original data space $\mathcal{D} = \text{span}(\boldsymbol{x}_1, \cdots, \boldsymbol{x}_M)$ for noise contaminated data.

To obtain the noised data, each snapshot is added with some independent random noise to mimic the case where noise is introduced by the measuring instruments.

$$\boldsymbol{x}_i' = \boldsymbol{x}_i + \Delta\boldsymbol{x}_i \tag{7.6}$$

$\Delta\boldsymbol{x}$ is the noise and follows normal distribution.

$$E(\Delta\boldsymbol{x}_i) = 0, \quad E(\Delta\boldsymbol{x}_i \Delta\boldsymbol{x}_j) = \sigma_N^2 \delta_{ij}. \tag{7.7}$$

δ_{ij} is the Dirac function. σ_N is the noise intensity (the standard deviation of noise). DMD-LS algorithm and DMD-TLS algorithm is then applied to data $\boldsymbol{x}'$.

Figure 7.6 shows the frequency and growth rate of DMD modes subject to three level of noise, $\sigma_N = 0$, $\sigma_N = 10^{-6}$ and $\sigma_N = 10^{-3}$. In the figure, we label the most important modes with a red square. For the noiseless data (two plots in the first row), the energy criterion is used. However, it is switched to the more stable residue criterion for noised data as the energy criterion becomes unstable.

Without noise, DMD-LS and DMD-TLS compute similar eigenvalues. However, with noise, the two algorithms give slightly different results. The growth rates of both algorithms are affected by the noise. They decrease with the increased noise level. However, DMD-TLS algorithm is more accurate than DMD-LS algorithm on noise data. The frequencies are not affected by noise.

Modes for noise level $\sigma_N = 10^{-3}$ are shown in figure 7.7. By the maximum MSNR filtering, modes are correctly captured except a few ones.

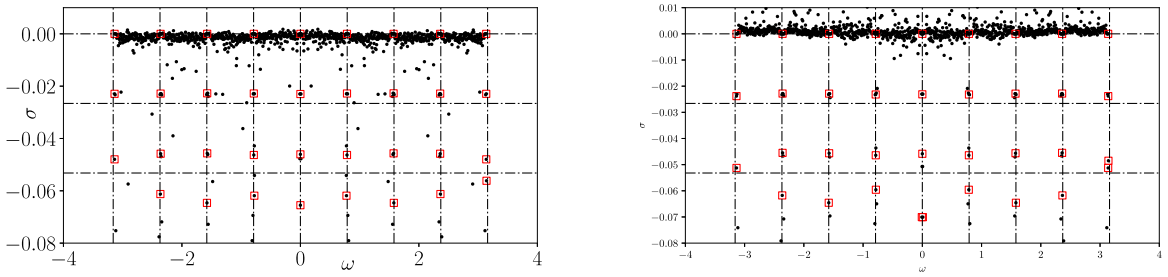

(a) $\sigma^N = 0$

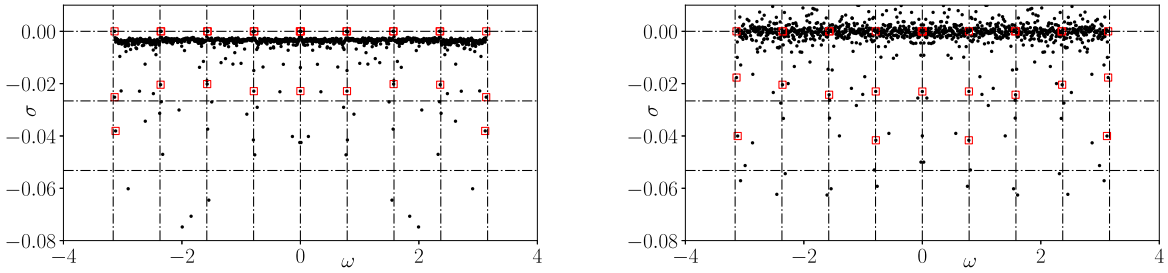

(b) $\sigma^N = 1.0 \times 10^{-6}$

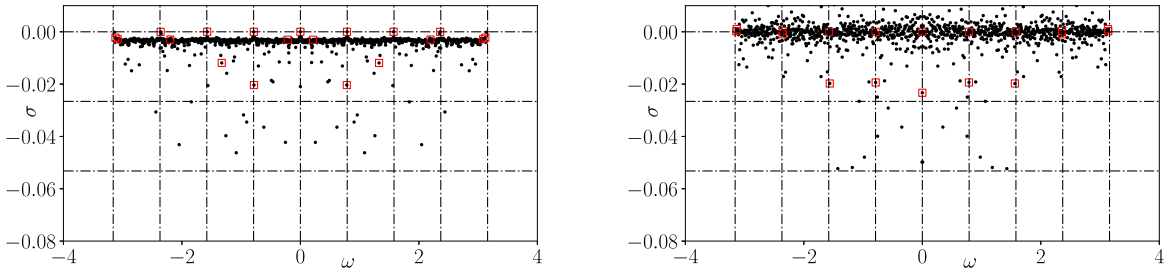

(c) $\sigma^N = 1.0 \times 10^{-3}$

Figure 7.6: *Eigenvalues of DMD-LS and DMD-TLS algorithm for noise data. The left column shows the DMD-LS algorithm, and the right column shows the DMD-TLS algorithm. From top to bottom, the noise intensity is* 0, 10^{-6}, 10^{-3}. *The first row labels the important DMD eigenvalues with red square by the energy criterion, the rest rows uses the residue criterion.*

7.3 algorithm efficiency

The efficiency of different DMD algorithm is compared by time used. Two major components, decomposition and the eigenvalue solver, are shown their time used in figure 7.8. The standard DMD and DMD-TLS algorithm both used SVD to decompose snapshots, while DMD-LS used a cheaper QR decomposition. Notice there are multiple SVD procedure available in LAPACK (Intel, 2007), *gesdd* (faster) or *gesvj* (slow but accurate for small

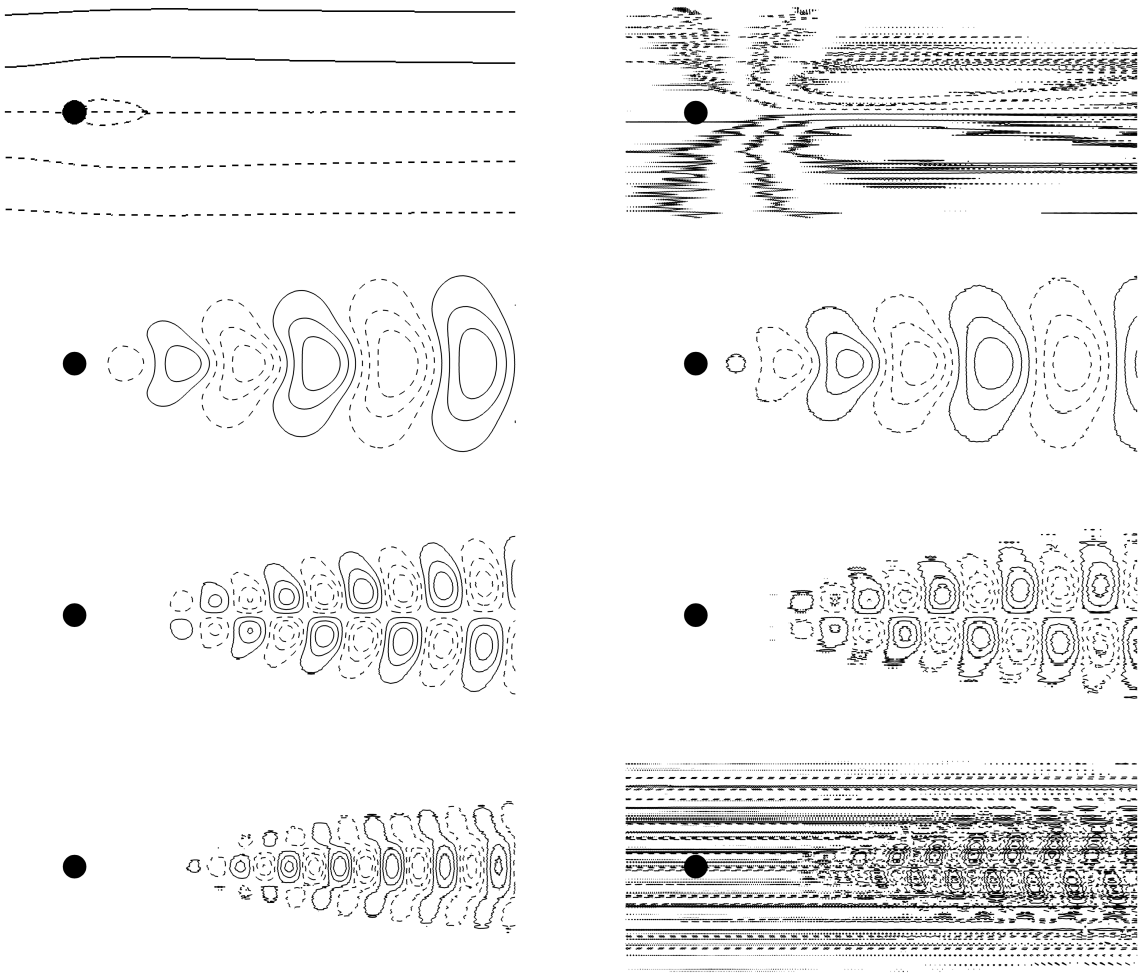

Figure 7.7: *DMD modes by DMD-TLS algorithm, figure shows stream function. From right to left, top to bottom , the corresponding* (ω, σ) *are* $(0.000, 0.000)$, $(0.000, -0.023)$, $(0.786, 0.000)$, $(0.786, -0.019)$, $(1.570, 0.000)$, $(1.553, -0.020)$, $(2.350, 0.000)$, $(3.140, 0.000)$. *Modes are filtered by maximum MSNR.*

eigenvalues). The latter may suitable for nearly singular data sets. Both subroutines are used. They are distinguished by 'DMD(gesdd)' and 'DMD(gesvj)'. At the eigensolver side, SEV uses the QR algorithm and needs $O(M^3)$ operation (Watkins, 2007). The QZ algorithm for a GEV problem needs $O(M^3)$ operation.

Our workstation has 2 Intel Xeon CPU E5-2680 installed. A total of 28 cores with 2.40GHz are available. The system is CentOS. The compiler is Intel Fortran with threaded MKL library. Single-core execution time for each algorithm is in figure 7.8. DMD-LS algorithm is comparable to the cheaper DMD(gesdd) algorithm, while much faster than the

Table 7.2: *Algorithm efficiency for various DMD algorithm and coefficients for A and B for different component.*

component	algorithm	A	B
Decomposition	QR	1.21E-5	1.80
	SVD	4.54E-5	1.87
Eigensolver	QR algorithm for SEV	1.45E-7	2.50
	QZ algorithm for GEV	5.56E-8	2.81

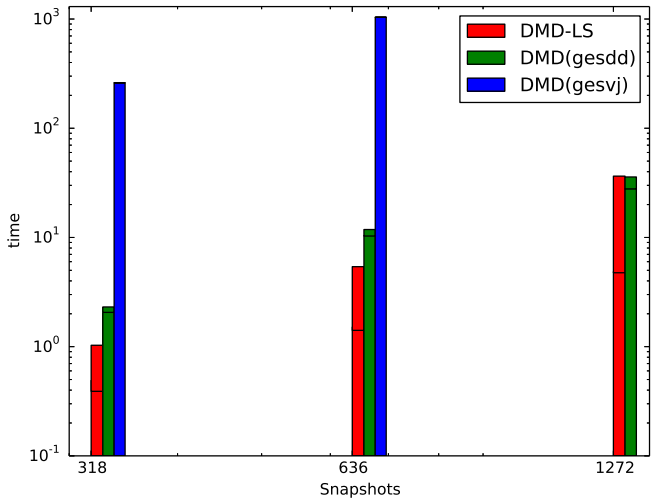

Figure 7.8: *Time for DMD-LS, DMD(gesdd), DMD(gesvj). Time and snapshots numbers are in log scale. For each bar, the bottom portion represents the time for decomposition and the top portion for eigensolver. DMD(gesvj) takes too much time in SVD decomposition not shown for 1272 snapshots.*

DMD(gesvj). The operation count for each DMD algorithm is estimated by fitting the time used.

$$t = AN^B. \tag{7.8}$$

t is time used, A and B are two constant. N is the size of the problem. The estimation of A and B are listed in table 7.2. The DMD-LS algorithm will benefit from the fast QR decomposition and fit for analysis for big data. Its overall performance is also excellent compared to the conventional DMD algorithm.

Chapter 8

Koopman analysis for constant spectrum systems

Koopman decomposition is applied to a linear system and an asymptotic nonlinear system as their spectrums are constant.

8.1 System identification for linear system

The linear dynamic system is an essential topic in structural analysis, electronics circuits, mechanics, and vibration. DMD, based on a linear system, is a perfect tool to identify dynamic information for the linear system.

8.1.1 High-order linear system and augmented snapshots

We consider a second-order vibration system and derive a system identification technique based on DMD. The technique considered here should equivally apply to any high-order linear dynamic system.

$$M\ddot{\boldsymbol{q}}(t) + C\dot{\boldsymbol{q}}(t) + K\boldsymbol{q}(t) = \boldsymbol{f}(t), \tag{8.1}$$

$\boldsymbol{q}(t) \in \mathcal{R}^n$ is the displacement of mass system. n is DOF of the vibration system. M, C, $K \in \mathcal{R}^{n\times n}$ is the inertial matrix, damping matrix and stiffness matrix. To identify the dynamics of the second-order differential equation using DMD algorithm, we reformulate the above equation into an augmented first-order linear equations. Let $\boldsymbol{v} = \begin{bmatrix} \boldsymbol{p}(t) \\ \boldsymbol{q}(t) \end{bmatrix}$, where $\boldsymbol{p}(t) = \dot{\boldsymbol{q}}(t)$.

$$\begin{bmatrix} M & 0 \\ 0 & I \end{bmatrix} \begin{bmatrix} \dot{\boldsymbol{p}}(t) \\ \dot{\boldsymbol{q}}(t) \end{bmatrix} = \begin{bmatrix} -C & -K \\ I & 0 \end{bmatrix} \begin{bmatrix} \boldsymbol{p} \\ \boldsymbol{q} \end{bmatrix} + \begin{bmatrix} \boldsymbol{f}(t) \\ \boldsymbol{0} \end{bmatrix} \tag{8.2}$$

The first-order formulation indicates DMD algorithm should apply to the augmented snapshots $\boldsymbol{v}_i$. Another difference of second-order linear dynamic system is that, a number of $2n$ eigenvalues and eigenvectors will be obtained instead of n. This conforms to the fact that vibration system generates the following quadratic eigenvalue problem (Tisseur and Meerbergen, 2001)

$$(\lambda^2 M + \lambda C + K)\boldsymbol{v} = 0,$$

where λ is the eigenvalue and $\boldsymbol{v}$ is the corresponding eigenvector.

8.1.2 Modified DMD-TLS algorithm for linear data

Not like the fluid dynamic system, where DMD handles data matrix of tall and skinny shape X, $Y \in \mathbb{R}^{N\times M}$ with $N \gg M$, a linear dynamic system usually contains a small number of DOF. In this case, $N \ll M$ may occur. To analyze a linear system with N-DOFs, one approach is to collect $M = N + 1$ snapshots and perform the DMD analysis.

To achieve more accurate results, another approach is to assimilate data with more snapshots by the TLS technique, thus a modified DMD-TLS algorithm is obtained. The modified DMD-TLS is performed in the following manner. Let $X = [\boldsymbol{x}_1\, \boldsymbol{x}_2 \cdots \boldsymbol{x}_M]$, $Y = [\boldsymbol{x}_2\, \boldsymbol{x}_3 \cdots \boldsymbol{x}_{M+1}]$ and a SVD of an augmented matrix is given by

$$\left[X^T | Y^T\right] = [P_1 | P_2] \begin{bmatrix} S_1 & \\ & S_2 \end{bmatrix} \begin{bmatrix} Q_{11} & Q_{12} \\ Q_{21} & Q_{22} \end{bmatrix}.$$

where $S_1 = \text{diag}(s_1, \cdots, s_{2*DOF})$.

A total least-square approximation for X and Y are given by

$$\hat{X}^T = P_1 S_1 Q_{11}, \quad \hat{Y}^T = P_1 S_1 Q_{12},$$

Thus modified data $\hat{X}^T$ and $\hat{Y}^T$ are in the column space of P_1. The modified DMD-TLS algorithm gives

$$\lambda \hat{X} \boldsymbol{v} = \hat{Y} \boldsymbol{v}$$

The eigenvector is assumed in the colume space of P_1, in the form $\boldsymbol{v} = P_1 \boldsymbol{y}$. Substituting $\hat{X}$ and $\hat{Y}$ and v into above GEV equation, the final GEV is reduced to

$$\lambda Q_{11}^T (S\boldsymbol{y}) = Q_{12}^T (S\boldsymbol{y}). \tag{8.3}$$

λ is the eigenvalue of the dynamic system, and $\hat{X}v = Q_{11}^T (S_1 y)$ produces the corresponding DMD modes, also known as the normal modes for linear analysis.

8.1.3 A mass-spring example

To illustrate our algorithm, a 2-DOF mass-spring vibration system was investigated, the configuration is shown in figure 8.1a. Let $M_1 = M_2 = 1$, $k_1 = k_2 = k_3 = 1$, the eigenvalues are $\lambda_{1|2} = \pm\sqrt{3}j$, $\lambda_{3|4} = \pm 1j$, and the corresponding eigenvectors are

$$\boldsymbol{v}_{12} = \frac{1}{4} \begin{bmatrix} -\sqrt{6} \\ \sqrt{6} \\ \pm\sqrt{2}j \\ \mp\sqrt{2}j \end{bmatrix}, \quad \boldsymbol{v}_{34} = \frac{1}{2} \begin{bmatrix} \pm 1j \\ \pm 1j \\ 1 \\ 1 \end{bmatrix},$$

where $j = \sqrt{-1}$.

For DMD analysis, the vibrating system is theoretically computed. The augmented snapshots are analyzed by the DMD algorithm. Figure 8.1 shows the eigenvalues and the

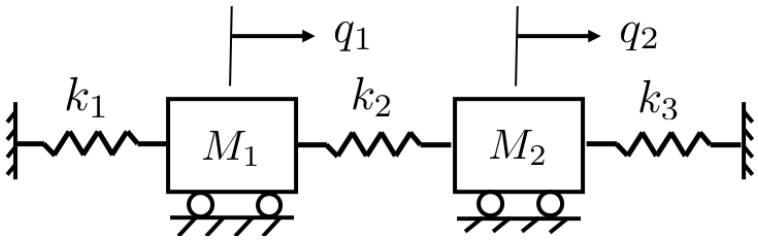

(a) *A 2-DOF mass-spring system.*

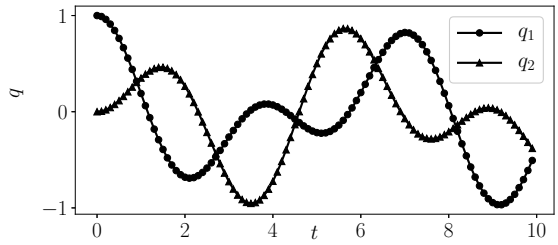

(b) *The history.*

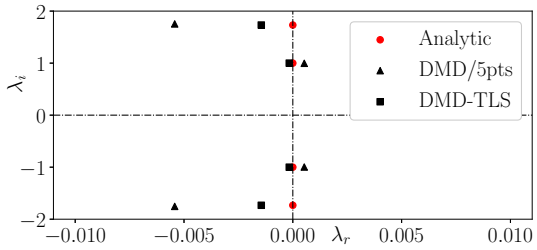

(c) *DMD eigenvalues*

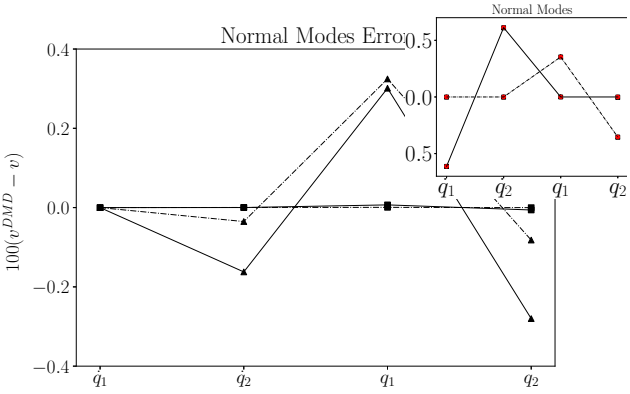

(d) *First pair DMD modes*

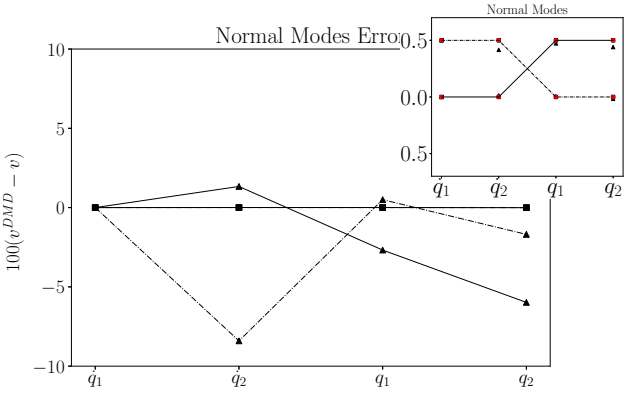

(e) *Second pair DMD modes*

Figure 8.1: *DMD analysis for a 2-DOF mass spring vibration system. (a) The configuration for a 2-DOF mass spring system. (b) Time history of location q_1 and q_2 for initial condition $q_1 = 1$, $\dot{q}_1 = q_2 = \dot{q}_2 = 0$. (c) Eigenvalues of the linear system. Solid (red) circles show analytic eigenvalues, triangles show value for 5-point DMD analysis, solid square show value for DMD-TLS analysis. (d), (e) show the normal modes of the analytic and DMD analysis on the upper right corner and the error of DMD modes at the bottom. As the DMD modes is close to the analytic value, errors of these modes are scaled by 100. As DMD modes are complexed conjugate pairs, (d) and (e) show the real and imaginary part separately, with solid line joining the real part and dashed line for imaginary part.*

eigenvectors. Notice the DOF of the augmented first-order differential equation is 4, with the 'N+1' snapshots approach, DMD analysis is applied on five snapshots. DMD provided an estimation of eigenvalue within 0.3% error and 0.6% error for the eigenvectors. The estimation was further improved by incorporating 100 snapshots and using the DMD-TLS algorithm. Error for eigenvalue and eigenvector is reduced to 0.09% and 0.01%, respectively. The error was summarized in table 8.1.

Table 8.1: *Error by DMD algorithm or modified DMD-TLS for the linear mass-spring system.*

	'$N+1$'-DMD	DMD-TLS
eigenvalue	0.3%	0.09%
eigenvector	0.6%	0.01%

8.2 DMD analysis for asymptotic system

The instability of nonlinear systems is critical to many applications. Linear stability theory (LST) provides an efficient linear approximation. Koopman decomposition, on the other hand, reveals the whole dynamics, including the nonlinear effects.

The primary and secondary instabilities are two important phenomena, representing the mechanism for complex flow. The following section studies the secondary instability of wake after a blunt body by Koopman decomposition, while the primary instability will be presented in the next chapter where the whole transition is studied.

8.2.1 Secondary instability overview

The primary mode is believed to grow exponentially initially and then saturate to a regular pattern. It will not break down to irregular turbulent flow directly. Instead, as the Reynolds number increases, the primary mode continues to grow and distort the mean flow, and a three-dimensional secondary wave will form and superimpose on the primary wave (Landahl, 1972).

Orszag and Kells (1980) expanded the perturbation around the periodic two-dimensional base solution, studied the resulting system by Floquet theory, and found the growth of three-dimensional perturbation to be exponential. Experiments (Miller and Williamson, 1994; Prasad and Williamson, 1997; Williamson, 1988, 1992) confirmed that the secondary instability for wake after cylinder would start when the Reynolds number reached $180 \sim 190$. Barkley and Henderson (1996) numerically determined the critical $Re = 188.5$, and the most critical wavelength in spanwise direction is $L_z = 3.96D$, where D is the diameter of the cylinder.

The secondary instability was numerically computed in chapter 6.4.3. Figure 8.2a shows the history of drag coefficient. To capture the asymptotic spectrum of the nonlinear fluid-solid dynamic system around the unstable two-dimensional periodic base flow, we apply the DMD algorithm to the initial stage of the three-dimensional simulation, from $t = 110$ to $t = 320$. The start and end snapshots used for DMD analysis are in figure 8.2. The isosur-

face of vorticity is contoured by the spanwise vorticity. The distortion of isosurface shows, during this period, the three-dimensional perturbation is small in magnitude. Therefore, these snapshots are suitable for estimating the asymptotic spectrum and eigenvector for the underlined Floquet system. A total of 701 snapshots are used, and time increment between snapshots is $\Delta t = 0.3$.

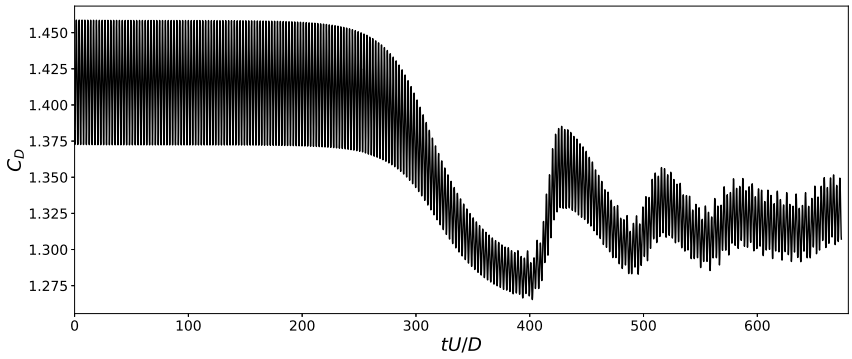

(a) C_D-t

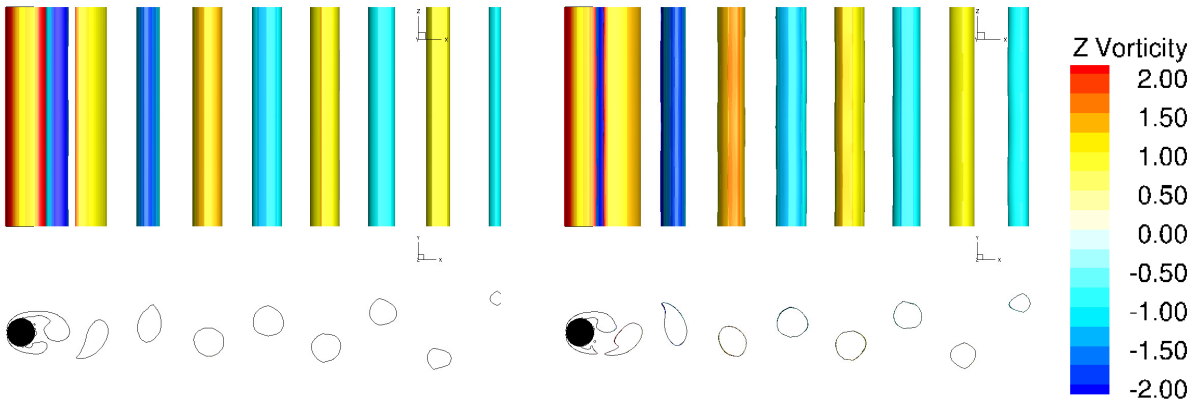

(b) *The initial and final snapshots*

Figure 8.2: *The initial and final snapshots used for secondary instability analysis, (figure shows The iso-surface of the Q-criterion). The isosurface is contoured with spanwise vorticity. Top view for x-z plane, bottom view for x-y plane. (a) The drag coefficient. (b) The initial and final snapshots.*

8.2.2 The Floquet analysis for asymptotic system

In chapter 2.3.2, the periodic LTV system is studied by the Floquet theory. Its solution is the superposition of a finite set of Floquet modes. From the solution (2.40)

$$\begin{aligned}\boldsymbol{x}(t) &= \Theta(t)\boldsymbol{x}_0 = P(t)e^{tR}P^{-1}(t_0)\boldsymbol{x}_0 \\ &= \left(P(t)V\right)e^{t\Lambda}\left(V^{-1}P^{-1}(t_0)\boldsymbol{x}_0\right) \\ &= \sum_{l=1}^{n}\sum_{m=-\infty}^{\infty} c_l \boldsymbol{q}_{ml} e^{\mu_{rl}+j(m\frac{2\pi}{T}+\mu_{il})}\end{aligned} \tag{8.4}$$

where $Q(t) = P(t)V$ is the T-periodic matrix, and $\boldsymbol{q}_{ml}$ is the Fourier component of the m-th wave of the i-th column of matrix $Q(t)$. The matrix R is assumed to be diagonalizable $R = VRV^{-1}$. μ_r and μ_i is the real and imaginary part of the eigenvalue μ. $\boldsymbol{c} = R^{-1}\boldsymbol{x}_0$ is the constant vector.

DMD algorithm will capture the eigenvalues $e^{\mu_{rl}+j(m\frac{2\pi}{T}+\mu_{il})}$ and modes $\boldsymbol{q}_{ml}$, since they are constant. μ_{rl} is the growth rate and $m\frac{2\pi}{T}+\mu_{il}$ is the corresponding angular frequency. Floquet solution is then efficiently rebuilt by DMD modes and frequencies, since

$$\boldsymbol{q}(t) = \sum_{m=-\infty}^{\infty} \boldsymbol{q}_{ml} e^{j\left(m\frac{2\pi}{T}+\mu_{il}\right)t}. \tag{8.5}$$

Correspondingly $\mu_r = 0$ captures the periodic Floquet modes, $\mu_r > 0$ for unstable Floquet modes and $\mu_r < 0$ for stable Floquet modes.

From the hierarchy of Koopman decomposition, the DMD algorithm can effectively capture the Floquet modes of the asymptotic system if the base flow is periodic. The Kármán vortex flow computed in chapter 7 is decomposed by DMD algorithm following the same reasoning. The following example applies the DMD algorithm to study the secondary instability where the base flow is the two-dimensional periodic flow, and perturbation is the superimposed three-dimensional wave.

The periodic LTV system differs from the asymptotic system since the latter is nonlinear. So the nonlinear proliferation rule applies. Therefore, the proliferated Koopman spectra are

expected to follow the lattice distribution.

8.2.3 Koopman decomposition for secondary instability

Figure 8.3 shows Koopman spectra for the secondary instability. The lattice distribution of spectra confirms that the underlined system is a Floquet system. Black dots are the computed DMD eigenvalues, with low residue ones labeled with a red square.

The modes with $\sigma = 0$ capture the periodic base flow. The unstable Floquet mode has a growth rate $\sigma = 0.017$. The corresponding Floquet multiplier $e^{(\sigma T)} = e^{0.017/0.0181} = 1.098$ is very close to 1.115 ± 0.005 obtained by a direct Floquet analysis (Abdessemed et al., 2009). The high order derived modes $\sigma = 0.034$ and $\sigma = 0.052$ are also captured. Besides these, a stable Floquet mode with decaying rate $\sigma = -0.044$ is captured. It may be due to the line perturbation to excite the system. After removing the initial perturbation, this stable Floquet mode eventually damped out.

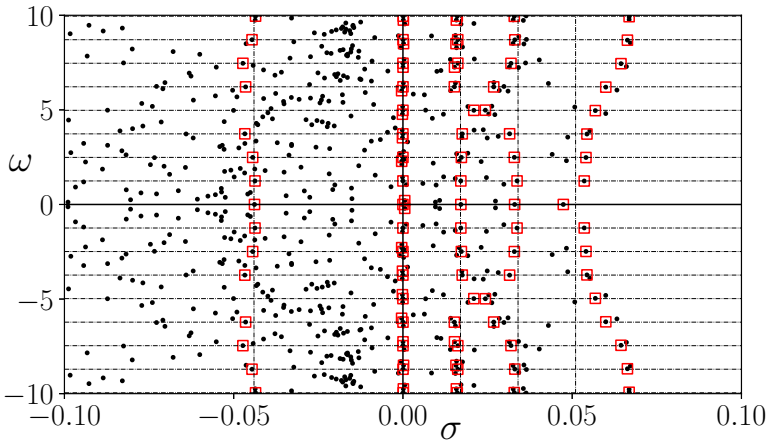

Figure 8.3: *The Koopman spectrum of 3-D flow past fixed cylinder at* $Re = 200$.

Similar to the 2-D case in chapter 7.1.1, multiple points at some harmonic frequencies ($\sigma = 0$) are because the high frequency modes are truncated into low frequency range $\frac{(-\pi,\pi]}{\Delta t} = (-\frac{10}{3}\pi, \frac{10}{3}\pi]$ due to the limitation of logrithmatic operation.

Spectrums in figure 8.3 may not exactly follow the lattice distribution predicted by the proliferation rule. It is because the Koopman spectra are local; however, DMD algorithm

applies on a piece of data, where the nonlinearity may be significant. This discrepancy therefore is reflected by figure 8.3.

The Koopman modes are shown in figure 8.4. The base flow is captured by the periodic modes shown in the first column. They are essential two-dimensionals modes, no wave in the spanwise direction. The most unstable Floquet mode is shown in column two. These Koopman modes have the same growth rate $\sigma = 0.017$. A remarkable feature of these unstable modes is that they contain only one wave in the z-direction. The third group shows the high order derived mode of the unstable Floquet mode. These modes have a twice growth rate of $\sigma = 0.034$ and contain two waves in the spanwise direction. The higher order, the more wave number is a universal feature, which is found in modes ϕ^{λ}, $\phi^{2\lambda}$ and $\phi^{3\lambda}$ in figure 9.3 in the next chapter.

With the DMD decomposition, we can reconstruct the Floquet modes by equation (8.5), which are shown in figure 8.5.

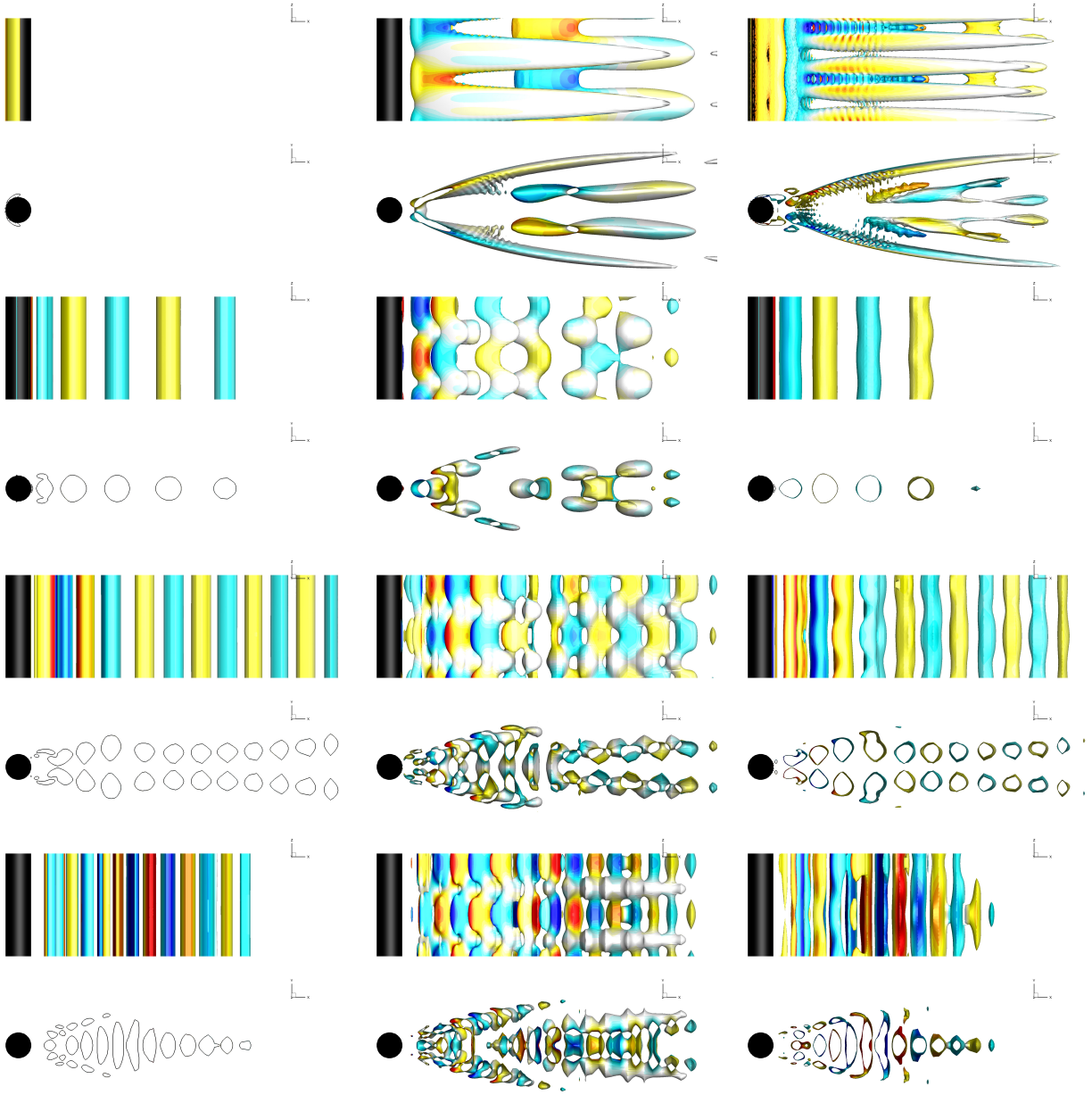

(a) $\sigma = 0$ **(b)** $\sigma = 0.017$ **(c)** $\sigma = 0.034$

Figure 8.4: *DMD modes for secondary instability of flow past fixed cylinder. (a) The first column shows the periodic base flow. (b) The second column shows Koopman modes corresponding to the most unstable Floquet modes (periodic part) decomposed into Fourier modes. (c) The third column shows the high order derived Koopman mode of the most unstable Floquet modes. The figures show the isosurface of Q-criterion and the isosurface is contoured by spanwise vorticity. For each mode, a top view (x-y plane) and a side view (x-z plane) are plotted.*

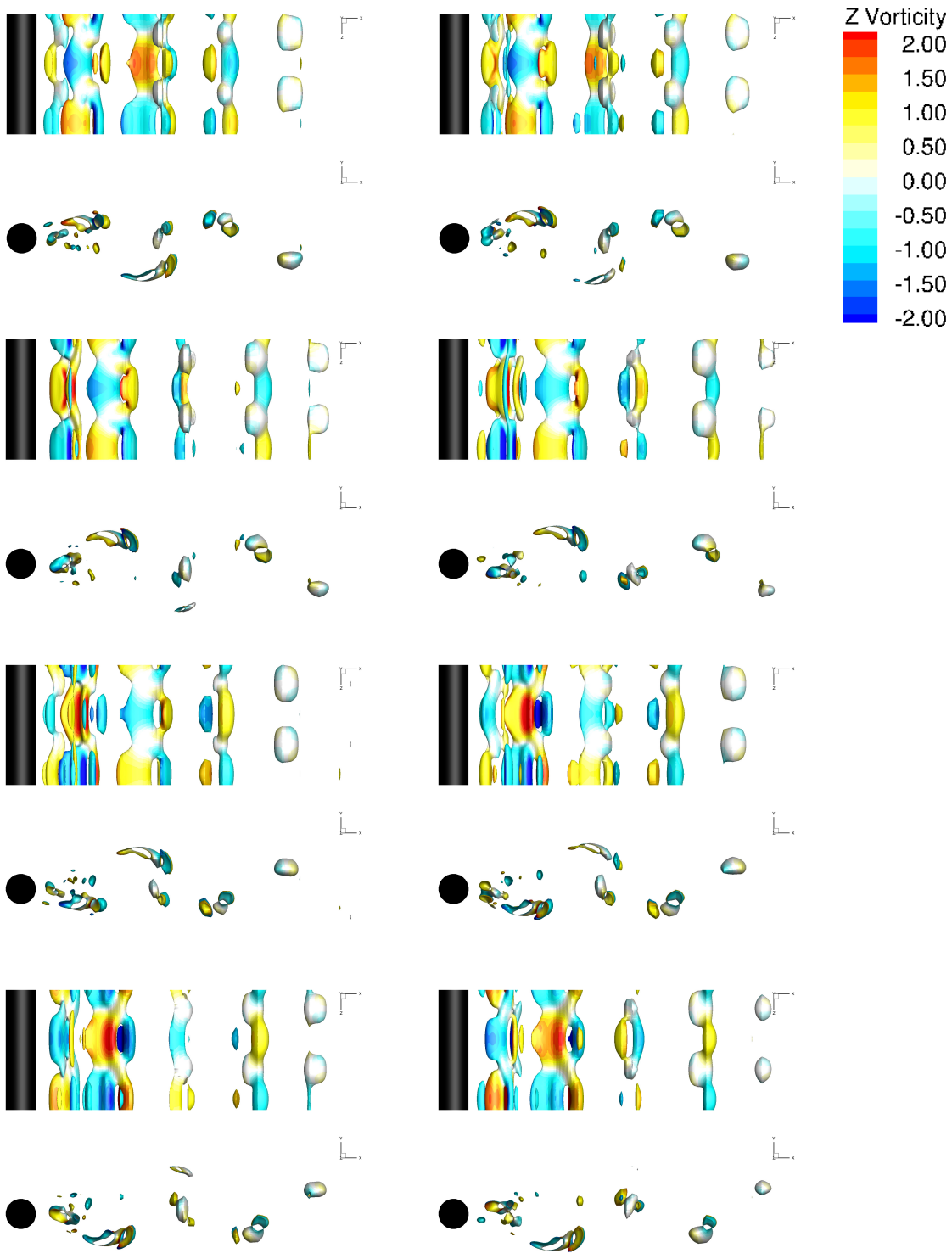

Figure 8.5: *Floquet modes in one shedding period, from top to bottom and from left to right,* $t = 0T, 0.125T, 0.25T, 0.375T, 0.5T, 0.625T, 0.75T, 0.875T$. *Figure show isosurface of Q-criterion and contoured by spanwise vorticity. For each mode, a top view (x-y plane) and a side view (x-z plane) are plotted.*

Chapter 9

Koopman analysis for nonlinear systems

9.1 Two asymptotic stages of primary instability

As stated earlier, at the primary instability stage, the normal mode grows exponentially with a small magnitude. The growth saturates as the perturbation grows and finally reaches periodic. Thus we divided the 2-D primary instability into two phases. The initial phase describes the initial growth of perturbation around the unstable equilibrium state. The final phase described the saturation of perturbation around the stable limit cycle solution. Koopman spectrums at each phase are studied separately. To help to illustrate the two phases lift coefficient of the cylinder from the simulation is shown in figure 9.1. The initial stage is chosen from $0 \sim 167$, and the final stage is chosen from $285 \sim 1400$, the dimensionless time.

9.1.1 Initial stage

The Koopman spectrum at the initial stage of primary instability is shown in figure 9.2a. The random perturbation at the incoming flow successfully excited the most unstable mode with spectrum $(0.0136, \pm 0.751)$. These unstable normal modes and the derived Koopman

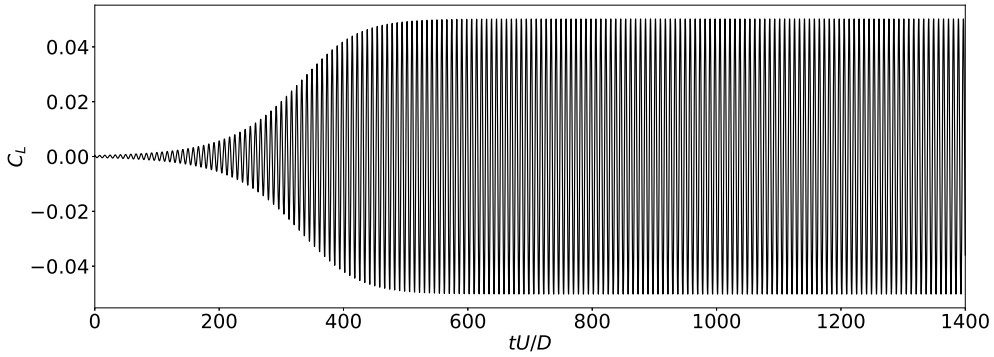

Figure 9.1: *The lift coefficient of 2D flow past fixed cylinder at* $Re = 50$.

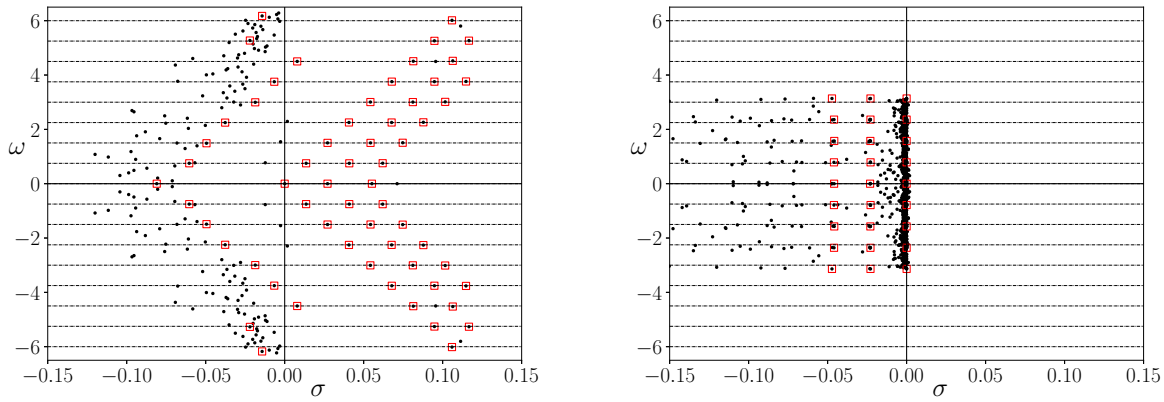

(a) *initial stage*

(b) *finial stage*

Figure 9.2: *Koopman spectrum of primary instability of flow past fixed cylinder at* $Re = 50$. *(•) Black dots show all DMD modes. (□) Red square indicates the most significant modes.*

modes (in the traid-like chain, all lies in the positive half plane) governs the wake. The chain of triad-like distribution is predicted by the proliferation rule. The spectrum $\lambda = 0$ at the origin captures the spectrum for the base flow, the fixed equilibrium solution. Besides these dominant modes, there is a stable mode $\lambda = -0.0810$ and two chains of modes starting from it, and the later is the cross interaction between mode $\lambda = -0.0810$ and the unstable Koopman modes.

Since the time interval between two consecutive snapshots is $\Delta t = 0.5$, the frequency is in the range $\frac{\mathrm{Im}(\ln(\lambda))}{\Delta t} \in (-2\pi, 2\pi]$, thus frequency are truncated between $(-2\pi, 2\pi]$ as shown in figure 9.2a.

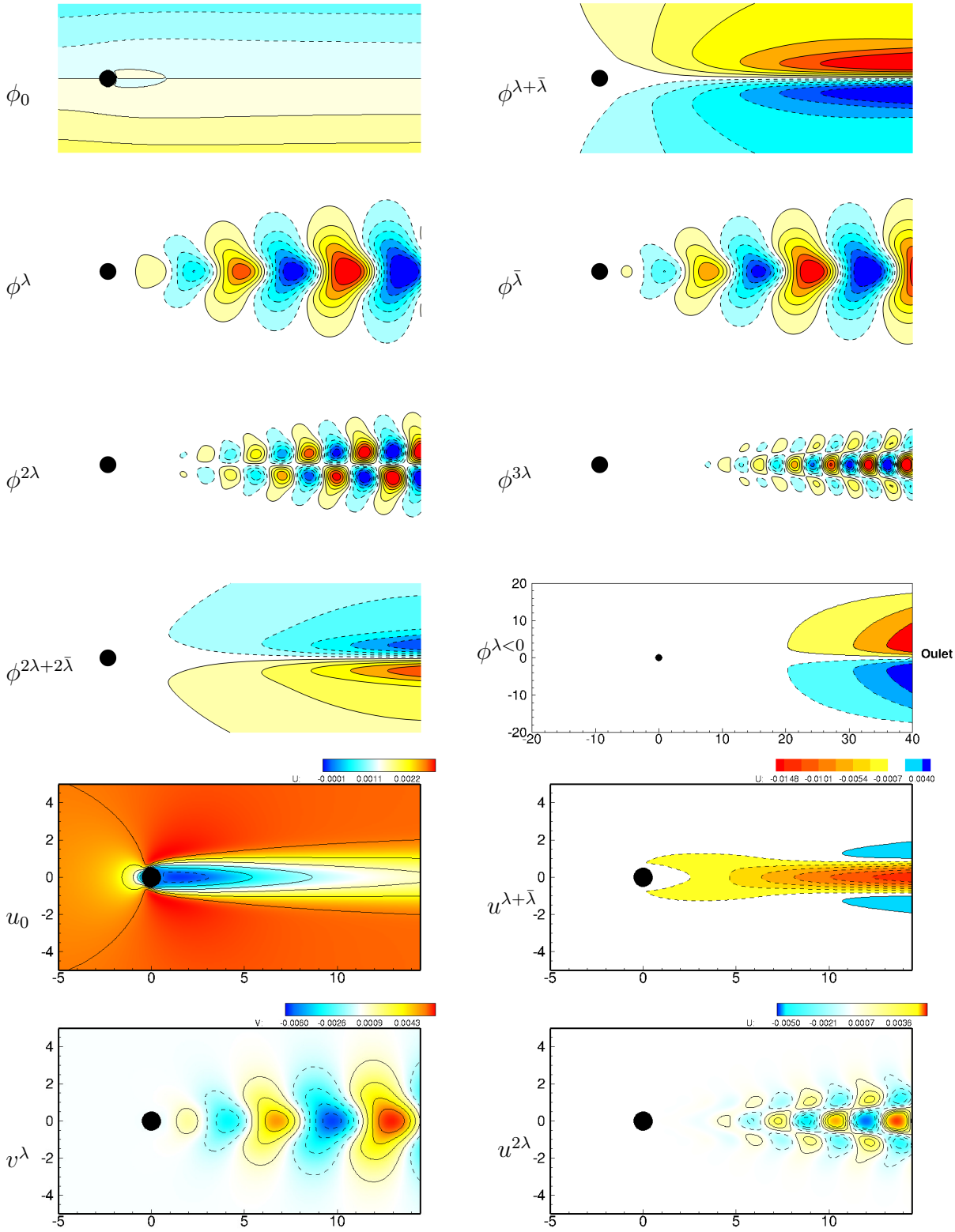

Figure 9.3: *DMD modes captured at the initial stage. First 4 rows show the stream function of the DMD modes with labels on the left. The streamwise velocity of the u_0, $u^{\lambda+\bar{\lambda}}$ and $u^{2\lambda}$ and cross flow velocity v^{λ} are also shown in the last two rows for comparison with Sipp and Lebedev (2007).*

Koopman modes are shown in figure 9.3, the mean flow $\boldsymbol{u}_0$ captures the base flow, the equilibrium solution at Re. This is the unperturbed state, symmetry with respect to centerline. The critical normal modes $\boldsymbol{u}^{\lambda}$ and $\boldsymbol{u}^{\bar{\lambda}}$ are a complex conjugate pair, so the stream function ϕ^{λ} and $\phi^{\bar{\lambda}}$ of the real and imaginary part are shown. These normal modes are confirmed with the ones computed by Jackson (1987), who numerically solved the eigenvalue problem of the homogeneous linearized Navier-Stokes equation by Arnoldi method at $Re = 50$. They are also similar to the global modes computed by Sipp and Lebedev (2007) by solving the homogeneous linearized equation at $Re_c = 46.6$. By definition our mean flow is different from Sipp et. al. in the sense our mean flow is the combination of their mean flow and Reynolds modification.

$$\boldsymbol{u}_0 = \boldsymbol{u}_0^{Sipp} + \epsilon \boldsymbol{u}_{F_2^1}^{Sipp}.$$

$\epsilon \boldsymbol{u}_{F_2^1}^{Sipp}$ is the Reynolds modification as the increase of Re_c to Re. In practice, as Re is close to Re_c, the normal modes $\boldsymbol{u}^{\lambda}$, $\boldsymbol{u}^{\bar{\lambda}}$ and the high order derived modes $\boldsymbol{u}^{2\lambda}$, $\boldsymbol{u}^{3\lambda}$ computed here ($Re = 50$) are all close to the one obtained by Sipp and Lebedev (2007) and Meliga and Chomaz (2011) at $Re = 46.6$ or 47. Mode $\boldsymbol{u}^{\lambda+\bar{\lambda}}$ and $\boldsymbol{u}^{2\lambda+2\bar{\lambda}}$ are the monotonic growing modes (spectrum with pure positive real part). These are symmetry modes which is generated by the interaction of $\boldsymbol{u}^{\lambda}$, $\boldsymbol{u}^{\bar{\lambda}}$ or $\boldsymbol{u}^{2\lambda}$, $\boldsymbol{u}^{2\bar{\lambda}}$. These monotonic modes' effect is to 'modify' on the base flow, shorten the recirculation zone after the cylinder until the base flow reaches the final equilibrium state.

Besides the unstable normal modes and their high order derived modes, a decaying mode $\boldsymbol{\Phi}^{\lambda<0}$ ($\lambda = -0.0810$) is also presented. From the figure, we know this mode has variation only at the outlet. This monotonic decaying mode is believed caused by the incompatibility of the initial uniform flow field and the convective outlet boundary condition used in the simulation

$$\frac{\partial \boldsymbol{u}}{\partial t} + U_{in}\frac{\partial \boldsymbol{u}}{\partial x} = 0.$$

U_{in} is the incoming flow velocity. This mode disappeared as the incompatibility was reduced

as the simulation continuous. Though this is an artificial mode, its cross interaction with the unstable Koopman modes is predicted by proliferation rule and captured by the DMD algorithm.

9.1.2 Finial stage

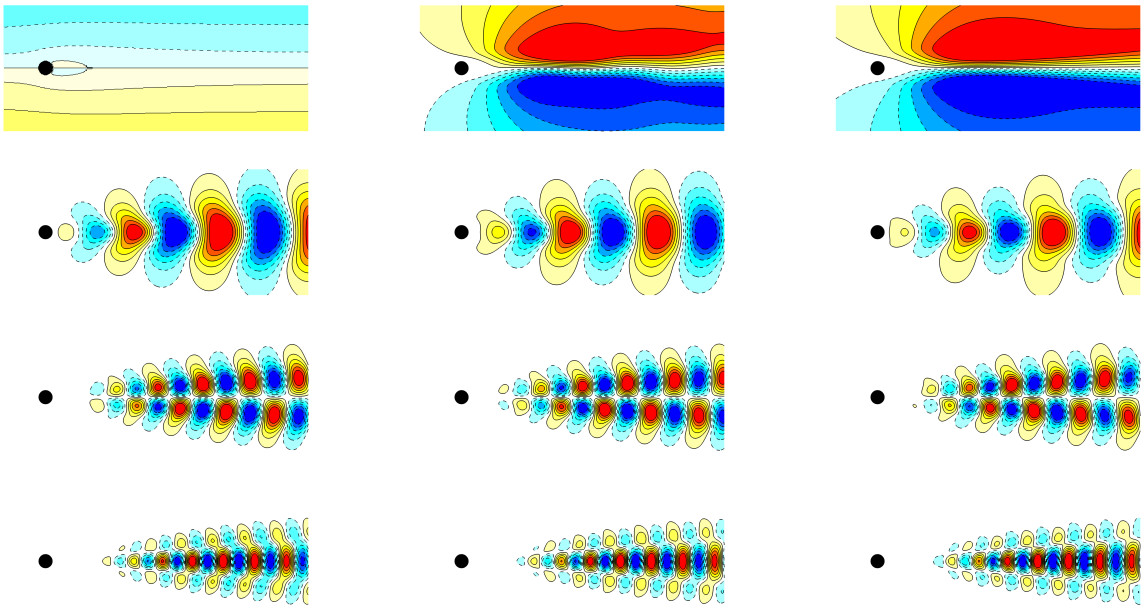

(a) $\sigma = 0$ **(b)** $\sigma = -0.023$ **(c)** $\sigma = -0.046$

Figure 9.4: *DMD modes capture the Floquet modes at finial stage. (a) The first column for periodic solution of wake after cylinder. (b) The second column for least stable Floquet modes. (c) The third column captures the high order derived modes.*

The Koopman spectra for the final stage are shown in figure 9.2b. Since the base flow is periodic, it is captured by the periodic modes ($\sigma = 0$). Furthermore, the nonlinear perturbation is dominated by a Floquet system. The least stable Floquet modes is $\sigma = -0.023$. $\sigma = -0.046$ captures the high order derived mode of $\sigma = -0.023$. The above base spectrum, the spectrum for an underlined Floquet system, and the children spectrum clearly show the hierarchy of Koopman eigenstructure for a periodic asymptotic system.

Since the time interval between snapshots is $\Delta t = 1$ for this analysis, the frequencies are truncated into the range $\omega = \frac{\mathrm{Im}(\ln(\lambda))}{\Delta t} \in (-\pi, \pi]$, as shown in figure 9.2b.

DMD modes of the asymptotic periodic flow are shown in figure 9.4. Fourier modes of the periodic base flow, the Least stable Floquet modes, and the high-order derived mode of the least stable Floquet mode are shown in the first, second, and third columns, respectively.

9.2 Dynamics of nonlinear transition via Koopman decomposition

So far, the nonlinear system is studied using an asymptotic manner, which is far from the goal of analyzing the nonlinear transition. Let us consider using properties of local Koopman spectrum properties mentioned earlier to study the dynamics of the nonlinear system.

Recall the three characteristics of Koopman decomposition from part I. First, the *proliferation rule* recursively proliferates the spectra, eigenfunction, and modes to infinite dimension by the nonlinear interaction. The spectra are orderly organized, and some possible distributions are shown in figure 2.2. Secondly, from operator perturbation theory, a system everywhere continuous differentiable has *continuous Koopman spectra*. The continuity extends the local Koopman decomposition to the global domain. As a result, the Koopman modes are *invariant*, which is the third convenient property of Koopman decomposition.

The three properties of Koopman decomposition then necessitate the study of dynamics of complex nonlinear dynamics. We will decompose the observable by Koopman eigenfunction, track their dynamics using the continuous spectra on the fixed modes.

9.2.1 Fourier expansion for periodic dynamics

For LTI systems, periodic solution results from a center equilibrium point, whose spectrum has the form $\pm j\omega$, where $j = \sqrt{-1}$. However, for nonlinear dynamics, the periodic solution is usually not the result of a center point. One of the examples is the above Hopf bifurcation process. Therefore, it will be useful to study the formation of nonlinear periodic solution. As a byproduct, the Fourier decomposition is rediscovered.

Figure 9.2 shows the critical Koopman spectrum $\lambda = 0.0136 \pm 0.751j$ and their derived

spectrum are unstable at the initial stage. The system then slides away from the unstable state until it reaches some kind of stable trajectory, the stable periodic solution, whose critical Koopman spectrum have zero growth rate and all other spectrum has negative real part, see figure 9.2b. During the nonlinear transition process, the movement of Koopman spectrum is sketched in figure 9.5. As the growth rate of the critical Koopman modes decreases, all these Koopman spectrum move to the imaginary axis simultaneously, keeping the triad-chain formation. As they asymptotically fall on the imaginary axis, periodic solution is obtained.

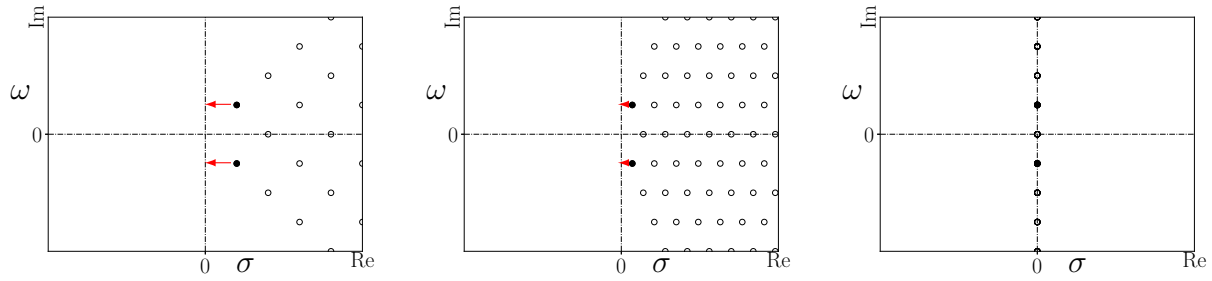

(a) t_{init} **(b)** t_{mid} **(c)** t_{final}

Figure 9.5: *The nonlinear saturation with decreasing growth rate. From left to right, the growth rate σ is decreasing. The infinite dimensional Koopman spectra collapse to the imaginary axis, producing the periodic solution.*

It is well known that periodic dynamics can be expanded by the Fourier series. It can be explained by Koopman decomposition using the Hopf bifurcation case. As all critical Koopman spectrums fall on the imaginary axis as shown by figure 9.5, there are infinite-dimensional Koopman spectrums fall on each $\pm jn\omega$, resulting in the dynamics of $e^{\pm jn\omega t}$. Therefore, Fourier decomposition is obtained. Notice that Fourier expansion contains high-frequencies with an integer multiple of the base frequency $\frac{\omega}{2\pi}$, which conforms to the proliferation rule.

Fourier modes are then generated by superimposing Koopman modes. As flow reaches periodic, the growth rate of critical Koopman modes decreases to 0. Modes with spectrum $m\sigma + jn\omega$, $m = 1, \cdots$, can not be distinguished since they have the same dynamics $e^{jn\omega t}$. As a result, these infinite-dimensional Koopman modes with the same frequency superimposing on top of another creating a 'new' mode, or the so-called Fourier mode.

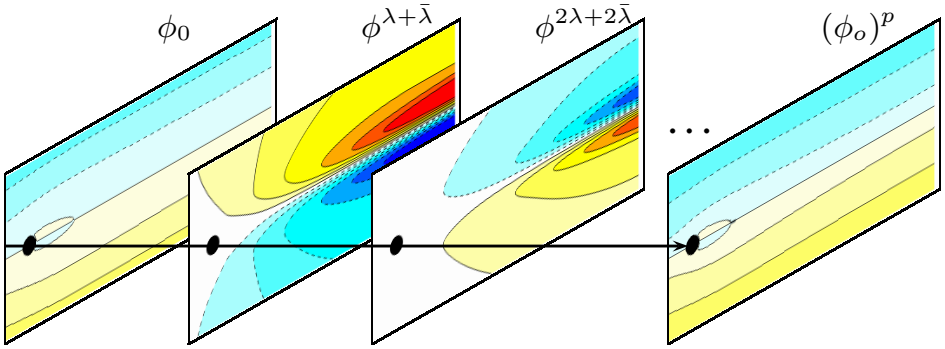

(a) folding of mean flow

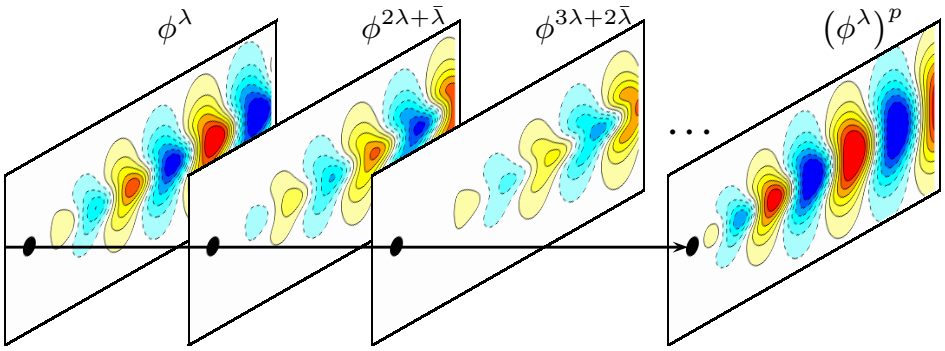

(b) folding of critical mode

Figure 9.6: *Modulation of modes as the flow reaches saturation.*

For instance there was guess that saturation of Hopf bifurcation was as the result of the 'nonlinear modulation' of mean flow (Landau and Lifshitz, 1959; Sipp and Lebedev, 2007). From current study, the magic 'nonlinear modulation' effect is as simple as superposition of Koopman modes

$$(\phi_0)^p = \phi_0 + \epsilon\phi^{\lambda+\bar{\lambda}} + \epsilon^2\phi^{2\lambda+2\bar{\lambda}} + \cdots . \tag{9.1}$$

where $(\phi_0)^p$ is the mean flow at the final periodic stage. ϕ_0 is the initial base flow, $\phi^{\lambda+\bar{\lambda}}$, $\phi^{2\lambda+2\bar{\lambda}}$, $\cdots$ are monotonic modes (with real spectrum) generated by the critical pair Koopman modes (with $\sigma \pm j\omega$). The ϵ terms are borrowed from GSA representing the magnitude of these modes. The superposition on the base flow is illustrated in figure 9.6(a).

Similarly the modulation on the critical modes ϕ^{λ} is also the result of linear superposition

which is illustrated by figure 9.6(b). By sperposition all the modes with frequency $\frac{\omega}{2\pi}$.

$$\left(\phi^{\lambda}\right)^{p} = \phi^{\lambda} + \epsilon\phi^{2\lambda+\bar{\lambda}} + \epsilon^{2}\phi^{3\lambda+2\bar{\lambda}} + \cdots . \tag{9.2}$$

For the current Hopf bifurcation case showed above, as ϵ is on the order

$$\epsilon = \sqrt{\frac{Re - Re_c}{ReRe_c}} \ll \frac{1}{Re_c}, \tag{9.3}$$

see equation 3.18. Koopman modes ϕ_0, $\phi^{n\lambda}$ play a dominant role in the final Fourier modes. Therefore Koopman modes presented in figure 9.3 are very similar to the Fourier modes showed in figure 9.4 but with slight difference.

For convenience, we call all modes in figure 9.5 the critical Koopman modes. The reason is twofold. First, they are derived from the critical Koopman mode (the unstable normal mode (Jackson, 1987)). Secondly, they develop the final periodic base flow (with the base flow ϕ_0).

9.2.2 Floquet solution around limit cycle dynamics

The solution of a periodic LTV system

$$\dot{x} = A(t)x, \quad A(t+T) = A(t) \tag{9.4}$$

is given by Floquet theory (Coddington and Levinson, 1955). Here $x \in \mathbb{R}^n, A(t) \in \mathbb{R}^{n\times n}, t, T \in \mathbb{R}$ and $T > 0$. The solution is given by

$$x(t) = \sum_i e^{\mu_i t} f_i(t) \tag{9.5}$$

where μ_i is the constant complex number called Floquet exponent, and $f_i(t)$ is a periodic function. If there is any Real$(\mu_i) > 0$, the periodic solution is unstable. This theory is a valuable tool to study stability of the limit cycle solution of nonlinear dynamics via linearization.

Table 9.1: *Case for Floquet modes.*

λ_1	λ_2	Floquet modes	high-order derived modes
$0.2 \pm 0.15j$	$-0.3 \pm 0j$	case 1	case 2
$0.2 \pm 0.15j$	$-0.25 \pm 0.3j$	case 3	case 4

Among the above Floquet exponents, there is one with $\mu_i = 0$ providing the periodic base flow, whose formation is already studied in the previous section. The rest Floquet modes are generated similarly but with difference.

The Floquet modes are the cross interaction between some other Koopman mode/modes and the critical Koopman modes in figure 9.5. This is illustrated in figure 9.7. Two cases generating Floquet modes are studied. Case 1 and case 3 are a real and a complex conjugate pair modes cross interaction with the critical Koopman modes. Case 2 and 4 studied the high-order derived modes cross interaction with the critical Koopman modes. These cases are summarized in Table 9.1.

Case 1 show the interaction between $\lambda_1 = 0.2 \pm 0.15j$ and $\lambda_2 = -0.3$. Red dots are the cross interaction spectrum between -0.3 and the critical Koopman modes generated by λ_1. As the growth rate of λ_1 decreases from 0.2 to 0, the spectrums of critical Koopman modes fall on the imaginary axis. At the same time, the cross spectrums fall on the line $\sigma = -0.3$, resulting in the Floquet spectrum. The infinite-dimensional Koopman modes at the same frequency are superimposed on top of each other, creating the Floquet modes.

It is known that nonlinearity will proliferate the linear Floquet modes to high-order ones. This is illustrated by case 2 in figure 9.7. The red dots show the interaction of -0.6 (-0.3+-0.3) with the critical Koopman modes generated by λ_1. As the growth rate of λ_1 decreases to 0, all cross spectrums fall on the line $\sigma = -0.6$, generating high-order Koopman modes derived from the Floquet mode in case 1.

Similarly, the cross interaction of a complex conjugate pair with the critical Koopman modes generating the Floquet modes and their high-order derived modes are illustrated by case 3 and 4, illustrated in figure 9.7(c) and (d).

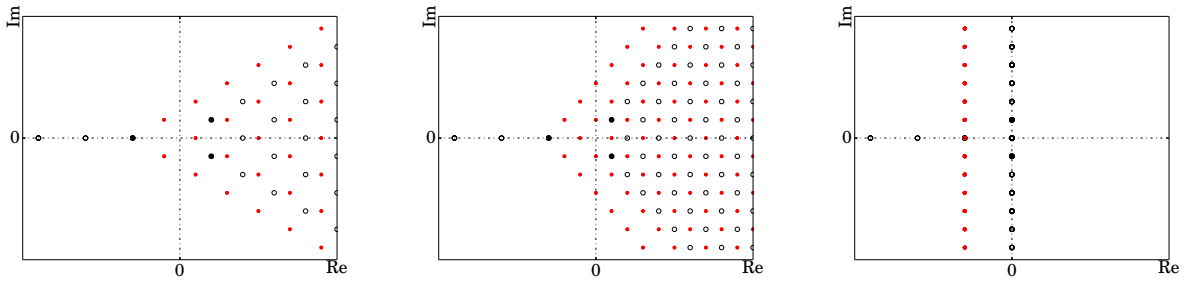

(a) *case 1, generation of Floquet modes.*

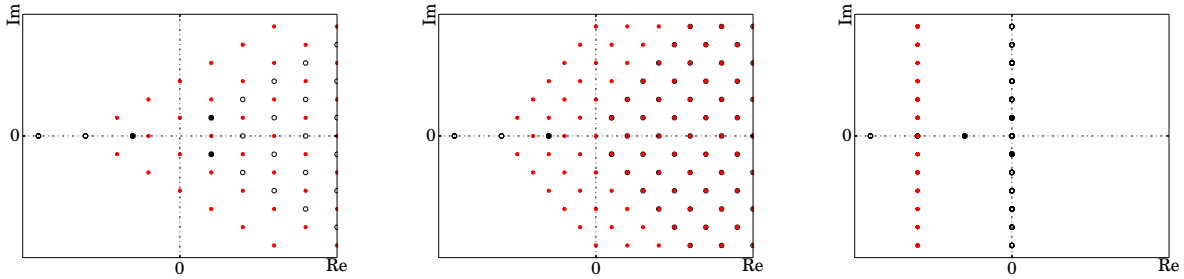

(b) *case 2, generation of high-order derived Floquet modes.*

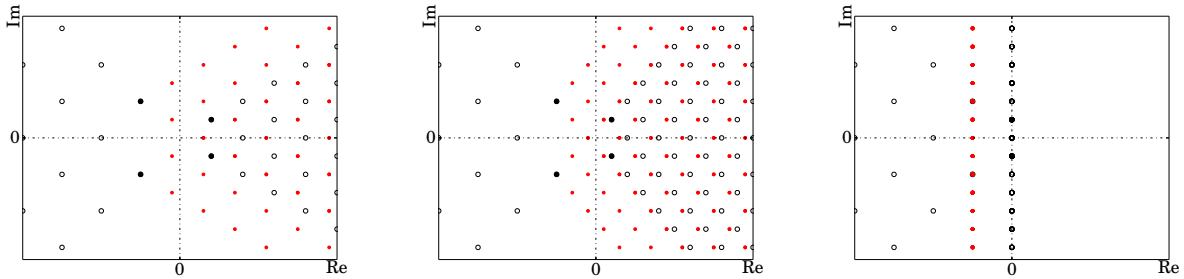

(c) *case 3, generation of Floquet modes.*

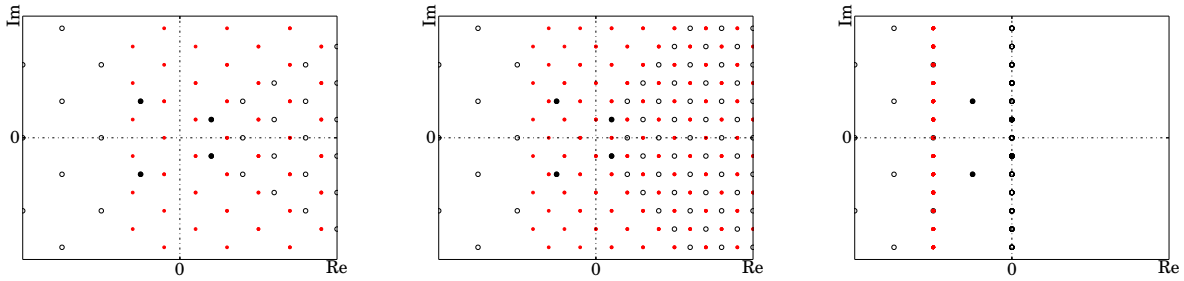

(d) *case 4, generation of high-order derived Floquet modes.*

Figure 9.7: *The formation of Floquet expansion as the growth rate decrease to 0.*

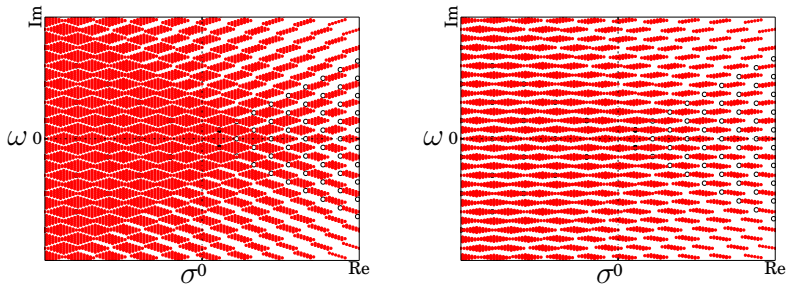

(a) $-0.2\pm0.15j$ *and* $0.11\pm0.71j$ **(b)** $-0.2\pm0.15j$ *and* $0.11\pm0.73j$

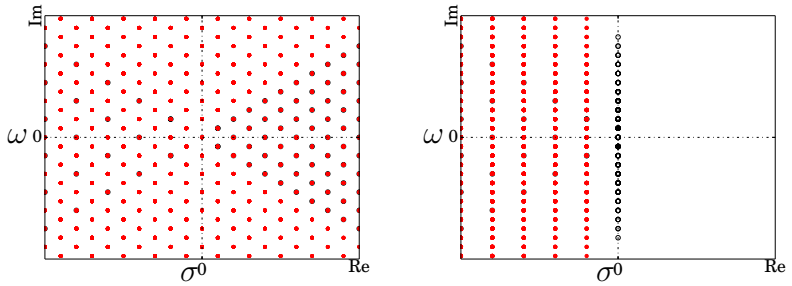

(c) $-0.2\pm0.15j$ *and* $0.1\pm0.75j$ **(d)** $-0.2\pm0.15j$ *and* $0.0\pm0.75j$

Figure 9.8: *The resonance effect*

9.2.3 The resonance phenomena

Another inspiring phenomenon is the DMD modes picked by the residue criterion all have an integer multiple of the base frequency, see figure 9.2. This phenomenon is not answered by the Floquet theory, where μ_i can be any complex number.

The discrepancy is the result of resonance and can be explained by figure 9.8. Figure 9.8a shows cross interaction spectrum by $-0.2 \pm 0.75j$ and $0.11 \pm 0.71j$. If two spectrum has no integer multiple relation, the cross interaction spectrum will scatter in the complex plane, resulting very weak dynamics, and hard to detect. However, if the two spectrum move towards some integer multiple relation, these scattered Koopman spectrum will aggregate, see figure 9.8b and 9.8c, This results in more strong dynamics. In the case the critical Koopman modes saturates, the above aggregated spectrum will further aggregate, resulting even aggregated spectrum in figure 9.8d. This further creates even stronger dynamics and easily detected. This is the reason that residue criterion picked modes with integer multiple of base frequency.

Moreover, it is well-known to disturb some systems, a perturbation of the system's natural frequency is more efficient, such as Cattafesta et al. (1997); Rathnasingham and Breuer (1997). It is explained similarly since, by the forced linear differential equation (3.24), perturbation close to natural frequency can be effectively excited. Thus those effective perturbations are usually of the same frequency or an integer multiple of the underlined linear system.

9.2.4 The coherent structure

The discover of coherent structure in turbulent flow has a long history. Leonardo da Vinci first recorded and sketched the repeated patterns in the fluids, and called them the coherent structure (Richter et al., 1970). Reynolds (1883) in his classic experiments also observed the repeated patterns with the help of spark light. Recently, coherent structures are well observed and documented in turbulence research. For instance, Holmes et al. (1996a) successfully identified them using the proper orthogonal decomposition (POD) techniques. However, none of them explained why these coherent structures exist.

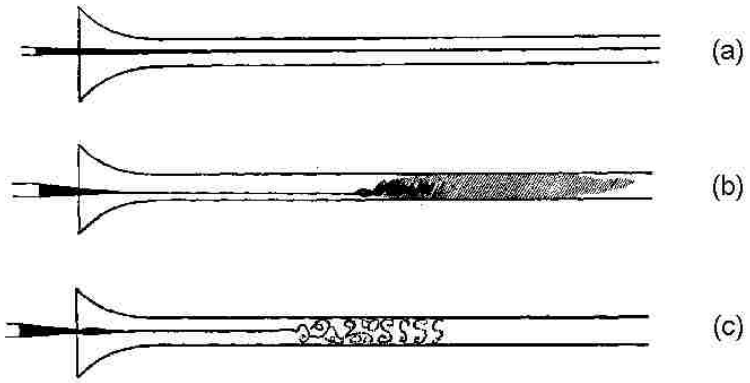

Figure 9.9: *Reynolds's experiments and coherent structure. With the spark light, the repeated flow pattern is observed in experiment (c).*

The coherent structure is simply the invariant Koopman modes. In part I, we used operator perturbation theory, and derived Koopman modes are state-independent for many 'smooth' systems. They are the reason for coherent structure in fluid systems. The alternating patterns are associated with the complex conjugate Koopman modes pair. In turbulent

flows, they may appear almost periodically.

Even for flow does not fully satisfy the continuity condition, such as the oscillating cylinder case (up and down) in figure 9.10. Spatial discontinuity at the boundary resulting unbounded operator, repeated patterns in the far field is still observed, implying certain discontinuity only influence local area. Seen from the computed DMD modes, figure 9.10c, spatial discontinuity may result in significant high-frequency modes, which are only significant around the moving boundary, similar to the Fourier expansion around discontinuity.

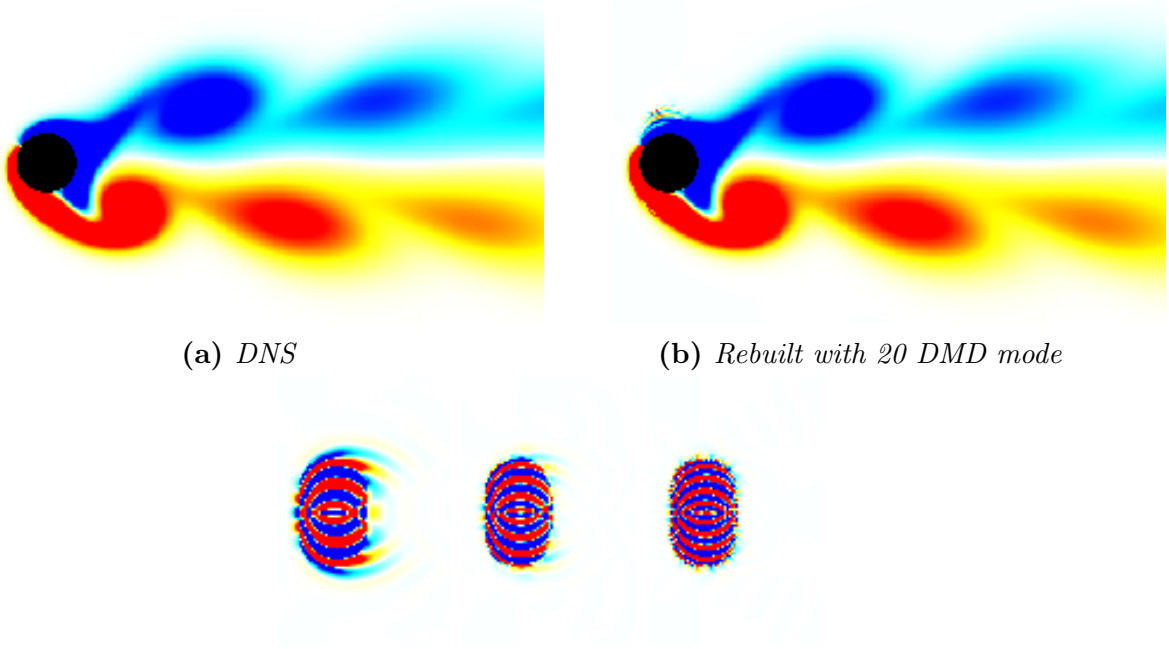

(a) *DNS*

(b) *Rebuilt with 20 DMD mode*

(c) *Three High-frequency modes around moving boundary.*

Figure 9.10: *DMD decomposition captures dynamics well far away from the moving solid.* $Re = 50$, $St = 0.2$

9.2.5 A least-square study for the sub-dynamics of Koopman modes

The nonlinear dynamics of the Hopf bifurcation was studied by Stuart (1958), by considering decomposition

$$\boldsymbol{x}_n = \boldsymbol{x}_0 + \{\boldsymbol{v}_1 A_1(t) + \boldsymbol{v}_2 A_2(t) + \cdots + c.c.\} \tag{9.6}$$

where $\boldsymbol{x}_0$ is the base flow, $\boldsymbol{v}_i$ are the normal modes of the linearized system at the equilibrium point. $A_i(t)$ are the corresponding coefficients. Let $\boldsymbol{v}_1$ to be the critical normal mode. For the weak nonlinear cases, $A_1(t)$ (or written as A) can be approximated by the Stuart-Landau equation (3.25). For the highly nonlinear system, high order Stuart-Landau equation can be used (Schmid and Henningson, 2012, see, chap. 5.3.2)

$$\frac{dA}{d\tau} = \lambda_1 A + \lambda_2 A|A|^2 + \lambda_3 A|A|^4 + \lambda_4 A|A|^6 + \cdots . \tag{9.7}$$

The temporal coefficients was numerically approximated by the least-square solution of the whole bifurcation process (the process in figure 9.1) using the mean and unstable modes, modes in the non-negative half plane shown in figure 9.2a except the $(0.008, \pm 4.5)$ one. Figure 9.11 shows the results of 5 Koopman modes (ϕ_0, $\phi^{\lambda+\bar{\lambda}}$, $\phi^{2\lambda+2\bar{\lambda}}$, ϕ^{λ}, $(\phi_0)^p$). Here are the results.

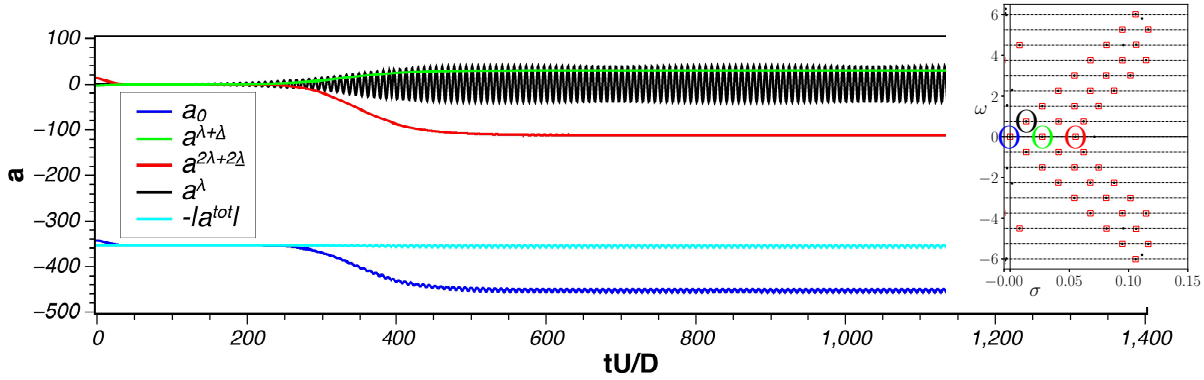

Figure 9.11: *The time history of modes ϕ_0, $\phi^{\lambda+\bar{\lambda}}$, $\phi^{2\lambda+2\bar{\lambda}}$, ϕ^{λ} (only the real part) shown in Fig. 9.6 and the first-three-term approximation of $(\phi_0)^p$ in Eqn. 9.1.*

First, the base flow ϕ_0 changed magnitude significantly during the nonlinear transition. As seen from figure 9.11, its magnitude increased during the transition process $200 < \frac{tU}{D} < 500$. The monotonic modes $\phi^{\lambda+\bar{\lambda}}$ and $\phi^{2\lambda+2\bar{\lambda}}$ increased significantly from trivial. However, the magnitude of the mean flow maintained a constant level as indicated by $|a^{tot}|$

$$|a^{tot}| = \frac{||a_0\phi_0 + a^{\lambda+\bar{\lambda}}\phi^{\lambda+\bar{\lambda}} + a^{2\lambda+2\bar{\lambda}}\phi^{2\lambda+2\bar{\lambda}}||}{||\phi_0||}. \tag{9.8}$$

This is because the DMD modes are not orthogonal. It is also noticed even the magnitude does not change, velocity profile has changed, see figure 9.6a. The critical mode ϕ^{λ} follows the Stuart-Landau equation as shown in figure 9.11 by a^{λ}

Chapter 10

Rebuild dynamics use DMD-ROM method

10.1 Introduction

Numerical simulation for the study of flow dynamics provides flexibility, detail information, and low cost in its comparison to most experiments. However, the computational cost, in terms of simulation time, for a large category of practical applications, is still too high for design and real-time control. The idea of model order reduction (MOD) is to find a reduced-order model (ROM) at a much lower space to still represent the most important dynamics of the original high-fidelity simulation model. The low-order model becomes attractive for its capability to provide both clear physical understanding and fast real-time computation. One of the most popular approaches for model reduction is POD-Galerkin projection, which uses proper orthogonal decomposition (POD) modes as base functions to maximize the energy captured by the same reduced number of modes. There have been many studies in the application of POD-Galerkin projection for incompressible and compressible flows (Balajewicz et al., 2013; Barone et al., 2009; Gao and Wei, 2014, 2016; Holmes et al., 1996a; Qawasmeh and Wei, 2013; Schlegel et al., 2009; Tabandeh et al., 2016; Tran et al., 2015; Wei and Rowley, 2009b; Wei et al., 2012).

Dynamic mode decomposition (DMD) is another emerging technique for data decomposition. Originated from the spectral analysis of Koopman operator (Mezić, 2005; Rowley et al., 2009), DMD algorithm by Schmid (2010) provides a numerical approximation. It characterizes the nonlinear system through an analysis of the approximate linear system (Tu et al., 2014). By its definition, the eigenvalues from DMD analysis provide both the frequency and the growth rate of corresponding modes, while the modes often identify coherent flow structures, like POD modes. Rowley et al. (2009) applied spectral analysis to a large scale of simulation of a jet in crossflow. Schmid used this method not only for DNS simulation as well as experimental data from time-resolved PIV data. More recently, there is a variation on streaming data (Hemati et al., 2014) or dealing with data with noise from experiments (Hemati et al., 2016).

DMD modes have distinct properties that each mode contains pure frequency. Besides, DMD modes represent certain similarities to POD modes, at least from the mathematic point of view, DMD modes a linear combination of POD modes. These motive efforts to use DMD modes for ROM as an alternative to POD modes. Tissot et al. (2014) combined DMD formula with a data assimilation technique for flow prediction. Chen et al. (2012) suggests using equilibrium base flow subtraction instead of mean subtracted flow to satisfy the boundary condition, to avoid the pitfall of mean subtracted DMD only resulting in Fourier modes.

The current work focuses on the application of DMD modes and their adjoint modes, with their bi-orthogonality, to build simple Galerkin models at low-order space. With the introduction of adjoint modes, DMD based ROM can be obtained readily and result in similar systems as the POD-ROM method.

10.2 Methodology

The non-orthogonality of DMD poses difficulty for Galerkin projection. In this work, the adjoint DMD modes are introduced for the projection. As the convectional DMD algorithm provides better adjoint modes. Therefore, traditional DMD algorithm (Schmid, 2010) is used

and described below.

10.2.1 Dynamic Mode Decomposition

Assuming a nonlinear system is sampled by a series of data

$$\boldsymbol{x}_{k+1} = f(\boldsymbol{x}_k), \quad k = 0, \cdots, n. \tag{10.1}$$

A linear approximation of the nonlinear system (10.1) reads

$$Y = AX. \tag{10.2}$$

where matrix X and Y are defined by

$$X \triangleq [\boldsymbol{x}_0, \boldsymbol{x}_1, \cdots, \boldsymbol{x}_{n-1}], \tag{10.3}$$

$$Y \triangleq [\boldsymbol{x}_1, \boldsymbol{x}_2, \cdots, \quad \boldsymbol{x}_n]. \tag{10.4}$$

Following the DMD algorithm, a best fit for matrix A is

$$\tilde{A} \triangleq U^* Y V \Sigma^{-1}, \tag{10.5}$$

where U, Σ, V are given by the singular value decomposition (SVD) of X

$$X = U \Sigma V^*. \tag{10.6}$$

$(^*)$ is the matrix Hermitian operator.

DMD eigenvalues λs and modes ϕs are obtained by solving the eigenvalue problem of $\tilde{A}$.

$$\tilde{A}w = \lambda w \tag{10.7}$$

$$\phi = Uw \tag{10.8}$$

The adjoint DMD modes

$$\phi^{ad} = U(w^l)^*, \tag{10.9}$$

are obtained similarly by the left eigenvectors of the system

$$w^l \tilde{A} = \lambda w^l \tag{10.10}$$

From matrix spectrum theory, DMD and adjoint DMD modes are bi-orthogonal. Therefore, if normalized,

$$||\phi|| = 1, \quad ||\phi^{ad} = 1||, \tag{10.11}$$

relation holds

$$(\phi_i^{ad}, \phi_i) = \delta_{ii}. \tag{10.12}$$

As a result, the temporal coefficients of DMD modes are obtained by

$$a(i,t) = (x_t, \phi_i^{ad}). \tag{10.13}$$

A more efficient approach is to use the SVD decomposition (10.6)

$$a(i,t) = (x_t, \phi_i^{ad}) = (U\Sigma V^*, Uw_i^l) = (\Sigma V^*, w_i^l). \tag{10.14}$$

A least-square procedure to compute the temporal coefficients is also presented in appendix A for reference.

10.2.2 DMD modes ranking, selection and the energy criterion

In previous work, a residue-based criterion to select modes was developed. For the purpose of rebuilding dynamics, an efficient modes ranking technique is required. For this purpose,

energy of each mode is computed. The kinetic energy reads

$$||u||^2 = (u,u) = \left(\sum_{i=1}^{N} a_i\phi_i, \sum_{j=1}^{N} a_j\phi_j\right) = \sum_{i=1}^{N}\sum_{j=1}^{N} a_i\overline{a}_j(\phi_i,\phi_j). \tag{10.15}$$

Because of non-orthogonality, energy are distributed in a matrix manner, a correlation matrix C and an energy distribution matrix E are defined as

$$C_{ij} \triangleq (\phi_i,\phi_j), \tag{10.16}$$

$$E_{ij} \triangleq \int_0^L (a_i\phi_i, a_j\phi_j)dt = C_{ij}\int_0^L a_i\overline{a}_j dt. \tag{10.17}$$

$(0,L)$ is the sampling period. Energy of each mode is obtained by summation all the associated terms.

$$E_i = \frac{1}{2}\sum_{j=0}^{N}\left(E_{ij}+E_{ji}\right), \quad i = 0,\cdots,N. \tag{10.18}$$

E_i is the energy-based criterion for DMD modes ranking.

10.2.3 Reduced order modeling using Galerkin projection

Galerkin projection method is a process of projecting full-system dynamics onto a set of modes and studying the dynamics on them. This transformation reduces a system usually described by partial differential equations to a simpler system described by ordinary differential equations. Here we consider model order reduction onto DMD modes for incompressible flow described by Navier-stokes equations

$$\nabla\cdot\boldsymbol{u} = 0, \tag{10.19}$$

$$\frac{\partial\boldsymbol{u}}{\partial t} = -\nabla p + \frac{1}{Re}\nabla^2\boldsymbol{u} - (\boldsymbol{u}\cdot\nabla)\boldsymbol{u}. \tag{10.20}$$

For simplicity, the above equations are projected onto the adjoint DMD modes,

$$(\phi_i^{ad}, \frac{\partial\boldsymbol{u}}{\partial t}) = (\phi_j^{ad}, -\nabla p + \frac{1}{Re}\nabla^2\boldsymbol{u} - (\boldsymbol{u}\cdot\nabla)\boldsymbol{u}), \quad i = 0,\cdots,r., \tag{10.21}$$

where the dynamics is replaced by DMD decomposition

$$\boldsymbol{u}(x,t) = \sum_{i=0}^{r} a_i(t)\phi_i(x). \tag{10.22}$$

The resulting ODEs are

$$\frac{\partial a_i}{\partial t} = \mathcal{G}_i(P) + \sum_{j=0}^{r} \frac{1}{Re} l_{ij} a_j - \sum_{j=0}^{r}\sum_{k=0}^{r} q_{ijk} a_j a_k, \quad i = 0, \cdots, r. \tag{10.23}$$

with coefficients $l_{ij} \triangleq (\phi_i^{ad}, \nabla^2\phi_j)$ and $q_{ijk} \triangleq (\phi_i^{ad}, (\phi_j \cdot \nabla)\phi_k))$.

10.2.4 Continuity, boundary condition and pressure term

Since DMD modes are the linear combination of the sampled data, they satisfy continuity equation automatically since the continuity equation is linear.

Chen et al. (2012) suggested to use a base flow that satisfied the boundary condition, and other modes have a homogeneous boundary to perform ROM. An equilibrium flow is suggested for this purpose. However, a separate flow solver for the equilibrium state is required for this purpose.

In this work, an approximate mean flow which satisfies the boundary condition is automatically obtained. DMD algorithm is applied on the unmodified snapshots rather than the base-flow-subtracted ones. It can be found, the mean flow is a fixed point of the system, since

$$\begin{aligned} A\boldsymbol{x}_{mean} =& A\frac{\boldsymbol{x}_0 + \boldsymbol{x}_1 + \cdots + \boldsymbol{x}_{n-1}}{n} \\ =& \frac{\boldsymbol{x}_1 + \boldsymbol{x}_2 + \cdots + \boldsymbol{x}_n}{n} \\ =& 1 \cdot \boldsymbol{x}_{mean} + \frac{\boldsymbol{x}_n - \boldsymbol{x}_0}{n}. \end{aligned}$$

As $N \to 0$, the mean flow is the fixed point of the system. We therefore call it mean mode. For periodic data set $\boldsymbol{x}_n = \boldsymbol{x}_0$, this equation is satisfied exactly.

Noack et al. (2005) studied the pressure term

$$\mathcal{G}_i(p) = (\phi_i^{ad}, \nabla p) = q_{ijk}^p a_j a_k.$$

Their results showed for 'closed' flow, or the Couette flow which had periodic boundary condition in streamwise and spanwise direction, and Dirichlet boundary condition in the wall-normal direction, the pressure term was exactly zero. For other open flow, such as the two-dimensional mixing layer, this term could be nontrivial for long term prediction. However, its effect on short term prediction, especially for three-dimensional applications, was small. Therefore, it is neglected in this study.

After applying the boundary condition and ignoring pressure term, the DMD-ROM equations (10.23) are reduced to:

$$\frac{\partial a_i}{\partial t} = \sum_{j=0}^{r} \frac{1}{Re} l_{ij} a_j - \sum_{j=0}^{r} \sum_{k=0}^{r} q_{ijk} a_j a_k, \quad i = 1, \cdots, r, \tag{10.24}$$

where a_0 is a constant number, so $a_0\phi_0$ satisfied the boundary condition, and a_is ($i = 1, \cdots, r$) are the unknowns.

10.3 Application: flow passing a fixed cylinder

A two-dimensional fixed cylinder flow is used as a benchmark problem for its simple geometry and complex flow phenomenon.

10.3.1 Problem setup

The fix cylinder problem is configured as Fig. 10.1. The computational domain is $l_x \times l_y = (-5, 15) \times (-5, 5)$. A unit cylinder is placed at the origin. The streamwise and spanwise is 20 and 10 times the cylinder diameter correspondingly. Uniform grid of size $N_x \times N_y = 401 \times 201$ is used. Grid resolution in both direction is $dx = dy = 0.05$. Reynolds number based on incoming velocity and cylinder diameter is 200.

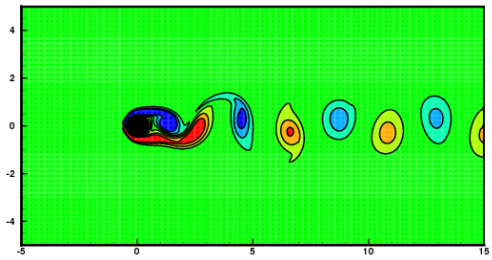

Figure 10.1: *Flow passing fixed cylinder at* $Re = 200$.

10.3.2 Result of numerical simulation

A velocity probe is placed at point $(5, 0)$. The history of velocity component v is shown in Fig. 10.2. The simulation contains two stages, the wake starting stage, and the periodic wake shedding stage. When fully developed, the shedding frequency is 0.181. The benchmark is applied to both of these stages. For the periodic stage, three shedding periods are chosen from $t = 160 \sim 176.4$ for DMD analysis and ROM rebuilt. For the developing stage, snapshots from $70 \sim 83.1$ are sampled.

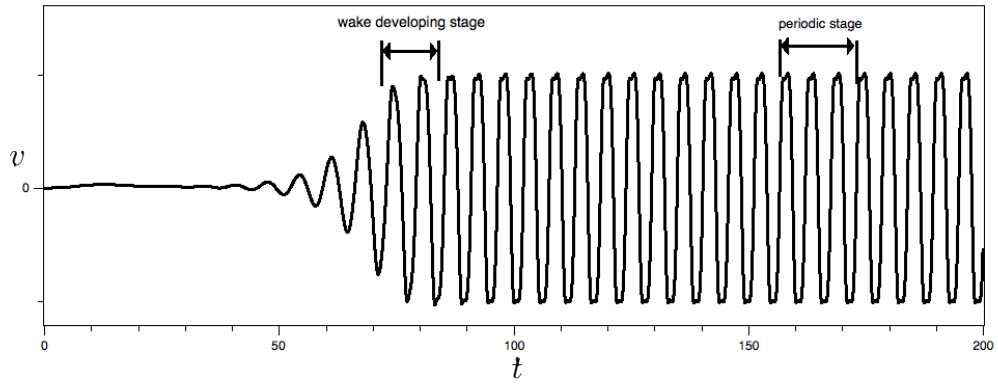

Figure 10.2: *Velocity history* v *from probe.*

10.4 DMD-ROM results

10.4.1 Periodic wake shedding stage

DMD analysis

At the periodic stage, the eigenvalues of DMD modes and their corresponding energy are shown in Figure 10.3. Eigenvalues on the unit circle represent periodic modes. The energy of DMD modes shown in Fig. 10.3b indicate DMD modes are also efficient in the view of energy, which makes them suitable for reduced-order modeling.

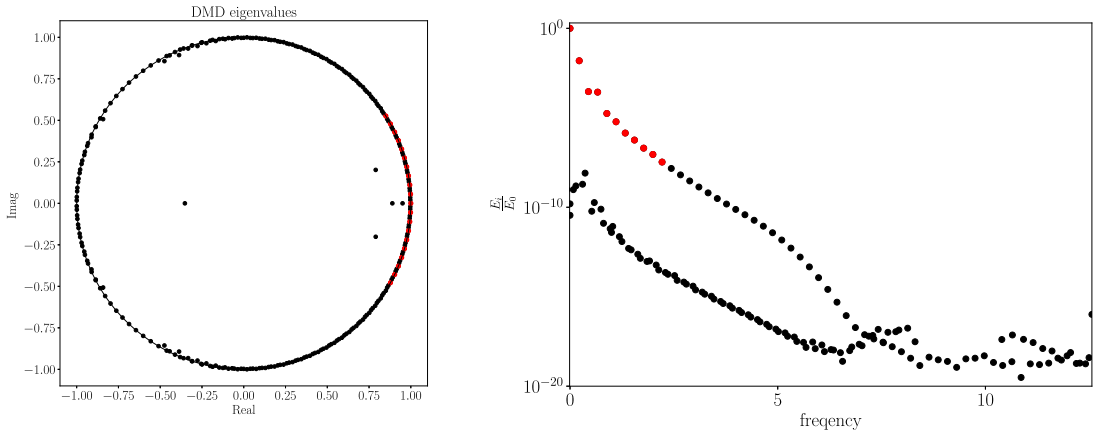

(a) *DMD eigenvalues* **(b)** *frequency spectrum of DMD modes*

Figure 10.3: *DMD analysis for periodic wake shedding stage. Red color indicates the most energetic modes.*

Matrix energy shown in figure 10.4 are diagonal dominant, which means the cross terms (ϕ_i, ϕ_j), $i \neq j$ contains much smaller energy than (ϕ_i, ϕ_i) term.

The mean flow and mean mode are compared in figure 10.5. Except the sign difference (due to eigensolver), two flow are almost identical.

DMD modes and adjoint DMD modes

Some of the leading DMD modes are shown in Fig. 10.8. The real and imaginary parts of the DMD modes are presented. They are similar to those obtained by Noack et al. (2003). The adjoint DMD modes are shown in Fig. 10.9, respectively.

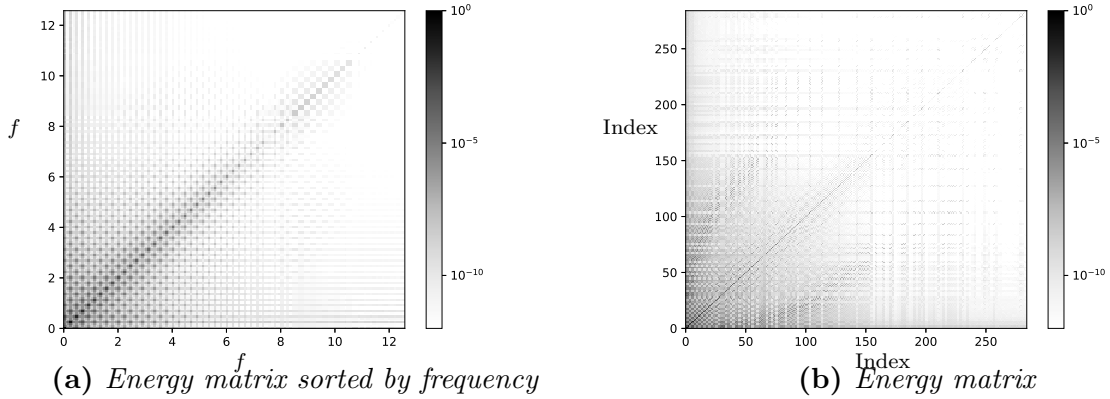

(a) *Energy matrix sorted by frequency* **(b)** *Energy matrix*

Figure 10.4: *Pixel plot for energy matrix. Values are in log scale.*

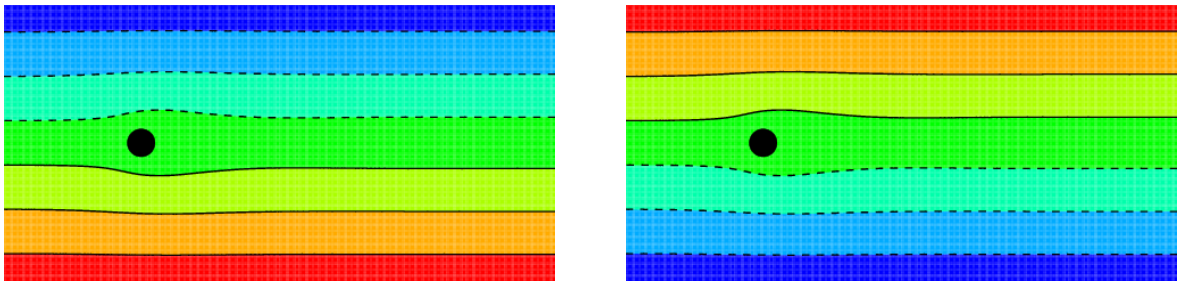

(a) *Mean mode* **(b)** *Mean flow*

Figure 10.5: *Comparison of mean mode and mean flow.*

Temporal coefficients from DMD-ROM

Table 10.1: *DMD modes selected for ROM*

mode#	frequency	mode#	frequency
0	0.000		
1	0.222	5	1.108
2	0.443	6	1.330
3	0.665	7	1.551
4	0.886	8	1.773

Seventeen modes (one mean mode and 8 paired complex-conjugated DMD modes) are used for dynamics rebuilt. Their frequency information is in Table 10.1. ROM results are shown in Fig. 10.6. DNS results of DMD temporal coefficients are obtained by projecting onto DMD modes. ROM correctly reproduced the original dynamics. However, there exists slight error in the frequency for some high-frequency modes. We believe that was because a

finite number of DMD modes introduced accumulated error.

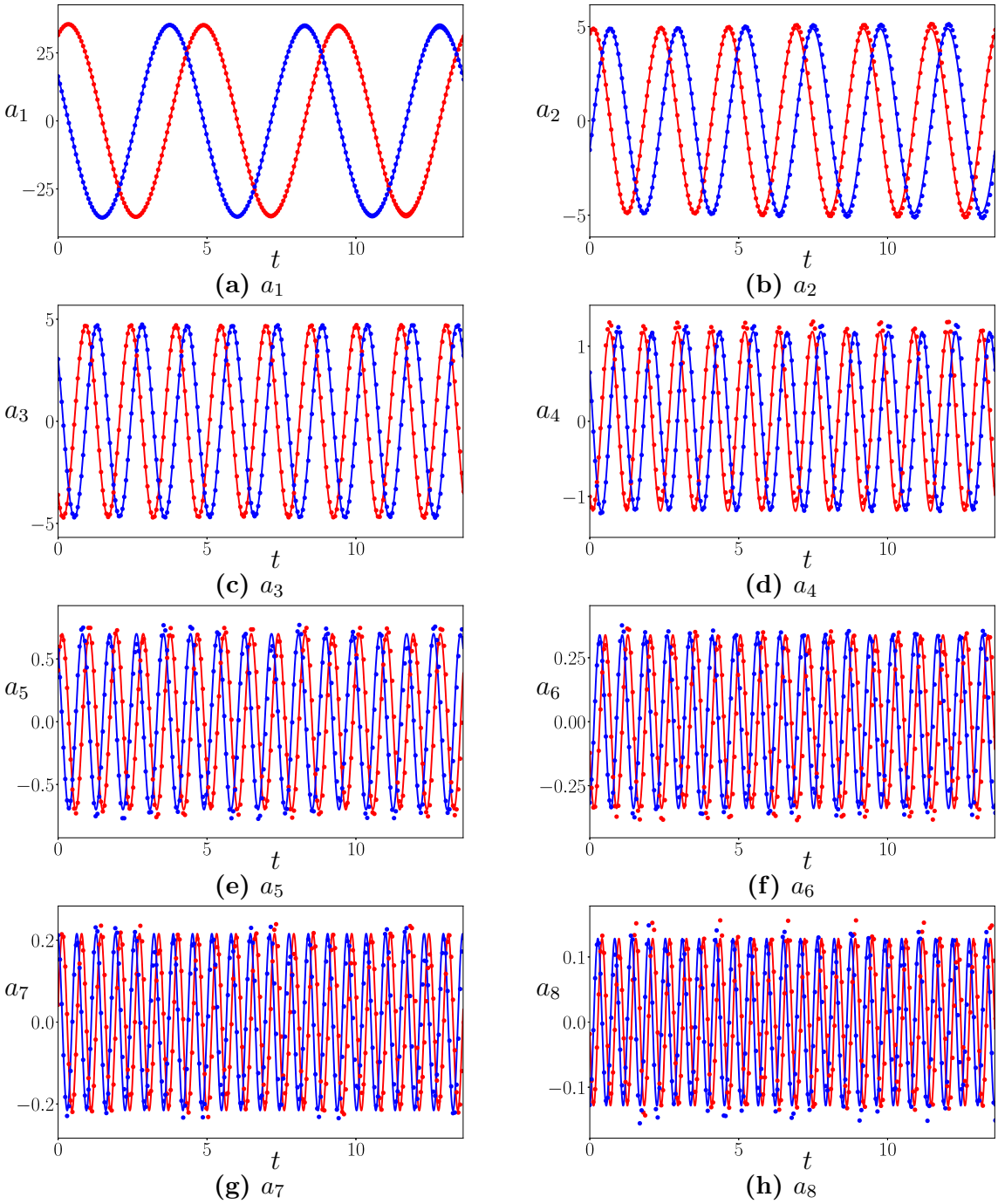

Figure 10.6: *ROM result for first 8 modes. Solid line from DNS result, and dots for ROM. Red for real part and blue for imaginary part.*

10.4.2 Wake developing stage

Previous section successfully applied the DMD-ROM method to the periodic flow. In this section, the ability of DMD-ROM to reconstruct the nonlinear transition is explored. A 2.5 shedding period is investigated for this purpose.

DMD analysis of wake starting stage

DMD decomposition on the data from dimensionless time $t = 70 \sim 83$ is obtained. Eigenvalues are shown in Fig. 10.7a. For the wake developing stage, many growing modes present. They are modes with spectrum outside the reference unit circle. Most of them are high-frequency modes with trivial temporal coefficients. However, there are a few dominant low-frequency ones. The corresponding energy are shown in Fig. 10.7b and 10.7c.

The leading 11 modes are shown in Fig. 10.11, including a mean mode and five complex-conjugate pairs. The corresponding adjoint DMD modes are shown in figure 10.12.

ROM rebuilt using DMD modes for wake starting period

29 DMD modes are used for flow dynamics reconstruction. Frequencies of them are listed in Table 10.2.

Table 10.2: *Most dominant modes frequency for periodic wake shedding*

mode#	frequency	mode#	frequency	mode#	frequency
0	0.000	5	0.369	10	0.625
1	0.186	6	0.300	11	0.773
2	0.039	7	0.424	12	0.706
3	0.130	8	0.574	13	0.833
4	0.226	9	0.511	14	0.976

The comparison of DNS and ROM results is shown in Fig. 10.10. ROM was able to reproduce the dynamics of the developing wake after the cylinder. However, some high-frequencies was not captured well by DMD-ROM.

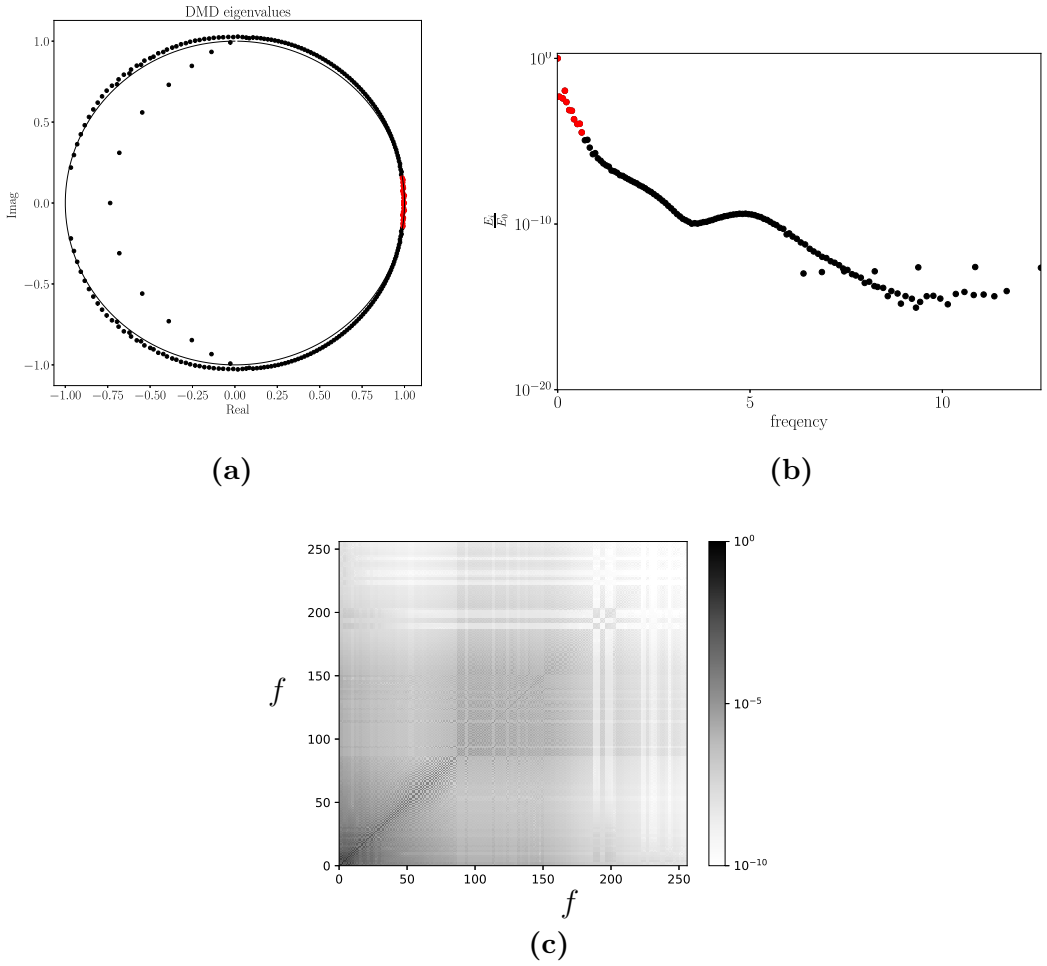

Figure 10.7: *The DMD eigenvalue of wake developing stage. (a). an overview of DMD eigenvalue. (b) frequency energy. (c) energy distribution matrix sorted by energy distribution, energy is in color and taken* log_{10}

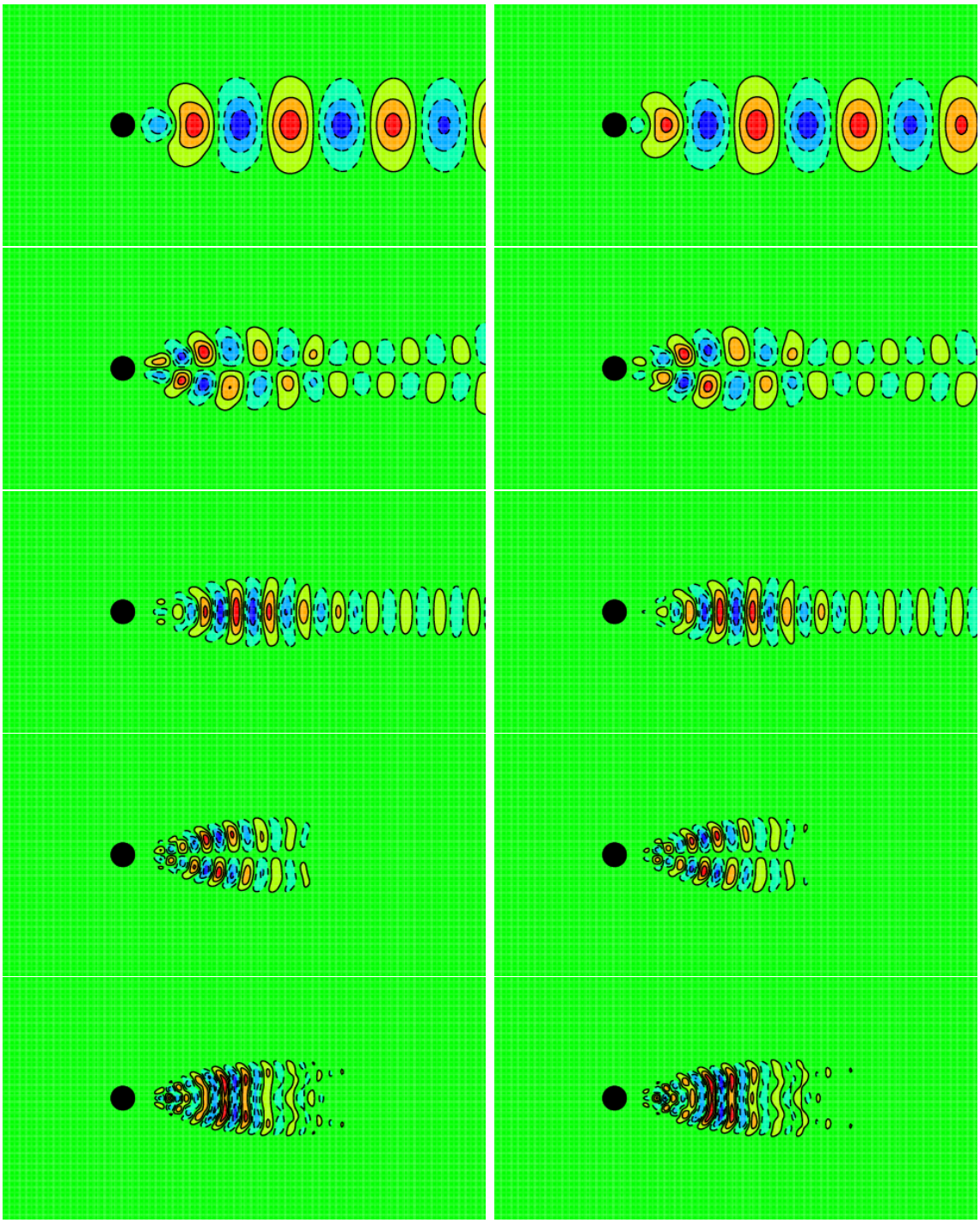

Figure 10.8: *Normalized stream function of first 4 pairs DMD modes at periodic wake shedding stage. The left column is the real part, and right column is for the imaginary part.*

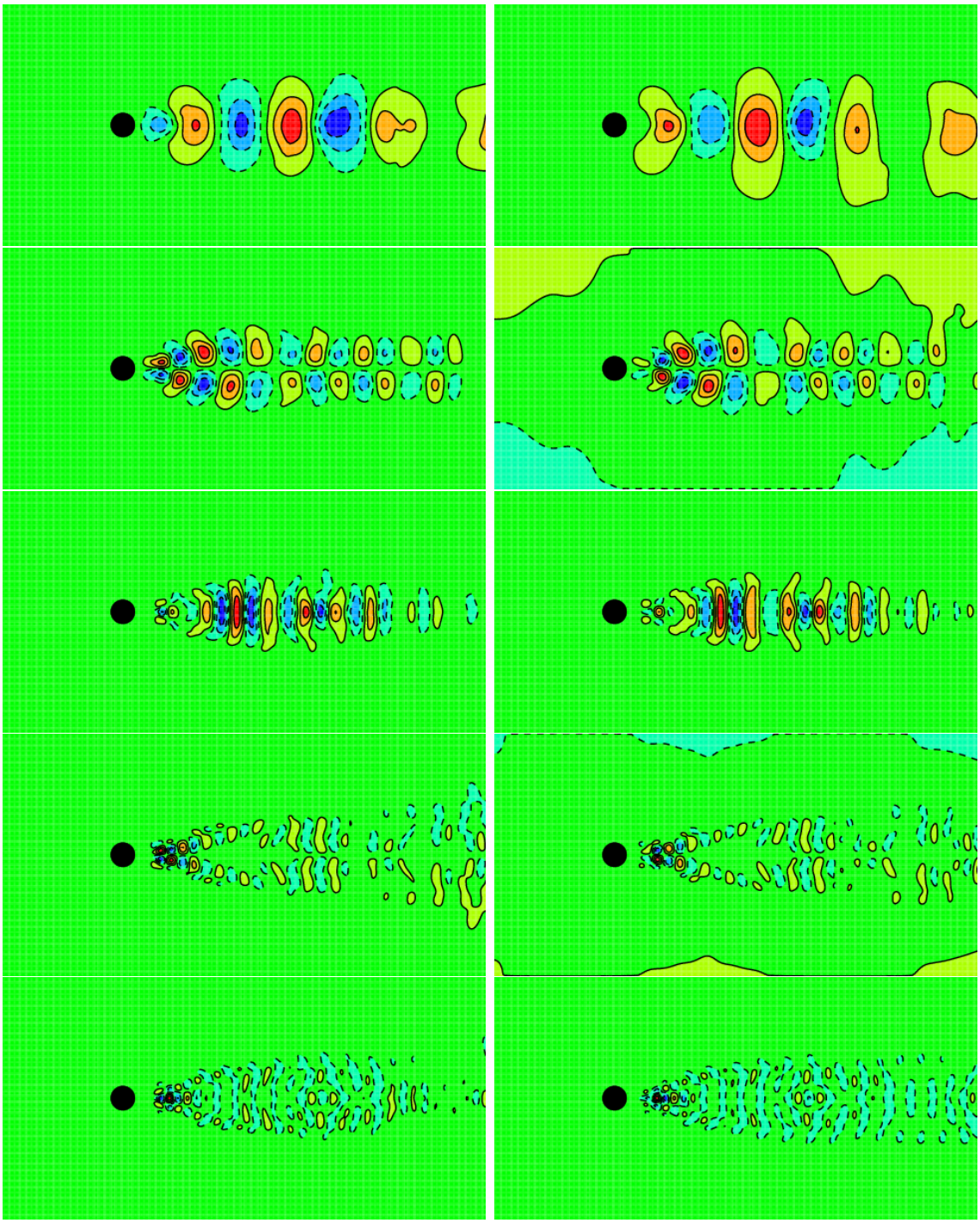

Figure 10.9: *Normalized stream function of first 4 pairs adjoint DMD modes at periodic wake shedding stage.*

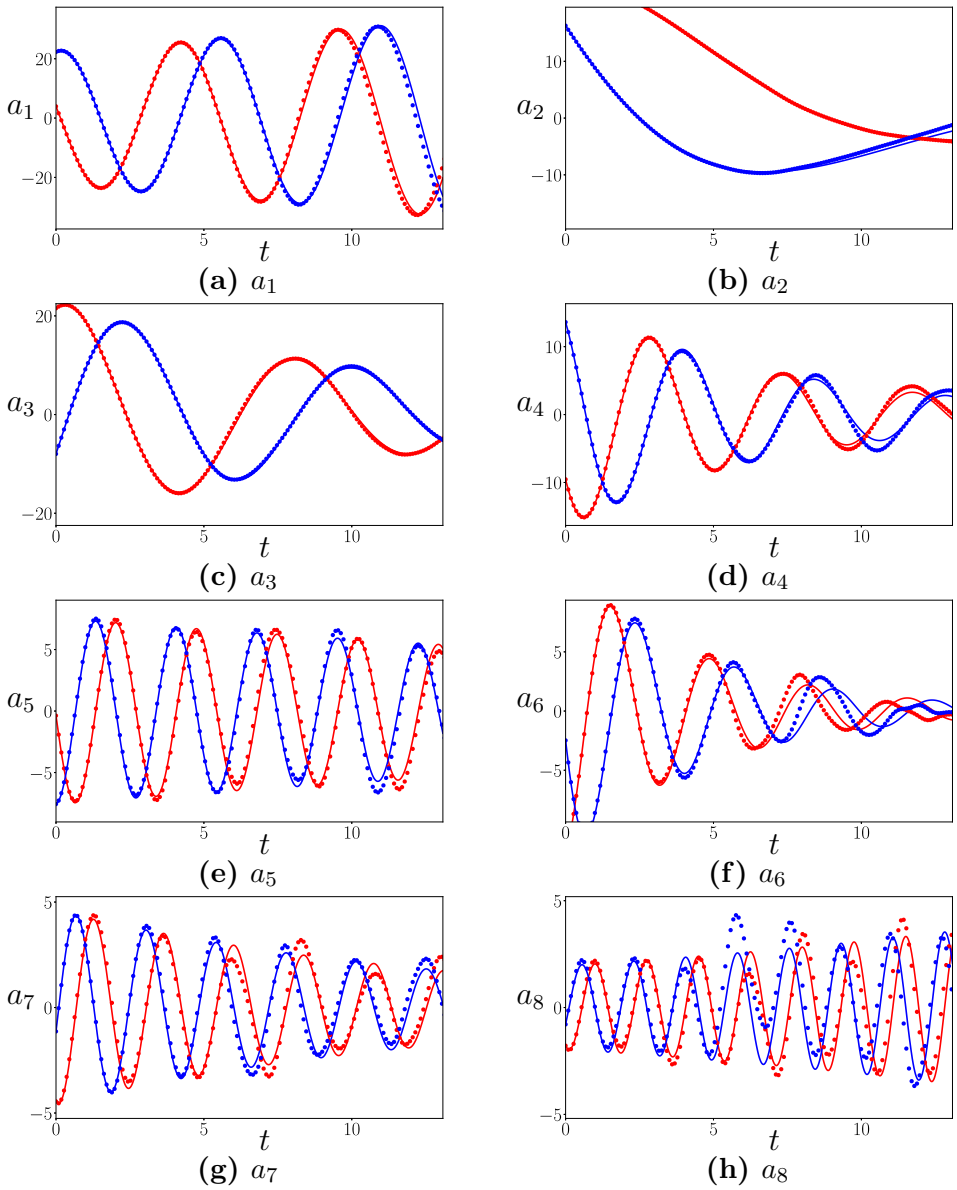

Figure 10.10: *ROM result for the first 8 modes. Solid line from DNS result, and dots for ROM. Red for real part blue for imaginary part.*

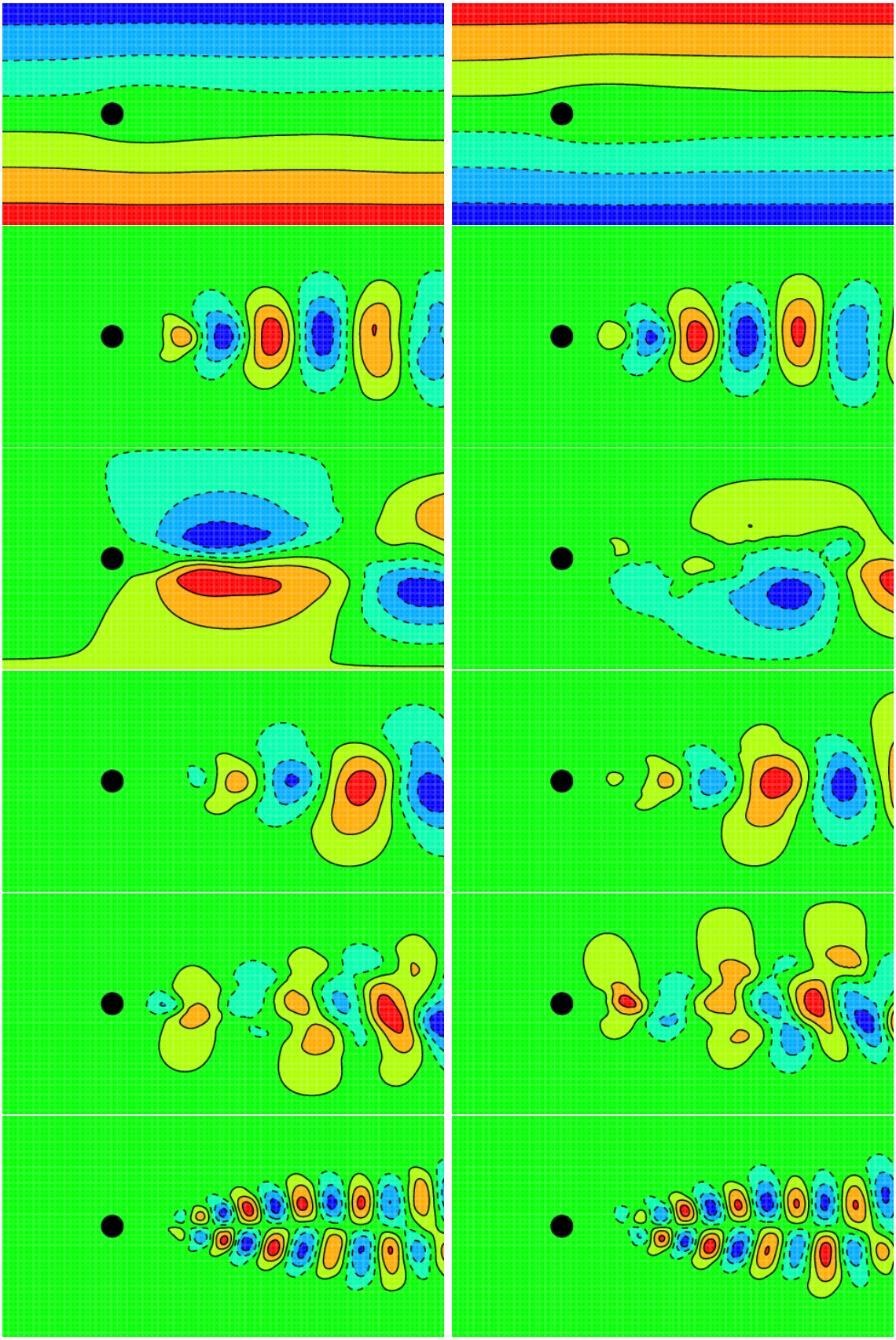

Figure 10.11: *Normalized stream function of first 9 DMD modes for wake developing stage. The first row is mean mode (left) and mean flow (right). The following are ϕ_1, ϕ_2, ϕ_3, ϕ_4. The left column is the real part, and right for the imaginary part.*

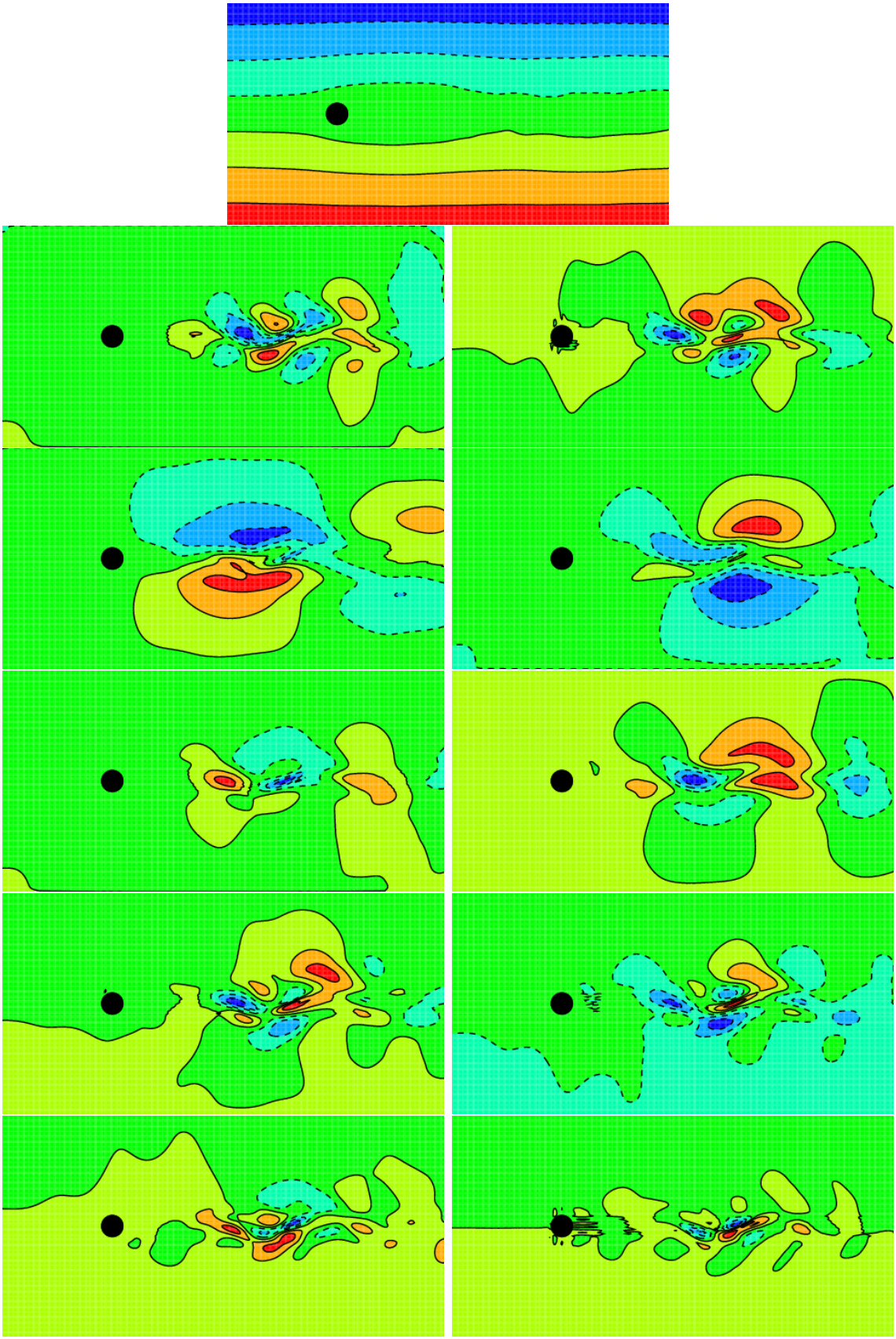

Figure 10.12: *Normalized steam function of first 9 adjoint DMD modes for wake developing stage.*

Chapter 11

Conclusion

In this work, we discussed the linear structure and invariant subspaces properties of dynamics, both linear and nonlinear, via spectrum Koopman decomposition. The nonlinear dynamics differ the linear dynamics in two ways, the locality of Koopman eigenfunction and spectrum and the infinite-dimensionality as nonlinear interaction, the later is conveniently described by the proliferation rule under spectrum Koopman decomposition, making the study of nonlinear dynamics easier.

Spectrums of Koopman operator defined on nonlinear dynamics is studied, and the local Koopman spectrum problem is introduced. Various systems are studied. For an LTI system, its spectrums provide the Koopman spectrum. For an LTV system, the spectrums of the fundamental matrix provide the Koopman spectrum, and the spectrums for periodic LTV system are found to be the Floquet exponents. Proliferation rule was developed for nonlinear observables. For a nonlinear dynamic system, the local spectrum problem is defined through the time-parameterized semi-group Koopman operator acting on it. The hierarchy structure of the nonlinear system is revealed. Dynamics, as well as the eigenvalues, are decomposed into the base and perturbation on top of it. Moreover, proliferation rule recursively proliferates eigenspaces into infinite dimensions because of the nonlinearity. The hierarchy structure is confirmed by the Koopman spectrum distribution in the numerical examples. The continuity of local Koopman spectrums is studied and found to be conditional continuous for the LTV

and nonlinear system, by which the local knowledge of dynamics is extended to the global domain. Using above understanding, the invariant subspaces of the nonlinear systems are the spaces spanned by Koopman eigenfunctions.

For an LTI system, the Koopman decomposition for both linear and nonlinear observables is explicitly obtained by solving the eigenvalue problem of the linear system. For a nonlinear system without an explicit formulation, the hierarchy structure is employed for understanding and computing the Koopman decomposition, by which, the dynamics are decomposed into base dynamics and nonlinear perturbation. The base dynamics can be studied either analytically or numerically. Furthermore, the perturbation is decomposed into a linear and nonlinear part. The linear part is studied via the linear system, then the spectrums are recursively proliferated the nonlinear part. We further demonstrated the GSA technique could be used to compute the Koopman decomposition by assuming small perturbation and separate time scales, or numerically computed by DMD algorithm, a time-averaged version of Koopman decomposition. POD algorithm provides a numerical and time-averaged algorithm for linear structure via Mercer's eigenfunction, which is by solving the eigenvalue problem of the second-order statistics kernel of dynamics.

DMD, a data-driven technique to extract Koopman modes and spectrum, is considered. This method can effectively apply to dynamic systems with constant spectrums. For systems with the variant spectrum, it may be used to capture the transient spectrums, the asymptotic spectrums. In this work, a new framework based generalized eigenvalue problem to extract dynamic relevant information such as frequency, growth, or decaying rate, is developed. This data-driven technique is matrix-free and avoids calculating a linear approximating system as conventional DMD algorithm. Therefore, it avoids the singular or nearly singular issues. An efficient projection approach was developed to transfer the otherwise singular GEV to a regular pencil. Current eigensolver can efficiently solve the regular problem. Different projection subspaces lead to different solutions – a least-square solution projects GEV to the unmodified data space suitable for data with no noise. The resulting DMD-LS algorithm is equivalent to the standard DMD algorithm but numerically more robust. On the other hand, the total least-square solution projects the GEV problem to the modified data space,

performing an unbiased estimation of the dynamic system when data is contaminated with random noise. Since above-proposed projection is orthogonal, projection error is orthogonal to the projected subspace. Increasing data space by including more samplings will reduce the error, therefore more accurate eigenvalues and eigenvectors. The residue of the computed eigenpair of the original GEV problem is proposed to assess the quality of DMD eigenpairs, which is a by-product of generalized DMD formulation. Our algorithm is simple and can be easily parallelized for big or distributed data analysis.

We numerically analyzed examples of primary and secondary instability using the DMD algorithm on the simulated data. Besides the instability modes that appear in linear stability analysis, other nonlinear modes are revealed by those high-order Koopman modes. This work numerically studied the transition process of fluid passing a fixed cylinder at $Re = 50$, when a Hopf bifurcation occurs. The flow system transits from the unstable equilibrium point to the stable limit cycle is examined. During this process, the spectrum of critical Koopman modes (complex conjugate pair) and their high-order derived modes asymptotically falls on the imaginary axis, resulting in infinite-dimensional Koopman modes with the same frequency folding on top of each other, generating the Fourier decomposition of the periodic solution. The Floquet solution is explained similar, by folding the cross-interactions of some Koopman modes with the previous critical group of Koopman modes as the growth rates decrease to 0, the Floquet modes are obtained, as well as their high-order derived ones. Therefore, both the Fourier and Floquet modes are the superposition of infinite-dimensional Koopman modes. The linear structure theory can easily explain some of the exciting flow phenomena. Besides the periodic solution and Floquet solution demonstrated above, the coherent structurer in turbulent flow is simply the invariant Koopman modes. The resonance effects occurred in nonlinear dynamics. The energy cascading from low frequency to high one, or energy backscattering merely is the nonlinear interaction of different Koopman modes.

A method for computing reduced-order models for incompressible flow has been developed based on DMD modes. We proposed the usage of the adjoint DMD modes to simplify the resulting Galerkin projection equations. The mean mode is suggested as a straightforward approach to satisfy the boundary condition. We solved the DMD modes ranking and selecting

by the introduction of energy criterion, and also notice the non-orthogonality of DMD modes requires more modes to rebuilt the dynamics. Two cases of different stages of a fixed cylinder flow were presented to demonstrate our method. ROM results show that the rebuilt system keeps the same dynamics of the original.

11.1 Future work

The reason to introduce the local Koopman spectrum is to include those important spectrums that appear in nonlinear dynamic systems. However, without developing a thorough theory for the local Koopman spectrum problem, the newly developed theory is only rigorous for bounded operators, which may limit its application. My future work is to develop a rigorous mathematic framework for the local Koopman spectrum problem, which involves the work on perturbation theory for unbounded operator and may require close collaboration with other experts in the field of applied math.

The extension of current work may also involve an extension of its application to practical but more complicated problems, such as using DMD analysis on turbulent flows in engineering problems with complex geometry and various flow conditions. Such analyses may lead to better understanding of flow mechanism and provide suitable flow control strategies.

Bibliography

Nadir Abdessemed, Atul S Sharma, SJ Sherwin, and V Theofilis. Transient growth analysis of the flow past a circular cylinder. *Physics of Fluids*, 21(4):044103, 2009.

John Adams, Paul Swarztrauber, and Roland Sweet. Fishpak: A package of fortran subprograms for the solution of separable elliptic partial differential equations. *The National Center for Atmospheric Research, Boulder, CO*, 1980.

E. Anderson, Z. Bai, C. Bischof, S. Blackford, J. Demmel, J. Dongarra, J. Du Croz, A. Greenbaum, S. Hammarling, A. McKenney, and D. Sorensen. *LAPACK Users' Guide*. Society for Industrial and Applied Mathematics, Philadelphia, PA, third edition, 1999. ISBN 0-89871-447-8 (paperback).

Panos J Antsaklis and Anthony N Michel. *A linear systems primer*, volume 1. Birkhäuser Boston, 2007.

Shervin Bagheri. Koopman-mode decomposition of the cylinder wake. *Journal of Fluid Mechanics*, 726:596–623, 2013.

Maciej J Balajewicz, Earl H Dowell, and Bernd R Noack. Low-dimensional modelling of high-reynolds-number shear flows incorporating constraints from the navier–stokes equation. *Journal of Fluid Mechanics*, 729:285–308, 2013.

Dwight Barkley and Ronald D Henderson. Three-dimensional floquet stability analysis of the wake of a circular cylinder. *Journal of Fluid Mechanics*, 322:215–241, 1996.

Matthew F Barone, Irina Kalashnikova, Daniel J Segalman, and Heidi K Thornquist. Stable galerkin reduced order models for linearized compressible flow. *Journal of Computational Physics*, 228(6):1932–1946, 2009.

Patrick Beaudan and Parviz Moin. Numerical experiments on the flow past a circular cylinder at sub-critical reynolds number. Technical report, STANFORD UNIV CA THERMOSCIENCES DIV, 1994.

M Behr, J Liou, R Shih, and TE Tezduyar. Vorticity-streamfunction formulation of unsteady incompressible flow past a cylinder: Sensitivity of the computed flow field to the location of the outflow boundary. *International Journal for Numerical Methods in Fluids*, 12(4): 323–342, 1991.

M Behr, D Hastreiter, S Mittal, and TE Tezduyar. Incompressible flow past a circular cylinder: dependence of the computed flow field on the location of the lateral boundaries. *Computer Methods in Applied Mechanics and Engineering*, 123(1-4):309–316, 1995.

Eberhard Berger and Rudolf Wille. Periodic flow phenomena. *Annual Review of Fluid Mechanics*, 4(1):313–340, 1972.

DA Bistrian and IM Navon. An improved algorithm for the shallow water equations model reduction: Dynamic mode decomposition vs pod. *International Journal for Numerical Methods in Fluids*, 78(9):552–580, 2015.

Sergio Bittanti and Patrizio Colaneri. *Periodic systems: filtering and control*, volume 5108985. Springer Science & Business Media, 2009.

Gregory Boutry, Michael Elad, Gene H Golub, and Peyman Milanfar. The generalized eigenvalue problem for nonsquare pencils using a minimal perturbation approach. *SIAM Journal on Matrix Analysis and Applications*, 27(2):582–601, 2005.

William E Boyce, Richard C DiPrima, and Douglas B Meade. *Elementary differential equations and boundary value problems*, volume 9. Wiley New York, 1992.

David L Brown, Ricardo Cortez, and Michael L Minion. Accurate projection methods for the incompressible navier–stokes equations. *Journal of computational physics*, 168(2):464–499, 2001.

Bingni W Brunton, Lise A Johnson, Jeffrey G Ojemann, and J Nathan Kutz. Extracting spatial–temporal coherent patterns in large-scale neural recordings using dynamic mode decomposition. *Journal of neuroscience methods*, 258:1–15, 2016.

Marko Budišić, Ryan Mohr, and Igor Mezić. Applied koopmanism. *Chaos: An Interdisciplinary Journal of Nonlinear Science*, 22(4):047510, 2012.

Oscar Buneman. A compact non-iterative poisson solver. *SUIPR report*, 294, 1969.

Alfredo Buttari, Julien Langou, Jakub Kurzak, and Jack Dongarra. Parallel tiled qr factorization for multicore architectures. *Concurrency and Computation: Practice and Experience*, 20(13):1573–1590, 2008.

L Cattafesta, III, S Garg, M Choudhari, F Li, L Cattafesta, III, S Garg, M Choudhari, and F Li. Active control of flow-induced cavity resonance. In *28th Fluid Dynamics Conference*, page 1804, 1997.

Kevin K Chen, Jonathan H Tu, and Clarence W Rowley. Variants of dynamic mode decomposition: boundary condition, koopman, and fourier analyses. *Journal of nonlinear science*, 22(6):887–915, 2012.

Alexandre Joel Chorin. Numerical solution of the navier-stokes equations. *Mathematics of computation*, 22(104):745–762, 1968.

Delin Chu and Gene H Golub. On a generalized eigenvalue problem for nonsquare pencils. *SIAM Journal on Matrix Analysis and Applications*, 28(3):770–787, 2006.

Earl A Coddington and Norman Levinson. *Theory of ordinary differential equations*. Tata McGraw-Hill Education, 1955.

Predrag Cvitanovic and Bruno Eckhardt. Periodic orbit expansions for classical smooth flows. *Journal of Physics A: Mathematical and General*, 24(5):L237, 1991.

Scott TM Dawson, Maziar S Hemati, Matthew O Williams, and Clarence W Rowley. Characterizing and correcting for the effect of sensor noise in the dynamic mode decomposition. *Experiments in Fluids*, 57(3):42, 2016.

Robert G Dean and Robert A Dalrymple. *Water wave mechanics for engineers and scientists*, volume 2. World Scientific Publishing Company, 1991.

James Demmel, Laura Grigori, Mark Hoemmen, and Julien Langou. Communication-optimal parallel and sequential qr and lu factorizations. *SIAM Journal on Scientific Computing*, 34(1):A206–A239, 2012.

Philip Drazin, William Reid, and FH Busse. Hydrodynamic stability, 1982.

David Eric Edmunds and W Desmond Evans. *Spectral theory and differential operators*. Oxford University Press, 2018.

Mark Embree and Lloyd N Trefethen. Generalizing eigenvalue theorems to pseudospectra theorems. *SIAM Journal on Scientific Computing*, 23(2):583–590, 2001.

N Benjamin Erichson, Steven L Brunton, and J Nathan Kutz. Compressed dynamic mode decomposition for real-time object detection. *Preprint*, 2015.

Mitchell J Feigenbaum. Universal behavior in nonlinear systems. *Physica D: Nonlinear Phenomena*, 7(1-3):16–39, 1983.

Octavian Frederich and Dirk M Luchtenburg. Modal analysis of complex turbulent flow. In *TSFP DIGITAL LIBRARY ONLINE*. Begel House Inc., 2011.

Georg Frobenius, Ferdinand Georg Frobenius, Ferdinand Georg Frobenius, Ferdinand Georg Frobenius, and Germany Mathematician. Über matrizen aus nicht negativen elementen. 1912.

Mohamed Gad-el Hak. Fluid mechanics from the beginning to the third millennium. *International Journal of Engineering Education*, 14(3):177–185, 1998.

Feliks Ruvimovich Gantmakher. *The theory of matrices*, volume 131. American Mathematical Soc., 1998.

Haotian Gao and Mingjun Wei. Global model reduction for flows with moving boundary. In *52nd Aerospace Sciences Meeting, AIAA paper 2014-0222*, page 0222, 2014.

Haotian Gao and Mingjun Wei. Domain decomposition in pod-galerkin projection for flows with moving boundary. In *54th AIAA Aerospace Sciences Meeting, AIAA paper 2016-1102*, page 1102, 2016.

Gene Golub and William Kahan. Calculating the singular values and pseudo-inverse of a matrix. *Journal of the Society for Industrial and Applied Mathematics, Series B: Numerical Analysis*, 2(2):205–224, 1965.

Gene H Golub and Charles F Van Loan. An analysis of the total least squares problem. *SIAM journal on numerical analysis*, 17(6):883–893, 1980.

Jacob Grosek and J Nathan Kutz. Dynamic mode decomposition for real-time background/foreground separation in video. *arXiv preprint arXiv:1404.7592*, 2014.

Francis H Harlow and J Eddie Welch. Numerical calculation of time-dependent viscous incompressible flow of fluid with free surface. *The physics of fluids*, 8(12):2182–2189, 1965.

Maziar Hemati, Eric Deem, Matthew Williams, Clarence W Rowley, and Louis N Cattafesta. Improving separation control with noise-robust variants of dynamic mode decomposition. In *54th AIAA Aerospace Sciences Meeting*, page 1103, 2016.

Maziar S Hemati, Matthew O Williams, and Clarence W Rowley. Dynamic mode decomposition for large and streaming datasets. *Physics of Fluids (1994-present)*, 26(11):111701, 2014.

Maziar S Hemati, Clarence W Rowley, Eric A Deem, and Louis N Cattafesta. De-biasing

the dynamic mode decomposition for applied koopman spectral analysis of noisy datasets. *Theoretical and Computational Fluid Dynamics*, 31(4):349–368, 2017.

Ronald D Henderson. Nonlinear dynamics and pattern formation in turbulent wake transition. *Journal of Fluid Mechanics*, 352:65–112, 1997.

Thorwald Herbert. Secondary instability of boundary layers. *Annual review of fluid mechanics*, 20(1):487–526, 1988.

P. Holmes, J.L. Lumley, and G. Berkooz. *Turbulence, Coherent Structures, Dynamical Systems and Symmetry*. Cambridge University Press, 1996a.

P Holmes, JL Lumley, and G Berkooz. *Turbulence, Coherent Structures, Dynamical Systems and Symmetry*. Cambridge University Press, New York, 1996b.

Miloš Ilak and Clarence W Rowley. Modeling of transitional channel flow using balanced proper orthogonal decomposition. *Physics of Fluids*, 20(3):034103, 2008.

MKL Intel. Intel math kernel library. 2007.

CP Jackson. A finite-element study of the onset of vortex shedding in flow past variously shaped bodies. *Journal of fluid Mechanics*, 182:23–45, 1987.

Mihailo R Jovanović, Peter J Schmid, and Joseph W Nichols. Sparsity-promoting dynamic mode decomposition. *Physics of Fluids*, 26(2):024103, 2014.

Bo Kågström and Peter Poromaa. Computing eigenspaces with specified eigenvalues of a regular matrix pair (a, b) and condition estimation: theory, algorithms and software. *Numerical Algorithms*, 12(2):369–407, 1996.

Tosio Kato. *Perturbation theory for linear operators*, volume 132. Springer Science & Business Media, 2013.

Jirair K Kevorkian and Julian D Cole. *Multiple scale and singular perturbation methods*, volume 114. Springer Science & Business Media, 2012.

John Kim and Parviz Moin. Application of a fractional-step method to incompressible navier-stokes equations. *Journal of computational physics*, 59(2):308–323, 1985.

Bernard O Koopman. Hamiltonian systems and transformation in hilbert space. *Proceedings of the National Academy of Sciences of the United States of America*, 17(5):315, 1931.

Arthur G Kravchenko, Parviz Moin, and Karim Shariff. B-spline method and zonal grids for simulations of complex turbulent flows. *Journal of Computational Physics*, 151(2): 757–789, 1999.

Peter A Kuchment. *Floquet theory for partial differential equations*, volume 60. Birkhäuser, 2012.

MT Landahl. Wave mechanics of breakdown. *Journal of Fluid Mechanics*, 56(4):775–802, 1972.

LD Landau and EM Lifshitz. *Course of theoretical physics. vol. 6: Fluid mechanics*. London, 1959.

A Lasota and James A Yorke. Exact dynamical systems and the frobenius-perron operator. *Transactions of the american mathematical society*, 273(1):375–384, 1982.

Andrzej Lasota and Michael C Mackey. *Chaos, fractals, and noise: stochastic aspects of dynamics*, volume 97. Springer Science & Business Media, 2013.

J Li, A Chambarel, M Donneaud, and R Martin. Numerical study of laminar flow past one and two circular cylinders. *Computers & fluids*, 19(2):155–170, 1991.

C Liu, X Zheng, and CH Sung. Preconditioned multigrid methods for unsteady incompressible flows. *Journal of Computational physics*, 139(1):35–57, 1998.

Yi Liu and W Steve Shepard Jr. Dynamic force identification based on enhanced least squares and total least-squares schemes in the frequency domain. *Journal of sound and vibration*, 282(1-2):37–60, 2005.

Edward N Lorenz. Deterministic nonperiodic flow. *Journal of the atmospheric sciences*, 20 (2):130–141, 1963.

VA Marchenko. Sturm-liouville operators and their applications. *Kiev Izdatel Naukova Dumka*, 1977.

Kristyn J Maschhoff and Danny C Sorensen. P_arpack: An efficient portable large scale eigenvalue package for distributed memory parallel architectures. In *International Workshop on Applied Parallel Computing*, pages 478–486. Springer, 1996.

Robert M May. Chaos and the dynamics of biological populations. *Nuclear Physics B-Proceedings Supplements*, 2:225–245, 1987.

Philippe Meliga and Jean-Marc Chomaz. An asymptotic expansion for the vortex-induced vibrations of a circular cylinder. *Journal of Fluid Mechanics*, 671:137–167, 2011.

James Mercer. Xvi. functions of positive and negative type, and their connection the theory of integral equations. *Philosophical transactions of the royal society of London. Series A, containing papers of a mathematical or physical character*, 209(441-458):415–446, 1909.

Carl D Meyer. *Matrix analysis and applied linear algebra*, volume 71. Siam, 2000.

Igor Mezić. Spectral properties of dynamical systems, model reduction and decompositions. *Nonlinear Dynamics*, 41(1-3):309–325, 2005.

GD Miller and Charles HK Williamson. Control of three-dimensional phase dynamics in a cylinder wake. *Experiments in Fluids*, 18(1-2):26–35, 1994.

R. Mittal, H. Dong, M. Bozkurttas, FM Najjar, A. Vargas, and A. Von Loebbecke. A versatile sharp interface immersed boundary method for incompressible flows with complex boundaries. *Journal of Computational Physics*, 227(10):4825–4852, 2008.

Cleve B Moler and Gilbert W Stewart. An algorithm for generalized matrix eigenvalue problems. *SIAM Journal on Numerical Analysis*, 10(2):241–256, 1973.

Bernd R Noack, Konstantin Afanasiev, MAREK MORZYŃSKI, Gilead Tadmor, and Frank Thiele. A hierarchy of low-dimensional models for the transient and post-transient cylinder wake. *Journal of Fluid Mechanics*, 497:335–363, 2003.

Bernd R Noack, Paul Papas, and Peter A Monkewitz. The need for a pressure-term representation in empirical galerkin models of incompressible shear flows. *Journal of Fluid Mechanics*, 523:339–365, 2005.

Christoffer Norberg, A Sohankar, and L Davidson. Numerical simulation of unsteady flows around a square twodimensional cylinder. In *Twelfth Australian Fluid Mechanics Conference*, pages 517–520, 1995.

Steven A Orszag and Lawrence C Kells. Transition to turbulence in plane poiseuille and plane couette flow. *Journal of Fluid Mechanics*, 96(1):159–205, 1980.

Steven A Orszag and Anthony T Patera. Secondary instability of wall-bounded shear flows. *Journal of Fluid Mechanics*, 128:347–385, 1983.

Jeongyoung Park, Kiyoung Kwon, and Haecheon Choi. Numerical solutions of flow past a circular cylinder at reynolds numbers up to 160. *KSME international Journal*, 12(6): 1200–1205, 1998.

Oskar Perron. Zur theorie der matrices. *Mathematische Annalen*, 64(2):248–263, 1907.

Helene Persillon and Marianna Braza. Physical analysis of the transition to turbulence in the wake of a circular cylinder by three-dimensional navier–stokes simulation. *Journal of Fluid Mechanics*, 365:23–88, 1998.

Stephen B Pope. Turbulent flows, 2001.

O Posdziech and R Grundmann. A systematic approach to the numerical calculation of fundamental quantities of the two-dimensional flow over a circular cylinder. *Journal of Fluids and Structures*, 23(3):479–499, 2007.

Oliver Posdziech and Roger Grundmann. Numerical simulation of the flow around an infinitely long circular cylinder in the transition regime. *Theoretical and Computational Fluid Dynamics*, 15(2):121–141, 2001.

Anil Prasad and Charles HK Williamson. Three-dimensional effects in turbulent bluff-body wakes. *Journal of Fluid Mechanics*, 343:235–265, 1997.

Joshua L Proctor and Philip A Eckhoff. Discovering dynamic patterns from infectious disease data using dynamic mode decomposition. *International health*, 7(2):139–145, 2015.

M Provansal, C Mathis, and L Boyer. Bénard-von kármán instability: transient and forced regimes. *Journal of Fluid Mechanics*, 182:1–22, 1987.

Bashar R Qawasmeh and Mingjun Wei. Low-dimensional models for compressible temporally developing shear layers. *Journal of Fluid Mechanics*, 731:364–393, 2013.

Ruben Rathnasingham and Kenneth S Breuer. System identification and control of a turbulent boundary layer. *Physics of Fluids*, 9(7):1867–1869, 1997.

M. Reed and B. Simon. *Methods of modern mathematical physics: Functional analysis*. Methods of Modern Mathematical Physics. Academic Press, 1972. ISBN 9780125850018.

M. Reed and B. Simon. *Methods of Modern Mathematical Physics: Vol.: 4. : Analysis of Operators*. Academic Press, 1978.

Osborne Reynolds. Xxix. an experimental investigation of the circumstances which determine whether the motion of water shall be direct or sinuous, and of the law of resistance in parallel channels. *Philosophical Transactions of the Royal society of London*, (174):935–982, 1883.

Jean Paul Richter et al. *The notebooks of Leonardo da Vinci*, volume 2. Courier Corporation, 1970.

A. Roshko and United States. National Advisory Committee for Aeronautics. *On the Development of Turbulent Wakes from Vortex Streets*. National Advisory Committee for Aeronautics, 1954.

Clarence W Rowley, Igor Mezić, Shervin Bagheri, Philipp Schlatter, and Dan S Henningson. Spectral analysis of nonlinear flows. *Journal of fluid mechanics*, 641:115–127, 2009.

David Ruelle and Floris Takens. On the nature of turbulence. *Les rencontres physiciens-mathématiciens de Strasbourg-RCP25*, 12:1–44, 1971.

J Scott Russell. Report on waves. In *14th meeting of the British Association for the Advancement of Science*, volume 311, page 1844, 1844.

M. Schlegel, B. R. Noack, O. Lehmann, E. Gröschel, W. Schröder, M. Wei, J. B. Freund, and P. Jordan. On least-order flow representation for aerodynamics and aeroacoustics. *J. Fluid Mech.* (in preparation), 2009.

Peter J Schmid. Dynamic mode decomposition of numerical and experimental data. *Journal of fluid mechanics*, 656:5–28, 2010.

Peter J Schmid. Application of the dynamic mode decomposition to experimental data. *Experiments in fluids*, 50(4):1123–1130, 2011.

Peter J Schmid and Dan S Henningson. *Stability and transition in shear flows*, volume 142. Springer Science & Business Media, 2012.

Peter J Schmid, Knud Erik Meyer, and Oliver Pust. Dynamic mode decomposition and proper orthogonal decomposition of flow in a lid-driven cylindrical cavity. In *8th International Symposium on Particle Image Velocimetry*, pages 25–28, 2009.

Abu Seena and Hyung Jin Sung. Dynamic mode decomposition of turbulent cavity flows for self-sustained oscillations. *International Journal of Heat and Fluid Flow*, 32(6):1098–1110, 2011.

Yuriy Shmaliy. *Continuous-time systems*. Springer Science & Business Media, 2007.

Denis Sipp and Anton Lebedev. Global stability of base and mean flows: a general approach and its applications to cylinder and open cavity flows. *Journal of Fluid Mechanics*, 593: 333–358, 2007.

Danny C Sorensen. Implicit application of polynomial filters in ak-step arnoldi method. *Siam journal on matrix analysis and applications*, 13(1):357–385, 1992.

Danny C Sorensen. Implicitly restarted arnoldi/lanczos methods for large scale eigenvalue calculations. In *Parallel Numerical Algorithms*, pages 119–165. Springer, 1997.

Gilbert W Stewart. A parallel implementation of the qr-algorithm. *Parallel Computing*, 5 (1-2):187–196, 1987.

Steven H Strogatz. *Nonlinear dynamics and chaos: with applications to physics, biology, chemistry, and engineering*. CRC Press, 2018.

John Trevor Stuart. On the non-linear mechanics of hydrodynamic stability. *Journal of Fluid Mechanics*, 4(1):1–21, 1958.

JT Stuart. On the non-linear mechanics of wave disturbances in stable and unstable parallel flows part 1. the basic behaviour in plane poiseuille flow. *Journal of Fluid Mechanics*, 9 (3):353–370, 1960.

Mehdi Tabandeh, Mingjun Wei, and James P Collins. On the symmetrization in pod-galerkin model for linearized compressible flows. In *54th AIAA Aerospace Sciences Meeting, AIAA paper 2016-1106*, page 1106, 2016.

Shaojie Tang and Nadine Aubry. On the symmetry breaking instability leading to vortex shedding. *Physics of Fluids*, 9(9):2550–2561, 1997.

Françoise Tisseur and Karl Meerbergen. The quadratic eigenvalue problem. *SIAM review*, 43(2):235–286, 2001.

Gilles Tissot, Laurent Cordier, Nicolas Benard, and Bernd R Noack. Model reduction using dynamic mode decomposition. *Comptes Rendus Mécanique*, 342(6-7):410–416, 2014.

Jason Tran, Jayant Sirohi, Haotian Gao, and Mingjun Wei. Reduced-order modeling of loads and deformation of a flexible flapping wing. In *56th AIAA SDM Conference, AIAA paper 2015-0177*, page 0177, 2015.

Lloyd N Trefethen. Pseudospectra of matrices. *Numerical analysis*, 91:234–266, 1991.

Lloyd N Trefethen and Mark Embree. *Spectra and pseudospectra: the behavior of nonnormal matrices and operators*. Princeton University Press, 2005.

D. J. Tritton. Experiments on the flow past a circular cylinder at low reynolds numbers. *Journal of Fluid Mechanics*, 6(4):547–567, 1959.

Jonathan H Tu, Clarence W Rowley, Dirk M Luchtenburg, Steven L Brunton, and J Nathan Kutz. On dynamic mode decomposition: Theory and applications. *Journal of Computational Dynamics*, 1(2):391–421, 2014.

Paul Van Dooren. The computation of kronecker's canonical form of a singular pencil. *Linear Algebra and its Applications*, 27:103–140, 1979.

Paul Van Dooren. The generalized eigenstructure problem in linear system theory. *IEEE Transactions on Automatic Control*, 26(1):111–129, 1981.

Sabine Van Huffel and Joos Vandewalle. *The total least squares problem: computational aspects and analysis*, volume 9. Siam, 1991.

Miguel R Visbal and Datta V Gaitonde. High-order-accurate methods for complex unsteady subsonic flows. *AIAA journal*, 37(10):1231–1239, 1999.

David S Watkins. *The matrix eigenvalue problem: GR and Krylov subspace methods*, volume 101. Siam, 2007.

M Wei and CW Rowley. Low-dimensional models of a temporally evolving free shear layer. *Journal of Fluid Mechanics*, 228:113–134, 2009a.

Mingjun Wei and Clarence W. Rowley. Low-dimensional models of a temporally evolving free shear layer. *J. Fluid Mech.*, 618:113–134, 2009b.

Mingjun Wei, Bashar R. Qawasmeh, Matthew Barone, Bart G. van Bloemen Waanders, and Lin Zhou. Low-dimensional model of spatial shear layers. *Physics of Fluids*, 24(1):014108, 2012. doi: 10.1063/1.3678016.

James H Wilkinson. Linear differential equations and kronecker's canonical form. In *Recent advances in numerical analysis*, pages 231–265. Elsevier, 1978.

James Hardy Wilkinson. *The algebraic eigenvalue problem*, volume 662. Oxford Clarendon, 1965.

James Hardy Wilkinson. Kronecker's canonical form and the qz algorithm. *Linear Algebra and its Applications*, 28:285–303, 1979.

Matthew O Williams, Ioannis G Kevrekidis, and Clarence W Rowley. A data–driven approximation of the koopman operator: Extending dynamic mode decomposition. *Journal of Nonlinear Science*, 25(6):1307–1346, 2015.

Charles HK Williamson. Vortex dynamics in the cylinder wake. *Annual review of fluid mechanics*, 28(1):477–539, 1996.

CHK Williamson. The existence of two stages in the transition to three-dimensionality of a cylinder wake. *The Physics of fluids*, 31(11):3165–3168, 1988.

CHK Williamson. The natural and forced formation of spot-like 'vortex dislocations' in the transition of a wake. *Journal of Fluid Mechanics*, 243:393–441, 1992.

Arthur T Winfree. Biological rhythms and the behavior of populations of coupled oscillators. *Journal of theoretical biology*, 16(1):15–42, 1967.

Thomas G Wright and Lloyd N Trefethen. Large-scale computation of pseudospectra using arpack and eigs. *SIAM Journal on Scientific Computing*, 23(2):591–605, 2001.

Thomas G Wright and Lloyd N Trefethen. Pseudospectra of rectangular matrices. *IMA Journal of Numerical Analysis*, 22(4):501–519, 2002.

M Wu. A note on stability of linear time-varying systems. *IEEE transactions on Automatic Control*, 19(2):162–162, 1974.

Fuzhen Zhang. *The Schur complement and its applications*, volume 4. Springer Science & Business Media, 2006.

Hong-Quan Zhang, Uwe Fey, Bernd R Noack, Michael König, and Helmut Eckelmann. On the transition of the cylinder wake. *Physics of Fluids*, 7(4):779–794, 1995.

Jianfeng Zhang and Charles Dalton. A three-dimensional simulation of a steady approach flow past a circular cylinder at low reynolds number. *International Journal for Numerical Methods in Fluids*, 26(9):1003–1022, 1998.

Qingshan Zhang, Yingzheng Liu, and Shaofei Wang. The identification of coherent structures using proper orthogonal decomposition and dynamic mode decomposition. *Journal of Fluids and Structures*, 49:53–72, 2014.

Wei Zhang and Mingjun Wei. Model order reduction using dmd modes and adjoint dmd modes. In *8th AIAA Theoretical Fluid Mechanics Conference*, page 3482, 2017.

Bin Zhou. On asymptotic stability of linear time-varying systems. *Automatica*, 68:266–276, 2016.

Vladimir Ivanovich Zubov. *Mathematical methods for the study of automatic control systems*. Pergamon Press, 1962.

Appendix A

An alternative of model selection method

We noticed Jovanović Jovanović et al. (2014), uses the sparsity-promoting DMD for ranking and selecting the DMD modes. We find their method can be used to minimize the decomposition error. This optimization procedure is detailed below. We include it here not only because it gives an optimized method to calculate temporal coefficients of DMD modes, but also an alternative way to rank DMD modes, as *alpha* in the diagonal matrix can represent corresponding mode's 'influence'.

This approach is based on the DMD decomposition of each snapshots

$$x_i = \sum_{k=0}^{N-1} \phi_k \lambda_k^i \alpha_0 \tag{A.1}$$

in matrix form

$$X = [x_0, x_1, \cdots, x_{N-1}] = \underbrace{[\phi_0, \phi_1, \cdots, \phi_{N-1}]}_{\Phi} \underbrace{\begin{bmatrix} \alpha_0 & & & \\ & \alpha_1 & & \\ & & \cdots & \\ & & & \alpha_{N-1} \end{bmatrix}}_{D_\alpha} \underbrace{\begin{bmatrix} 1 & \lambda_0 & \cdots & \lambda_0^{N-1} \\ 1 & \lambda_1 & \cdots & \lambda_1^{N-1} \\ \vdots & \vdots & \cdots & \vdots \\ 1 & \lambda_{N-1} & \cdots & \lambda_{N-1}^{N-1} \end{bmatrix}}_{V_{and}} \tag{A.2}$$

Where Φ is DMD modes; V_{and} is the time coefficients and diagonal matrix D_α is the magnitude of each modes. If we drew analogous this form (A.2) with POD. D_α is can be viewed as the 'influence' of each modes and can be used to rank DMD modes as for POD.

An optimal D_α will give the minimal error.

$$J(\alpha) = ||X - \Phi D_\alpha V_{and}||_F^2 = \alpha^* P \alpha - q^* \alpha - \alpha^* q + s \tag{A.3}$$

where

$$P \triangleq (W^* W) \circ (\overline{V_{and} V_{and}^*}), \quad q \triangleq \overline{diag(V_{and} V \Sigma^* W)}, \quad s \triangleq trace(\Sigma^* \Sigma).$$

W is the eigenvector matrix from (10.7), and V is from (10.6). The ($\circ$) operator is Hadamard product for matrix. We noticed the two sides of Hadamard product are positive-definite matrix. Following Schur product theorem Zhang (2006) , P is also positive-definite. Then the quadratic minimization problem is well determined and have a unique solution:

$$\alpha^0 = P^{-1} q \tag{A.4}$$

As an result, we can obtain an error-minimized DMD temporal coefficients (A.5).

$$a(i,t) = \alpha_i^0 \lambda_i^t \tag{A.5}$$

To distinguish with our projection method, we call it optimization method.

Appendix B

Floquet system and coordinate transformation

From Floquet theory in chapter 2.3.2, the periodic LTV system

$$\dot{X}(t) = A(t)X(t), \quad A(t+T) = A(t) \tag{B.1}$$

has the solution

$$X(t) = P(t)e^{tR}. \tag{B.2}$$

Substitute the solution into original equation, the relation of $P(t)$, R and $A(t)$ is obtained

$$\dot{P}(t)e^{tR} + P(t)Re^{tR} = A(t)P(t)e^{tR}. \tag{B.3}$$

$\frac{de^{tR}}{dt} = Re^{tR}$ is derived from equation 2.11. Times e^{-tR} from both side

$$\dot{P}(t) = A(t)P(t) - P(t)R \tag{B.4}$$

The time-dependent coordinate transformation

$$X(t) = P(t)Y(t) \tag{B.5}$$

transfer the LTV system to

$$\dot{P}(t)Y(t) + P(t)\dot{Y}(t) = A(t)P(t)Y(t) \tag{B.6}$$

substitute B.3 into above equation

$$\left(A(t)P(t) - P(t)R\right)Y(t) + P(t)\dot{Y}(t) = A(t)P(t)Y(t) \tag{B.7}$$

canceling $A(t)P(t)Y(t)$ from both side and time $P(t)^{-1}$ from left on both side

$$\dot{Y} = RY \tag{B.8}$$

Thus the $X(t) = P(t)Y(t)$ transfer the periodic LTV to LTI system.

If we further assume R is diagonalizable and $R = V\Lambda V^{-1}$, let

$$Z(t) = V^{-1}Y = V^{-1}P(t)^{-1}X(t) \tag{B.9}$$

Then $Z(t)$ satisfy the equation

$$\dot{Z}(t) = \Lambda Z(t) \tag{B.10}$$

which gives the solution

$$\begin{aligned} Z(t) &= V^{-1}P(t)^{-1}X(t) \\ &= e^{t\Lambda}Z(0) = e^{t\Lambda}V^{-1}P(0)^{-1}X(0) \end{aligned} \tag{B.11}$$

which can be reformulated to

$$X(t) = P(t)Ve^{t\Lambda}V^{-1}P(0)^{-1}X(0). \tag{B.12}$$

Appendix C

Multi-scale asymptotic expansion for Navier-Stokes equation

The Navier-Stokes equation can be solve by the asymptotic expansion, which is usually performed to study the nonlinear dynamics. As stated in chapter 3.2, for weakly nonlinear case, it is often found the dynamics exhibit disparate time scale motion, the fast time scale osciallation and slow scale change of magnitude. Stuart (1960) found the time scale to be

$$\tau \equiv \epsilon^2 t \tag{C.1}$$

where $\epsilon^2 = \frac{1}{Re_c} - \frac{1}{Re}$. Thus the time derivative will be modified as

$$\frac{\partial}{\partial t} q(t,\tau) = \frac{\partial}{\partial t} q(t,\tau) + \epsilon^2 \frac{\partial}{\partial \tau} q(t,\tau) \tag{C.2}$$

The asymptotic expansion is given by

$$\boldsymbol{q}(t) = \boldsymbol{q}_0 + \epsilon \boldsymbol{q}_1(t,\tau) + \epsilon^2 \boldsymbol{q}_2(t,\tau) + \epsilon^3 \boldsymbol{q}_3(t,\tau) + \cdots . \tag{C.3}$$

where $\boldsymbol{q} = \begin{bmatrix} \boldsymbol{u} \\ p \end{bmatrix}$.

Substitute equation (C.2) into the incompressible Navier-Stokes equation

$$\begin{aligned} \frac{\partial \boldsymbol{u}}{\partial t} + \nabla \boldsymbol{u} \cdot \boldsymbol{u} &= -\nabla p + \frac{1}{Re} \nabla^2 \cdot \boldsymbol{u}, \\ \nabla \cdot \boldsymbol{u} &= 0. \end{aligned} \tag{C.4}$$

We have

$$\begin{aligned} \frac{\partial \left(\sum_{i=0}^{\infty} \epsilon^i \boldsymbol{u}_i \right)}{\partial t} + \nabla \left(\sum_{i=0}^{\infty} \epsilon^i \boldsymbol{u}_i \right) \cdot \left(\sum_{i=0}^{\infty} \epsilon^i \boldsymbol{u}_i \right) &= -\nabla \left(\sum_{i=0}^{\infty} \epsilon^i p_i \right) + \frac{1}{Re} \nabla^2 \left(\sum_{i=0}^{\infty} \epsilon^i \boldsymbol{u}_i \right), \\ \nabla \cdot \left(\sum_{i=0}^{\infty} \epsilon^i \boldsymbol{u}_i \right) &= 0. \end{aligned} \tag{C.5}$$

Expand the time derivative term in equation (C.3)

$$\frac{\partial \left(\sum_{i=0}^{\infty} \epsilon^i \boldsymbol{u}_i \right)}{\partial t} = \mathbf{0} + \epsilon \left(\frac{\partial \boldsymbol{u}_1}{\partial t} + \epsilon^2 \frac{\partial \boldsymbol{u}_1}{\partial \tau} \right) + \epsilon^2 \left(\frac{\partial \boldsymbol{u}_2}{\partial t} + \epsilon^2 \frac{\partial \boldsymbol{u}_2}{\partial \tau} \right) + \cdots \tag{C.6}$$

The convective term is expand by

$$\begin{aligned} \nabla \left(\sum_{i=0}^{\infty} \epsilon^i \boldsymbol{u}_i \right) \cdot \left(\sum_{i=0}^{\infty} \epsilon^i \boldsymbol{u}_i \right) &= \nabla \boldsymbol{u}_0 \cdot \boldsymbol{u}_0 \\ &+ \epsilon \left(\nabla \boldsymbol{u}_0 \cdot \boldsymbol{u}_1 + \nabla \boldsymbol{u}_1 \cdot \boldsymbol{u}_0 \right) \\ &+ \epsilon^2 \left(\nabla \boldsymbol{u}_0 \cdot \boldsymbol{u}_2 + \nabla \boldsymbol{u}_1 \cdot \boldsymbol{u}_1 + \nabla \boldsymbol{u}_2 \cdot \boldsymbol{u}_0 \right) \\ &+ \epsilon^3 \left(\nabla \boldsymbol{u}_0 \cdot \boldsymbol{u}_3 + \nabla \boldsymbol{u}_1 \cdot \boldsymbol{u}_2 + \nabla \boldsymbol{u}_2 \cdot \boldsymbol{u}_1 + \nabla \boldsymbol{u}_3 \cdot \boldsymbol{u}_0 \right) \\ &\cdots \end{aligned} \tag{C.7}$$

We then insert equations (C.6) and (C.7) into equation (C.5) and collect terms according the order of ϵ.

On ϵ^0, we have

$$\begin{aligned} \mathbf{0} + \nabla \boldsymbol{u}_0 \cdot \boldsymbol{u}_0 &= -\nabla p_0 + \frac{1}{Re} \nabla^2 \cdot \boldsymbol{u}_0, \\ \nabla \cdot \boldsymbol{u}_0 &= 0. \end{aligned} \tag{C.8}$$

This is the steady Navier-Stokes equation. After applying the original boundary condition, the steady base flow $(\boldsymbol{u}_0, p_0)$ is obtained.

On ϵ^1 order

$$\begin{aligned} \frac{\partial \boldsymbol{u}_1}{\partial t} + \nabla \boldsymbol{u}_0 \cdot \boldsymbol{u}_1 + \nabla \boldsymbol{u}_1 \cdot \boldsymbol{u}_0 = -\nabla p_1 + \frac{1}{Re} \nabla^2 \cdot \boldsymbol{u}_1, \\ \nabla \cdot \boldsymbol{u}_1 = 0. \end{aligned} \tag{C.9}$$

It can be rewritten into the form

$$\begin{bmatrix} \frac{\partial}{\partial t} + \nabla() \cdot \boldsymbol{u}_0 + \nabla \boldsymbol{u}_0 \cdot () - \frac{1}{Re} \nabla^2 & \nabla \\ \nabla^T & 0 \end{bmatrix} \boldsymbol{q}_1 = \boldsymbol{0}. \tag{C.10}$$

This is the first-order homogeneous equations, with homogeneous boundary ($\boldsymbol{q}_1$ is the expansion for perturbation). This is an eigenvalue problem, whose solution can be written

$$\boldsymbol{q}_1 = \begin{bmatrix} \boldsymbol{u}_1 \\ p_1 \end{bmatrix} = A(\tau) e^{iwt} \begin{bmatrix} \boldsymbol{U}_1 \\ P_1 \end{bmatrix} + c.c. \tag{C.11}$$

$\begin{bmatrix} \boldsymbol{U}_1 \\ P_1 \end{bmatrix}$ is the most unstable mode, and $A(\tau)$ is its magnitude varying on the slow time scale τ, at initial stage $A(\tau)$ grows at $e^{\epsilon^2 t}$ or e^{τ}.

On ϵ^2 order

$$\begin{aligned} \frac{\partial \boldsymbol{u}_2}{\partial t} + \nabla \boldsymbol{u}_0 \cdot \boldsymbol{u}_2 + \nabla \boldsymbol{u}_1 \cdot \boldsymbol{u}_1 + \nabla \boldsymbol{u}_2 \cdot \boldsymbol{u}_0 = -\nabla p_2 + \frac{1}{Re} \nabla^2 \cdot \boldsymbol{u}_2, \\ \nabla \cdot \boldsymbol{u}_2 = 0. \end{aligned} \tag{C.12}$$

where $\nabla \boldsymbol{u}_1 \cdot \boldsymbol{u}_1$ is the forcing term. We can rewrite the above equations to

$$\begin{bmatrix} \frac{\partial}{\partial t} + \nabla() \cdot \boldsymbol{u}_0 + \nabla \boldsymbol{u}_0 \cdot () - \frac{1}{Re} \nabla^2 & \nabla \\ \nabla^T & 0 \end{bmatrix} \boldsymbol{q}_2 = \begin{bmatrix} |A|^2 \boldsymbol{F}_2^{|A|^2} + A^2 e^{2iwt} \boldsymbol{F}_2^{A^2} + \bar{A}^2 e^{-2iwt} \boldsymbol{F}_2^{\bar{A}^2} \\ 0 \end{bmatrix} \tag{C.13}$$

where the forcing terms $\nabla \boldsymbol{u}_1 \cdot \boldsymbol{u}_1$ is expanded by solution (C.11), and the $\boldsymbol{F}$s are given by

$$\begin{aligned}
\boldsymbol{F}_2^{|A|^2} &= -\nabla \boldsymbol{U}_1^A \cdot \boldsymbol{U}_1^{\bar{A}} - \nabla \boldsymbol{U}_1^{\bar{A}} \cdot \boldsymbol{U}_1^A \\
\boldsymbol{F}_2^{A^2} &= -\nabla \boldsymbol{U}_1^A \cdot \nabla \boldsymbol{U}_1^A \\
\boldsymbol{F}_2^{\bar{A}^2} &= -\nabla \boldsymbol{U}_1^{\bar{A}} \cdot \boldsymbol{U}_1^{\bar{A}}
\end{aligned} \tag{C.14}$$

For each forcing term, the solution is in the following form $A_2^1(\tau)\boldsymbol{U}_2^1$, $A_2^{A^2}\boldsymbol{U}_2^{A^2}e^{j2\omega t}$, $A_2^{\bar{A}^2}\boldsymbol{U}_2^{\bar{A}^2}e^{-j2\omega t}$.

On ϵ^3 order

$$\begin{aligned}
\frac{\partial \boldsymbol{u}_3}{\partial t} + \frac{\partial \boldsymbol{u}_1}{\partial \tau} + \nabla \boldsymbol{u}_0 \cdot \boldsymbol{u}_3 + \nabla \boldsymbol{u}_1 \cdot \boldsymbol{u}_2 + \nabla \boldsymbol{u}_2 \cdot \boldsymbol{u}_1 + \nabla \boldsymbol{u}_3 \cdot \boldsymbol{u}_0 &= -\nabla p_3 + \frac{1}{Re}\nabla^2 \cdot \boldsymbol{u}_3, \\
\nabla \cdot \boldsymbol{u}_3 &= 0.
\end{aligned} \tag{C.15}$$

Now $\nabla \boldsymbol{u}_1 \cdot \boldsymbol{u}_2 + \nabla \boldsymbol{u}_2 \cdot \boldsymbol{u}_1$ is the forcing term on momentum equation. Moreover, the derivative $\frac{\partial \boldsymbol{u}_1}{\partial \tau}$ appears in above equation, and the forcing term include the secular term which has the eigenvalue $\lambda = \sigma + j\omega$. We thus assume the $\frac{\partial \boldsymbol{u}_1}{\partial \tau}$ will equival to those secular terms. Since

$$\begin{aligned}
\nabla \boldsymbol{u}_1 \cdot \boldsymbol{u}_2 + \nabla \boldsymbol{u}_2 \cdot \boldsymbol{u}_1 =& \nabla \left(A e^{j\omega t}\boldsymbol{U}_1 + \bar{A} e^{-j\omega t}\bar{\boldsymbol{U}}_1 \right) \cdot \left(A_2^1 \boldsymbol{U}_2^1 + A_2^{A^2}\boldsymbol{U}_2^{A^2} e^{j2\omega t} + A_2^{\bar{A}^2}\boldsymbol{U}_2^{\bar{A}^2} e^{-j2\omega t} \right) + \\
& \nabla \left(A_2^1 \boldsymbol{U}_2^1 + A_2^{A^2}\boldsymbol{U}_2^{A^2} e^{j2\omega t} + A_2^{\bar{A}^2}\boldsymbol{U}_2^{\bar{A}^2} e^{-j2\omega t} \right) \cdot \left(A e^{j\omega t}\boldsymbol{U}_1 + \bar{A} e^{-j\omega t}\bar{\boldsymbol{U}}_1 \right) \\
=& e^{j\omega t} \left(A A_2^1 \nabla \boldsymbol{U}_1 \cdot \boldsymbol{U}_2^1 + \bar{A} A_2^{A^2} \nabla \bar{\boldsymbol{U}}_1 \cdot \boldsymbol{U}_2^{A^2} + A A_2^1 \nabla \boldsymbol{U}_2^1 \cdot \boldsymbol{U}_1 + \bar{A} A_2^{A^2} \nabla \boldsymbol{U}_2^{A^2} \cdot \bar{\boldsymbol{U}}_1 \right) \\
& + e^{j3\omega t} \left(A A_2^{A^2} \nabla \boldsymbol{U}_1 \cdot \boldsymbol{U}_2^{A^2} + A A_2^{A^2} \nabla \boldsymbol{U}_2^{A^2} \cdot \boldsymbol{U}_1 \right) \\
& + c.c
\end{aligned} \tag{C.16}$$

Those $e^{j\omega t}$ terms are the secular term of the system, which is then removed from above equation with $\frac{\partial \boldsymbol{u}_1}{\partial \tau}$, resulting the Stuart-Landau equation. The remaining terms give the equation

$$\begin{bmatrix} \frac{\partial}{\partial t} + \nabla() \cdot \boldsymbol{u}_0 + \nabla \boldsymbol{u}_0 \cdot () - \frac{1}{Re}\nabla^2 & \nabla \\ \nabla^T & 0 \end{bmatrix} \boldsymbol{q}_3 = \begin{bmatrix} e^{j3\omega t} \left(A A_2^{A^2} \nabla \boldsymbol{U}_1 \cdot \boldsymbol{U}_2^{A^2} + A A_2^{A^2} \nabla \boldsymbol{U}_2^{A^2} \cdot \boldsymbol{U}_1 \right) + c.c. \\ 0 \end{bmatrix} \tag{C.17}$$

We can continue the expanding into high order of ϵ, such as

$$\begin{bmatrix} \frac{\partial}{\partial t} + \nabla() \cdot \boldsymbol{u}_0 + \nabla \boldsymbol{u}_0 \cdot () - \frac{1}{Re}\nabla^2 & \nabla \\ \nabla^T & 0 \end{bmatrix} \boldsymbol{q}_i = \begin{bmatrix} \boldsymbol{f}_i + c.c. \\ 0 \end{bmatrix} \tag{C.18}$$

However, the detailed discussion is beyond the scope of this work.